UNIVERSITY OF OKLAHOMA

GRADUATE COLLEGE

OPTIMIZATION OF ENERGY STORAGE MATERIALS THROUGH AB-INITIO CALCULATIONS AND DEEP LEARNING TECHNIQUES IN MATERIAL SCIENCE

A THESIS

SUBMITTED TO THE GRADUATE FACULTY

in partial fulfillment of the requirements for the

Degree of

DOCTOR OF PHILOSOPHY

by ARJUN SATHYAN KULATHUVAYAL

Norman, Oklahoma

2026

Downloaded from SHAREOK. Persistent Handle URL: https://hdl.handle.net/11244/342825

OPTIMIZATION OF ENERGY STORAGE MATERIALS THROUGH AB-INITIO CALCULATIONS AND DEEP LEARNING TECHNIQUES IN MATERIAL SCIENCE

A THESIS APPROVED FOR THE
SCHOOL OF AEROSPACE AND MECHANICAL ENGINEERING

BY THE COMMITTEE CONSISTING OF

Dr. Yanqing Su (Chair)

Dr. Hanping Ding

Dr. Bin Xu

Dr. Binbin Weng

©Copyright by ARJUN SATHYAN KULATHUVAYAL 2026

All Rights Reserved.

Acknowledgments

I would like to express my sincere gratitude to my advisor, Dr. Yanqing Su, for her continuous guidance, encouragement, and support throughout my doctoral studies. Her insight, patience, and mentorship have been instrumental in shaping this research and my growth as a researcher. I am deeply thankful for the opportunity to work under her supervision.

I would also like to acknowledge Dr. Shuozhi Xu, Dr. Cheng Sun, Dr. Alexander Lindsay and Prof. Sudha Kappalli for their valuable mentorship, constructive discussions, and encouragement at different stages of my academic work. Their perspectives and guidance contributed meaningfully to the scientific direction of this thesis.

This work was made possible through access to several high-performance computing facilities. I gratefully acknowledge the Center for High Performance Computing (CHPC), University of Utah; the Pittsburgh Supercomputing Center (PSC); the Supercomputing Facility at the National Lab of Rockies; and Idaho National Laboratory for providing the computational resources and technical support required for the simulations and machine-learning training carried out in this thesis.

On a personal note, I owe my deepest gratitude to my family. To my amma and achan, thank you for your unconditional love, sacrifices, encouragement, and unwavering belief in me. I am equally grateful to my sister for her constant support and motivation. I would especially like to thank my wife, Megan, for her love, patience, understanding, and endless support throughout this challenging and rewarding journey. I also extend my heartfelt thanks to the Couture family for their warmth and support.

Finally, I am grateful to my friends and colleagues who made this journey memorable. Special thanks to Dr. Namsheer K., Dr. Reshma A. Thomas, Dr. Hemanth D., and Abdulla Mamun for their friendship, discussions, and encouragement.

Table of Contents

Acknowledgments iv

List of Tables viii

List of Figures x

Abstract xxi

1 Introduction 1
1.1 Lithium-ion Batteries; State of the Art 1
1.2 Lithium-Metal Batteries: Merits and Demerits 3
1.3 Solid Electrolyte Interphase: Formation, Structure, and Function 4
1.4 Complexity of the SEI: Chemical and Microstructural Heterogeneity . . 6
1.4.1 Recent Advances in SEI
. 10
1.5 Scope and Objectives 12

2 Motivation and Background 17
2.1 Ionic Transport in the SEI Components 17
2.1.1 Lithium fluoride 20
2.1.2 Lithium carbonate 24
2.1.3 Lithium hydroxide 26
2.1.4 Lithium oxide 27
2.2 Crystalline factors affecting the ionic migration in SEI 30
2.2.1 Crystal Growth Surfaces 30
2.2.2 Grain Boundaries 31
2.3 Battery components affecting the structure of SEI
. 34
2.3.1 Binders 34
2.3.2 Separator 35
2.4 Dendrite Formation and Thermal Runaway 37
2.5 Modeling Diffusion Coefficient 39

3 Methodology 46

3.1 Ab-initio Modeling for Elemental Diffusion . . . 46
3.1.1 Density Functional Theory . . . 46
3.1.2 Migration Barrier From First-principle Calculations . . . 47
3.1.3 Phonon Scattering in SEI Components . . . 52
3.1.4 Modeling Grain and Grain Boundaries . . . 55
3.2 Machine Learning Aspects in Modeling Elemental Diffusion . . . 56
3.2.1 Data Mining: The Diffusion Coefficient . . . 56
3.2.2 Feature Engineering . . . 60
3.2.3 ML Models . . . 63
3.2.4 Generative Models for Materials . . . 67
3.3 Model Evaluation Schemes . . . 69
3.3.1 Evaluation Matrices . . . 69
3.3.2 Uncertainty Quantification . . . 69

4 Predictive Modeling of Diffusion Coefficient . . . 71
4.1 Machine Learned Models of Diffusion Coefficient . . . 72
4.1.1 Impurity Diffusion in Impure Metallic Media . . . 72
4.1.2 Self Diffusion in Impure Metallic Media . . . 77
4.1.3 Self Diffusion in Conventional Alloys . . . 82
4.1.4 Impurity Diffusion in Conventional Alloys . . . 86
4.1.5 Chemical Diffusion in Conventional Alloys . . . 90
4.2 Performance Analysis of Models . . . 95

5 GNN Assisted Modeling of Li-ion Transport in SEI . . . 97
5.1 Motivation for Data-Driven Modeling . . . 98
5.2 Dataset Description and Design Space . . . 102
5.2.1 Diffusion Coefficient Data Generation . . . 103
5.2.2 Grain Diffusion . . . 104
5.2.3 Training Data . . . 109
5.2.4 Graph Neural Network . . . 116
5.2.5 Graph Variational Auto Encoder . . . 119
5.2.6 Training and Validation . . . 120
5.3 Model Performance and Analysis . . . 134

6 MXene Integration in SEI: A Case Study . . . 138
6.1 Motivation for MXene-Assisted SEI Engineering . . . 138
6.2 Literature Review: MXenes as an Auxiliary Layer for SEI . . . 141
6.3 MXene Database and Candidate Selection . . . 144
6.4 High-Throughput Screening . . . 147
6.4.1 MXene–Lithium Electrode: Adsorption Energy . . . 147
6.4.2 Mechanical Property Screening . . . 149
6.4.3 Electronic Compatibility . . . 153
6.4.4 Selection of MXene Candidates for MXene–SEI Interfaces . . . 156

6.4.5 Screening Score . . . 157
6.4.6 Score Analysis . . . 158

7 Conclusions and Future Directions . . . 162
7.1 Modeling Diffusion Coefficient . . . 163
7.2 SEI Design Insights . . . 165
7.3 Future Research Directions . . . 168

Appendix A Computational Resources . . . 172

Appendix B Database and Codes . . . 174

Appendix C Supplementary Figures and Tables . . . 175
C.1 Elemental Diffusion Coefficient Prediction in Conventional Alloys Using Machine Learning . . . 175
C.1.1 Model Feasibility . . . 175
C.1.2 Data Preprocessing Steps . . . 176
C.1.3 Feature Information . . . 177
C.1.4 Standard Deviation of Target Variable and Temperature . . . 178
C.1.5 Uncertainty Analysis . . . 179
C.1.6 Correlation Analysis . . . 180
C.2 Deep learning assisted modeling of Li-ion transport in SEI: A Graph neural network based study . . . 185
C.2.1 SEI Components Considered for GNN Predictive Modeling . . . 185
C.2.2 Construction of Heterogeneous Interfaces . . . 186
C.2.3 Feature Information . . . 189
C.2.4 Crystal Graph Construction . . . 190
C.2.5 Graph Variational Autoencoder . . . 193
C.2.6 Convergence test and benchmarking . . . 196
C.3 MXene: Case Study . . . 199
C.3.1 MXene band gap . . . 199

Reference List . . . 200

List of Tables

1.1 Recent advances in SEI components with their associated anode, cathode, and electrolytes (2019 – 2022). 9

2.1 Major inorganic SEI components are listed along with their most probable defect types, diffusion mechanisms, and migration barriers. 20

2.2 Surface energy of all possible orientations of crystallographic planes of reported SEI (inorganic) components. 32

3.1 Statistical parameters of target data – diffusion coefficient*. 59

4.1 Performance overview of all models. 95

5.1 Statistical overview of grain surface energy for the SEI components considered in this study. 105

5.2 Coincident site lattice parameters used to construct low-Σ GB in SEI components. 106

6.1 Top Li–MXene candidates ranked using the composite screening score based on adsorption stability, mechanical stiffness, lattice compatibility, structural strain, and charge transfer characteristics. 159

A.1 Summary of computational resources utilized for NEB calculations carried out using CHPC, PSC, and NREL computational facilities. 172

A.2 Summary of GPU computational resources utilized for machine learning model development, hyperparameter optimization, and graph-based diffusion coefficient prediction. 173

C.1 Composition features along with the statistical operations considered for featurization of diffusing elements and diffusion media. 177

C.2 Name of features of diffusion media along with their respective indices from the heatmap. 181

C.3 Name of features of diffusion media along with their respective indices from the heatmap. 183

C.4 Optimized lattice parameters and DFT energy per atom of the SEI components considered in this study. 185

C.5 Heterogeneous grain-boundary (GB) configurations included in the dataset. Each case is defined by the top grain and bottom grain together with their exposed surfaces used to construct the interface. The final column is reserved for representative GB images. 188

C.6 Retained composition features and the corresponding statistical operations used for featurization of diffusing elements and diffusion media. . 189

C.7 Comparison of Li-ion migration barriers obtained in the present work with previously reported literature values for representative grain and grain-boundary diffusion pathways in SEI components. 196

List of Figures

1.1 An illustration of different layers of a typical Lithium-based battery pack with their relative thickness. 2

1.2 A generic illustration of multi-component, bi-layered mosaic-model of SEI. The inorganic part mostly composed of lithium halides, oxides, sulfides and carbonates while inorganic part includes short-chain alkyl carbonates, poly-sulfides and polymeric species formed from reduction products of additives and organic solvents in electrolyte[44, 45]. 7

1.3 Schematic representation of the thesis workflow for understanding and engineering Li-ion diffusion in the SEI. The study begins with the development of a generalized diffusion coefficient modeling framework for multicomponent materials using curated experimental datasets and machine learning approaches. This is followed by SEI-specific diffusion modeling, involving targeted data generation, physicochemical feature engineering, and predictive modeling to capture Li-ion transport behavior within the complex SEI environment. Finally, a design-oriented case study on MXene-based interfacial coatings is conducted using combined DFT and machine learning methods to identify optimized surface terminations that promote uniform Li-ion transport and enable stable SEI formation. 16

2.1 Diffusion profiles of the different ionic migration mechanisms for bulk (a) LiF, (b) Li_2CO_3 (c) LiOH, and (d) Li_2O. Respective models used for the calculation have been given in the first row where the circles represent the lithium vacancies. Reproduced with permission from reference [61] . Copyright 2021 The Royal Society of Chemistry. 22

2.2 Diffusion profiles of the different ionic migration mechanisms for (a) LiF, (b) Li_2CO_3. Adapted with permission from reference [25]. Copyright 2018 American Chemical Society. 23

2.3 Total electronic density of states and the crystal structure of (a) LiOH, (b) Li_2O, (c) Li_2CO_3, and (d) LiF. The dashed line indicates the location of the valence band maxima, which is set to zero.Reproduced with permission from reference [61] . Copyright 2021 The Royal Society of Chemistry. 27

2.4 (a–c) are energy profiles of different migration pathways of single lithium-ion migration in Li_2O. (d) illustrates the cubic structure and migration pathways, marked with arrows. Red and green spheres are O and Li atoms, respectively, and the white sphere indicates the Li vacancy position. Adapted with permission from reference [111]. Copyright 2011 American Chemical Society. 29

3.1 Potential energy terrain of a MEP for a chemical reaction[44, 45]. . . . 48

3.2 Dataset overview: a) diffusion mode present in dataset for IM media and b) MCA media. Frequency of temperature range of diffusion for c) IM media and d) MCA media. 57

3.3 Workflow of predictive modeling of diffusion coeffieint in conventional alloys. 61

3.4 Proposed generative modeling workflow for SEI structure generation and Li-ion migration barrier screening. An input structure is encoded into a latent space using a variational autoencoder-based model, followed by random sampling and decoding to generate new POSCAR variants. The generated structures are filtered based on their suitability for NEB calculations, exported for DFT validation, and compared with GNN-predicted migration barriers before being considered for experimental relevance. 68

4.1 Feature spaces – impurity diffusion in IM media for a) diffusing elements, b) diffusion media, and c) the combined feature space used for training. Features of diffusing elements and diffusion media are indexed sequentially and the respective indices are marked in the combined feature space for reference. Common abbreviations such as 'min.' for minimum, 'avg.' for average, and 'dev.' for deviation are used. 73

4.2 PC analysis; a) PCs that explain cumulative variance with inset graph that depicts variance of features represented by 25PCs and b) most contributed features in PC space spanned by first two PCs. The eigenvectors of features are projected as arrows. The important features of diffusing element are marked in red, diffusion media in blue, and other less contributing features in green color. The scatter plot in the background illustrates the scaled distribution of data points in PC space. 75

4.3 Performance of model – impurity diffusion in IM media: a) when trained with the entire feature space (dimension: 2497× 49) and b) with principal components of the entire feature space(dimension: 2497× 39). The gray solid lines depict the uncertainty associated with each data point. 76

4.4 Feature importance – impurity diffusion in IM media: features of diffusing elements are highlighted in bold fonts and diffusion media are given in normal fonts. 77

4.5 Feature spaces – self diffusion in IM media for a) diffusing elements, b) diffusion media, and c) the combined feature space used for training. Features of diffusing element and diffusion media are indexed sequentially and the respective indices are marked in the combined feature space for reference. Common abbreviations such as 'min.' for minimum, 'avg.' for average, and 'dev.' for deviation are used. 79

4.6 PC analysis; a) PCs that explain cumulative variance with inset graph that depicts variance of features represented by 24PCs and b) most contributed features in PC space spanned by first two PCs. The eigenvectors of features are projected as arrows. The important features of diffusing elements are marked in red, diffusion media in blue, and other less contributing features in green color. The scatter plot in the background illustrates the scaled distribution of data points in PC space. 80

4.7 Performance of model – self diffusion in IM media: a) when trained with entire feature space (dimension: 2506 × 30) and b) with principal components of the entire feature space (dimension: 2506 × 24). The vertical gray solid lines depict the uncertainty associated with each data point. 80

4.8 Feature importance – self diffusion in IM media: features of diffusing elements are highlighted in bold font and diffusion media are given in normal font. 81

4.9 Feature space – self diffusion in MCA media: combined feature space of diffusing element and diffusion media used for training. Features of diffusing elements are highlighted in bold fonts and diffusion media in regular fonts(Individual feature space of diffusing element and diffusion media for this model are given in Figure C.6a and b respectively). Common abbreviations such as 'min.' for minimum, 'avg.' for average, and 'dev.' for deviation are used. 83

4.10 PC analysis – self diffusion in MCA media; a) PCs that explain cumulative variance with inset graph that depicts variance of features represented by 40 PCs and b) most contributed features in PC space spanned by first two PCs. The eigenvectors of features are projected as arrows. The important features of diffusing elements are marked in red, diffusion media in blue and other less contributing features in green color. The scatter plot in the background illustrates the scaled distribution of data points in PC space. 84

4.11 Performance of model – self diffusion in MCA media when trained with a) the entire feature space (dimension: 3431×54) and with b) the principal components of the entire feature space (dimension: 3431×40). The gray solid lines depict the uncertainty associated with each test data point. 85

4.12 Feature importance – self diffusion in MCA media: *MLPRegressor* were used with feature permutation scheme. Features of diffusing elements are highlighted in bold font and diffusion media are given in normal font. 86

4.13 Feature space – impurity diffusion in MCA media: combined feature space used for training. Features of diffusing elements are highlighted in bold characters and diffusion media in regular fonts(Individual feature space of diffusing element and diffusion media for this model are given in Figure C.7a and b respectively). Common abbreviations such as 'min.' for minimum, 'avg.' for average, and 'dev.' for deviation are used. . . . 87

4.14 PC analysis – impurity diffusion in MCA media; a) PCs that explain cumulative variance with inset graph that depicts variance of features represented by 43PCs and b) most contributed features in PC space spanned by first two PCs. The eigenvectors of features are projected as arrows. The important features of diffusing elements are marked in red, diffusion media in blue, and other less contributing features in green color. The scatter plot in the background illustrates the scaled distribution of data points in PC space. 88

4.15 Performance of model – impurity diffusion in MCA media when trained with a) the entire feature space (dimension: 2567 × 49) and b) principal components of the entire feature space (dimension: 2567 × 43). The vertical gray solid lines depict the uncertainty associated with each data point. 89

4.16 Feature importance – impurity diffusion in MCA media: *MLPRegressor* were used with feature permutation scheme. Features of diffusing elements are highlighted in bold font and diffusion media are given in normal font. 90

4.17 Feature space – chemical diffusion in MCA media: combined feature space used for training. Features of diffusing elements are highlighted in bold characters and diffusion media in regular fonts(Individual feature space of diffusing element and diffusion media for this model are given in Figure C.8a and b respectively). Common abbreviations such as 'min.' for minimum, 'avg.' for average, and 'dev.' for deviation are used. . . . 91

4.18 PC analysis; a) PCs that explain cumulative variance with inset graph that depicts variance of features represented by 12PCs and b) most contributed features in PC space spanned by first two PCs. The eigenvectors of features are projected as arrows. The important features of diffusing elements are marked in red, diffusion media in blue, and other less contributing features in green color. The scatter plot in the background illustrates the scaled distribution of data points in PC space. 92

4.19 Performance of model – chemical diffusion in MCA media: a) when trained with the entire feature space (dimension: 483 × 20) and b) with principal components of the entire feature space (dimension: 483 × 12). The gray solid lines depict the uncertainty associated with each data point. 93

4.20 Feature importance – chemical diffusion in MCA media: Features of diffusing elements are highlighted in bold font and diffusion media are given in normal font. 94

5.1 Workflow of modeling Li-ion transport in SEI. Diffusion minimum energy path and migration barrier estimated using nudged elastic band method implemented in DFT computational code. Graph variational autoencoder used to augment data and GNN transformer model for predictive modeling. 103

5.2 Representative homogeneous ($\Sigma 3$) grain boundaries constructed by cleaving along the (-111) plane for (a) LiF, (b) LiCl, (c) LiBr (d) LiI, (e) Li_2O, (f) Li_2S, (g) Li_3N, and (h) Li_2CO_3. The grain-boundary interface is highlighted in blue. 107

5.3 Overview of Li-ion grain diffusion through SEI components; a) box plot of average nudged elastic force b) energies of intermediate images in minimum energy path, c) migration barrier and number of NEB runs and their test–train partition in SEI components. Prima facie, lithium halides exhibit comparatively lower migration barriers for grain-boundary diffusion than other SEI components. 111

5.4 Summary of the diffusion dataset generated from grain boundaries formed between SEI components: (a) Numbers of homogeneous and heterogeneous grain boundary diffusion cases for each SEI component, (b) homogeneous grain-boundary structures according to the CSL parameter Σ, (c) heterogeneous grain-boundary pairs formed between different SEI components, and (d) train–test split of the total dataset for each SEI component, with the numbers above the bars indicating the corresponding counts of train and test samples used. 112

5.5 Statistical overview of NEB dataset for grain boundary diffusion: Boxplots of the (a) NEB force values along the diffusion pathway for converged NEB images, (b) energies of intermediate images in minimum energy path, (c) Li-ion migration barriers and (d) grain boundary energy. A lower migration barrier in grain boundaries composed lithium halides can be observable, wherein especially LiCl based grain boundary exhibit lower among all other lithium halides. 114

5.6 Schematic illustration of the (a) predictive GNN model architecture. A grain-boundary NEB data point for LiF is shown as an illustrative example. The NEB images marked in white indices represent the initial and final structures, those in yellow indicate intermediate structures, and marked in red corresponds to the saddle point. The representative boxes illustrated beneath each structure denote the compositional features. Black connecting lines represent pre-processing operations, while gray lines depict the on-the-fly training and testing pathway of the model. Panel (b) depicts architecture of of GVAE model where M is the ground truth structure and $\hat{M}$ is the noised counterpart. A, X, and L denotes atom types, atom positions and lattice parameters. Role of GVAE in this design is to provide embedded representation of a complete NEB calculation (include all images and their features) to the GNN. 118

5.7 For grain diffusion, performance of the GVAE model in terms of convergence of the (a) total test loss and (b) KL divergence for different values of the weighting parameter β ranging from 0.2 to 1.0. The reconstruction performance of the GVAE for lattice parameters, atomic coordinates, and atom types is shown in (c), and the corresponding R^2 score for predicting MEP using GNN model is shown in (d). 122

5.8 Comparison between the MEPs predicted by the GNN model and those obtained from NEB calculations for grain diffusion of (a) LiF (100), (b) LiCl (110), (c) LiBr (110), (d) LiI (110), (e) Li_2O (110), (f) Li_2S (110), (g) Li_3N (110), and (h) Li_2CO_3 (100). The exposed surface corresponding to each grain is indicated in the brackets. The model achieves a point-wise MEP MAE of approximately 0.05 – 0.08 eV and a migration barrier MAE of about 0.10 eV, which reduces to a range of 0.04 – 0.05 eV when clear outliers reported in the case of Li_2O and Li_3N are excluded. 123

5.9 Feature importance analysis of grain diffusion: important features identified from the subset of a) composition-derived and b) structural features are listed based on mean accuracy decrease score. The statistical measures mentioned in the beginning of each composition-derived descriptors is attributed to the number and type of elements present in SEI component. A dominance of structure related features (grain exposed surfaces, DFT and surface energies) can be observable with the highest feature importance score compared to composition-derived features. 125

5.10 Data sampling scheme in latent space: (a) distribution of grain-diffusion data for different SEI components in the GVAE latent space, visualized in a 3-D Cartesian basis after t-SNE dimensionality reduction; (b and c) violin plots of the data generated from the hulls of the respective SEI components. The red dot in each hull indicates the hull center. Panel (b) shows that halide SEI components exhibit generally low migration barriers with narrow distributions, with LiCl and LiI being more favorable to Li-ion conduction and LiBr displaying comparatively broader variability. 127

5.11 For grain boundary diffusion, performance of the GVAE model in terms of convergence of the (a) total test loss and (b) KL divergence for different values of the weighting parameter β ranging from 0.2 to 1.0. The reconstruction performance of the GVAE for lattice parameters, atomic coordinates, and atom types is shown in (c), and the corresponding R^2 score for migration-barrier prediction using GNN model is shown in (d). 129

5.12 Feature importance analysis of grain boundary diffusion: important features identified from the subset of a) composition-based and b) structural features are listed based on mean accuracy decrease score. The statistical measures mentioned in the beginning of each composition-derived descriptors is attributed to the elements present in SEI component. A close examination on feature importance can tell that grain boundary diffusion is strongly governed by localized structural descriptors (saddle point and grain boundary energetics) showing a sharper and strong feature importance distribution compared to grain diffusion, where structural effects are more distributed across surface-related features. 131

5.13 Data sampling scheme in latent space: (a) distribution of grain boundary diffusion data for different SEI components in the GVAE latent space, visualized in a 3-D Cartesian basis after t-SNE dimensionality reduction; (b) violin plots of the data generated from the hulls of the respective SEI components. The red dot in each hull indicates the hull center. A few clusters have been illustrated here for a better visualization. Panel (b) shows that grain boundary diffusion generally exhibits higher and more broadly distributed migration barriers compared to bulk, with more variability depending on the specific interface chemistry, particularly for mixed-component boundaries. Due to numerous grain boundary structures involved in the analysis, only important one selected based on migration energy barrier is included in the illustration. 132

6.1 MXene phases considered for high-throughput screening for for integrating into SEI. Total of 4356 different MXene structures. In the figure M stands for transition metals, X for carbides/nitrides, T for surface terminations, and n is number of the layers in MXene phase. This structure database refereed from MXgap dataset developed by Ontiveros et al. [308] 145

6.2 (a) Distribution of adsorption energies for Li–MXene heterostructures, showing adsorption energies ranging from -1.3 to -2.0 eV. (b) Selected top-performing MXenes exhibiting the strongest interfacial binding with Li metal. Stacking orientation mentioned in MX phase's name as ABA and ABC with termination configurations as H, HM, and HMX. 148

6.3 C_{11} and C_{22} of top 30 MXene phases along with their stacking orientation (ABA and ABC) and termination hollow-site configurations (H, HM, and HMX). 151

6.4 Scatter plot showing the relationship between lattice mismatch and average structural strain after MXene adsorption on Li metal. A positive correlation between the two descriptors is observed, indicating that larger lattice mismatch generally leads to increased interfacial distortion after adsorption. The color scale represents the adsorption energy of the corresponding Li–MXene heterostructures. 152

6.5 A comparative overview of charge transfer between MXene and Li-metal illustrated as box-plots. As expected, MXene with oxygen and fluorine surface terminations exhibits elevated charge transfer that point towards the comparatively better stability of adsorbed MXene. 155

6.6 PBE0 bandgap distribution of the most stable MXene configurations with different transition metals, carbon/nitrogen compositions, and surface terminations. Numerical values correspond to the calculated PBE0 bandgap in eV, while cells marked as dark blue indicate metallic MXenes with negligible or zero bandgap. The results show that semiconducting behavior is more frequently observed in $n = 1$ MXenes, whereas increasing layer thickness generally promotes metallic character. Plots corresponding to $n = 2, 3$ are given in Figure C.18 155

6.7 Pearson correlation coefficient between the normalized descriptors of Li-metal-MXene heterosystems. 158

C.1 Diffusing elements (highlighted in red color) and their cumulative percentage from each block (pie chart in the inset) of the periodic table for IM media a) and b) MCA media present in the data. 175

C.2 Frequency of weighted percentage of elements present in the composition of a) IM media and b) MCA media present in the training data. 176

C.3 Schematic diagram of material data proprocessing. The program used for preprocessing is available in GitHub repository, https://github.com/yanqingsu/ML-DiCE 176

C.4 In each graph set, the leftmost figure represents the standard deviation of the diffusion coefficient, the middle figure illustrates the standard deviation of the diffusion coefficient after taking the logarithm, and the rightmost figure displays the standard deviation of temperature. The data for a) impurity and b) self-diffusion modes in IM media, and impurity, self, and chemical diffusion in MCA media are represented by c), d), and e), respectively. 178

C.5 Probability density distributions of normalized residuals, calculated through eight-fold cross-validation. Each graph set consists of two figures: on the left, it is assumed that all entries have constant error (out-of-bag errors), while on the right, the error distribution is depicted using *Lolo* uncertainty estimates calculated based on variability and correlation with inclusion of points in their randomly drawn training set. Graph sets a – d illustrate the uncertainty behavior of the impurity and self diffusion models in an IM media, while, graph sets c up to l present the uncertainty behavior of the self, impurity, and chemical diffusion in MCA media. 179

C.6 Correlation values of features of a) diffusing elements and b) diffusion media for the model self diffusion in MCA media. Name of features of diffusion media with respective indices are given in Table C.2 180

C.7 Correlation values of features of a) diffusing elements and b) diffusion media for the model impurity diffusion in MCA media. Name of features with respective indices are given in Table C.3 182

C.8 Mutual correlation values of features of diffusing elements and diffusion media for the model impurity diffusion in MCA media. 184

C.9 Representative heterogeneous grain boundaries built using Zur–McGill algorithm for (a) LiF(111)-LiCl(111), (b) LiCl(111)-LiBr(001), (c) LiBr(110)-Li_3N(100) (d) Li_2S(001) -Li_3N(100), (e) Li_2O(001)-Li_2CO_3(100), and (f) LiI(001)-Li_2S(111). 187

C.10 Results of GVAE model tuning; a) total loss of test with varying batch sizes, b) normalization among feature/target, and latent dimension. . . 194

C.11 Comparison of GNN model performance with three training schemes: a) total loss curves, R^2 scatter plots of training with a) composition derived features, b) GVAE latent embeddings, and c) combined features. . . . 194

C.12 Latent diffusion noise conditioning: Three trials with noise range 0.1 – 0.001 that used to perturb atomic positions. 195

C.13 Samples of ground truth and reconstructed grain structures of a) LiF, b) Li_2S, c) Li_2O, Li_2CO_3. Grain boundary structures of same components are given in (e – h) respectively. All structures are reconstructed with good accuracy for lattice and atomic positions. However it can also be seen that atom types of four oxygen atom are reconstructed as sulfur atoms. 195

C.14 Visualization of latent space clustering of SEI components using (a) PCA and (b) t-SNE based dimensionality reduction. A clear clustering can be observed in PC space three PCs compared to t-SNE based cluster classification. 196

C.15 Tuning of GVAE for grain boundary diffusion: a) latent dimension (d_{latent}), b) batch, c) learning rate and (d) weight decay rate in Adam optimizer. 197

C.16 Comparison of GNN model performance with three training schemes: R^2 scatter plots of training with a) composition derived features, b) GVAE latent embeddings, and c) combined features. 197

C.17 Convergence test on slab thickness vs migration barrier in Li_2S, Li_2O and LiF. 198

C.18 PBE0 bandgap distribution of the MXene configurations with $n = 2, 3$. 199

Abstract

The growing demand for high-energy-density and long-cycle-life lithium-based batteries has intensified the need to understand and optimize the interfacial phenomena that govern electrochemical stability, ion transport, cycling performance, and safety. Among these interfacial phenomena, the solid electrolyte interphase (SEI) is of central importance as it mediates Li-ion transport while passivating the electrode surface and suppressing continuous electrolyte decomposition. The SEI is a thin, complex layer formed through electrolyte decomposition at the electrode–electrolyte interface. Despite its critical role, the SEI remains one of the least understood components of electrochemical cells because of its chemical heterogeneity, structural complexity, and dynamically evolving nature. These characteristics make direct experimental characterization of Li-ion transport mechanisms within the SEI especially challenging. To address this challenge, this thesis combines first-principles calculations and machine learning approaches to investigate and model Li-ion diffusion processes in lithium-based energy-storage materials, with particular emphasis on Li-ion transport through the inorganic sublayer of the SEI.

The first part of this work focuses on the development of a generalized machine learning framework, named the Machine Learned Diffusion Coefficient Estimator (ML-DiCE), for predictive modeling of diffusion coefficients in multicomponent materials. A large experimental diffusion-coefficient dataset covering impurity, self-, and chemical-diffusion mechanisms in impure metallic and multicomponent alloy systems was curated and used to train Random Forest, Deep Neural Network, and Support Vector Regression models. Through composition-aware feature engineering and systematic hyperparameter optimization, the developed models achieved strong predictive per-

formance, demonstrating the capability of data-driven approaches to capture complex atomic diffusion behavior across diverse material systems. This work represents one of the first systematic efforts to model diffusion coefficients in complex solid-state material systems using machine learning techniques. The predictive framework and physical insights developed from this study provide a foundation for extending data-driven diffusion modeling toward Li-ion transport in SEI materials.

The second part of this thesis investigates Li-ion diffusion in inorganic SEI components using density functional theory (DFT) combined with deep graph neural network models. A comprehensive diffusion-coefficient dataset was generated using nudged elastic band (NEB) calculations for eight major inorganic SEI components: LiF, LiCl, LiBr, LiI, Li_2O, Li_2S, Li_3N, and Li_2CO_3. The dataset includes both grain and grain-boundary diffusion pathways across homogeneous and heterogeneous interfaces. A path-aware graph variational autoencoder (GVAE) was employed to learn latent representations of diffusion trajectories, which were subsequently integrated into graph neural network (GNN) models for potential-terrain-aware migration-barrier prediction. The combined GVAE–GNN framework achieved strong predictive performance, with test-set R^2 values of 0.93 and 0.94 for grain and grain-boundary diffusion, respectively. The training strategy enabled the model to learn features associated with the potential-energy terrain governing Li-ion diffusion in both grain and grain-boundary systems. The analysis revealed that Li-ion migration is governed not only by SEI chemistry but also by local microstructural features such as exposed surface orientation, grain-boundary character, and interfacial mismatch. These results establish a clear relationship between the structure of inorganic SEI components and Li-ion transport. It also suggest that suppressing dendrite growth may require uniform Li-ion migration barriers and evenly distributed migration channels across the inorganic sublayer of the SEI. Achieving this uniformity depends on careful control of both phase composition and interfacial microstructure in

SEI design.

Finally, this thesis explores MXene-assisted interfacial engineering as a case study for stabilizing lithium-metal/SEI interfaces and regulating Li-ion flux. Using combined DFT calculations and numerical descriptor analysis, Li-metal/MXene heterostructures with different surface terminations were systematically screened. The study demonstrates that mechanically optimized and electrochemically compatible MXene coatings can form stable interfaces with lithium metal while promoting uniform ion transport and minimizing interfacial distortion. In particular, ABC-stacked, Cr-based, fluorine-terminated MXenes exhibited favorable adsorption energetics and enhanced interfacial stability, indicating their potential as auxiliary SEI layers for Li-metal electrodes to suppress dendrite growth and improve long-term electrochemical performance.

Overall, this thesis establishes integrated computational frameworks that combine atomistic simulations, diffusion-coefficient modeling, and machine learning to accelerate the understanding of ionic transport phenomena in SEI materials and guide the rational design of stable SEI. The methodologies and insights developed in this work provide a foundation for engineering SEI architectures through controlled ion transport, optimized interfacial chemistry, and microstructural regulation, thereby enabling the design of high-performance interfaces for next-generation lithium-based energy-storage systems.

Chapter 1

Introduction

1.1 Lithium-ion Batteries; State of the Art

Lithium-ion batteries (LIB), one type of metal ion batteries, are the gateway to reliable and sustainable energy storage. Given the emerging scenario of electric vehicles (EVs), where lithium-ion batteries are one of the integral parts, these greenhouse emissions can be reduced by a great extent. Global sales of electric passenger vehicles are projected to surpass 10.5 million in 2022, which is about 4 million above the year-2021 level, the research firm Bloomberg NEF said in a recent report [1]. Despite being a promising candidate, LIBs still need to be improved for far-reaching high energy density applications for high-mileage electric vehicle applications[2, 3]. The energy density of the commercialized LIBs used in EVs ranges from 140 to 250 $W \cdot h\ kg^{-1}$ [4, 5]. Apart from the energy density, other properties of LIBs need to be improved, including reliability, cost-effectiveness, and charging speed; in addition, factors affecting the thermal runaways have to be optimized further.

The structure of a LIB is similar to any other electrochemical cell in that it has a solid anode and cathode, and an electrolyte which could be either in a solid or liquid phase [6, 7]. An illustration of major components of a typical LIB with their relative thickness has been depicted in Figure 1.1. In contemporary LIBs, graphite remains the most widely used commercial anode material due to its structural sta-

bility, low cost, and reliable cycling performance, though alternatives such as silicon and silicon–graphite composites are increasingly explored for their significantly higher theoretical capacities. On the cathode side, layered transition metal oxides dominate, particularly $LiCoO_2$, $LiNi_xMn_yCo_zO_2$ (NMC), and $LiNi_xCo_yAl_zO_2$ (NCA), due to their high energy density and well-established manufacturing processes[8]. More recently, there has been a growing shift toward high-nickel NMC compositions and cobalt-reduced or cobalt-free materials to improve capacity while lowering cost and sustainability concerns. Additionally, $LiFePO_4$ (LFP) has gained renewed prominence, especially in large-scale and electric vehicle applications, due to its excellent thermal stability, long cycle life, and enhanced safety characteristics[9].

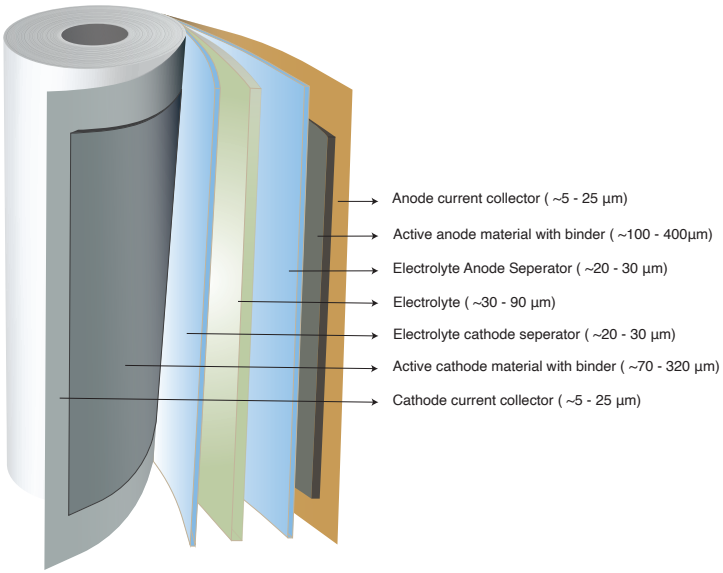


Figure 1.1: An illustration of different layers of a typical Lithium-based battery pack with their relative thickness.

Despite the remarkable progress in LIB chemistry, the energy density of conventional systems remains fundamentally constrained by the intercalation-based graphite anode. In addition to this intrinsic limitation, the formation and evolution of the solid electrolyte interphase (SEI) on electrode surface plays a decisive role in governing the

long-term performance, safety, and efficiency of lithium-ion batteries. The SEI, formed via electrolyte decomposition at low potentials, acts as a passivating layer that enables lithium-ion transport while suppressing further electrolyte degradation; however, its instability and continuous growth often lead to capacity fade and increased cell resistance.

To overcome the energy density limitations of conventional LIBs, lithium-metal batteries have emerged as a promising next-generation technology. These systems employ metallic lithium as the anode, owing to its ultrahigh theoretical capacity of 3860 mAh g^{-1} and its lowest electrochemical potential of -3.04 V vs SHE. However, this transition introduces critical challenges, including dendritic lithium growth, poor cycling stability, and the formation of an unstable SEI. Therefore, understanding and controlling interfacial phenomena in lithium-ion based battery systems has become essential for enabling their safe and practical application.

1.2 Lithium-Metal Batteries: Merits and Demerits

Lithium-metal batteries (LMBs) are widely regarded as one of the most promising next-generation energy-storage technologies because they can deliver significantly higher energy densities than conventional lithium-ion batteries. Lithium metal possesses both the highest theoretical specific capacity (3860 mAh g^{-1}) and the lowest electrochemical potential (-3.04 V vs SHE) among known anode materials. Despite these advantages, the practical deployment of LMBs is severely limited by the instability of the lithium/electrolyte interface. Lithium as an electrode lies at the most reducing end of the electrochemical series and is therefore highly reactive toward electrolyte components. As a result, spontaneous electrolyte decomposition occurs during cycling, leading to the formation of a SEI, a chemically and structurally complex passive layer on the electrode

surface[10, 11]. Ideally, the SEI should electronically insulate the anode while allowing fast Li-ion transport, thereby suppressing continued electrolyte decomposition. In practice, however, the SEI formed on Li metal is often heterogeneous and mechanically fragile, and it distributes Li ions nonuniformly across the electrode surface, undermining electrochemical performance. This results in uneven Li stripping and plating, low Coulombic efficiency, continuous interfacial side reactions, and eventual capacity decay. More importantly, spatial inhomogeneity in the SEI promotes nonuniform current distribution and localized Li deposition, which can trigger uneven growth of Li-metal, interfacial failure, and leads to cell short circuit. Although lithium electrode is an ideal anode from a theoretical standpoint, the unstable nature of the SEI remains one of the principal barriers to the practical realization of LMBs. Therefore, understanding and controlling Li-ion transport through the SEI is critical for enabling stable LMBs.

1.3 Solid Electrolyte Interphase: Formation, Structure, and Function

The concept of SEI was introduced by Peled [12] in 1979 and later improved by Aurbach et al. [13] in 1999. The major components of SEI are the precipitates of inorganic salts, and together with the organic components this interphase plays an imperative role in the cycling stability of anode[14]. Moreover, SEI has a significant role in ionic transport through LIBs as this layer is permeable to Li-ions and prevents the tunneling of electrons and electrolyte molecules between electrode and electrolyte, thereby providing the electrochemical stability to the cell[15]. Nevertheless, this passive layer consumes nearly 2 - 5% of active Li-ions for its irreversible formation and a few more percentages in the subsequent cycles while resulting in the gradual fading of the capacity, Coulombic efficiency, and the overall performance of the battery[16]. Further, the cracking

of SEI accelerates the lithium dendrite formation which leads to short-circuiting and hence the thermal runaways of the battery pack. In short, SEI is a necessary layer for Lithium-based battery systems that control battery lifespan, efficiency, and reliability.

The SEI is not limited to a specific electrode but is a ubiquitous feature in lithium-based battery systems, forming on both anode and cathode surfaces as a result of electrolyte decomposition. While the SEI is most prominently discussed in the context of low-potential anodes such as graphite and lithium metal, analogous interfacial layers also form on cathode surfaces, often referred to as the cathode electrolyte interphase (CEI)[17]. These interphases originate from thermodynamic instability between the electrolyte and electrode materials and evolve dynamically during electrochemical cycling. Regardless of the electrode type, such interfacial layers play a crucial role in regulating ion transport, suppressing continuous electrolyte degradation, and maintaining electrochemical stability. However, their composition, structure, and stability vary significantly depending on the electrode chemistry and operating conditions, making their comprehensive understanding essential for improving the overall performance and longevity of lithium-based batteries[18].

The major components of the SEI layer associated with lithium metal and graphite electrodes are lithium fluoride (LiF), lithium oxide (Li_2O), lithium carbonate (Li_2CO_3), lithium hydroxide (LiOH), lithium oxalate ($Li_2C_2O_4$), lithium nitride (LiN), dilithium ethylene glycol dicarbonate $(CH_2OCO_2Li)_2Li_2EDC$, lithium methyl carbonate ($LiOCO_2CH_3$), dilithium butylene dicarbonate (Li_2BDC) and lithium ethyl carbonate ($LiOCO_2C_2H_5$) at temperatures in the range of 250–400 K[19]. SEI is generally modeled as a complex multilayered mosaic-type structure with an inorganic inner layer close to the electrode and an organic-porous-heterogeneous outer layer close to electrolyte[20]. There are models such as 'two-layer-two-mechanism diffusion' developed by Shi et al. [21], and studies by Lu et al. [22] corroborate the multi-layer structure of SEI[23]. Since the

organic layer of SEI has a porous structure, Li-ion transport through this part can be understood through Fick's laws of diffusion and must be optimized to obtain a higher ionic transport rate[21, 24]. Ionic transport through the inorganic layer of SEI varies from component to component and is mainly carried out through vacancy diffusion, concerted exchange, knock-off, and direct hopping mechanisms[25]. Also, a substantial Li-ion transport is also happening through grain boundaries of the aforementioned inorganic components. Meanwhile, analysis of ionic transport through electrolytes and separators shall be accounted for the complete understanding of ionic dynamics in battery pack. There are many review articles available on the ionic transport through separators including various solid and liquid electrolytes in Lithium-based battery systems[26–32]. Further, SEI formation, growth, dendrite growth, properties, functionalities, failure modes, and artificial SEI designs are well documented in the past decades[33–35].

1.4 Complexity of the SEI: Chemical and Microstructural Heterogeneity

The formation of SEI is due to the redox reaction between electrolyte and electrode in all LIBs. The structure and composition of this film are highly influenced by the surface morphology of the electrode and the chemical composition of the electrolyte[36]. Electrochemistry of the formation reaction states that when the energy of the lowest unoccupied molecular orbital of an electrolyte molecule stays lower than the highest occupied molecular orbital of an electrode's molecule, the electrons reduce the electrolyte and forms a complex bi-layer on the surface of the electrode. Beginning from the primitive work of Peled [12], a lot of advances have been contributed to obtaining the modern picture of SEI. Up to this date, a promising model explaining the struc-

ture of SEI is the 'the multi-component, multilayer structure'[37–40]. According to this model, SEI is a two-layer thin film composed of an organic outer layer close to the electrolyte and an inorganic inner layer close to the electrode. Figure 1.2 provides a detailed illustration of SEI as described in the aforementioned model. During the first charging phase, lithium ions from the cathode drift through the electrolyte and get reduced by the anode along with a fraction of electrolyte molecules thus forming a complex bi-layer on the anode. A very similar redox reaction also takes place on the cathode surface and forms an SEI on its surface. SEI formed on lithium-based cathode has been subjected to vigorous research activities in the last decade because it has a direct influence on dendrite-growth and prevention measures[41–43].

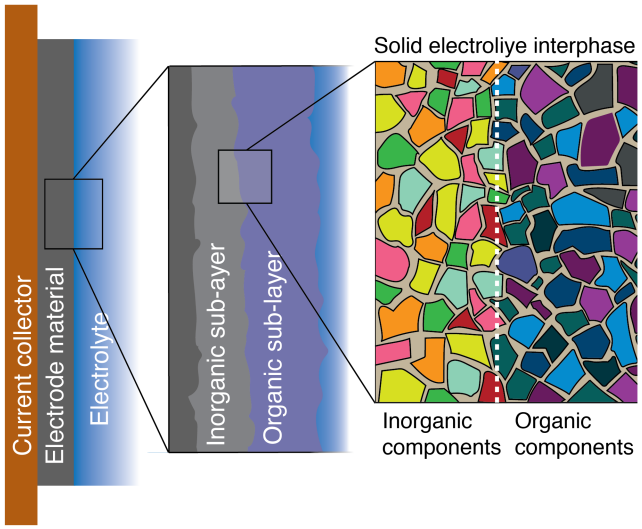


Figure 1.2: A generic illustration of multi-component, bi-layered mosaic-model of SEI. The inorganic part mostly composed of lithium halides, oxides, sulfides and carbonates while inorganic part includes short-chain alkyl carbonates, poly-sulfides and polymeric species formed from reduction products of additives and organic solvents in electrolyte[44, 45].

The nature of chemical components present in the inorganic layer of SEI depends upon the electrolyte (along with the additives and stabilizers) and the electrode material. A summary of the recently emerged LIB configurations and the associated SEI

components are listed in Table 1.1. Structural properties of the SEI depend upon surface chemistry, temperature, voltage range during cycling, and cycling numbers, wherein the time spent at low potentials is a crucial factor[46]. Generally, the inorganic layer is composed of grains of LiF,Li_2O,LiOH, Li_2CO_3, and the lithium-ion transport through this layer takes place through grains and grain boundaries of aforesaid components [47]. After the charging phase, a negligible fraction of electrons from the anode tunnels through the formed inorganic layer reduces a fraction of the electrolyte molecules, hence forms a thicker-porous-outer-organic layer. The components of this layer are mostly organic complex molecules based on the chemical composition of the electrolyte and additives[38].

The fabric of the inorganic layer associated with carbonaceous electrodes was put forward by Peled, Golodnitsky, Menachem, and Bar-Tow[56]. They suggested that LiF, Li_2CO_3, $LiCO_2$-R (R represents the organic species linked to the carbon atom), Li_2O, lithium alkoxides, and nonconductive polymers are the major components of this layer. Later this fact was corroborated through surface analysis that the inorganic layer is mainly formed by LiF, Li_xPF_y, PF_y, Li_2CO_3 and Li_2O, based on the cycling stage and electrolyte's chemical composition [57–60]. The phase of this inorganic layer was revealed in a cryogenic electron microscopic study conducted by Zheng et al. [61], showing that the nanocrystalline inorganic components, namely LiOH, Li_2O, Li_2CO_3, and LiF, are embedded as the amorphous organic phase. Shi et al. [21] have corroborated the concept of conductivity across this layer and have postulated that the electronic conduction is primarily obstructed by the inorganic constituents. However, they also suggest that rapid Li-ion conduction is facilitated by Li_2CO_3 and Li_2O components.

In SEI, the organic and inorganic layers together serve as a dielectric membrane, and its dielectric characteristics significantly influence uniform lithium deposition on the electrode by maintaining a uniform current/potential distribution throughout the

Table 1.1: Recent advances in SEI components with their associated anode, cathode, and electrolytes (2019 – 2022).

Cathode	Electrolyte	Anode	SEI Components	Comments
Li foil (thickness: 0.25 mm)	$1M$ LiTFSI in 1,1,2,2 - tetraethoxyethane with microporous polypropylene (Celgard 2325) and glass fiber as separators.	Si–graphite composite [1]	Li_2SO, and Li_3N, hydrocarbons, functional groups such as H_3C-O^- or $-H_2C-O-$, $-CO_2$, $-CF_3$, $-O-C-O-$ etc.[48]	SEI accommodates the volume changes in Si/graphite electrode hence gives a good electrochemical performance. Also, the formed SEI is smooth and continuous.
Li-based cathode	$1.2M$ $LiPF_6$ in EC:EMC (3:7 w/w)	Pseudographite	polyethylene oxide-type polymers, alkyl carbonate ($R-CH_2OCO_2-$, $R-CH_2OCO_2-$) LiF, lithium alkoxide ($R-O-Li$), LixPOyFz [49]	A specially synthesized graphite electrode (from 'University of Idaho thermolyzed asphalt reaction') with defects.
NMC622/ CNT /super P/pvdf [2]	$1M$ $LiPF_6$ electrolyte in ethylene carbonate:diethylene carbonate:ethyl methyl carbonate; In a ratio of 3:3:4 with SC1622 as the separator.	Graphite/super P/pvdf [3]	LiF, $LiPF_6$, Li_2CO_3, Li_2O, LixPOyFz, carbonate groups, oxy fluorophosphate group. [50]	Li_2CO_3, Li_2O, and LixPOyFz are the inner inorganic SEI components and carbonate groups, Li_2O, and the oxy-fluorophosphate groups are the outer inorganic components stems from the electrolyte decomposition.
Pure Li	$1M$ $LiPF_6$ dissolved in an ethylene carbonate (EC) and diethyl carbonate (DEC) mixture(1:1 volume percentage).	Graphite	LiF, Li_2CO_3, components on graphite surface showing covalent CF bonds and semi-ionic CF bonds.[51]	Celgard 2400 has been used as the separator. Also, here Fluorine atoms have been introduced on the graphite surface using CF_4 gas.
Li foil	$1M$ LiPF6 in ethylene carbonate (EC: dimethyl carbonate (DMC) (1:1, vol.) with glass microfiber filter as the separator and Fluorosulfonyl isocyanate as the electrolyte additive.	Graphite	LiF, LiPxOyFz, Li_2CO_3, Li_2O, Li_2SO_4, $ROSO_2Li$, Li_2S, Li_2SO_3 [52]	LiF from either $LiPF_6$ or FI decomposition, inorganic layer composed of LiF, Li_2SO_4, $ROSO_2Li$, Li_2S, Li_2SO_3 and low concentration of Li_2CO_3, Li_2O and LixPFyOz. Outer layer with organic polymeric species.
Pure Li	Adiponitrile/dimethyl carbonate-based electrolytes with lithium bis borate or lithium bis imide and Freudenberg FS2026 non-woven polypropylene separator.	Graphite	LiF, ROLi, Li_2CO_3, organic carbonates, lithium carbide[2] groups such as SO_3^{-2} and polysulfur (or polysulfide) and decomposition products of lithium difluoro(oxalato)borate (LiDFOB) with $B-O$ bond[53]	ROLi form as a reduction product of DMC and deposits close to the graphite surface. LiDFOB reduction leads to a more protective SEI layer. The combination of LiDFOB with FEC leads to low resistant SEI with high LiF content.
NMC111 [4]	Fluorine-free electrolyte based on lithium bis(oxalato)borate and vinylene carbonate(VC).	Si–graphite composite	Polymeric species formed by VC, reduction products of the bis(oxalato)borate anion.[54]	Forms a stable oxygen-rich SEI. Capacity fading occurs during long-term cycles due to the higher impedance across SEI while showing good cycling stability at higher temperatures.
NMA90[5]	FEC and lithium 4,5-dicyano-2-(trifluoromethyl)imidazole (LiTDI) in $LiPF_6$-in-EMC electrolyte.	Graphite	Inorganic layer of $LiPF_6$ and carbonate solvents decomposition products and organic layer with LiTDI derived and N-containing species.[55]	Forms passivation layer as SEI evolved from fluoroethylene carbonate. LiTDI decomposes and modifies the SEI layer, mitigates electrolyte decomposition.

[1] Binder: lithium polyacrylate & LiF, Li_2S, $Li_2S_2O_4$, Li_2SO_3.
[2] In a ratio of 94.0/0.75/3.0/2.25, and was cast onto an Al foil. The loading level is $15.84 mg/cm^2$ and thickness is $68 \mu m$.
[3] In a ratio of 91.0/1.0/8.0 and deposited on Cu foil with a loading level of $8.55 mg/cm^2$ and thickness was $69 \mu m$.
[4] LiNi1/3Mn1/3Co1/3O_2
[5] $LiNi_{0.9}Mn_{0.05}Al_{0.05}O_2$

layer and suppressing lithium protrusions[62, 63]. Various types of dielectric breakdowns are reported in LIB (electrolytes, separators, and electrode materials have dielectric characteristics). These breakdowns usually end up in thermal runaways. The thermal runaways originating from SEI are particularly associated with the metastable components present in the organic layer of SEI[64, 65]. Therefore, proper attention to this layer shall be given when designing a battery pack. In addition to this, a ideal SEI must have high elasticity, strong lithium-ion affinity, and hydrophilic properties, which make them withstand the dielectric breakdown and prevents dendrite formation[66]. Furthermore, the consumption of active Li-ions (2 - 18%) during the formation of SEI and successive cycles shall be optimized for the long term efficient cycling performance of the battery.[67].

1.4.1 Recent Advances in SEI

Artificial SEI is a crucial and growing field related to LIBs, especially when designing SEI with particular properties, such as the capacity to mitigate dendrite growth and volume expansion of electrodes (in silicon based electrodes) and the ability to facilitate fast and uniform ionic distribution to the electrode[68]. The need for the development of an artificial SEI is significant when the naturally formed SEI degrades during the cycling of the battery[69]. The initial concepts of artificial SEI put forwarded by Kim et al. [70] in a work on the Kawasaki mesophase fine carbon electrode (KMFC). In that work, the authors coated a Li_2CO_3 layer on KMFC electrode using PVdF as a binder and found that artificial SEI provides good ionic conductivity and suppresses the electrolyte decomposition. Later, Menkin et al. [71] proposed an artificial SEI that stabilizes the structure of graphite and tin–copper anode on cycling, synthesized

through electropainting and vacuum-insertion techniques. Recent work of Luo et al. [72] shows that Li_3N, popular for its high mechanical strength along with cellulose, is a promising candidate for artificial SEI on lithium based electrodes. The cellulose was introduced using nitrocellulose as an electrolyte additive, and their results demonstrate a uniform lithium-ion distribution and suppression of dendrites growth on the lithium electrode. In another work, Chen et al. [73] constructed an artificial inorganic SEI layer composed of ZrO_2, Li_2O, Li_3N, and LiNxOy rich with GBs on the surface of Li metal and found that the resulting $LiZrO(NO_3)_2$@Li electrode has a stable cycle life of about 550 hours at a high current density of 10 $mAcm^{-2}$ and mitigates dendrite growth.

A novel material derived from an elastic nano-parylene layer was found as a promising artificial SEI layer capable of handling large volumetric changes exhibited by Si based electrodes. Specifically, parylene F and N are found to be very stable and compatible with the conventional carbonate-based electrolyte and have capacity retention of greater than 75% after 480 cycles[74]. Gradient-type Li-rich artificial SEI has been reported with a fast and stable ionic conductivity for polymer-based poly(ethylene oxide)-lithium bis(trifluoromethanesulfonyl)imide composite solid electrolyte[75]. In another study by Zhong et al. [76] states that lithium alginate-based artificial SEI over lithium electrode exhibits a more stable lithium plating/stripping behavior along with effective dendrite suppression and maintains capacity retention of about 94.0% coupled with a Coulombic efficiency of 99.6 % after 1000 cycles at 4 C in a $LiFePO_4$-Li full cell. In a recent review on artificial SEI, Gao et al. [77] pointed out that artificial SEI films containing the ceramic electrolyte provide excellent Li-ion transfer channels with sufficient mechanical robustness that can mitigate the growth of lithium dendrites. Their review concluded by stating that the rational design of polymeric materials with high interactions between lithium-ions and lithium metal significantly suppresses the lithium dendrite growth and side reaction between the electrolyte and lithium metal.

In short, the challenges associated with unstable SEI formation, dendrite growth on the anode (especially Li-metal electrodes), uncontrolled interfacial reactions, low Coulombic efficiency (thus short cycling lifetime), and the volume expansion from the anode end can be resolved to a large extent by designing an artificial SEI.

1.5 Scope and Objectives

The increasing demand for high-energy-density battery systems, particularly for applications such as electric vehicles and large-scale energy storage, necessitates not only enhanced performance but also improved reliability and safety of lithium-based batteries. While significant progress has been made from conventional LIBs to next-generation LMBs, further optimization, particularly on developing high-energy density batteries remains essential. Critical factors governing such battery systems including performance, stability, and lifetime is the formation and evolution of the SEI on electrode surface. As described earlier, this interphase forms spontaneously at the electrode–electrolyte interface due to electrolyte decomposition and is inherently unavoidable in electrode-based battery chemistries. Despite its nanoscale thickness, the SEI plays a pivotal role in regulating ion transport, preventing continuous electrolyte degradation, and maintaining interfacial stability. Therefore, the design and control of a stable and functional SEI is central to achieving reliable and high-performance lithium-based battery systems across both existing and emerging technologies.

When examining failure mechanisms of SEI in battery systems, it is generally understood that SEI degradation can be categorized into three primary modes: thermal, chemical, and mechanical. Thermal and chemical degradation are the dominant failure modes for the SEI formed on graphite anodes in conventional lithium-ion batteries, whereas mechanical failure is more prevalent in the SEI formed on silicon and lithium-

metal electrodes.[78] Wherein especially, mechanical failure of the SEI associated with lithium dendritic growth is a major challenge in developing high-energy density batteries with Lithium metal electrode. In general, dendrite formation proceeds through three stages: nucleation, growth, and penetration. Among these, the nucleation stage is especially critical, as achieving spatially uniform nucleation is essential to prevent dendrites from becoming formed.[78] One important factor that can trigger dendrite nucleation is the accumulation of low-energy Li-ion diffusion channels at specific regions of the electrode surface.[79, 80] This phenomenon with the repeated cycling amplifies deposition inhomogeneities, leading to interfacial instability, and ultimately the growth of filamentary lithium dendrites. Therefore, uniform Li-ion diffusion through the grains and grain boundaries of the inorganic SEI is essential for stable lithium depositionFigure and long-term battery operation.

Earlier computational studies on dendrite formation and SEI behavior have largely focused on mapping Li-ion transport in a limited set of representative SEI components. Most of these investigations rely on density functional theory (DFT), particularly nudged elastic band (NEB) calculations, to determine Li-ion migration pathways and activation barriers. A notable study by Ramasubramanian et al. [81] examined LiF, Li_2O, and Li_2CO_3 and demonstrated Li-ion transport through the grain boundaries of these phases. Their results showed that grain boundaries create multiple open diffusion channels that facilitate faster Li-ion transport, with the highest diffusion rate observed for the heterogeneous LiF/Li_2O grain boundary compared with the corresponding homogeneous LiF/LiF and Li_2O/Li_2O boundaries. However this work include a few selected diffusion pathways and limited surface terminations for a given grain boundary. Similarly, Zheng et al. [82] investigated several ionic migration mechanisms in bulk LiF, Li_2CO_3, LiOH, and Li_2O. While this work attributed the relatively fast Li-ion transport in LiF compared to other components, the broader transport

picture within the SEI remains unaddressed, as the SEI is inherently an amalgam of crystalline grains and grain boundaries. Soto et al. [83] reported, in their NEB study of Li-ion diffusion mechanisms in the grains of LiF and Li_2CO_3, that among the mechanisms considered—including knock-off, concerted exchange, vacancy diffusion, and direct hopping—vacancy diffusion and knock-off are the most energetically favorable in these two components. Existing studies of Li-ion transport in SEI materials largely focus on one or a few components particularly about LiF, Li_2O and Li_2CO_3, with relatively limited attention to the halide-rich SEI chemistry observed in modern electrolytes.[84–87]. Also the studies incorporating grain boundary rich SEI model concentrate only on a limited number of migration pathways within selected grains or grain boundaries. This demands the need of an collective SEI modeling that include grain and grain boundary diffusion in SEI through all reported SEI components and their possible grain boundary configurations.

Building upon the identified research gaps in understanding Li-ion transport within the complex, multicomponent, and grain boundary–rich morphology of the SEI, this thesis aims to develop a comprehensive and data-driven framework to model diffusion processes in SEI materials. Since the diffusion coefficient is the key physical parameter governing Li-ion transport, the study begins with the development of a generalized predictive approach by compiling and curating a sufficiently large dataset of experimentally reported diffusion coefficients across material systems. However, due to the scarcity of such data specifically for SEI components, this work further extends into generating relevant physicochemical descriptors for SEI materials through targeted substudies. These efforts enable the construction of machine learning models capable of predicting diffusion behavior in complex SEI chemistry. Finally, guided by the design principle that a stable SEI should promote homogeneous Li-ion flux through uniformly distributed low-energy migration pathways, a focused case study on MXene-based in-

terfacial systems is conducted. Using a combination of ab initio simulations and machine learning techniques, this study seeks to identify optimal MXene structures with tailored surface terminations that can act as functional coatings on Li-metal electrode, thereby stabilizing the SEI and enabling uniform lithium deposition for high-energy density applications.

In short the overview of this thesis is summarized into three main bullet points as described below;

- Development of a generalized diffusion coefficient modeling framework for multi-component material systems, based on curated experimental datasets to establish robust, transferable predictive capability.

- SEI-specific diffusion modeling, including diffusion coefficient data generation and physicochemical feature engineering for SEI components, followed by the development of deep learning models to predict Li-ion diffusion behavior within the complex SEI environment.

- Design-oriented case study on MXene as an auxiliary layer for SEI, employing a combined DFT and machine learning approach to identify optimized surface terminations that promote uniform Li-ion transport and enable stable SEI formation on L-metal electrode surfaces.

A illustration of workflow of the aforementioned three points along with the outcomes is also given in Figure 1.3.

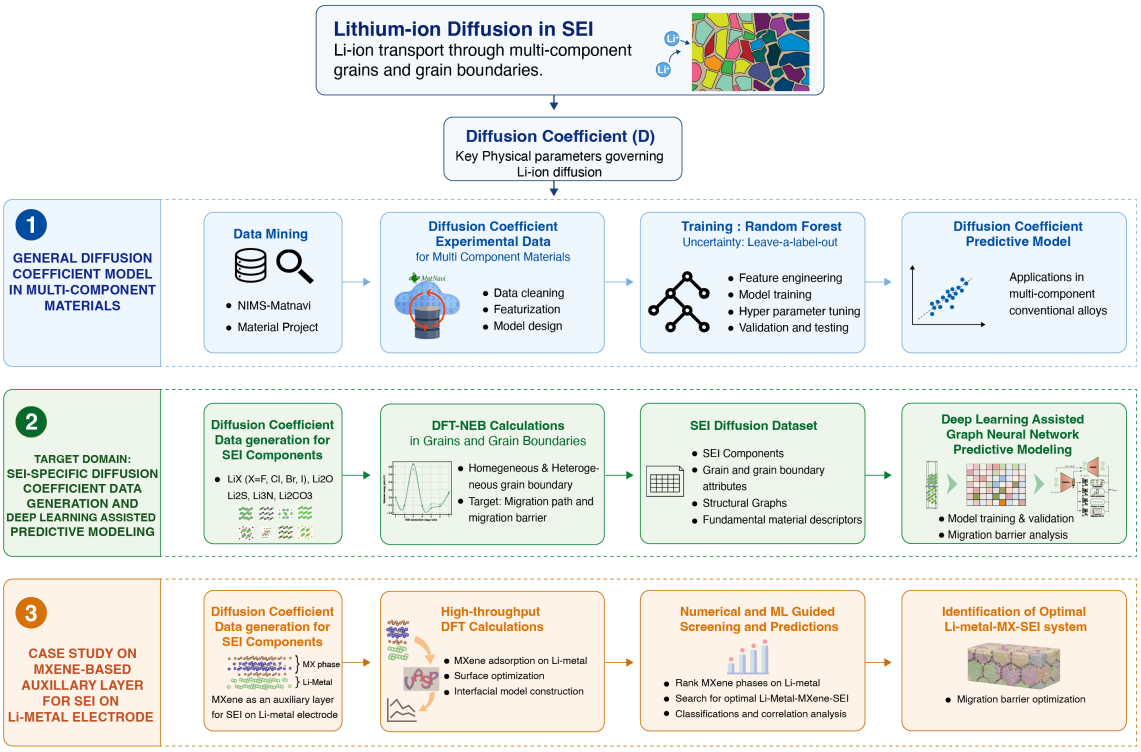


Figure 1.3: Schematic representation of the thesis workflow for understanding and engineering Li-ion diffusion in the SEI. The study begins with the development of a generalized diffusion coefficient modeling framework for multicomponent materials using curated experimental datasets and machine learning approaches. This is followed by SEI-specific diffusion modeling, involving targeted data generation, physicochemical feature engineering, and predictive modeling to capture Li-ion transport behavior within the complex SEI environment. Finally, a design-oriented case study on MXene-based interfacial coatings is conducted using combined DFT and machine learning methods to identify optimized surface terminations that promote uniform Li-ion transport and enable stable SEI formation.

Chapter 2

Motivation and Background

2.1 Ionic Transport in the SEI Components

Ionic transport within the SEI is governed by diffusion processes driven by gradients in chemical potential and constrained by thermodynamic and kinetic factors. However, the inherently complex and heterogeneous structure of the SEI—often described as a multi-layered or mosaic-like assembly of organic and inorganic phases—poses significant challenges for directly probing Li-ion transport using experimental or in situ techniques. Furthermore, Li-ion diffusion spans a wide range of time and length scales, from localized atomic vibrations occurring on the order of 10^{-13} s to long-range transport across grains, grain boundaries, and electrode interfaces that can extend over several seconds.[88]

To achieve a comprehensive understanding of ionic transport in such a system, it is therefore essential to analyze the transport characteristics of individual SEI components and their interfaces. In this context, the mechanisms of ionic diffusion—broadly referred to as ionic migration—are reviewed here for the major stable SEI constituents reported in the literature.

Theoretical modeling of ionic transport is predominantly carried out using first-principles-based computational methods. These approaches focus on identifying migration pathways, transition states, and associated activation barriers, which together

determine diffusion kinetics.

The thickness of the SEI and the crystallographic nature of its constituent phases play a critical role in determining ionic transport properties. Notably, Li-ion transport in nanoscale SEI environments can differ significantly from bulk behavior.[89] For instance, electrochemical impedance spectroscopy studies by Guo and Gallant [90] have shown that the ionic conductivity and diffusivity of Li_2O formed on Li metal are several orders of magnitude higher than those measured in bulk pellet samples. This enhancement is attributed to the distinct chemical environment, high defect density, and unique microstructural features present within the SEI.

In addition to microstructural effects, ionic size and lattice compatibility strongly influence diffusion mechanisms. Soto et al. [25] demonstrated that Li-ions preferentially diffuse via interstitial mechanisms in Na-based SEI structures due to their smaller ionic radius relative to Na^+. Conversely, Na^+ ions tend to favor concerted-exchange mechanisms in Li-based lattices. Such findings highlight the importance of lattice geometry and ion size mismatch in determining dominant transport pathways.

The primary diffusion mechanisms in SEI components include vacancy-mediated hopping, interstitial diffusion (direct hopping), and interstitialcy (knock-off) mechanisms. These processes are mediated by point defects such as vacancies and interstitials.[25, 89]

In the interstitial mechanism, Li-ions migrate through available interstitial sites without significantly perturbing the host lattice.[91] In contrast, the interstitialcy mechanism involves an interstitial ion displacing a lattice atom, which in turn moves into a neighboring interstitial site. The concerted-exchange mechanism represents a coordinated movement of multiple atoms, minimizing lattice distortion and bond breaking during migration.[92] These mechanisms predominantly govern diffusion within crystalline grains, commonly referred to as bulk diffusion.

A molecular simulations study by Borodin et al. [93] suggest that Li-ion transport in certain SEI environments may resemble diffusion in a highly polar, liquid-like medium, further emphasizing the dynamic and non-uniform polycrystalline nature of the SEI. Given that the inorganic SEI layer is typically polycrystalline, ionic transport also occurs along grain boundaries (GBs).[94] It is well established that Li-ion diffusion along GBs can be several orders of magnitude faster than through the bulk lattice due to increased free volume and structural disorder at grain boundaries.[95]

Many earlier studies have treated the SEI as a homogeneous medium, thereby overlooking its heterogeneous-polycrystalline nature. There are also models such as that proposed by Shi et al. [21] distinguish between organic and inorganic layers, suggesting that diffusion in the outer layer can be described by Fick's law based transport, while transport in the inner layer remains less well understood. Notably, such models often simplify the composition of the inner layer (e.g., assuming dominant Li_2CO_3), whereas experimental evidence indicates that it consists of a complex mixture of inorganic phases.

Crystalline defects play a crucial role in facilitating Li-ion transport within SEI components. As summarized in Table 2.1, various defect types—including vacancies, interstitials, and defect complexes—significantly influence diffusion pathways and activation energies. It is well understood that defects enhance ionic conductivity by increasing the availability of migration sites.[96]

At a given temperature, the equilibrium concentration of defects depends on both the atomic structure of the material and its electronic properties.[97] In the context of the SEI, defect populations are further influenced by the local electrochemical environment, including the electrode potential and interfacial conditions.[98] Consequently, understanding defect formation energies and migration barriers is essential for capturing the full dynamics of ionic transport in SEI materials.

In the following sections, the dominant defect types, their formation energetics, and their associated diffusion mechanisms are systematically discussed for major SEI components.

Table 2.1: Major inorganic SEI components are listed along with their most probable defect types, diffusion mechanisms, and migration barriers.

SEI inorganic components	Major defects	Diffusion mechanism	Migration energy barriers (eV)
LiF	Schottky pairs [99]	vacancy diffusion [25]	8.17
	Li-ion vacancies [99]	concerted exchange [25]	4.07
		knock-off [25]	6.10
		direct hopping [25]	5.96
Li_2CO_3	Li-ion interstitials [21]	knock-off	0.67–1.07
	Li-ion vacancies [21]	direct hopping	0.92–1.32
		vacancy diffusion [25]	0.28
		concerted exchange [25]	1.60
Li_2O	cation–Frenkel pairs [100]	knock-off	1.10–2.50
	Vacancy defect		0.30–1.00 [101]
	Interstitial defect		0.60–1.20 [101]
LiOH	Vacancy defect	knock-off	0.20 [61]
	Interstitial defect		

2.1.1 Lithium fluoride

LiF is a stable component of SEI that forms from electrolytes containing fluorine. It is one of the major components of SEI along with other components – Li_2O, LiOH, and Li_2CO_3. The stability property of LiF has been utilized for generating long-lasting interphases because it forms highly stable interfaces with the electrolyte[102]. LiF is also well known for its temperature tolerance. For that reason, using it as a major component of SEI improves the high-temperature cycle performance of the battery[103]. It has been reported that LiF can be formed through the decomposition of salt such as $LiPF_6$ [104–106] and LiTFSI[107, 108], additives such as fluoroethylene carbonate, or via reactions involving trace HF[105, 109, 110]. Cao et al. [46] says that it is challenging to predict the mechanism of LiF formation. Given the popular precursors $LiPF_6$ and carbonates, they concluded that formulation of LiF at 1.5 V

proceeds through a concomitant occurrence of both direct PF_6^- anion reduction and electrocatalytic transformation of hydrogen fluoride (HF).

Most of the diffusion studies in LiF were performed using the first principles-based methods. These studies are performed in two parts: (1) the concentration of defects in SEI in contact with electrodes and (2) the transport of the dominant defects (e.g., Li vacancy)[99]. Pan et al. [99] have correlated the chemical potential of lithium with the voltage of electrodes. This is a promising approach to model ionic transport as defect properties are linked to an electrochemical parameter. Furthermore, Pan et al. [99] analyzed ionic conductivity of a total of seventeen possible native defects with their relevant charge states in LiF and concluded that the main defect type in the intrinsic region was Schottky pair and in the p-type region was Li-ion vacancy (here, the regions are defined to describe the main defect reactions with different electrodes). They have also conducted a fruitful comparison between lithium and sodium ions in terms of the defect properties in their respective SEI component and found that the energy required to create defects in LiF is the lowest when Na ions replace Li ions due to the smaller size of the lithium-ion when compared to the sodium ion. Besides that, lithium ions in Na-based SEI components prefer a mechanism involving the migration of the interstitial ion through the knock-off or direct hopping mechanism.

In 2018, Soto et al. [25] reported in their NEB study on defects that the diffusion barrier of positively charged F-vacancy is 0.69 eV and negatively charged Li-vacancy ranges from 0.57 to 0.60 eV in LiF. In the same work, the authors also mentioned that Li-ion migration in LiF is much higher (0.73 eV) when compared to Li_2O (0.15 eV) and Li_2CO_3 (0.23 eV to 0.49 eV). This finding has also been verified in another work by Zheng et al. [61] in which they claim that the key reason behind this fast transport phenomenon is because similar ions are being localized in the surrounding environments between the initial state and transition state during the diffusion process.

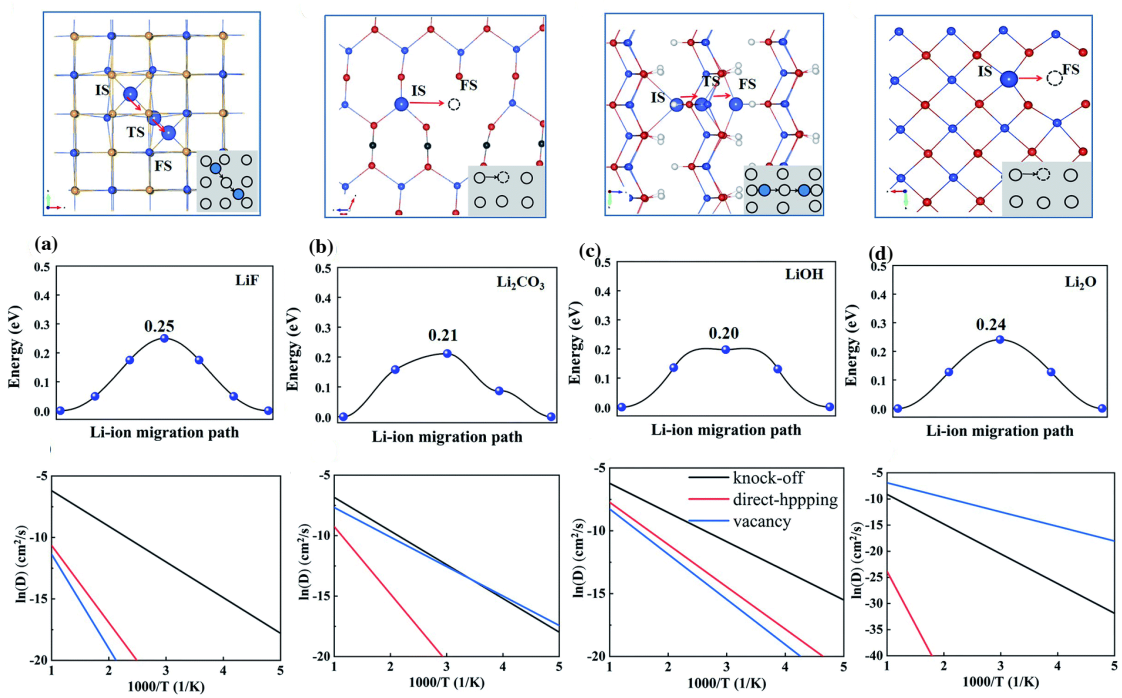


Figure 2.1: Diffusion profiles of the different ionic migration mechanisms for bulk (a) LiF, (b) Li_2CO_3 (c) LiOH, and (d) Li_2O. Respective models used for the calculation have been given in the first row where the circles represent the lithium vacancies. Reproduced with permission from reference [61] . Copyright 2021 The Royal Society of Chemistry.

The Li-ion diffusion through bulk LiF also points towards a higher diffusion barrier as shown in Figure 2.1 (a) with vacancy-assisted mode as the favorable mechanism of diffusion.

Energy profile of the diffusion barrier for various mechanisms of Sodium-ion diffusion through LiF has given in Figure 2.2 (a). Among the given mechanisms mentioned in the figure, concerted exchange between two lattice positions has the lowest activation energy (4.07 eV). However, this mechanism requires a significant change in the structure, resulting in a migration barrier of 3.32 eV. Due to this high barrier, it can be inferred that Na diffusion through LiF is not very likely compared to its diffusion through NaF. Also for the same diffusion process, the direct hopping mechanism was found to have the lowest energy barrier (0.38 eV), whereas the knock-off mechanism

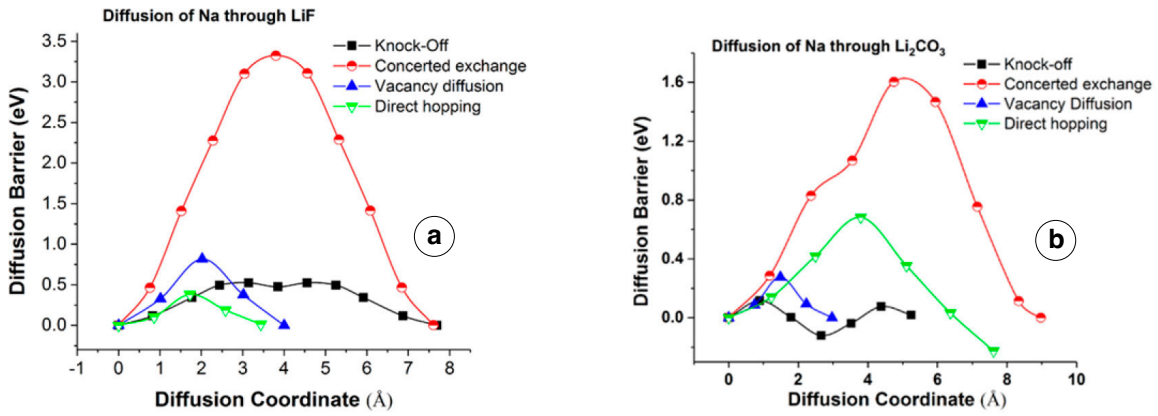


Figure 2.2: Diffusion profiles of the different ionic migration mechanisms for (a) LiF, (b) Li_2CO_3. Adapted with permission from reference [25]. Copyright 2018 American Chemical Society.

had a slightly higher barrier (0.52 eV).

When examining the ionic conductivity of LiF, a strong correlation to the electrochemical environment can be deciphered. For instance, the ionic conductivity of LiF is reported to be approximately 10^{-31} Scm^{-1} when it is in contact with a negative electrode and it increases to 10^{-12} Scm^{-1} on a positive electrode [99].

When investigating the ionic conductivity of LiF, a notable correlation with the electrochemical environment becomes apparent. Specifically, it has been observed that the ionic conductivity of LiF is approximately 10^{-31} Scm^{-1} when it is in contact with a negative electrode, and this value increases to 10^{-12} Scm^{-1} when it is in contact with a positive electrode. This finding highlights the significance of the electrochemical conditions in which LiF operates, and emphasizes the importance of understanding the diffusion properties based on the surrounding media in order to optimize the performance of LiF-based SEI.

An NEB study on bulk LiF suggests that lithium vacancy-assisted diffusion is difficult to happen at room temperature due to the higher migration energy barrier (0.729 eV)[111]. Also, this migration barrier is much higher than the lithium-ion migration

barrier in graphite (0.48 eV to 0.49 eV) [112].

LiF is well-known for its insulating properties when it is in an SEI environment. Theoretical studies have shown that crystalline LiF has a wide band gap of 10.8 eV, which effectively prevents electronic tunneling through its lattice. Experimental measurements, however, have shown the band gap to be even wider at 14.1 eV. The electronic density of states depicted in Figure 2.3 provides further evidence of this insulating behavior. These findings highlight the importance of the unique electronic properties of LiF, particularly in the context of its presence in LiF[61, 99].

2.1.2 Lithium carbonate

Lu and Harris [23] provided a brief summary of their TEM, HRTEM, and XPS studies, outlining the presence of Li_2CO_3 as one of the stable components of the SEI. They noted that the inner inorganic layer is dense, and that the primary component is crystalline-monoclinic Li_2CO_3. In a separate study, Shi and Lu reported the presence of Li_2CO_3 on both cathode and anode surfaces, and suggested that Li-ion interstitials are the primary carriers of Li-ions in the voltage range of 0 – 0.8 VShi et al. [21].

In a follow-up study utilizing DFT calculations, they found that excess Li-ion interstitials (below 0.98 V) and Li-ion vacancies (above 3.98 V) are the primary diffusion carriers in Li_2CO_3. Both carriers are equally dominant within the voltage range of 0.98 –3.98 V. Additionally, they observed that Li^+ interstitials are the dominant diffusion carriers in Li_2CO_3 on the anode (graphite), whereas Li^+ vacancies play this role on the cathode (NCA).

A study conducted on bulk Li_2CO_3 that formed on graphite anode, identified five crystallographically distinct migration pathways generated on a vacancy defect. The study showed that the lowest energy barrier is approximately 0.227 eV, while the highest energy barrier is approximately 0.491 eV. This indicates that Li-ions can rapidly

diffuse through the Li_2CO_3 compound when vacancies are present in the lattice. Additionally, Figure 2.1 (b) in the study supports this finding, displaying a migration barrier of 0.21 eV. The study also determined that direct hopping is the energetically favorable mechanism for diffusion in bulk Li_2CO_3.

The energy profiles for various mechanisms of diffusion of Sodium-ion through Li_2CO_3 are given in the Figure 2.2 (b). The said figure depicts the knock-off mechanism as an easy way of ionic diffusion through Li_2CO_3 with less energy expenditure. Further, the underlying mechanism of the interstitial diffusion is knock-off mechanism, which is controlled by the coordination number with Oxygen anions rather than by the size of the open channels in Li_2CO_3 [21]. This mechanism generally applies to ionic conductors with isolated polyhedral anions or layered tetrahedral networks [21]. In addition to this, Iddir and Curtiss [113] has reported that vacancy-mediated Li-ion diffusion is negligible when compared to the interstitial Li-ion diffusion along the (010) plane of Li_2CO_3 through which an easy migration occurs with an energy barrier of 0.28 eV.

Although Li_2CO_3 contributes to strong mechanical rigidity of the SEI with a mechanical strength range of 192 to 330 MPa, its effect on Li-ion transport is still uncertain[114]. Some studies suggest that crystalline Li_2CO_3 is a typical Li-ion conductor[115]. A previous study by Zhang and colleagues demonstrated that doping Li_2CO_3 with Li_3PO_4 can enhance its ionic conductivity for temperatures up to $400°C$[116]. However in 2004, Zhuang's research group has shown strong evidence of particle isolation that resulted from the formation of Li_2CO_3 on $LiNi_{1-x}Co_xAl_yO_2$ (NCA) particles[117]. In their study, some NCA particles could not be lithiated/delithiated after the surface was covered with Li_2CO_3; however, it is not clear if this was a result of Li_2CO_3 blocking Li-ion transport or electronic tunneling [118].

Furthermore, Li_2CO_3's lithiophobic nature is still evident in certain garnet com-

posite electrolytes such as PLLA electrolyte, where removing Li_2CO_3 from its continuous conductive interlayers leads to higher Lithium-ion carrier concentration and faster Lithium-ion transport[119].

Meanwhile, the electronic band gap data of Li_2CO_3, which is theoretically 7.07 eV and experimentally 7.5 eV, indicates that it exhibits electronic insulating behavior[15].

2.1.3 Lithium hydroxide

LiOH has a unique tetragonal layered-like crystal structure with the $P4nmm$ space group, with Lithium-ions occupying the central sites of the layered-like structure while the OH^- groups are vertically connected with the layer structure. Electrically, LiOH is an insulator with a band gap of 5.481 eV. It is formed in lithium-ion batteries through the reaction between $LiPF_6$ salt and trace amounts of moisture in the battery electrolyte, and can also form from the reaction between Li_2O with water[120, 121]. The presence of LiOH in the SEI is well-established, and it is primarily found in aged electrodes, likely due to the reaction of water with the methoxide and oxalate[122]. The presence of LiOH in the SEI plays a critical role in forming a protective layer on the surface of the anode, which prevents further electrolyte reduction and degradation of the electrode material.

Research has shown that bulk phase LiOH has the lowest migration barrier, estimated at 0.20 eV, and tends to prefer diffusion via the knock-off mechanism (as illustrated in Figure 2.1 (c)). This mechanism is initiated by the diffusion of Li-ion located at the interstitial site along the [001] direction, while simultaneously knocking off an existing Li-ion from the lattice site, leading to the transition state. Compared to other bulk diffusion mechanisms, LiOH also exhibits faster diffusion (with a diffusion coefficient of 9.236×10^{-6} cm^2 s^{-1} at 300 K), similar to that observed in LiF. Furthermore, adsorption studies using Bader charge and differential charge density

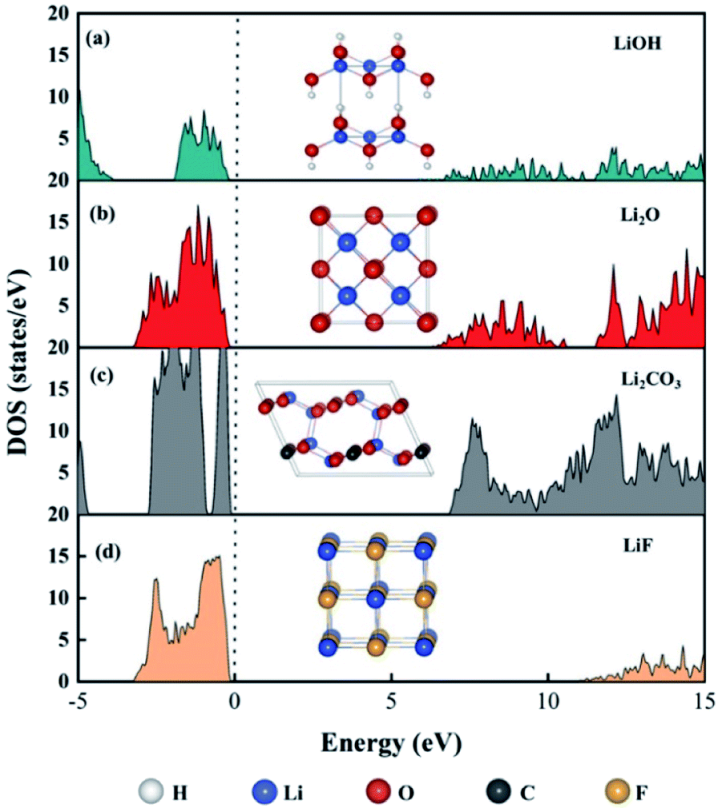


Figure 2.3: Total electronic density of states and the crystal structure of (a) LiOH, (b) Li_2O, (c) Li_2CO_3, and (d) LiF. The dashed line indicates the location of the valence band maxima, which is set to zero.Reproduced with permission from reference [61] . Copyright 2021 The Royal Society of Chemistry.

have indicated a significant charge transfer between the Li adatom and LiOH, which is greater than those observed in LiF, Li_2CO_3, and Li_2O. This supports the bonding nature between the lithium and oxygen atoms in LiOH[61].

2.1.4 Lithium oxide

Li_2O is an active participant in SEI with an antifluorite crystal structure, which forms when low-voltage anodes come into contact with solid or liquid electrolytes containing oxygen[123]. Li-ion migration via knock-off, direct-hoping and vacancy assisted has

been reported in Li_2O and their corresponding energy profile is illustrated in Figure 2.1 (d). The dominant intrinsic defects in Li_2O are cation-Frenkel pairs, which consist of an interstitial Li^+ and a negatively charged vacancy, according to Chadwick et al. [100]. Ionic migration in fluorite-structured materials is typically associated with thermally induced Frenkel-type disorder at temperatures below the melting point[124]. The ionic conductivity of Li_2O is therefore moderately low ($\sim 10^{-12}$ S/cm at room temperature), similar to that of Li2CO3 ($\sim 10^{-8}$ Scm^{-1}), but it can be increased through appropriate doping[101, 125]. A change in activation energy is consistently observed at 650–800°C and conductivity is insensitive to doping beyond this temperature region. However, Lorger et al. [101] reported that ionic conductivity in Li_2O is relatively insensitive to doping for a temperature range of range 250–900°C, due to the low solubility of most plausible dopants. In their defect chemical model of Li_2O, they also mentioned that the electronic conductivity is much lower than the ionic conductivity at least under oxidizing conditions, which helps reduce the growth rate of SEI layers over anodes. They concluded the findings by putting forward a controversial fact that, while ionic transport is too slow in bulk Li_2O, the Li_2O present in SEI exhibits a faster ionic conductivity. This fact could stem from the collective action of other SEI components and the presence of more GBs, where faster Li-ion transmission occurs.

In more detail, the faster diffusion of vacancies in Li_2O may result from lithium vacancy-assisted migration along the cubic edges where Li atoms are located at the corners of the simple cubic structure, as illustrated in Figure 2.4. The activation energy for edge-oriented migration (0.152 eV) is much lower than that for migration over the face or body diagonals[111]. In addition, the vacancy is located in an octahedral void surrounded by six other lithium atoms (three on top and three on bottom), enabling vacancies along the cubic edges to diffuse rapidly in a three-dimensional network.

In a related study, Guo and Gallant [90] investigated the ionic migration through

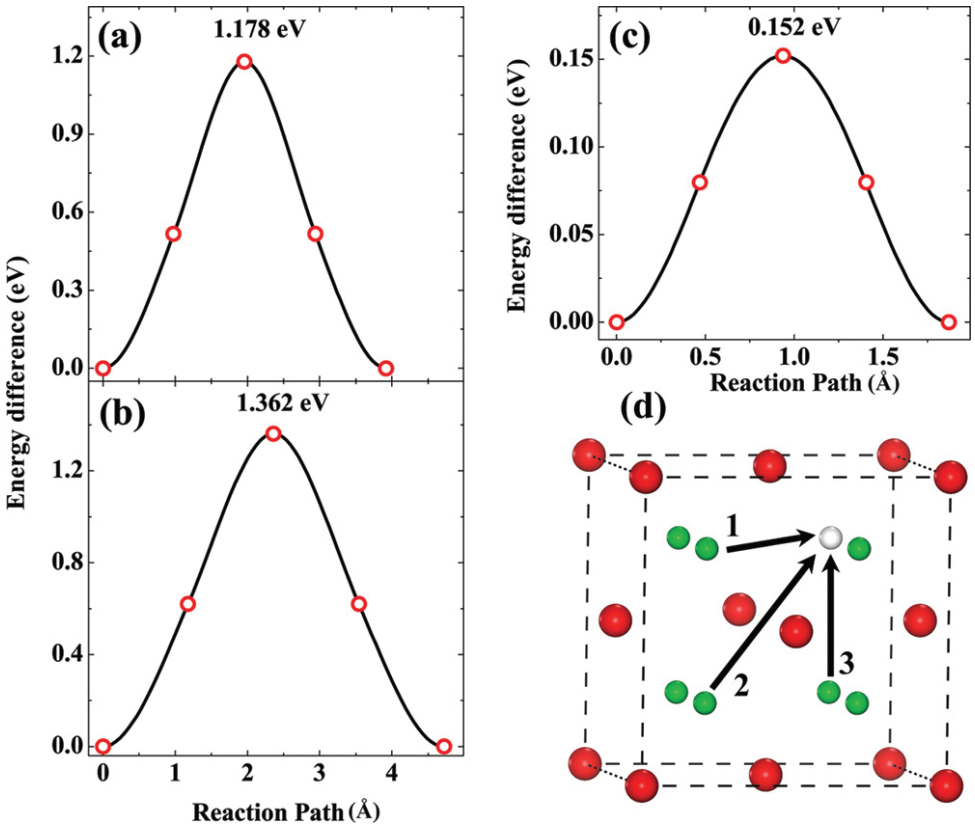


Figure 2.4: (a–c) are energy profiles of different migration pathways of single lithium-ion migration in Li_2O. (d) illustrates the cubic structure and migration pathways, marked with arrows. Red and green spheres are O and Li atoms, respectively, and the white sphere indicates the Li vacancy position. Adapted with permission from reference [111]. Copyright 2011 American Chemical Society.

the solid-state Li_2O interface on the lithium cathode end. Their research found that the formation temperature significantly influences the transport parameters of Li_2O due to the emergence of larger grains and the decrease in grain boundary density resulting from the higher reaction temperature. Furthermore, they reported that the ionic conductivity and diffusivity of Li_2O on lithium are several orders of magnitude higher than the values obtained through bulk pellet measurements. This observation is similar to that of Li_2O present in the SEI formed on the anode.

2.2 Crystalline factors affecting the ionic migration in SEI

2.2.1 Crystal Growth Surfaces

The formation of ionic migration channels in the inorganic sublayer of SEI is greatly affected by the crystallographic planes of constituent components and their corresponding directions. Typically, planes with lower surface energy are formed. As a result, the grain boundaries of components in the inorganic sub-layer typically consist of planes with the lowest surface energy. Furthermore, crystal planes with a larger specific surface area hence have more exposed planes are beneficial for facilitating rapid transport of Li-ions.[126]. Additionally, the formation of SEI is influenced by the surface energy and stability of the cathode/anode material.[127]. Studies have shown that certain planes ({111} and {110}) of Mn spinel cathode with a truncated octahedral shape exhibit enhanced Li-ion diffusion, resulting in improved cycling properties[128–130].

Another notable correlation between ionic migration with planes and directions has been demonstrated in a study conducted by Shi et al. [118]. According to the study, the diffusion of Li^+ and Li^- in Li_2CO_3 results in the formation of a lithium Frenkel pair

when their distance is approximately between 3 to 5 Å on the same (100) plane. The motion of the interstitial and vacancy in the formed Frenkel pair is highly correlated along [010] in the (001) plane. Another DFT-based study by Iddir and Curtiss [113], found that the activation energy for Li-ion diffusion across the plane of Li_2CO_3 was 0.60 eV, which is higher than that for the diffusion along the open channels (0.28 eV) in the [010] directions. This indicates that the diffusion of Li-ions across the plane of Li_2CO_3 is slower compared to the diffusion along the open channels. Their subsequent research on the same topic revealed that the energy barriers for Li^+ ion to hop through the open channel and for a neutral Li vacancy to move along [001] are 0.28 eV and 0.23 eV, respectively. Islam and Bredow [131] conducted a study that showed a similar trend in other SEI components as well. According to their investigation, the most likely migration pathway for Li^+ in Li_2O on its (111) plane is a zigzag pathway, rather than a straight line along a direction parallel to the surface plane, with an activation energy of 0.25 eV.

For further reference, the surface energies for selected planes of various SEI components have been listed in Table 2.2. All the data in Table 2.2 have been validated with VASP to check the consistency of the data. In addition to this, the surface energy of unexplored components has also been added to the table. The trend in the table shows that the most stable crystal surface for LiF, Li_2CO_3, and LiOH, is (001), and it is (111) for Li_2O. Also, it is clearly visible that the surface energy of slabs with non-zero dipole terminations (Ex: (111) surface of LiF, (100) surface of Li_2O, and (001) surface of LiOH) is higher when compared to the slabs with zero dipole symmetric terminations.

2.2.2 Grain Boundaries

Li-ion transport through GBs is faster than migration through lattice spaces. In a study on GBs conducted by Chen et al. [73], it was shown that Li_3N based SEI films

Table 2.2: Surface energy of all possible orientations of crystallographic planes of reported SEI (inorganic) components.

SEI components	Surface orientation	Surface energy per atom	Theoretical - DFT (meV/Å^2)	Experimental (meV/Å^2)
LiF	(001)		18.97	20[132]
	(110)	-4.82	46.09	49[132]
	(111)		56.40	55[132]
Li_2CO_3	(001)		P.S *	11.23 [133]
	(110)	-6.37	P.S *	13.47[133]
	(110)		P.S *	35.57[133]
Li_2O_2	(0001)		P.S *	41[134]
	(1100)	-4.86	P.S *	52[134]
	(1100)		P.S *	105[134]
Li_2O	(100)		74.78	75[135]
	(110)	-4.78	57.00	56[135]
	(111)		29.25	30[135]
LiOH	(001)		160.28	13[136]
	(100)	-5.09	21.46	16.22[136]
	(111)		30.35	N.A
LiN	(100)		127.23	N.A
	(110)	-3.73	40.51	N.A
	(111)		38.22	N.A
Li_2S	(100)		P.S *	52[137]
	(110)	-4.07	32.60	33 [137]
	(111)		22.52	21 [137]

* Polar surface termination: The conventional method used to calculate surface energy is not efficient for polar surfaces because of its inability to decouple the two inequivalent surfaces generated. Polar surface termination can be treated as compensating the charge by capping with foreign atoms to satisfy the electron counting rule, hence nullifying the polarity of exposed surfaces.

rich in GBs on the surface of Li metal exhibit enhanced rate performance and long-term cycle stability without dendrite formation. Similar to this, work on La−LiF interface suggests that the GB with a stable vacancy structure and a smaller transport energy barrier facilitates efficient Li-ion migration in the interface system[138]. Another remarkable comment on this is from the work of Zhang et al. [139], in which they state that abundant heterogeneous GBs among LiF, LiN_xO_y, and Li_2O contribute to uniform and rapid diffusion of Li-ions through SEI, which guarantees uniform Lithium deposition.

A recent work of Ramasubramanian et al. [140] demonstrates the Li-ion transport through GBs of Li_2O, LiF, and Li_2CO_3, in which they clearly mentioned that a faster lithium diffusion occurs through numerous open channels formed by the GBs. Particularly, their DFT studies shows that the fastest Lithium diffusion rate is observed in the heterogeneous LiF/Li_2O GB, compared to the homogeneous LiF/LiF and Li_2O/Li_2O GBs. In terms of electronic transport, their studies suggest that achieving a dense SEI structure with well-ordered grain boundaries (GBs) and sharp interfaces is essential to maintain electronic passivity, which in turn helps suppress dendrite growth and electrolyte reduction.Feng et al. [141].

2.3 Battery components affecting the structure of SEI

2.3.1 Binders

Binders ensure the cohesion of the active material (electrode) particles to the current collector plate while being electrochemically stable. The popular binder used in Li-ion batteries are polyvinylidene fluoride (PVdF) and carboxymethylcellulose sodium salt (CMC); wherein CMC is found as an excellent binder for carbonaceous as well as non-carbonaceous silicon-based electrodes[142]. In addition to this, CMC has a beneficial role in the irreversible capacity of a graphite electrode and helps form a stable SEI with a low carbon content[143]. When it comes to the PVdF, which is also a good binder but cannot endure the substantial volume changes on lithiation and hence cannot be used in silicon-graphite based electrodes[144].

Binder material chemistry influences the formation of SEI. Chai, Qu, and Zhang have reported that the presence of less reductive species in SEI during the first cycle significantly improved the coulombic efficiency of their newly proposed chitosan-based electrode when compared to the conventional PVDF-based anode[145]. The selection of a polymer binder, such as carboxymethyl cellulose (CMC) or polyvinylidene fluoride (PVdF), has a noteworthy impact on the irreversible deformation of the electrode, which implies that the formation and growth of the SEI layer is influenced by the polymer binder[146]. Similarly, Nafion – a binder additive has been reported as optimizing the morphology and structural stability of the SEI[147]. These studies point towards the fact that SEI's structure can be influenced by the chemical composition

of the binder and its physical properties. In short, the development of an efficient binder material that is compatible with the SEI is inevitable for developing a stable and efficient battery pack.

2.3.2 Separator

The separator is the packing component in LIBs that serves as the boundary between the electrode and electrolyte and stays very close to the SEI. The position of the separator and its relative thickness is shown in Figure 1.1. The separator provides structural integrity to the battery pack in such a way that it serves as a rigid, selectively permeable wall between the cathode, electrolyte, and anode. A good separator should have properties including good porosity, temperature tolerance, mechanical strength, and chemical inertness toward the battery components. Moreover,this thin layer (thickness $\sim$ 20–30 μm) facilitates the ionic shuttling through its micropores between electrodes[148, 149]. The role of a separator in a battery is to prevent the internal short circuit arising from various reasons, such as dendrite growth, leakage of liquid electrolytes, and extrusion of metal electrodes [150]. For safety reasons, most separators are multilayered, designed with a circuit breaking feature, where certain layers have different phase transition temperatures. As the temperature of a cell increases, the lower melting component melts and seals the pores of the adjacent separator layer and stops the ionic transport, hence the current flow in the battery pack[150]. Generally, there are three classes of separators based on their synthesis mode and porosity, which are (1) composite separators – synthesized by coating organic/inorganic materials on the surface of commercial polyolefin, (2) nonwoven separators – prepared by reinstating organic or inorganic materials inside or on the fiber surface of commercial polyolefin, and (3) the porous separators prepared by solution casting method[151]. A work on ultrathin multilayers of commercial PE separators made with polyacrylic acid

and ZrO_2 found that the surface chemistry of the separator influences the formation of SEI and provides additional stability to the layer[152].

Ionic transport through the separator occurs through a convection-driven mechanism if the pore size is in the order of nanometers, and it becomes a diffusion-driven mechanism when the porous size reduces further [153]. In an in-situ study on hydraulic pressure of the electrolyte in vanadium redox battery, Li et al. [154] examined the convection through a microporous separator and found that the convection is mediated by differential hydraulic pressures on both sides of the separator. Diffusion-mediated ionic movement depends on the size, configuration, and total volume of the pore spaces which hold the electrolyte. Apart from that, the chemical interaction effect, associated with polar groups or sites in the membrane substrate, also affects the diffusion by either elevating or depressing the diffusion coefficient selectively[155]. The area to improve in a separator is the development of a potential and chemically compatible separator that can sense and circumvent the thermal runaways and maintain a uniform ionic conductivity from the electrolyte to the electrode.

Additives: Additives are chemicals mixed with electrolytes at a particular proportion to prevent or enhance specific properties of electrolytes and the SEI layer. Fluoroethylene carbonate (FEC) and vinylene carbonate (VC) are widely used for commercialized additives[156, 157]. These additives facilitate the formation of inorganic LiF and Li_2CO_3 components in the SEI[158]. There are diverse categories of additives with specific usages. One example is that the addition of flame-retardant additives (such as phosphorus and halogen-based compounds) into traditional flammable electrolytes mitigates thermal runways to an extent[159]. However, such additives depress the ionic conductivity of the electrolyte and deteriorate the electrodes[160, 161]. Jankowski et al. [162] reported that special functional additives are helpful for the controlled and rapid

formation of SEI, which circumvents the capacity decay of the battery. Similarly, Yang et al. [163] reported that an additive named octadecylamine (ODA) in a conventional electrolyte ($1.2M$ $LiPF_6$ in EC/DMC) with vinyl carbonate (VC) additive enhances the ionic conductivity and physicochemical stability of the SEI in NCM-811 ‖ Ti-SiOx@C full cells. Also, they posit that ODA additives can be easily decomposed on the surface of Ti−SiOx@C anodes compared to VC additives. In a DFT-based work on additives, Park et al. [164] states that lithium tetrafluoro(fluoromalonato)phosphate (LFMP) as a dual-functional electrolyte induces a LiF-rich SEI on graphite anode NCM811/graphite cells at 60° C. Also, they observed that the SEI formed has a weak binding affinity to PF_5 and favors the formation of LiF. Recently, Xu et al. [165] put forward a gradient SEI model with surface-rich polycarbonate in which they combined the advantages of flexible polymer and high touristy ceramic through liquid alloy electrolyte additive. Moreover, they have theoretically and experimentally verified that the gradient SEI created by liquid alloy electrolyte additive accommodates the volume change and mitigates the dendrite suppression. Such additives are suitable for silicon-graphite-based electrodes, where volume expansion is challenging [166].

2.4 Dendrite Formation and Thermal Runaway

Dendrite formation is a critical degradation process in Li based electrodes, particularly Li metal electrode that ultimately limits safety and battery cycle life. In general, dendrite evolution proceeds through three sequential stages: nucleation, growth, and penetration. Among these, the nucleation stage is particularly crucial, as the spatial distribution of initial lithium nuclei dictates the morphology of subsequent deposition. Uniform nucleation leads to smooth and dense lithium growth, whereas localized nucleation promotes the formation of high-aspect-ratio structures that evolve into

dendrites.[78] One of the key factors governing nucleation heterogeneity is the presence of spatially non-uniform Li-ion transport pathways within the SEI. Specifically, the accumulation of low-energy Li-ion diffusion channels at certain regions of the electrode surface can locally enhance ionic flux, resulting in preferential lithium deposition at these sites.[79, 80]

With repeated electrochemical cycling, these localized deposition events become progressively amplified due to feedback between ionic transport and surface morphology. Regions with initially faster Li-ion transport continue to attract higher ionic flux, leading to uneven lithium plating and the development of protrusions[167]. As these protrusions grow, they intensify local electric fields and current densities, further accelerating dendritic growth. Eventually, these needle-like filamentary lithium structures can penetrate the SEI and, in severe cases, the separator, creating internal short circuits.

The implications of dendrite penetration extend beyond mechanical failure to severe thermal consequences. Internal short circuits can trigger rapid heat generation due to localized Joule heating, which, when coupled with exothermic reactions between lithium metal and electrolyte components, can initiate thermal runaway. This cascade of heat generation and chemical decomposition can lead to catastrophic cell failure, leading to thermal runaway. Therefore, controlling dendrite formation is not only essential for electrochemical performance but also for ensuring battery safety particularly for Li-metal based electrodes.

In this context, achieving uniform Li-ion diffusion across both grains and grain boundaries of the inorganic SEI (which forms directly on electrode surface) is of paramount importance. A structurally and chemically homogeneous SEI that facilitates isotropic ionic transport can suppress localized flux variations, thereby promoting uniform lithium deposition and mitigating dendrite nucleation at its origin[168]. There

are reviews and studies which corroborates the role of inorganic SEI components in trapping active Li-ion which eventually gives dendrites. A review by Li et al. [168] describes SEI as a double-edged factor in dendrite growth such that it can both suppress and promote dendrites depending on its structure, uniformity, and transport properties. An important point mentioned in this review is that non-uniform Li-flux is the key reason behind the nucleation sites for dendrite growth. Author also mention about localized current density and SEI morphology evolution are also important factors that triggers dendrite growth. In another study by Cipolla et al. [169] observes the similar logic behind dendrite evolution. They states that variations in SEI thickness create non-uniform lithium-ion flux, leading to preferential deposition at regions of lower resistance, while mechanical instability and cracking of the SEI generate localized hotspots for dendrite nucleation. In short, the microstructure of SEI is the crucial factor that determine the evolution and propagation of dendrites. In view of this, understanding and engineering Li-ion transport pathways within the heterogeneous SEI structure is a key step toward the development of stable and safe lithium-based batteries.

2.5 Modeling Diffusion Coefficient

Diffusion Coefficient, a key material property that is being extensively discussed throughout this thesis. By definition, diffusion coefficient of an element in a host material is defined as proportionality constant that defines the rate at which a substance transfers through a unit surface in a unit time due to a concentration gradient. Diffusion coefficient in solids is usually described by the Arrhenius equation:

$$D = D_0 \exp \frac{E_a}{RT} \tag{2.1}$$

where D_0 is denoted as the pre-exponential factor and E_a as the activation energy.

T denotes the absolute temperature and R the universal gas constant. The parameters D_0 and E_a are usually evaluated from the measurements of diffusion coefficients at a series of temperatures.

Experimentally determining diffusion coefficients typically involves two main approaches: the tracer method and the interdiffusion method. The tracer method involves tracking diffusing species tagged with radioactive isotopes, allowing for the determination of tracer diffusion coefficients by applying known diffusion solutions to measured concentration profiles. However, this method necessitates numerous independent measurements across various homogeneous alloys, with the number of required compositions scaling exponentially with the number of components, making the tracer method a time-consuming process. In addition to this, the availability and stability of radioactive isotopes present further challenges especially when elements like Al and Ca are employed as diffusing species[170]. In such scenarios, the secondary ion mass spectrometry-based thin-film technique mitigates the stability problem to an extent by employing enriched stable isotopes[171]. Additionally, such diffusion coefficient calculation is hampered by the dependence on heavy isotopes as tracers especially when comparing different isotopic species of the same molecule. This is because potential functions are invariant with isotopic substitution within the bounds of the Born-Oppenheimer approximation, potentially overlooking many important but poorly understood factors[172]. On the other hand, chemical diffusion, or interdiffusion, is measured by bringing alloys of different compositions into contact and inducing diffusion transport through chemical potential gradients. In this approach, techniques like the Boltzmann-Matano method in binary systems and the Matano-Kirkaldy method in ternary systems are commonly employed to determine the diffusion coefficients, offering efficient alternatives to the tracer method[173, 174]. However, for multi-element materials (number of elements in a composition ≥ 4) it is generally impossible to apply

this Onsager-formalism-based scheme to estimate the entire matrix of independent interdiffusion coefficients, as the given number of independent diffusion paths, which are one-dimensional by definition, cannot intersect in a multi-component space[175–177].

On the other hand, first-principles calculations and molecular dynamics simulations have become efficient methods for determining diffusion coefficients with the increase in computing resources. Particularly, the NEB and its modified version (climbing image algorithm) implemented in the first principle codes are well-proclaimed for accuracy in determining minimum energy paths and hence the diffusion coefficient[178, 179]. NEB relies on harmonic transition state theory which uses quadratic approximations of the energy surface around saddle points where reaction intermediates situates[180]. Generally, reactions proceed through a minimum energy path (MEP), connected by saddle points in the potential energy terrain commonly known as images in NEB[181]. First-order saddle points, where energy is at a maximum along the MEP but at a minimum in all normal directions, determine the activation energy which can be further solved for diffusion coefficient using Arrhenius equation[182, 183]. One major drawback of NEB-based methods is the immense computational resources required when the system becomes sufficiently large and multi-component.

Through various learning approaches, ML has already been established in material science to understand complex interdependencies among material parameters, thereby offering invaluable insights into tuning properties of materials for target-specific applications. Such approaches are particularly advantageous given the time-consuming process of experimentally understanding material properties such as in the case od diffusion coefficient. This opens a new dimension in material designing, enabling the identification and optimization of the most promising diffusive element for a given material. The knowledge of diffusion coefficient can be applied to the design of material for various engineering applications ranging from alloy design to energy material opti-

mization. For instance, a study by Lü et al. [184] investigated the impact of a solution heat treatment at 693 K on Mg_2Si particles in $Mg-Al-Si$ alloys. The study revealed that the treatment led to spheroidization of Mg_2Si particles due to Si atom diffusion along the Mg_2Si/Mg interface, resulting in superior mechanical properties for the alloys. Similarly in Titanium alloys with $(\alpha+\beta)$ dual phases, the diffusion of α-stabilizing elements (Al, O, etc.) and β-stabilizing elements (Mo, V, etc.) into corresponding phases during heat treatments is identified as a critical aspect of microstructural evolution, which in turn makes the alloy apt for aerospace and marine application[185].

In general, predictive modeling in material science encompasses two main domains. The first domain revolves around the prediction of a material's mechanical properties, including fundamental factors like lattice parameters, lattice volume, density, and a range of elastic features. These properties play a crucial role in determining how a material responds to mechanical forces and deformations. For instance, the work of Li et al. [186] predicts lattice constants from the fundamental features of material composition. In a similar work, Peng et al. [187] examines the link between geometry parameters, relative densities, and range of lattice constants to predict mechanical and fatigue properties of lattice structures with different relative densities and crystalline systems. Another paper by Lee et al. [188] explores high-order Bézier curves to optimize lattice structures by using learning techniques, enhancing mechanical properties like modulus and strength while maintaining efficiency in load bearing and energy absorption. On the other hand, the second domain is mostly on predicting electrical and thermodynamic properties, encompassing key aspects like melting point, electrical conductivity, thermal conductivity, specific heat capacity, and diffusion parameters. Recent review articles have highlighted the optimum performance of ML-based models over analytical models in predicting thermal transport properties and advancing thermo-electric materials research[189, 190]. Parallelly, similar studies are also ac-

celerated in optimizing battery performance by targeting high-cycling efficiency, and durability with superior safety precautions[191–193]. In the literature on ML-based diffusion studies, most research focuses on liquid or gas diffusion media. For instance, a study by Zhao et al. [194] utilized training data from molecular dynamics simulations to estimate the diffusion coefficients of binary and ternary supercritical water mixtures, employing neural networks with the aid of transfer learning. Similarly, other ML-based studies have predicted self-diffusion coefficients in pure liquids, Lennard-Jones fluids, and binary diffusion coefficients in gases[195, 196]. A detailed literature survey reveals that while diffusion studies in fluid media are prevalent, there is a notable absence of ML-based diffusivity studies in solids, particularly in alloy media[197–200].

From the literature on diffusion coefficients in materials, it is evident that the availability of reliable data remains significantly limited across the research domain. Although diffusion coefficients are fundamental transport parameters governing mass transport processes, their experimental determination is often complex, method-dependent, and resource-intensive. Consequently, the limited data that exists is largely concentrated on conventional alloy systems and well-characterized materials. Given the absence of prior ML studies that systematically utilize such sparse diffusion data, this work motivates and establishes an ML-based predictive framework for conventional alloys and impure metallic systems considering the available experimental data.

In the context of energy materials, particularly battery systems, diffusion coefficient data is comparatively more available, primarily for alkali ions such as Li, Na, and K in selected electrolyte systems. These include both conventional liquid electrolytes and emerging solid-state electrolytes[201]. However, even within these systems, the available data remains limited in scope and often exhibits inconsistencies arising from variations in experimental methodologies. That being said, Li-ion diffusion data in electrode materials is relatively accessible through well-established repositories such as

the Materials Project and the NIMS Materials Database.

In contrast, diffusion coefficient data within the SEI is extremely scarce. The limited experimental data available is largely restricted to a few inorganic SEI components, such as LiF, Li_2O, and Li_2CO_3, and often lacks consistency due to insufficient information about control parameters of experiment. On the computational side, most reported diffusion data has been generated using NEB calculations, with comparatively fewer studies employing molecular dynamics simulations. Furthermore, existing studies predominantly focus on Li-ion diffusion in isolated, pristine SEI components for specific defect sites, without capturing the complexity of realistic SEI environments (multi-component structure). A comprehensive review of these studies is provided in Section 2.1.

In light of these research gaps, the second part of this thesis focuses on the development of a systematic and unified diffusion dataset for eight major inorganic SEI components, namely LiF, LiCl, LiBr, LiI, Li_2O, Li_2S, Li_3N, and Li_2CO_3. This dataset encompasses both grain and grain-boundary diffusion across representative low-energy surfaces and interfaces, including both homogeneous and heterogeneous grain boundaries, thereby establishing a comprehensive design space for Li-ion migration in SEI environments. Based of this dataset, a path-aware graph variational autoencoder (GVAE) is employed to learn latent representations of NEB trajectories, which are subsequently integrated into a graph neural network (GNN) framework for predicting minimum-energy pathways and migration barriers which ultimately gives diffusion coefficient of Li-atom.

Finally, beyond intrinsic SEI properties, this work also explores the role of an auxiliary thin interfacial layer as a strategy to regulate Li-ion flux and enhance SEI performance. This case stuidy is inspired by recent advances in two-dimensional (2D) materials, particularly MXenes, such layers can provide high electronic conductivity,

tunable surface chemistry, and robust thermo-chemical stability[202–204]. Their ability to facilitate uniform Li-ion distribution and offer abundant active sites makes them promising candidates for interfacial engineering. Although MXenes have been extensively studied as electrode materials, their application as a functional interlayer for SEI modulation remains largely unexplored. Incorporating such 2D materials as auxiliary layers offers a potential pathway to achieve uniform ion transport, suppress dendrite formation, and improve the long-term stability and performance of electrodes in lithium-based battery systems.

Chapter 3

Methodology

3.1 Ab-initio Modeling for Elemental Diffusion

3.1.1 Density Functional Theory

Density Functional Theory (DFT) calculations were employed to investigate the atomistic structure, energetics, and charge transfer characteristics of the systems under study[205]. All simulations were performed within the framework of the Kohn–Sham formalism, as implemented in a plane-wave-based computational package. The exchange–correlation interactions were described using the generalized gradient approximation (GGA), typically with the Perdew–Burke–Ernzerhof (PBE) functional. The interaction between valence electrons and ionic cores was treated using the projector augmented wave (PAW) method[206, 207]. A plane-wave basis set was used with an energy cutoff chosen based on systematic convergence testing to ensure accuracy in total energies and forces.

The Brillouin zone was sampled using Monkhorst–Pack k-point grids, with the density of the mesh determined through convergence studies to balance computational efficiency and precision. For slab or low-dimensional systems, reduced k-point sampling along the non-periodic direction was employed. All atomic structures were fully relaxed until the total energy and force convergence criteria were satisfied, typically within thresholds of 10^{-6} eV for energy and < 0.05 eV/Å for atomic forces. Additional

convergence tests with respect to vacuum spacing, supercell size, and k-point density were performed to eliminate spurious interactions and ensure reliable representation of isolated systems.

These first-principles calculations enabled the evaluation of key properties such as adsorption energetics, diffusion barriers, and charge redistribution, often complemented by charge analysis methods such as Bader partitioning. Overall, DFT provides a robust framework for linking electronic structure to macroscopic behavior, offering critical insights into the mechanisms governing interfacial and transport phenomena.

3.1.2 Migration Barrier From First-principle Calculations

Transition state theory (TST) is based on statistical mechanics, explaining the elementary step reaction of slow thermal processes on a hypothetical 'dividing surface' separating reactant and product regions of phase space. The conventional TST is based on a potential energy surface with a saddle point between reactants and products, where a transition state is a plane determined by normal coordinate analysis of small vibrations around the saddle point. In other words, the plane referred to here is obtained by minimizing displacement along the reaction's normal coordinate[208]. The conventional TST valid at relatively low temperatures and in higher temperature saddle point regions may no longer control the reaction rate[209]. Therefore, the generalized transition state is more significant in such scenarios. According to TST, the rate constant at temperature T is defined as

$$k_{\mathrm{TST}} = \frac{k_{\mathrm{B}}T}{2\pi\hbar}\frac{Z_{\dagger}}{Z_{\mathrm{eq}}}\exp\left(\frac{-E_a}{k_{\mathrm{B}}T}\right) \tag{3.1}$$

where k_{B} and $\hbar$ are the Boltzmann and reduced Planck constants, respectively; $Z_{\dagger}$ is the partition function of the transition state without the contribution of the reactive

mode, Z_{eq} is the total partition function of the reactant state, and E_a is the activation energy defined as,

$$E_a = V_\dagger + \frac{1}{2}\Sigma_i \hbar\omega_{i,\dagger} - V_{\text{eq}} - \frac{1}{2}\Sigma_j \hbar\omega_{j,\text{eq}} \tag{3.2}$$

where the frequency $\omega_{i,r}$ corresponds to the square root of the i^{th} positive eigenvalue of the Hessian of the potential energy surface evaluated at the state r.

TST has several applications including the ability to predict temperature and time dependence of defect nucleation[210], rate constants analysis for intersystem crossings, spin-forbidden reactions, and spin-crossovers in large complex systems[211].

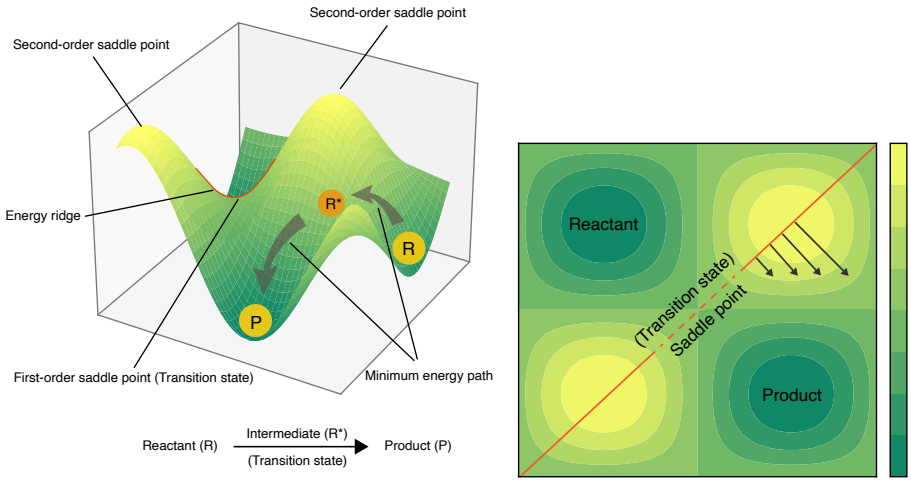


Figure 3.1: Potential energy terrain of a MEP for a chemical reaction[44, 45].

3.1.2.1 Harmonic Transition State Theory

The application of TST is challenging due to the complexity of the equation for the rate constant (k) [210]. This complexity in the expression (Equation 3.1) for k was simplified by Vineyard [212] by introducing quadratic approximations to the energy surface around the critical points, hence giving harmonic TST (HTST) approximation[212, 213]. Generally, the chemical reaction proceeded through a minimum energy path (MEP) as illustrated in Figure 3.1 (a) and this path is connected over saddle points

(where most probable transition states are located) in the potential energy terrain. Figure 3.1 (b) depicts the terrain of potential energy, where the initial and final configurations are separated by a hyperplane passing through a first-order saddle point on the energy ridge. Here the hyperplane normal is pointed towards the direction of the unstable mode, the eigenvector of the Hessian matrix along which the saddle point is a maximum[214]. In some reactions, the second-order saddle points may occur above first-order saddle points on the ridge, relevant to the fact that a particular transition mechanism and a certain product state are associated with those first-order saddle points. For a reaction, the MEP is extrapolated by advancing each degree of freedom of the system in such a way that the energy is minimal with respect to all degrees of freedom normal to the path. Further, MEPs are not unique for a given initial and a final configuration. For a first-order saddle point (SP), at each point on the MEP, the energy is at a minimum with respect to all normal directions and maximum along the MEP[215]. The global maximum energy of the first-order saddle points refers to the activation energy for the reaction.

Vineyard's approach in HTST, in line with TST, assumes that thermodynamic functions can also be defined at the saddle points. Further, the theory holds good for particularly solids at relatively low temperatures. This temperature approximation is fulfilled through the assumption that the energy difference between the second saddle point and the transition state shall be larger than $k_{\mathrm{B}}T$, i.e.,

$$E^{2^{\mathrm{nd}}\mathrm{SP}} - E^{\mathrm{TS}} \gg k_{\mathrm{B}}T \tag{3.3}$$

hence the rate of a chemical reaction in HTST is given as,

$$k_{\mathrm{HTST}} = \frac{\Pi i = 1^{3N}\nu_i}{\Pi j = 1^{3N-1}\nu_i^*} \exp\left(\frac{-E_a}{k_{\mathrm{B}}T}\right) \tag{3.4}$$

where ν_i are vibrational frequencies of a hopping atom at its equilibrium position pre-hop, and ν_i^* are the two real vibrational frequencies at the static saddle point. Further, HTST treatment on diffusion obeys first-order kinetics and agrees with the empirically observed Arrhenius expression for the temperature dependence of the rate constant[216].

The HTST is subjected to quantum mechanical corrections in certain circumstances. For instance, at very low temperatures, one has to consider the zero point energy of the vibrational ground state. Otherwise, this may cause an underestimation of activation energy[217]. Also, based on the nature of the system, one may expect the tunneling from the reactant configuration to the final product configuration especially when the barrier potential is thin. Neglecting the tunneling effect may result in an underestimation of activation energy[218]. Similarly, replacing the classical partition function with their quantum mechanical analogs for the harmonic vibrations of the system can also influence the results of the rate constant[216].

3.1.2.2 Nudged Elastic Band Theory

Finding MEP is based on connecting the initial and final configuration of the reacting species through a number of transition configurations (known as images in NEB calculations). According to the plain elastic band method (PEBM), these transition states are assumed to be connected over a hypothetical spring of springs of zero natural length (chain of states) in the potential terrain; optimizing the spring forces with respect to the intermediate images while keeping the end point images yields the MEP [219]. In PEBM, the effective force acting on the i^{th} image in two-dimensional London-Eyring-Polanyi-Sato (LEPS) potential[220] is expressed as,

$$\vec{F}_i = -\vec{\nabla} V(\vec{R}_i) + \vec{F}_i^s \tag{3.5}$$

where $\vec{F}_i^s$ is the spring force defined as

$$\vec{F}_i^s = k_{i+1}(R_{i+1} - R_i) - k_i(R_i - R_{i-1}) \tag{3.6}$$

where k is the spring constant between pairs of images.

However, the plain elastic band scheme suffers from the corner-cutting problem, and thus overestimates the saddle point region in the terrain.

Since PEBM is weak in most of the cases in predicting the MEP, Jónsson et al. [219] introduced a modified version, known as nudged elastic band (NEB) approach. In this method, the spring force acting on the i^{th} image in the same potential terrain is modified in such a way that the component of force acting on the image along the MEP's local tangent (parallel) component and its perpendicular one are considered instead of the net force. The local tangent is expressed as,

$$\hat{\tau}_i = \frac{R_{i+1} - R_{i-1}}{|R_{i+1} - R_{i-1}|} \tag{3.7}$$

And the spring force, $\vec{F}_i^{\mathrm{NEB}}$, becomes

$$\vec{F}_i^{\mathrm{NEB}} = \vec{F}_i^{\perp} + \vec{F}_i^{\parallel} \tag{3.8}$$

where

$$\vec{F}_i^{\perp} = -\left(\nabla V(R_i) - \nabla V(R_i) \cdot \hat{\tau}_i\right) \tag{3.9}$$

and

$$\vec{F}_i^{\parallel} = k\left(|R_{i+1} - R_i| - |R_i - R_{i-1}|\right)\hat{\tau}_i \tag{3.10}$$

In short, the parallel component of the true force and perpendicular component of the spring force is projected out while minimizing the effective elastic force.

NEB has been further improved by Henkelman et al. [221] on introducing a climbing image algorithm for an accurate estimation of local tangent thereby mitigating the problems with kinks on the elastic band in certain reactions. They have also mentioned a new strategy where the NEB is combined with the dimer method for minimizing the computational effort in the estimation of the MEP[222, 223].

Furthermore, NEB has been improved by Zhu et al. [224] for finding the SPs of the stress-assisted, thermally-activated dislocation process in FCC metals[225]. This modification is known as free-end NEB which is efficient particularly when the MEP is distorted by a high load, such that SPs comes close to the initial state. This is implemented by cutting short the elastic band and allowing the end of the shortened band to move freely on the potential energy surface close to the initial state[224].

3.1.3 Phonon Scattering in SEI Components

Thermal conductivity analysis of SEI components carried using standard phonon transport theory, where key phonon properties, including frequency, group velocity, mean free path, and relaxation time, are calculated using 2nd order harmonic and third-order anharmonic FCs. The thermal conductivity analysis was carried out in the *ShengBTE* framework, which is efficient in calculating the lattice thermal conductivity of wide-bandgap crystalline solids [226, 227]. The Born effective charge and dielectric constant are included to account for the nonanalytic behavior of the potential energy surface in the Brillouin zone due to Coulombic interactions. The second-order FCs and third-order FCs for this computation were generated using *Phonopy* and *Thirdorder.py* frameworks, respectively[228, 229]. The force convergence criterion was set at -0.01 eV/Å to calculate second-order harmonic and third-order anharmonic interatomic FCs with exchange-correlation functional suitable for respective calculations. All phonon calculations described here are carried out in $2 \times 2 \times 2$ supercells after

the convergence test carried out on supercells of various sizes. The K-point mesh and the plane wave cutoff energy are selected based on the crystal system and the type of elements present in the system. Density functional perturbation theory was used to extract second-order FCs. For third-order FCs, the finite displacement approach was used with an atomic displacement of 0.01 Å from the equiLMBrium position and with a closest neighbor cutoff distance of 3 Å. Using dynamic FC matrices of the second and third order, phonon relaxation times and the thermal conductivity tensor were calculated using Fermi's Golden rule in conjunction with the iterative solution of the Boltzmann Transport Equation (BTE). Using BTE, the phonon scattering rates are calculated, where the accuracy essentially depends on the number of sampling points in the first Brillouin zone[230]. Combining the BTE and Fourier's law[231, 232], the phonon lattice thermal conductivity tensor can be calculated as

$$\kappa^{\alpha\beta} = \frac{1}{3}\Sigma C_{v,\lambda} v_{\lambda}^{\alpha} v_{\lambda}^{\beta} \tau_{\lambda}^{p} \tag{3.11}$$

where $\lambda = (q, v)$ denotes the phonon mode with polarization v and wave vector q, $C_{v,\lambda}$ is the volumetric specific heat, v_{λ}^{α} and v_{λ}^{β} are the α and β component of the phonon group velocity vector v_{λ}, and τ_{λ}^{p} is the phonon relaxation time[233]. Here, phonon volumetric specific heat can be obtained using Bose-Einstein statistics and phonon relaxation time from Matthiessen's rule[232, 233]. Through an iterative process using Equation 3.11, the thermal conductivity tensor can be solved from the full solution of the linearized phonon Boltzmann equation[234]. We used system-specific K-space meshes for each system after convergence tests to solve the BTE.

In general, the total phonon scattering rate (inverse of phonon relaxation time) in a crystalline system can be calculated using Equation 3.12[235].

$$\tau_{tot}^{-1} = \tau_{pp}^{-1} + \tau_b^{-1} + \tau_d^{-1} + \tau_i^{-1} \tag{3.12}$$

where τ_{pp}^{-1}, τ_b^{-1}, τ_d^{-1}, and τ_i^{-1} represent the scattering rates due to phonon-phonon (Umklapp) scattering, phonon-boundary scattering, phonon-defect scattering, and phonon-isotope scattering, respectively. In this study, the temperature-dependent lattice thermal conductivity in SEI grains is calculated by considering only Umklapp phonon scattering and is then compared with results that included phonon–grain boundary scattering, accounting for the grain–structured characteristics of SEI. Since *ShengBTE* is not explicitly accounting for boundary scattering, we added the boundary scattering term to the code such that the relaxation time governed by boundary scattering as $T_b = \frac{L}{|v_\lambda|}$ where L is the characteristic length, i.e, grain size and v_λ is the phonon group velocity vector for the respective mode. Now, τ_λ^p can be written as the sum of the Umklapp scattering rate (τ_{pp}^{-1}) and the boundary scattering rate as

$$\tau_\lambda^p = \frac{1}{\tau_{pp}^{-1} + T_b^{-1}} = \frac{1}{\tau_{pp}^{-1} + \frac{|v_\lambda|}{L}} \tag{3.13}$$

Therefore, the lattice thermal conductivity is evaluated for grain sizes ranging from L=2 nm to 10 nm, with increments of 2 nm, to capture the influence of grain boundary scattering on heat transport. It is important to note that Equation 3.13 assumes perfectly diffusive grain boundary scattering, which simplifies the boundary interactions by neglecting the possibility of partial specularity. In real polycrystalline materials, phonon scattering at grain boundaries may exhibit partially specular behavior depending on phonon wavelength, boundary structure, and surface roughness. Additionally, the model does not account for Kapitza resistance, which can become significant at low temperatures due to phonon mismatch across grains. These simplifications may introduce discrepancies between the calculated and experimental values, particularly

in the low-temperature regime[232].

3.1.4 Modeling Grain and Grain Boundaries

Accurate modeling of material structures is a critical prerequisite for DFT simulations, as it directly influences the convergence of both total energy and atomic forces. A well-converged geometry is essential for reliably extracting key physical quantities such as ground-state energy, interatomic forces, and free energy. In this thesis, all DFT simulations were performed using the Vienna *Ab initio* Simulation Package (VASP). VASP requires the input crystal structure to be defined in the form of a POSCAR file, which contains detailed information about the lattice parameters as well as the atomic positions, specified either in fractional or Cartesian coordinates.

3.1.4.1 Slab Models

To construct these input geometries, slab models of varying sizes were employed, with careful consideration of the number of atomic layers and system dimensions to adequately represent surface and interfacial phenomena. The choice of slab thickness and atomic configuration was guided by the need to balance computational efficiency with physical accuracy, ensuring that the modeled systems capture the essential structural and chemical characteristics relevant to the study.

To facilitate the construction, manipulation, and analysis of atomic structures, several computational tools were employed in this study. The Atomic Simulation Environment (ASE) was used for programmatic generation and modification of atomic configurations, enabling efficient creation of slab models and automation of simulation workflows[236]. Pymatgen (Python Materials Genomics) was utilized for advanced materials manipulation, including structure conversion, symmetry analysis, and interfacing with databases such as the Materials Project[237]. Visualization and manual

inspection of structures were carried out using VESTA, which provides detailed three-dimensional representations of crystal geometries and atomic arrangements[238]. Additionally, OVITO (Open Visualization Tool) was used for post-processing and analysis of atomic structures, particularly for visualizing defects, grain boundaries, and diffusion pathways. Together, these tools form an integrated workflow for robust structure generation, validation, and analysis in DFT-based studies[239].

3.1.4.2 Nearest Neighbor Algorithm

Diffusion coordinates were identified using a nearest-neighbor search algorithm. For each NEB image, the slab model was first converted into a *Pymatgen* `Structure` object. Periodic neighboring sites around each atom were then identified using the built-in neighbor-search methods in Pymatgen. A cutoff distance of 1.5–2.0 Å was used, depending on the crystal structure and local bonding environment of each SEI component. The resulting neighbor list was used to define possible Li-ion hopping pathways and to track the corresponding diffusion coordinates across the NEB images.

3.2 Machine Learning Aspects in Modeling Elemental Diffusion

3.2.1 Data Mining: The Diffusion Coefficient

Input feature data : This study utilized diffusion data extracted from the material database popularly known as *MatNavi*, developed by the National Institute of Material Science, Japan[240]. *Kakusan* is the diffusion database subset under *MatNavi* material database that aims to encompass fundamental diffusion data of metallic and inorganic materials, primarily sourced from relevant literature references[241, 242]. The

dataset used for this study includes attributes such as the diffusion coefficient (m^2/s), temperature (K), diffusing element, diffusion mode, reference literature, and composition of alloy with weight percentages of constituent elements. The diffusing media presented in the dataset encompasses both multi-component alloys and impure metals, with purity quantified as a percentage.

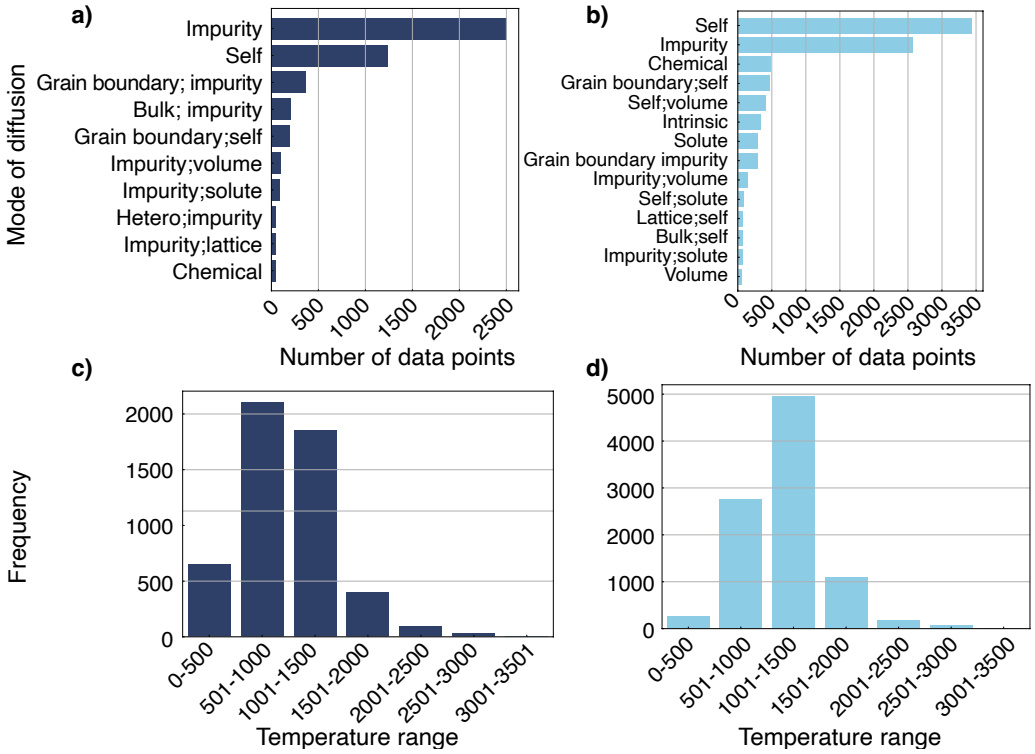


Figure 3.2: Dataset overview: a) diffusion mode present in dataset for IM media and b) MCA media. Frequency of temperature range of diffusion for c) IM media and d) MCA media.

A comprehensive overview of the data collected for Impure Metallic (IM) and Multi-Component Alloy (MCA) media is depicted in Figure 3.2. The choice selection of diffusion modes for modeling is based on the dataset size. For example, Figure 3.2a illustrates the IM media dataset, where the impurity and self diffusion modes comprise a larger number of diffusion data points (3431 and 2567, respectively) compared to other modes, thus making them suitable for training. Similarly, in MCA media (Figure 3.2b),

self diffusion (3431 data points), impurity diffusion (2567 data points), and chemical diffusion (483 data points) modes have been selected due to the sufficient amount of data available. Some diffusion modes are ambiguously labeled in the dataset; for instance, 471 data points are categorized under a diffusion mode termed 'grain boundary, self' in MCA dataset. Despite the sufficient number of data points in such modes, the ambiguity in diffusion mode classification led to the exclusion of such modes of diffusion from further study. Figure 3.2c and d display the experimental temperature range, mostly between 500 and 1500 K, for calculating the diffusion coefficients in IM and MCA media respectively. The periodic tables given in Figure C.1a and b highlight the diffusing elements considered for IM and MCA media respectively. The percentage contribution from each block is shown in the pie diagram given in the inset of the periodic table. The pie diagram illustrates the distribution pattern of diffusing elements across both media types. It shows that a minority of diffusing elements originate from the s and f blocks, while the majority stem from the d and p blocks in both media. This visualization also facilitates the assessment of the model's applicability to specific diffusing elements and diffusion media, offering valuable insights for users.

Data preprocessing: The *MatNavi* database offers diffusion data along with essential descriptors such as temperature, diffusion mode, diffusion medium composition, and diffusion element for a diffusion coefficient. Specifically, in alloy compositions, it provides the constituent ratios of elements as percentages, while in elemental media, purity of the media is expressed as a percentage. Since most of the experimental data are based on isotope tracer method, corresponding diffusing elements were tagged with the information (mass number) of isotope used.

The data was initially categorized according to diffusion modes, with subsequent removal of rows containing missing data points. Additionally, we identified and eliminated extraneous alphanumeric characters within the diffusion media representation,

along with isotope labels associated with diffusing elements. Similarly, the dataset was further treated to address outliers, missing values, and duplicate data. Before being input into the featurization algorithm, the diffusion system was subjected to representation alterations that guarantee the process of diffusing element X across AaBbCcDd (or Aa in the case of IM media) media at a specific temperature, where uppercase letters denote the element and lowercase letters indicate the corresponding percentage of the element. The overall preprocessing treatments are illustrated in a diagram given in Figure C.3

Target data – the diffusion coefficient: The diffusion coefficient (D) presented in the dataset is calculated based on Arrhenius representation of diffusivity given by Equation 3.14.

$$D = D_0 \exp\left(\frac{-Q}{RT}\right) \tag{3.14}$$

where D_0 is a temperature-independent constant, Q the activation energy for diffusion, R the gas constant and T the temperature. The statistical parameters of diffusion coefficient for respective models are given in Table 3.1.

Table 3.1: Statistical parameters of target data – diffusion coefficient*.

Medium	Diffusion mode	Types of diffusion medium#	Number of data	Minimum ($\times 10^{-25}$)	Maximum ($\times 10^{-7}$)	Mean (μ) ($\times 10^{-10}$)	Standard deviation (σ) ($\times 10^{-9}$)	Coefficient of variation ($\frac{\sigma}{\mu}$) (%)
Impure metallic media	Impurity	33	2506	0.099	1800	1520	4220	3336.35
	self	32	1240	0.028	0.011	0.046	0.058	1260.25
	self	191	3431	22.70	0.009	0.020	0.022	1126.92
Multi-component alloy media	impurity	271	2567	0.230	6.840	9.080	15.601	1724.90
	chemical	14	483	5000	0.011	0.448	10.500	23.54

* Unit of Diffusion coefficient is given in m^2/s in the table.
# Number of different types of diffusion media present in data.

Prima facie, it can be seen that the diffusion coefficient has extremely low order of magnitude ranging from 10^{-25} – 10^{-7} m^2/s in the overall data. Secondly, the aggregation of data points at certain frequencies is evident (Figure C.4) because the diffusion

coefficients corresponding to most of the alloys are collected for a widely varying range of temperatures from the experiment. This results in an elevated value for the coefficient of variation as given in Table 3.1. In particular, self-diffusion in IM media, and self and chemical diffusion in MCA media show higher variance compared to other modes of diffusion. Considering this higher variability in target data, log-transformed values of the diffusion coefficients were used for training. This study prefers the log-transformed diffusion coefficient as the target variable since it exhibits close proximity to the normal distribution behavior as seen in Figure C.4, aiding in better performance of models.

3.2.2 Feature Engineering

Performance of predictive models in the ML domain is highly influenced by both the quantity and quality of data, as well as the choice of training algorithms. This study observes that the choice of descriptors plays a significant role in predicting diffusion coefficients. Descriptors encompass factors that have direct or indirect influence on diffusion coefficients and are therefore considered meticulously in this study. In light of this, we included a detailed set of descriptors separately for diffusing elements and diffusion media for predicting diffusion coefficients, acknowledging that certain descriptors may pertain specifically to the chemical and structural characteristics of the chemical species involved. In addition to this, the temperature corresponding to the diffusion is placed as an important feature considering its direct influence on the target variable.

3.2.2.1 Fundamental Material Attributes

Figure 5.1 presents an overview of our modeling approach through featurization, where we utilize the *Magpie* featurization preset available in the *Matminer* library to fea-

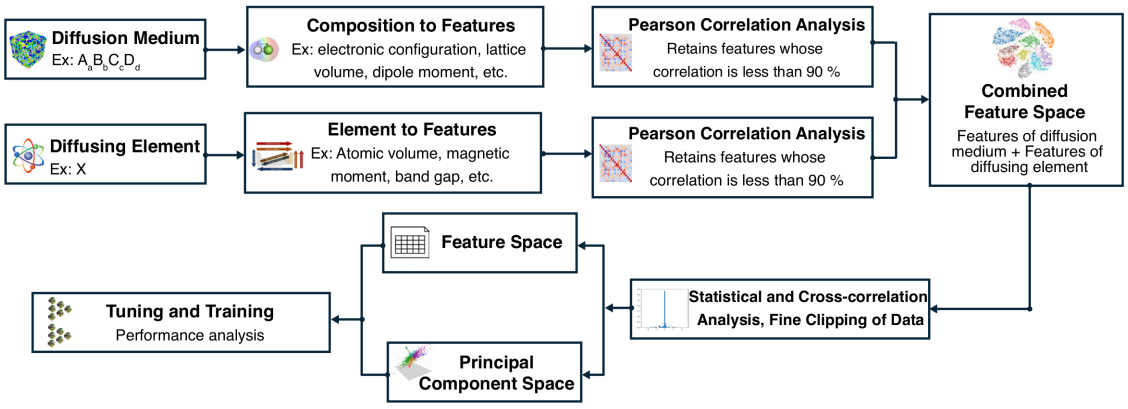


Figure 3.3: Workflow of predictive modeling of diffusion coeffieint in conventional alloys.

turize the composition of the diffusion medium and the diffusing element. *Matminer*, an open-source Python library designed for material data mining, serves as a valuable resource in our featurization scheme and model development.[243]. The *Magpie* featurization preset includes statistical computations for elemental attributes as mean, average deviation, range, mode, minimum, and maximum [244]. A detailed overview of all such attributes along with the statistical operation considered is given in Table C.6. When employing the *Magpie* algorithm to extract composition features, we considered descriptors weighted by the composition fraction of each element. However, this weighted scheme was omitted when featurizing the diffusion element. Consequently, two sets of descriptors were generated, one corresponding to the diffusion media and the other to the diffusing element. Then, these two sets of features underwent separate Pearson's correlation analyses implemented through *Pandas* – a Python library, wherein features exhibiting a correlation exceeding 90% were excluded[245, 246]. For instance, in cases where two features displayed a correlation above 90%, we retained the feature with the greater Mean Absolute Deviation (MAD). Pearson's correlation ($r_{f1,f2}$)

between feature-1 (f1) and feature-2 (f2), was computed using the Equation 3.15.

$$r_{f1,f2} = \frac{\sum \left(f1_i - \bar{f}1\right)\left(f2_i - \bar{f}2\right)}{\sqrt{\sum \left(f1_i - \bar{f}1\right)^2 \left(f2_i - \bar{f}2\right)^2}} \tag{3.15}$$

where $f1_i$ and $f2_i$ are the feature values, and $\bar{f}1$ and $\bar{f}2$ respective sample mean. Pearson's coefficient, a statistical metric, quantifies the magnitude and direction of a linear correlation between two continuous variables. This coefficient varies between -1 and 1, with 1 indicating a flawless positive linear relationship, -1 denoting a perfect negative linear correlation, and 0 signifying no linear association. The correlation-based filtering was applied separately to each set of features, the features of the diffusion medium and element were merged, and then another correlation analysis was performed in the combined feature space. However this time features with a correlation greater than 75% were omitted, by retaining the feature with the highest MAD ($= \frac{1}{n}\sum_{i=1}^{n} |x_i - \bar{x}|$ where n is the number of data and, x_i and $\bar{x}$ are data point and mean of the data respectively). This feature space is then considered for further analysis and training.

Feature space analysis: Scaled principal component analysis (PCA) based on the covariance matrix was utilized to minimize the dimension of the data due to the large number of features. There are various ways to calculate the number of PCs [247, 248]. In this study, the choice of the number of PCs to be retained was based on the explained variance. Finally, the training was performed using both decomposed feature space (PC space that explains 99% of variance in data) and pristine feature space for a comparative analysis of the model's performance.

3.2.3 ML Models

3.2.3.1 Random Forest

For the predictive modeling of diffusion coefficient in conventional alloys, considering the size of data, number of features, and complexity among features, the Random Forest (RF) has been chosen as the main algorithm for training purposes with hyperparameters optimized through `GridSearchCV()` method implemented thorough *scikit-learn*[249] library. Here, a computationally intensive tuning scheme, incorporating a broad range of hyperparameters, is employed to maximize the R^2 and minimize the MSE scores to ensure the optimum performance of model. For a comparative study of performance of models based on the algorithm chosen, we also included the training and testing results of Support Vector Regression and Deep Neural Networks. In all models, training and testing were carried out in segmented data intervals in order to determine the ideal range of target data that provides maximum model performance with a larger number of training data. Furthermore, we conducted 10 random trials to assess the stability of the model's performance across different test-train sampling sizes while maintaining a test-train ratio of 20% and 80% throughout.

3.2.3.2 Support Vector Machine Regression

Support Vector Machine Regression (SVR) is a supervised learning method that extends the principles of support vector machines to regression problems. Instead of minimizing the training error directly, SVR aims to find a function that deviates from the target values by at most ϵ while maintaining maximum flatness. This is achieved by solving the optimization problem:

$$\min_{\mathbf{w},b,\xi_i,\xi_i^*} \frac{1}{2}\|\mathbf{w}\|^2 + C\sum_{i=1}^{N}(\xi_i + \xi_i^*) \tag{3.16}$$

subject to

$$y_i - (\mathbf{w}\cdot\mathbf{x}_i + b) \leq \epsilon + \xi_i, \quad (\mathbf{w}\cdot\mathbf{x}_i + b) - y_i \leq \epsilon + \xi_i^*, \tag{3.17}$$

$$\xi_i, \xi_i^* \geq 0, \tag{3.18}$$

where ϵ defines the width of the insensitive tube, C is a regularization parameter controlling the trade-off between model complexity and tolerance to deviations, and ξ_i, ξ_i^* are slack variables. By introducing kernel functions, SVR can effectively model non-linear relationships in high-dimensional feature spaces, making it a powerful tool for regression tasks with complex underlying patterns.

3.2.3.3 Deep Neural Networks

Deep Neural Networks (DNNs) are a class of machine learning models composed of multiple layers of interconnected neurons, capable of learning complex non-linear relationships from data. A DNN maps an input $\mathbf{x}$ to an output $\mathbf{y}$ through a sequence of transformations, where each layer applies a linear operation followed by a non-linear activation function:

$$\mathbf{h}^{(l)} = \sigma\left(\mathbf{W}^{(l)}\mathbf{h}^{(l-1)} + \mathbf{b}^{(l)}\right), \tag{3.19}$$

where $\mathbf{h}^{(l)}$ represents the activations of the l-th layer, $\mathbf{W}^{(l)}$ and $\mathbf{b}^{(l)}$ are the weights and biases, and σ is a non-linear activation function such as ReLU or sigmoid. The final output layer produces the prediction $\hat{\mathbf{y}}$:

$$\hat{\mathbf{y}} = f(\mathbf{x}; \theta), \tag{3.20}$$

where θ denotes all learnable parameters. The model is trained by minimizing a loss function $\mathcal{L}(y, \hat{y})$ over the dataset, typically using gradient-based optimization:

$$\theta \leftarrow \theta - \eta \nabla_\theta \mathcal{L}, \tag{3.21}$$

where η is the learning rate. Due to their depth and flexibility, DNNs are particularly effective in capturing high-dimensional and highly non-linear patterns in data.

3.2.3.4 Graph Neural Networks

Graph Neural Networks (GNNs) are a class of deep learning models designed to operate on graph-structured data, where relationships between entities are explicitly represented. In a graph $\mathcal{G} = (\mathcal{V}, \mathcal{E})$, nodes $\mathcal{V}$ are associated with feature vectors, and edges $\mathcal{E}$ encode their interactions. GNNs learn node representations by iteratively aggregating information from neighboring nodes through a message-passing scheme. At layer l, the node embeddings are updated as:

$$\mathbf{h}_i^{(l+1)} = \sigma\left(\sum_{j \in \mathcal{N}(i)} \mathbf{W}^{(l)} \mathbf{h}_j^{(l)} + \mathbf{b}^{(l)}\right), \tag{3.22}$$

where $\mathbf{h}_i^{(l)}$ denotes the feature vector of node i at layer l, $\mathcal{N}(i)$ represents the set of neighboring nodes, $\mathbf{W}^{(l)}$ and $\mathbf{b}^{(l)}$ are learnable parameters, and $\sigma(\cdot)$ is a non-linear activation function. After several such layers, the learned node embeddings can be used to predict graph-level or node-level properties:

$$\hat{\mathbf{y}} = f(\mathcal{G}; \theta), \tag{3.23}$$

where θ denotes all model's learnable parameters. By explicitly incorporating relational structure, GNNs are particularly well-suited for modeling complex systems such as materials, molecules, and crystalline interfaces.

This thesis used GNN mainly to include material structure data (as POSCAR –a VASP format) into training which used for GNN based predictive modeling of Li-ion through SEI components.

3.2.3.5 Variational Autoencoders

Variational Autoencoders (VAEs) developed by Kingma and Welling [250] are generative models that learn a probabilistic latent representation of data by combining principles from neural networks and variational inference. In this thesis used VAE as a main tool for meaningful and scientifically consistent data augmentation.

In VAE, instead of mapping inputs to a deterministic latent space, it assume that the data $\mathbf{x}$ is generated from a latent variable $\mathbf{z}$ with a prior distribution, typically Gaussian. The encoder learns an approximate posterior $q_\phi(\mathbf{z}|\mathbf{x})$, while the decoder reconstructs the input via $p_\theta(\mathbf{x}|\mathbf{z})$. The latent variables are sampled using the reparameterization trick:

$$\mathbf{z} = \boldsymbol{\mu} + \boldsymbol{\sigma} \odot \boldsymbol{\epsilon}, \quad \boldsymbol{\epsilon} \sim \mathcal{N}(0, \mathbf{I}), \tag{3.24}$$

where $\boldsymbol{\mu}$ and $\boldsymbol{\sigma}$ are outputs of the encoder. The model is trained by maximizing the evidence lower bound (ELBO):

$$\mathcal{L} = \mathbb{E}_{q_\phi(\mathbf{z}|\mathbf{x})} \left[\log p_\theta(\mathbf{x}|\mathbf{z}) \right] - D_{\mathrm{KL}} \left(q_\phi(\mathbf{z}|\mathbf{x}) \,\|\, p(\mathbf{z}) \right), \tag{3.25}$$

which balances reconstruction accuracy and regularization of the latent space. By learning a continuous and structured latent representation, VAEs enable efficient sam-

pling, interpolation, and generation of new data instances.

3.2.4 Generative Models for Materials

A generative modeling approach was also explored in this study as a possible route for designing SEI structures with controlled Li-ion diffusion behavior. The general objective was to learn the structural manifold of Li-containing inorganic SEI components and generate candidate structures that could provide more uniform Li-ion transport pathways. The selected framework was based on a latent-variable generative model in which the material structure, represented by atomic numbers (A), atomic coordinates (X), and lattice parameters (L), is encoded into a latent vector (z). The decoder then reconstructs the structure either from a noise-perturbed representation or directly from the latent space, with the loss function defined by comparing the reconstructed structure with the target relaxed structure. In one attempt, the model was trained to learn the transformation from POSCAR to CONTCAR, where the initial and relaxed structures were compared and the reconstruction loss was optimized. In a second attempt, only relaxed CONTCAR structures were used: Gaussian noise was added to the atomic coordinates and structural representation, and the model was trained to denoise and recover the original relaxed configuration. This strategy was intended to help the model learn physically meaningful local distortions around equilibrium structures.

Figure 3.4 presents the proposed generative modeling workflow for generating candidate SEI structures for Li-ion diffusion studies. In this framework, an input structure is first encoded into a latent representation using a variational autoencoder-type architecture, where the encoder estimates the latent mean μ and variance σ. A random noise term is then used to sample points from the latent space, allowing new structural variants to be generated rather than only reconstructing the original input. The sampled latent vector is decoded to produce candidate POSCAR-like structures, which

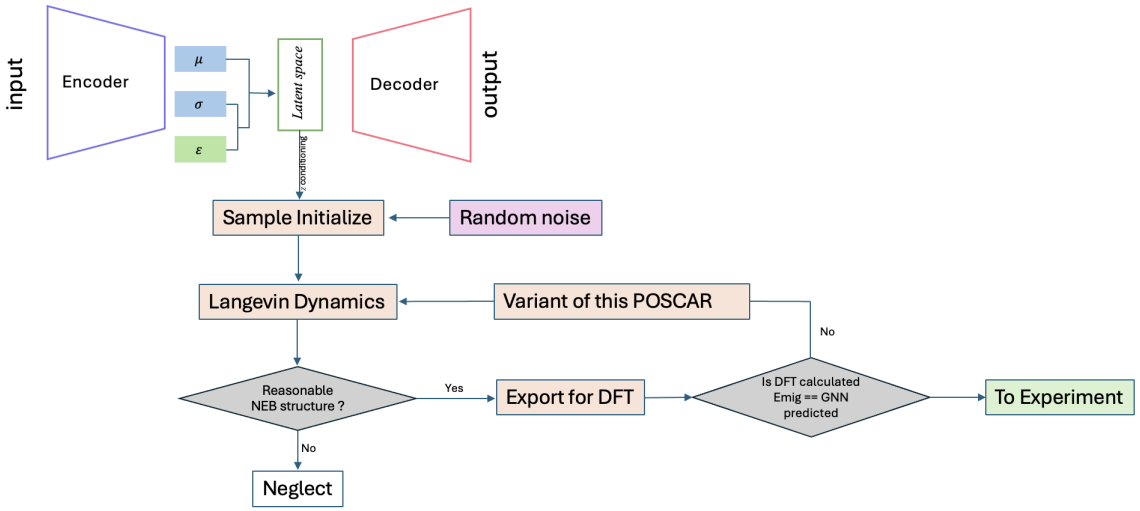


Figure 3.4: Proposed generative modeling workflow for SEI structure generation and Li-ion migration barrier screening. An input structure is encoded into a latent space using a variational autoencoder-based model, followed by random sampling and decoding to generate new POSCAR variants. The generated structures are filtered based on their suitability for NEB calculations, exported for DFT validation, and compared with GNN-predicted migration barriers before being considered for experimental relevance.

can then be screened for physical and geometric validity. Structures that provide a reasonable NEB pathway are exported for DFT-based migration barrier calculations. The resulting DFT migration barrier can then be compared with the value predicted by the trained GNN model. If the DFT and GNN-predicted barriers are consistent, the structure can be considered as a possible candidate for further experimental consideration. If not, the generated structure can be treated as a new variant and reintroduced into the workflow for further refinement. In this study, this workflow was considered as a future-facing approach because the available dataset was not large enough to train a fully reliable generative model.

However, the generative model work could not be advanced into a fully predictive generative design framework because the available dataset was limited in both size and diversity. A good generative model for SEI design would require a substantially larger number of relaxed structures, diffusion pathways, and corresponding migration

barriers across different SEI chemistries and interfaces. Therefore, this part of the study should be considered an initial attempt toward generative structure modeling for SEI materials rather than a completed generative design workflow.

3.3 Model Evaluation Schemes

3.3.1 Evaluation Matrices

As a standard regression problem, the following three evaluation criteria have been used to compare the performance of all models, including the Root Mean Squared Error (RMSE), Mean Absolute Error (MAE) and coefficient of determination (R^2) calculated as follows.

$$RMSE = \sqrt{\frac{1}{n}\sum_{i=1}^{n}(D_i^{exp} - D_i^{pred})^2} \tag{3.26}$$

$$MAE = \left|\frac{1}{n}\sum_{i=1}^{n}(D_i^{exp} - D_i^{pred})^2\right| \tag{3.27}$$

$$R^2 = \left(\frac{\sum(D_i^{exp}D_i^{pred}) - \frac{\sum(D_i^{exp}D_i^{pred})}{n}}{\sqrt{\left[\sum D_i^{exp^2} - \frac{\left(\sum D_i^{exp^2}\right)}{n}\right]\left[\sum D_i^{pred^2} - \frac{\left(\sum D_i^{pred^2}\right)}{n}\right]}}\right)^2 \tag{3.28}$$

3.3.2 Uncertainty Quantification

In addition to error estimation, we have also performed an uncertainty analysis in our modeling. Our findings demonstrate that the errors generated by the *RF* algorithm implemented in *LoLo* (an RF-centered machine learning library in Scala) library are

well-calibrated[251]. As mentioned in Ling et al. [252]'s work, an ideally calibrated uncertainty estimate should have a particular relationship with the errors of an ML model. Specifically, the distribution of $r(x)/\sigma(x)$ where $r(x)$ is the normalized residuals of the prediction given by $r(x) = \frac{\hat{f}(x)-f(x)}{\sigma(x)}$ (here, $\hat{f}(x) - f(x)$ is the difference between the predicted and actual value) and $\sigma(x)$is the uncertainty of the prediction given by Equation 3.29,

$$\sigma(x) = \sqrt{\left(\sum_{i=1}^{n} max[\sigma_i^2(x), \omega]\right) + \tilde{\sigma}^2(x)} \tag{3.29}$$

where $\sigma_i^2(x)$ is the sample-wise variance at test point x due to training point i, ω is the noise threshold in the sample-wise variance estimates, and $\tilde{\sigma}(x)$ is an explicit bias function. The noise threshold is set to $\omega = min_i\sigma^2(x_i)$, the magnitude of the minimum variance over the training data as suggested by Ling et al. [252]. If the uncertainty estimates were perfectly well-calibrated and the samples in the data set were independently distributed, then the normalized residuals would follow a Gaussian distribution with zero mean and unit standard deviation.

Chapter 4

Predictive Modeling of Diffusion Coefficient

Machine Learned Diffusion Coefficient Estimator (ML - DiCE) – a collection of ML models that can predict the diffusion coefficient for two modes of diffusion in impure metallic (IM) media and three modes of diffusion in multi-component alloy (MCA) media with an accuracy above 90%. In particular, our model considers self and impurity diffusion modes in IM media, and self, impurity, and chemical modes of diffusion in MCA media. The choice of these models are based on three key criteria: 1) the quality of the data which ensures the diversity in DM and DE; 2) quantity of data that ensures the availability of sufficient number data points for a given ML algorithm to perform optimally; 3) variability in diffusion coefficient that aims for a lower standard deviation which results in reliably across different DM present in data. The model has been trained with a sufficiently large experimental dataset using the Random Forest(RF), Deep Neural Network (DNN) and Support Vector Regression (SVR) algorithms from the $Scikit-learn$ library. A separate featurization scheme was employed for diffusing elements and diffusion media that include fundamental atomic properties as well as composition level features of the diffusion media for multi-component diffusion media. Remarkably, our model encompasses 95% of elements from the periodic table, either as diffusing elements or part of the diffusion medium's composition, allowing it to predict

diffusion coefficients across a wide verity of diffusion processes. The model performs optimally for a temperature range of 100–3500 K. Rigorous cross-testing against experimental data ensures the reliability and accuracy of our predictions, establishing our model as a valuable tool in understanding and predicting diffusion processes.

This chapter is structured as follows: Section 3.2 presents an overview of the data types used, data preprocessing, accessible experimental features, statistical considerations regarding the data, and the criteria employed for model selection. Section 3.2.2 delves into a comprehensive analysis of feature engineering alongside the training scheme. In section 4.2, we discuss a comparative analysis of model's performance with RF, DNN and SVR algorithms and potential bias and limitations of the model. This section also includes an individual assessment of model performance, key feature extraction techniques, and an uncertainty analysis. Finally, the conclusions drawn and the model's accessibility are discussed in section 7.1.

4.1 Machine Learned Models of Diffusion Coefficient

4.1.1 Impurity Diffusion in Impure Metallic Media

In the impurity diffusion mode comprising 2506 data points, correlation analysis revealed that among the 19 features of diffusing element and 35 features of diffusion media show correlations below 90%. The heatmaps illustrating the correlation between features after removing highly correlated features are given in Figure 4.1. Figure 4.1a describes the feature space of diffusing element, characterized by a predominantly negative correlation trend compared to the feature space of diffusion media shown in Figure 4.1 b, where a more positive correlation trend is evident on average, denoted

by the red squares. Merging these two feature spaces yields a combined feature space, excluding features with correlations exceeding 75%. Specifically, three features were eliminated from diffusing element's feature space, and four from diffusion media's. The correlation heatmap of the combined feature space, depicted in Figure 4.1 c, indicates an average feature correlation of less than 25% after the final correlation correction. Finally, the *temperature* feature is integrated into the combined feature space, leading

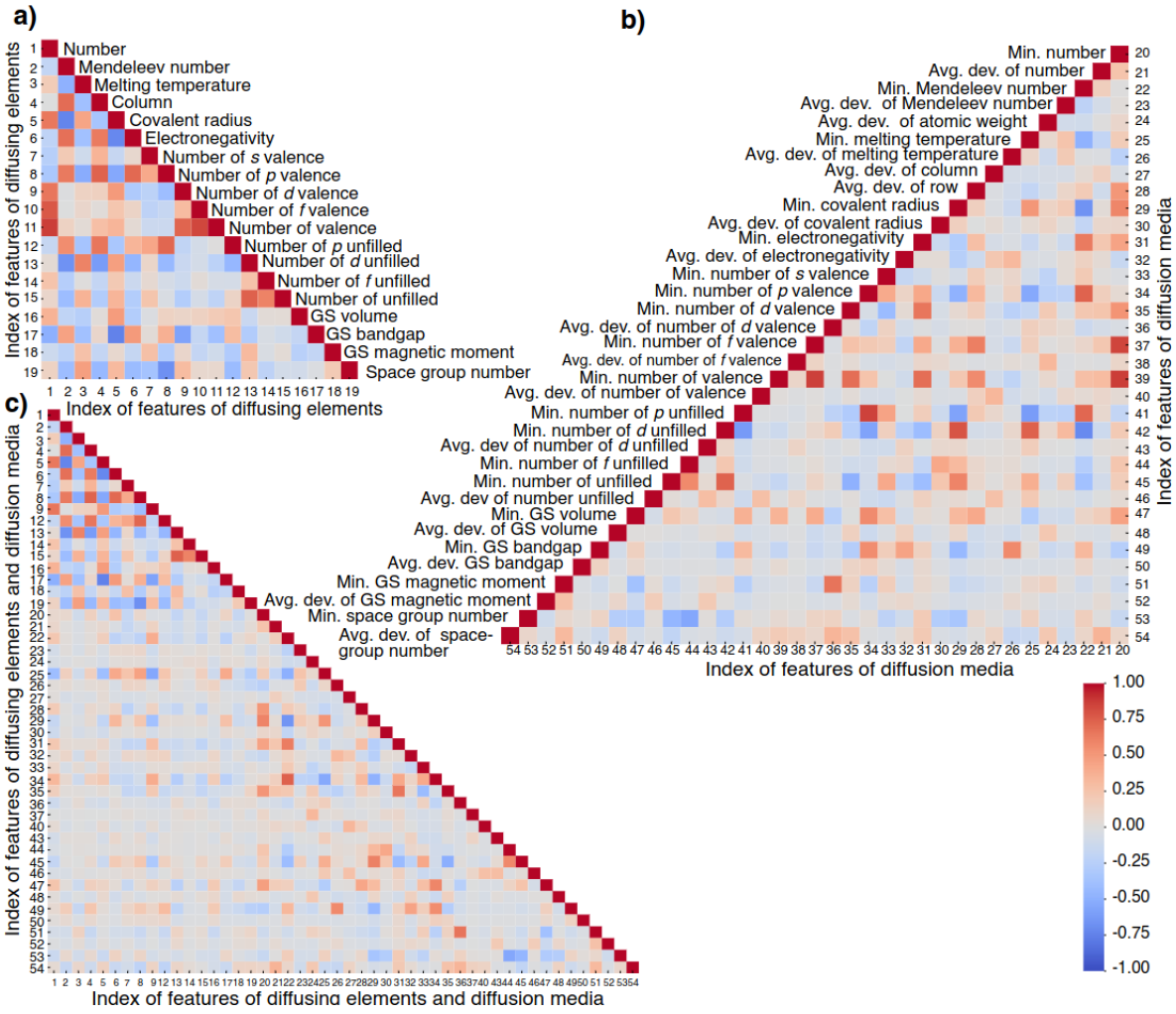


Figure 4.1: Feature spaces – impurity diffusion in IM media for a) diffusing elements, b) diffusion media, and c) the combined feature space used for training. Features of diffusing elements and diffusion media are indexed sequentially and the respective indices are marked in the combined feature space for reference. Common abbreviations such as 'min.' for minimum, 'avg.' for average, and 'dev.' for deviation are used.

to a training dataset dimension of 2497 $\times$ 49 (comprising 48 diffusion features and temperatures). Notably, some rows with missing variables in the feature space have been omitted, which accounts for the dataset's dimension of 2497.

After analyzing the distribution of the target variable, the diffusion coefficient, it is apparent that the log-transformed diffusion coefficient exhibits a more normal distribution compared to the pure diffusion coefficient. In this model, using the log of the diffusion coefficient as the target variable proves beneficial (with a better $R2$ score). The Figure C.4a illustrates this shift, with the mean and standard deviation for the pure diffusion coefficient being 1.15×10^{-7} m^2/s and 2.64×10^{-6} m^2/s, respectively. After applying the logarithm transformation, these values become 31.00 and 7.06, respectively. The log-transformed diffusion coefficient is more suitable for modeling due to its normalized distribution characteristics. Similarly, the feature, *temperature* also exhibits a normal distribution, with a mean of 1010.39 K and a standard deviation of 450.69 K.

PC analysis (Figure 4.2a) reveals that 25 PCs can represent 90% of the variance in the data, whereas 39 PCs can represent 99% of the variance. Notably, the number of PCs needed to represent at least 90 % variance is remarkably higher, indicating the presence of complex relationships among the descriptors[253]. Figure 4.2b depicts the important features when projecting eigenvectors of features in the PC space spanned by the first two PCs that together represent $\approx 24\%$ of variance in data. In this figure, red and blue arrows represent important features of diffusing elements and diffusion media, and other trivial features are marked by green arrows. Further, the features of diffusing element namely the *GS bandgap*, *electronegativity*, *number of p valance*, *number of p unfilled*, *Mendeleev number*, *column*, and *covalent radius* are identified as the most contributing features to the PC1 and PC2. In contrast, only one feature of diffusion media, the *min. melting temperature*, is identified as the most contributing

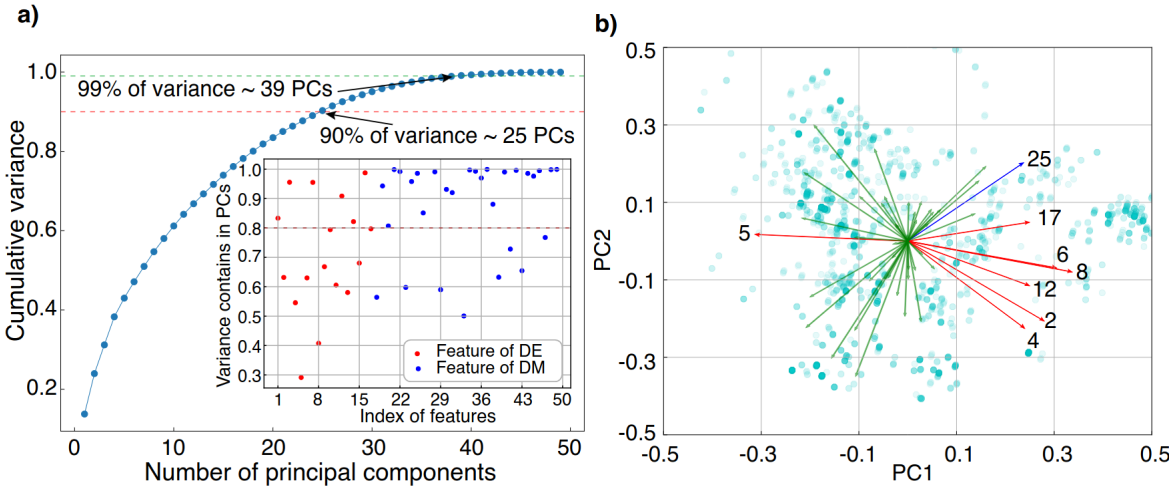


Figure 4.2: PC analysis; a) PCs that explain cumulative variance with inset graph that depicts variance of features represented by 25PCs and b) most contributed features in PC space spanned by first two PCs. The eigenvectors of features are projected as arrows. The important features of diffusing element are marked in red, diffusion media in blue, and other less contributing features in green color. The scatter plot in the background illustrates the scaled distribution of data points in PC space.

feature in the same PC space. The decreased variance ($\approx 24\%$)of the data represented in PC 1 and 2 is the prime reason for this. However, when considering the magnitude of eigenvectors of features in 39-dimensional PC space, as given in the inset of Figure 4.2a, it can be seen that the majority of features exhibit a variance above 80%. Therefore, 39 PCs that explain 99% of the variance in data are used when training with PCs.

Figure 4.3a displays the model's performance when trained using feature space, yielding a R^2 score of 0.94; b, on the other hand, displays the model's performance when trained with PCs, yielding a R^2 value of 0.90. Although the feature-trained model outperforms PC-trained model in terms of the R^2 score, it is noteworthy that the PC-trained model exhibits a slightly lower MSE compared to the feature-trained model.

When examining the model's uncertainty as given in Figure C.5a, both models show that the root mean square out-of-bag approach is not a well-calibrated metric;

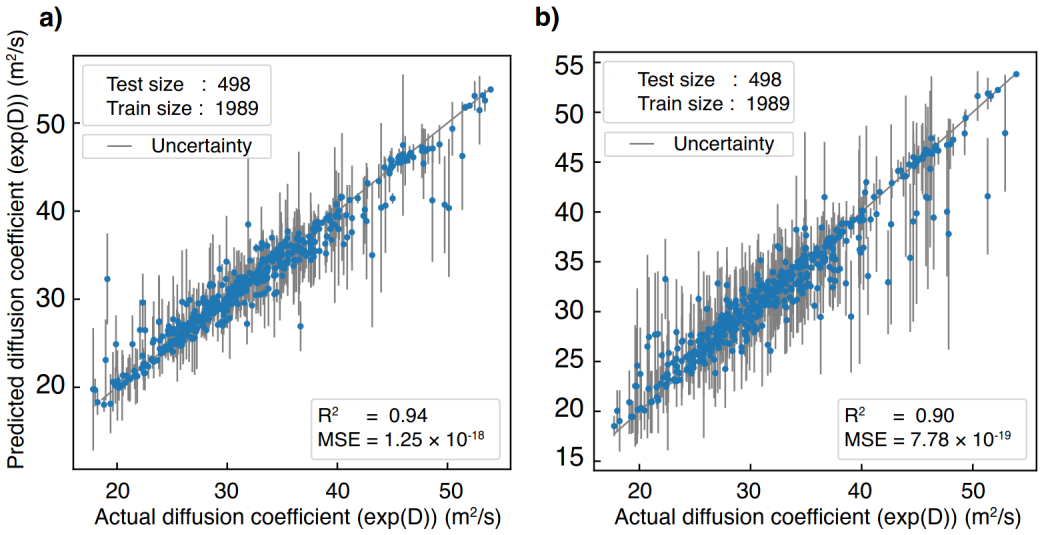


Figure 4.3: Performance of model – impurity diffusion in IM media: a) when trained with the entire feature space (dimension: 2497× 49) and b) with principal components of the entire feature space(dimension: 2497× 39). The gray solid lines depict the uncertainty associated with each data point.

it significantly overestimates the error for a substantial portion of the data points. In contrast, employing the *Lolo* uncertainty approach results in comparatively well-calibrated uncertainty estimates (Figure C.5b), indicating that the samples in the dataset are independently distributed. On comparing *Lolo* uncertainty estimates between feature-trained and PC-trained models as shown in Figure C.5b, histograms are closer to normalized distributions of residuals in feature-trained rather than PC-trained models. Nevertheless, the *Lolo* uncertainty approach cannot comprehensively address all sources of uncertainty as seen from the small outgrowth of histogram in Figure C.5b. This is particularly due to the uncertainties arising from factors not explained by the existing feature set—commonly referred to as 'unknown unknowns' as mentioned in Ling et al. [252]'s work. For example, the diffusion coefficient data is unavailable for certain temperature steps, leading to gaps in information. The absence of such information may slightly undermine the reliability of uncertainty estimates.

Upon examining the feature importance derived from the *RF* algorithm used dur-

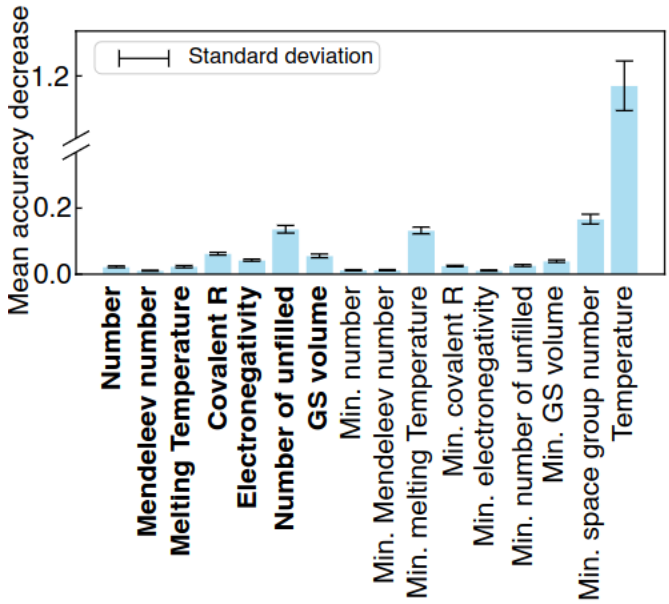


Figure 4.4: Feature importance – impurity diffusion in IM media: features of diffusing elements are highlighted in bold fonts and diffusion media are given in normal fonts.

ing training, we noted that 16 out of the 49 features used hold significance based on their mean accuracy decrease score. These crucial features, along with their respective standard deviations, are detailed in Figure 4.4. Notably, the *temperature* of the diffusion process emerges as the most pivotal feature among them. Furthermore, within the subset of seven important features pertaining to diffusion elements, the *number of unfilled orbitals* stands out as the most critical. Likewise, within the nine important features associated with diffusion media, both the *minimum melting temperature* and *GS volume* were identified as significant.

4.1.2 Self Diffusion in Impure Metallic Media

The dataset for self-diffusion in IM media has 2506 data points. 19 features of diffusing elements and 35 features of diffusion media were identified to have mutual correlations of less than 90% by correlation analysis. Figure 4.5a describes the feature space of

diffusing element, characterized by negative and positive correlation trends in equal proportion compared to the feature space of diffusion media shown in Figure 4.5b, where a more positive correlation trend is evident on average, denoted by the reddish squares. After merging the feature spaces of diffusing element and diffusion media and removing features with correlations over 75%, one feature from diffusing element and sixteen features from diffusion media were eliminated. The resulting correlation heatmap (Figure 4.5c) shows an average feature correlation below 25% after the final correction. Additionally, the *temperature* feature was incorporated into the combined space, resulting in training data of dimension 2506 $\times$ 30 (29 diffusion features and temperatures).

Statistical analysis reveals that the log-transformed diffusion coefficient displays a more normalized distribution compared to the original diffusion coefficient, leading to better modeling performance (with an improved R^2 score). As illustrated in Figure C.4b, the mean and standard deviation of the pure diffusion coefficient are 8.09×10^{-12} m^2/s and 7.68×10^{-11} m^2/s, respectively. Following the logarithmic transformation, these values shift to 34.90 m^2/s and 6.01 m^2/s. This transformation enhances modeling performance due to the normalized distribution trend. Similarly, the *temperature* feature also demonstrates a normal distribution, with a mean of 1027.98 K and a standard deviation of 500.71 K.

PC analysis (Figure 4.6 a) shows that 16 PCs capture 90% of the data's variance, while 24 PCs capture 99%. Notably, representing at least 90% variance requires significantly more PCs, indicating complex relationships among descriptors[253]. In Figure 4.6 b, important features are shown using eigenvectors projected onto the first two PCs, explaining 28% of the variance. Diffusing element's features such as *covalent radius*, *Mendeleev number*, *melting temperature*, *electronegativity*, *number of p*, and *d valence*, and *number d unfilled*, and *GS volume* contribute most to PC1 and PC2. Con-

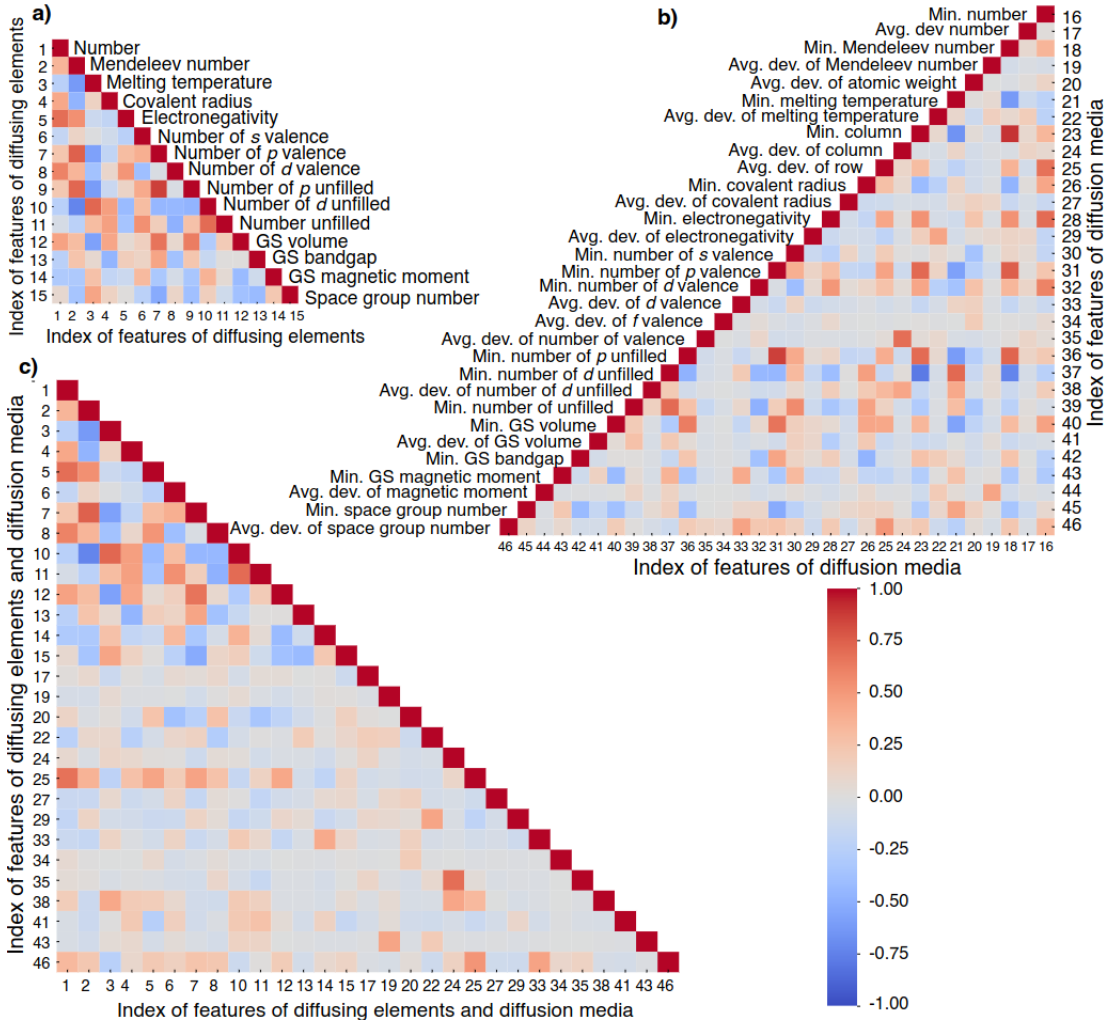


Figure 4.5: Feature spaces – self diffusion in IM media for a) diffusing elements, b) diffusion media, and c) the combined feature space used for training. Features of diffusing element and diffusion media are indexed sequentially and the respective indices are marked in the combined feature space for reference. Common abbreviations such as 'min.' for minimum, 'avg.' for average, and 'dev.' for deviation are used.

versely, only one feature of diffusion medium, the *average deviation of row*, is identified as the most contributing feature in the same PC space. The decreased variance of the data ($\approx 28\%$) represented by PC 1 and 2 is the prime reason for this. However when considering the magnitude of eigenvectors of features in 24-dimensional PC space, as given in the inset of Figure 4.6a, it can be seen that the majority of features exhibit a variance above 80%. Therefore, 24 PCs that explain 99% of the variance in data are

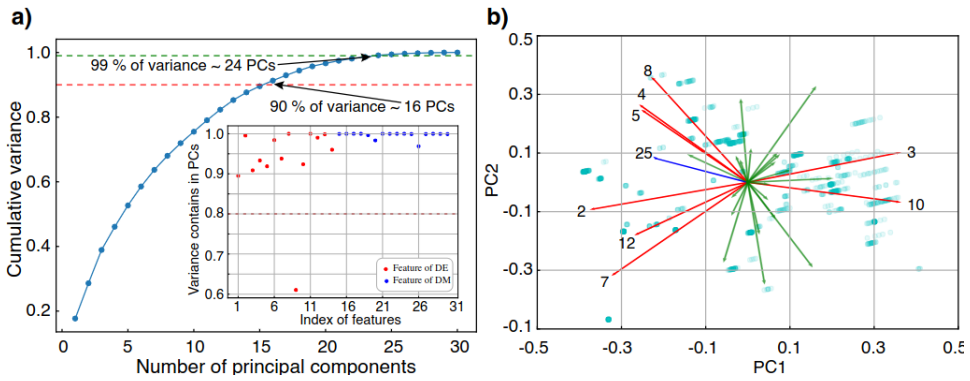


Figure 4.6: PC analysis; a) PCs that explain cumulative variance with inset graph that depicts variance of features represented by 24PCs and b) most contributed features in PC space spanned by first two PCs. The eigenvectors of features are projected as arrows. The important features of diffusing elements are marked in red, diffusion media in blue, and other less contributing features in green color. The scatter plot in the background illustrates the scaled distribution of data points in PC space.

used when training with PCs.

Figure 4.7a shows the model's performance when trained with feature space, achieving an R^2 score of 0.95; in comparison, Figure 4.7b shows the model's performance when trained with PCs, resulting in an R^2 value of 0.91. Despite the feature-trained model

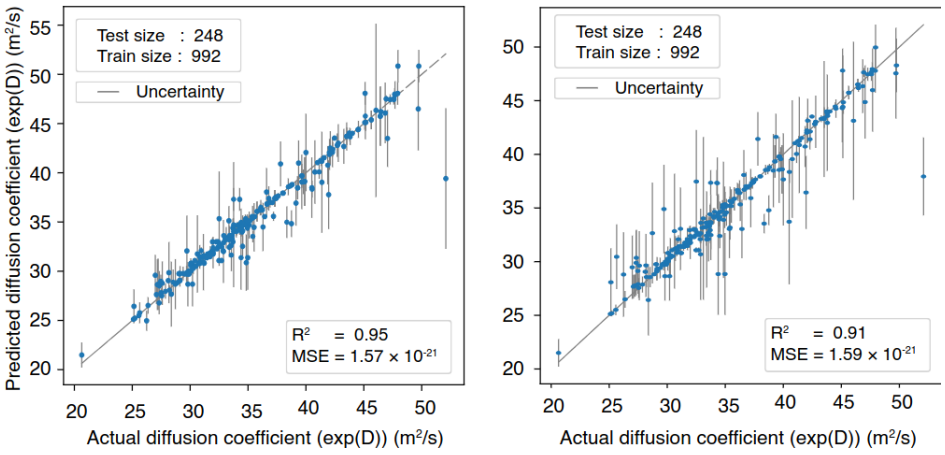


Figure 4.7: Performance of model – self diffusion in IM media: a) when trained with entire feature space (dimension: 2506 × 30) and b) with principal components of the entire feature space (dimension: 2506 × 24). The vertical gray solid lines depict the uncertainty associated with each data point.

outperforming the PC-trained model in R^2 score, both models exhibit a very similar

MSE score of approximately 1.5×10^{-21}.

When examining the model's uncertainty (Figure C.5c), both models reveal that the root mean square out-of-bag approach is not well-calibrated; it tends to overestimate errors significantly for many data points. Conversely, using the *Lolo* uncertainty approach yields comparatively well-calibrated uncertainty estimates (Figure C.5d), indicating independently distributed samples in the dataset. Comparing *Lolo* uncertainty estimates between feature-trained and PC-trained models (Figure C.5d), histograms show closer-to-normalized distributions of residuals in the feature-trained models than in the PC-trained ones. However, as mentioned in Sec. 4.1.1, the *Lolo* uncertainty approach cannot comprehensively address all sources of uncertainty, as evidenced by the histogram's outgrowth in Figure C.5d. This is mainly due to the missing diffusion coefficient data for certain temperature steps, resulting in the overestimation of uncertainty.

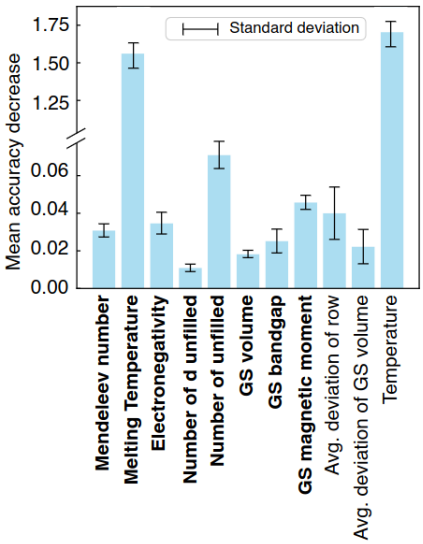


Figure 4.8: Feature importance – self diffusion in IM media: features of diffusing elements are highlighted in bold font and diffusion media are given in normal font.

When analyzing the feature importance derived from the *RF* algorithm used during

training, we observed that 11 out of the 29 features used are significant based on their mean accuracy decrease score. These important features, along with their respective standard deviations, are detailed in Figure 4.8. As expected, the *temperature* of the diffusion process emerges as the most crucial feature among them. Furthermore, within the subset of eight important features related to diffusing elements, *melting temperature* and *number of unfilled orbitals* are highlighted as the most pivotal. Similarly, within the two important features associated with diffusion media, both *average deviation of row* and *average deviation in GS volume* were identified as highly significant.

4.1.3 Self Diffusion in Conventional Alloys

In the context of self diffusion mode, with 3431 data points, 18 features of diffusing elements and 87 features of diffusion media have been identified that correlate less than 90%. The heatmap presented in Figure 4.9 visualizes the feature space following the post-correlation filtration. In Figure 4.9 a, diffusing element's feature space shows predominantly positive correlations, similar to diffusion medium's feature space depicted in Figure 4.9 b, where a positive correlation trend is also noticeable on average, highlighted by reddish squares. Then, the combined feature space was formed by excluding highly correlated features (over 75%), resulting in the elimination of 6 features from diffusing elements and 47 from diffusion media. The correlation heatmap of the combined feature space (Figure 4.9 c) indicates an average feature correlation of less than 25%. Finally, incorporating *temperature* into the combined feature space expanded the dataset to dimensions of 3431×54, comprising 53 diffusion features and *temperature*.

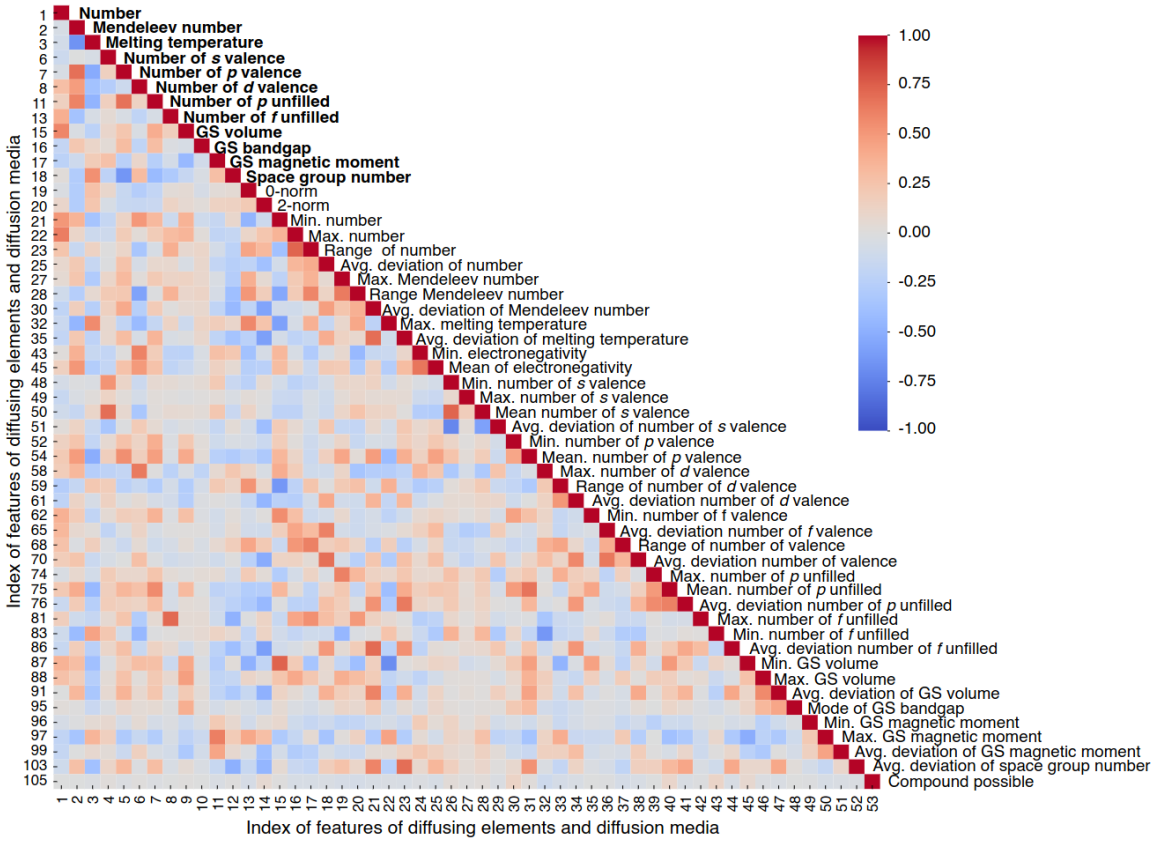


Figure 4.9: Feature space – self diffusion in MCA media: combined feature space of diffusing element and diffusion media used for training. Features of diffusing elements are highlighted in bold fonts and diffusion media in regular fonts(Individual feature space of diffusing element and diffusion media for this model are given in Figure C.6a and b respectively). Common abbreviations such as 'min.' for minimum, 'avg.' for average, and 'dev.' for deviation are used.

A statistical examination of the distribution of the diffusion coefficient, reveals that log-transformed diffusion coefficient follows a more normal distribution compared to the normal diffusion coefficient. Employing the log of the diffusion coefficient as the target variable in this model results in a better R^2 score. Figure C.4c visually depicts this transformation, with the mean and standard deviation for the normal diffusion coefficient being 3.27×10^{-12} m^2/s and 2.89×10^{-11} m^2/s, respectively. After the logarithm transformation, these values shift to 33.80 m^2/s and 5.37 m^2/s, respectively. The log-transformed diffusion coefficient is favored for modeling because it closely aligns

with normal distribution. Likewise, the *temperature* feature also exhibits a normal distribution, with a mean of 1234.19 K and a standard deviation of 374.52 K.

PC analysis (Figure 4.10 a) indicates that 21 PCs capture 90% of variance of data, while 40 PCs capture 99%. This disparity suggests complex relationships among descriptors, as more PCs are needed to represent at least 90% variance. In Figure 4.10 b, important features are displayed using eigenvectors projected onto the basis of first two PCs, together explaining approximately 28% of the total variance in data. diffusing

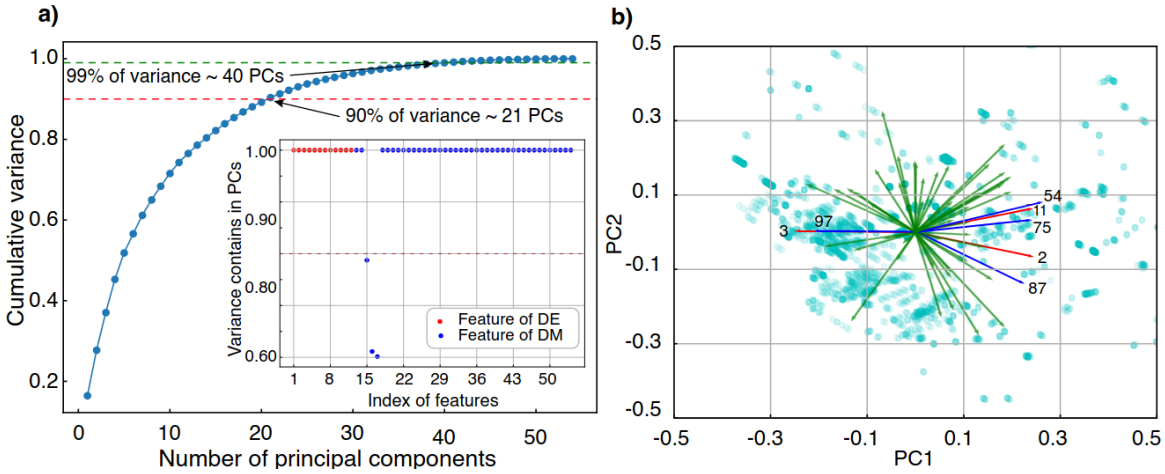


Figure 4.10: PC analysis – self diffusion in MCA media; a) PCs that explain cumulative variance with inset graph that depicts variance of features represented by 40 PCs and b) most contributed features in PC space spanned by first two PCs. The eigenvectors of features are projected as arrows. The important features of diffusing elements are marked in red, diffusion media in blue and other less contributing features in green color. The scatter plot in the background illustrates the scaled distribution of data points in PC space.

element's features such as *Mendeleev number*, *melting temperature*, and *number of p unfilled orbitals* are significant contributors mainly to PC1. In the same PC space, important diffusion medium's features include *mean number of p valence*, *minimum GS volume*, and *maximum GS magnetic moment*. Given the fact that PC1 and PC2 collectively represent approximately 28% of the variance in the data, considering a higher-dimensional PC space that incorporates greater variance is recommended for

training. The scatter plot given in the inset of Figure 4.10a suggests that training with 40 PCs is beneficial as most features capture above 90% variance.

This model exhibits overfitting when trained with the feature space using RF. This is primarily due to the high diversity in diffusion media within the self diffusion dataset, which comprises 191 distinct types of diffusion media, as given in Table 3.1. Therefore we choose *MLPRegressor* to train the model using feature space that gives R^2 score of 0.93 with MSE 2.48×10^{-22}. Training was also performed using 40 PCs that captured 99% of variance in training data. Figure 4.11b illustrates the model's performance when trained using the PC space with *RF*, achieving an R^2 score of 0.92 with MSE 1.65×10^{-22}. These results are very similar to those obtained from the *MLPRegressor* using the feature space. This indicates that despite the high diversity in the feature space leading to *RF* overfitting, projecting the features to PC space and then using PCs for *RF* training yields accurate results and precise uncertainty estimates.

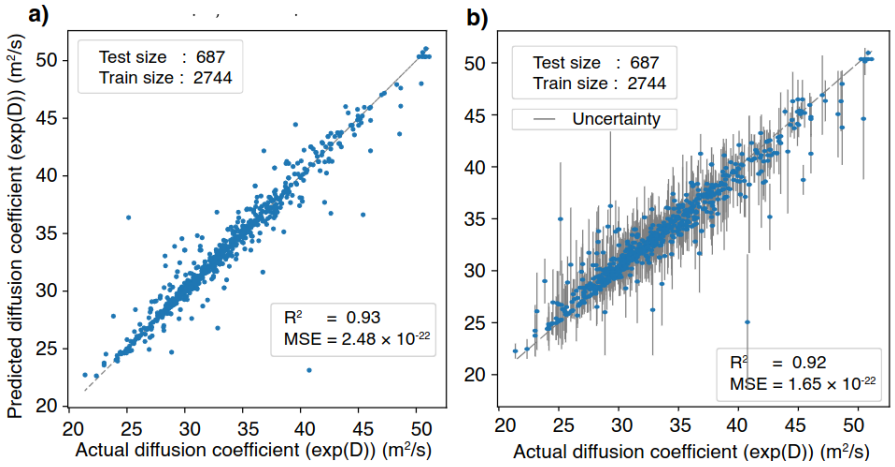


Figure 4.11: Performance of model – self diffusion in MCA media when trained with a) the entire feature space (dimension: 3431 × 54) and with b) the principal components of the entire feature space (dimension: 3431 × 40). The gray solid lines depict the uncertainty associated with each test data point.

On comparing out-of-bag uncertainty estimates calculated using feature space (trained with *MLPRegressor* since *RF* is overfitting) and PC space (trained with *RF*) as given

in Figure C.5e it can be seen that both training schemes overestimates errors for many data points. However using *Lolo* approach, as given in Figure C.5f the uncertainty estimates are more normally distributed for most of the data points.

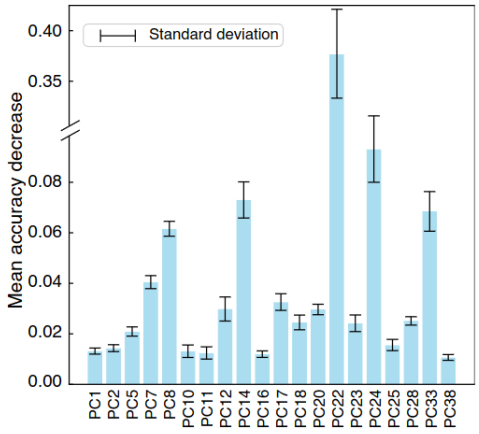


Figure 4.12: Feature importance – self diffusion in MCA media: *MLPRegressor* were used with feature permutation scheme. Features of diffusing elements are highlighted in bold font and diffusion media are given in normal font.

Figure 4.12 summarizes the feature importance analysis calculated using *MLPRegressor* based on feature permutation. Among the six key features of diffusing elements, *minimum number of p* and *d valence* were identified as most important. For diffusion media, out of twenty important features, *mean electronegativity* and *range of d valence* of the composition elements were highlighted as most important. Furthermore, *temperature* of diffusion process stands out as the most important feature among all other features.

4.1.4 Impurity Diffusion in Conventional Alloys

In the impurity diffusion mode, encompassing 2567 data points, 19 features of diffusing elements and 85 features of diffusion media were identified to correlate less than 90%. As depicted in Figure C.7a, diffusing element's feature space predominantly exhibits negative correlations, contrasting with diffusion media's feature space shown in

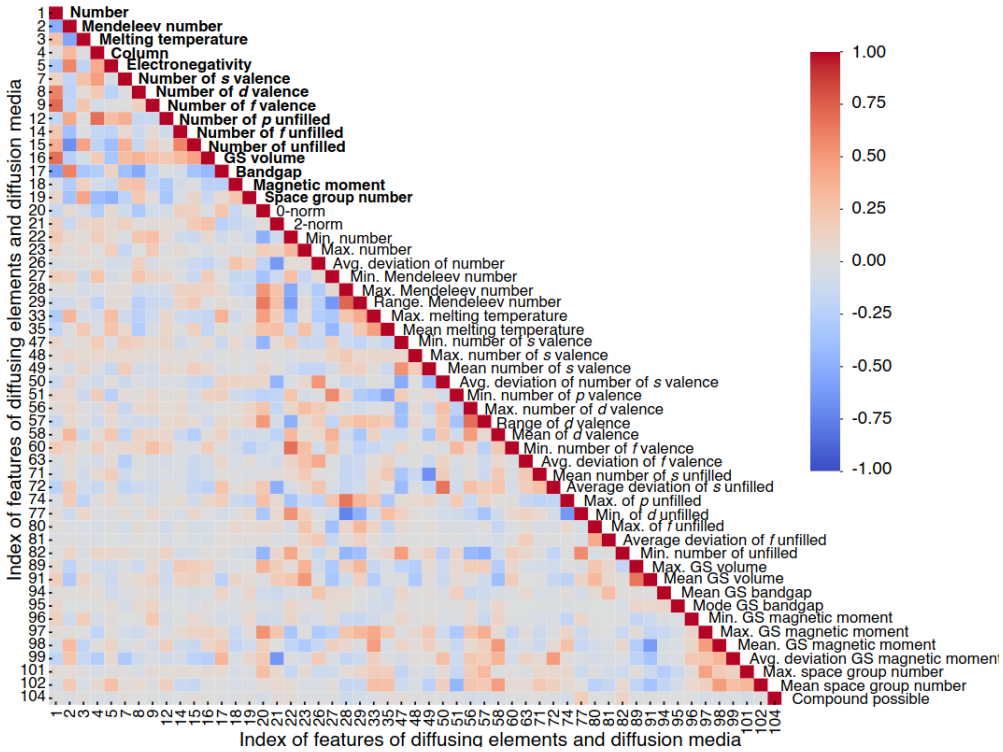


Figure 4.13: Feature space – impurity diffusion in MCA media: combined feature space used for training. Features of diffusing elements are highlighted in bold characters and diffusion media in regular fonts(Individual feature space of diffusing element and diffusion media for this model are given in Figure C.7a and b respectively). Common abbreviations such as 'min.' for minimum, 'avg.' for average, and 'dev.' for deviation are used.

Figure C.7b, where a positive correlation trend is evident on average, highlighted by reddish squares. Subsequently, the combined feature space was created by excluding highly correlated features (over 75%), resulting in the removal of 4 features from diffusing elements and 47 from diffusion media. The correlation heatmap of the combined feature space (Figure 4.13c) indicates an average feature correlation of less than 25%. Finally, integrating *temperature* into the combined feature space expanded the dataset to dimensions of 2567 $\times$ 49, comprising 50 diffusion features and temperatures.

To enhance the model performance during training, the diffusion coefficient is transformed to a log scale, resulting in a more normal distribution and a better R^2 score.

The mean and standard deviation for the original diffusion coefficient are 1.66×10^{-9} m^2/s and 1.98×10^{-6} m^2/s, respectively, while after the logarithm transformation, these values shift to 32.90 m^2/s and 8.53 m^2/s, respectively as shown in Figure C.4d. Similarly, the *temperature* feature exhibits a normal distribution with a mean of 1049.33 K and a standard deviation of 422.75 K.

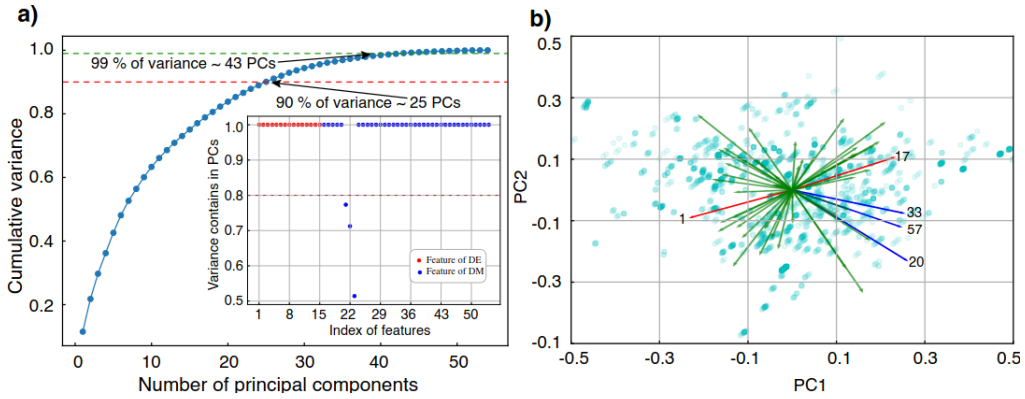


Figure 4.14: PC analysis – impurity diffusion in MCA media; a) PCs that explain cumulative variance with inset graph that depicts variance of features represented by 43PCs and b) most contributed features in PC space spanned by first two PCs. The eigenvectors of features are projected as arrows. The important features of diffusing elements are marked in red, diffusion media in blue, and other less contributing features in green color. The scatter plot in the background illustrates the scaled distribution of data points in PC space.

PC analysis (Figure 4.14a) reveals that 25 PCs capture 90% of the data's variance, while 43 PCs capture 99%. This discrepancy indicates complex relationships among descriptors, requiring more PCs to represent at least 90% variance. In Figure 4.14b, important features are displayed using eigenvectors projected onto the first two PCs, explaining approximately 22% of the total variance in data. Diffusing element's features such as *number* and *band gap* significantly contribute to PC1. Similarly, notable diffusion media's features include *0-norm*, *maximum melting temperature*, and *range of d valence* in the same PC space. Considering that PC1 and PC2 collectively represent only 22% of the variance in the data, we selected a 43-dimensional PC space

that captures 99% of the variance for PC-based training, as shown in the inset of Figure 4.14a. In this space, most features contribute over 80% variance ensuring the effective inclusion of all of the features.

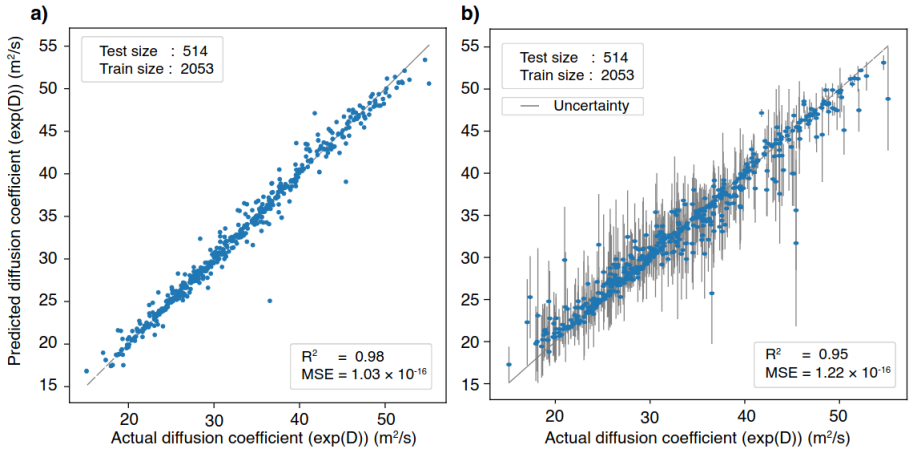


Figure 4.15: Performance of model – impurity diffusion in MCA media when trained with a) the entire feature space (dimension: 2567 × 49) and b) principal components of the entire feature space (dimension: 2567 × 43). The vertical gray solid lines depict the uncertainty associated with each data point.

Similar to the self diffusion model in MCA media described in Sec. 4.1.3, this model also displays overfitting when trained with the feature space, mainly because of the highly diverse diffusion media (271 types) present in the data. For this reason, we used the *MLPRegressor* for training with the feature space, achieving a higher R^2 score of 0.98, as shown in Figure 4.15a. However, *RF* performs well when trained using 43 PCs but a comparatively lower R^2 score of 0.95 as depicted in Figure 4.15b. When examining the MSE of both training schemes, the differences are minimal, with MSE values on the order of 10^{-16}.

When comparing out-of-bag uncertainty estimates calculated using the feature space (trained with *MLPRegressor* since *RF* is overfitting) and the PC space (trained with *RF*) as shown in Figure C.5g, it is evident that both training methods tend to overestimate errors for many data points. In contrast, the *Lolo* approach, depicted in

Figure C.5h, provides uncertainty estimates that are more normally distributed across most data points.

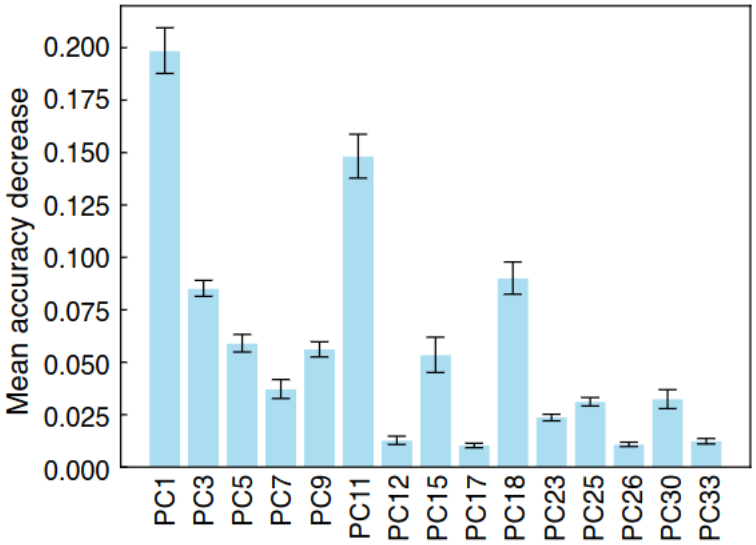


Figure 4.16: Feature importance – impurity diffusion in MCA media: *MLPRegressor* were used with feature permutation scheme. Features of diffusing elements are highlighted in bold font and diffusion media are given in normal font.

Figure 4.16 summarizes the feature importance analysis calculated using *MLPRegressor* based on feature permutation. Among the four key features of the diffusing elements, *minimum GS bandgap* was identified as the most significant. For diffusion media, out of six important features, *mean melting temperature* and *minimum number of unfilled orbitals* of composition elements were highlighted as the most important. Further, *temperature* of diffusion process was identified as the most influential feature overall.

4.1.5 Chemical Diffusion in Conventional Alloys

The dataset for self-diffusion in IM media comprises 483 data points. From correlation analysis, 9 features of diffusing elements and 45 features of diffusion media were identified with correlations below 90%. Figure C.8a depicts the feature space of dif-

fusing elements, showcasing mainly positive correlation trends. Similarly, Figure C.8b illustrates the feature space of diffusion media, also with predominantly positive correlations, indicated by the reddish squares. Upon merging these feature spaces and filtering out features with correlations exceeding 75%, 5 features from diffusing elements and 30 features from diffusion media were removed. The resulting correlation heatmap (Figure 4.17) exhibits an average feature correlation below 25% after these adjustments. Lastly, incorporating the *temperature* feature into the combined space

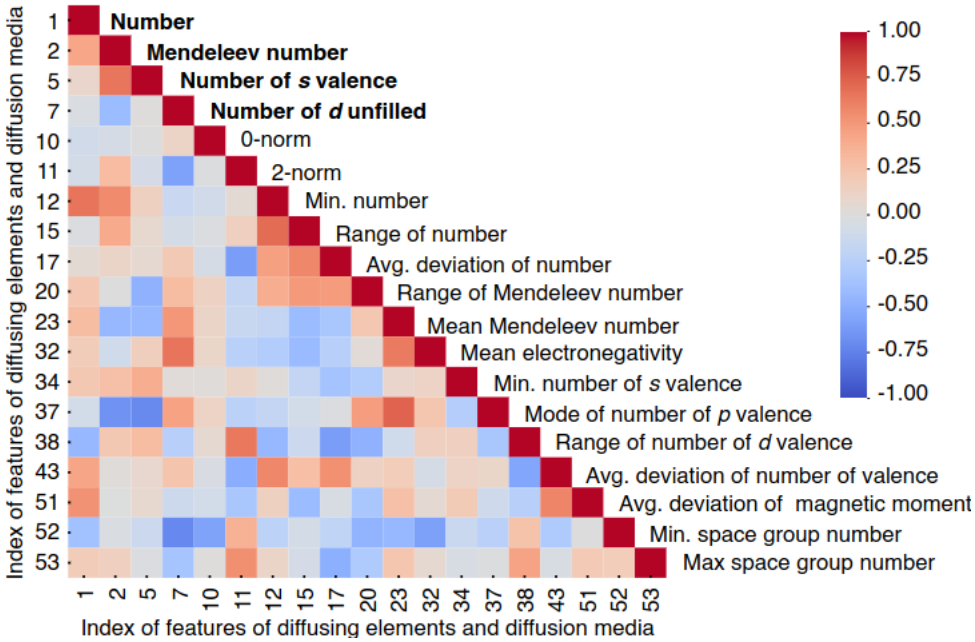


Figure 4.17: Feature space – chemical diffusion in MCA media: combined feature space used for training. Features of diffusing elements are highlighted in bold characters and diffusion media in regular fonts(Individual feature space of diffusing element and diffusion media for this model are given in Figure C.8a and b respectively). Common abbreviations such as 'min.' for minimum, 'avg.' for average, and 'dev.' for deviation are used.

led to training data dimensions of 483 × 20 (19 diffusion features and *temperature*).

The statistical analysis indicates that the log-transformed diffusion coefficient exhibits a more normalized distribution compared to the original diffusion coefficient. This normalization leads to improved modeling performance, reflected in an enhanced

R^2 score. In Figure C.4e, the log-transformed standard deviation graph displays two bell-shaped curves, indicating higher data variability, mostly symmetric around the mean. Specifically, for the pure diffusion coefficient shown in Figure C.4e, the mean and standard deviation are 5.83×10^{-11} m^2/s and 1.17×10^{-10} m^2/s, respectively. After logarithmic transformation, these values shift to 30.01 m^2/s and 5.59 m^2s, respectively. This transformation contributes to improved modeling performance due to the normalized distribution trend. Additionally, the *temperature* feature also demonstrates a normal distribution, with a mean of 1264.02 K and a standard deviation of 426.21 K.

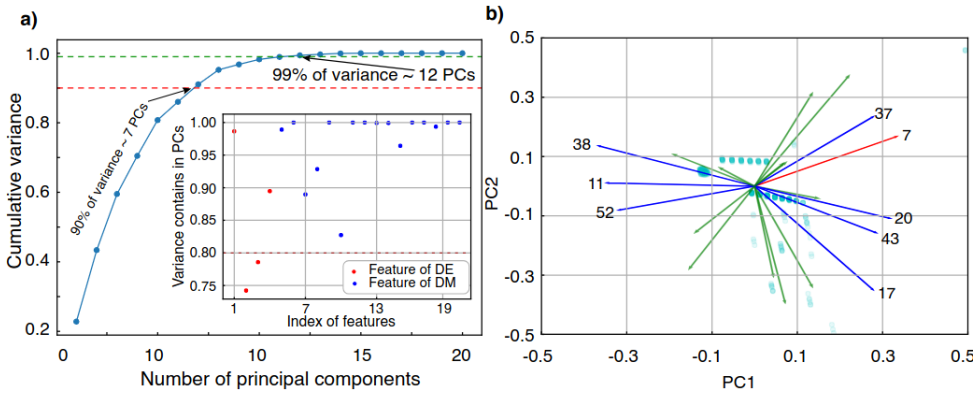


Figure 4.18: PC analysis; a) PCs that explain cumulative variance with inset graph that depicts variance of features represented by 12PCs and b) most contributed features in PC space spanned by first two PCs. The eigenvectors of features are projected as arrows. The important features of diffusing elements are marked in red, diffusion media in blue, and other less contributing features in green color. The scatter plot in the background illustrates the scaled distribution of data points in PC space.

The PC analysis (Figure 4.18 a) reveals that 7 PCs capture 90% of the data's variance, while 12 PCs capture 99%. It is noteworthy that achieving a representation of at least 90% variance necessitates a considerably higher number of PCs, indicating complex relationships among descriptors. In Figure 4.18 b, important features are depicted using eigenvectors projected onto the first two PCs, explaining 43% of the variance. Notably, a single feature of diffusing element, the *number of d unfilled orbitals*, appears

as the strongest feature which is more leaned to PC1. And, features of diffusion media, such as the *2-norm*, *average deviation of number*, *range of Mendeleev number*, *mode of the number of p valence*, *range of the number of p valence*, *average deviation of valence*, and *minimum space group number*, are identified as the most contributing features in the same PC space. However, when considering the magnitude of eigenvectors of features in the 12-dimensional PC space that includes higher variance of data, as shown in the inset of Figure 4.18a, it is visible that the majority of features exhibit a variance above 80%. Therefore, 24 PCs that explain 99% of the variance in the data are used during training with PCs.

Figure 4.19a shows the model's performance when trained using the feature space, resulting in an R^2 score of 0.94. Conversely, Figure 4.19b displays the model's performance when trained with PCs, achieving an R^2 value of 0.96. Comparing these models, the PC-trained model slightly outperforms the feature-trained model, despite similar MSE scores.

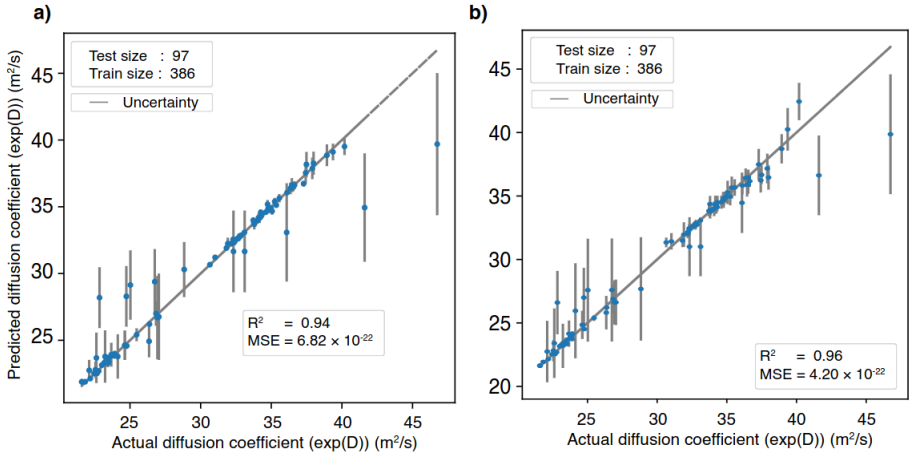


Figure 4.19: Performance of model – chemical diffusion in MCA media: a) when trained with the entire feature space (dimension: 483 × 20) and b) with principal components of the entire feature space (dimension: 483 × 12). The gray solid lines depict the uncertainty associated with each data point.

When examining the model's uncertainty (Figure C.5k), both models demonstrate

that the root mean square out-of-bag approach is poorly calibrated, tending to overestimate errors significantly for many data points. In contrast, using the *Lolo* uncertainty approach yields comparatively well-calibrated uncertainty estimates (Figure C.5l), indicating independently distributed samples in the dataset. Comparing *Lolo* uncertainty estimates between feature-trained and PC-trained models (Figure C.5l), histograms show closer-to-normalized distributions of residuals in the feature-trained models than in the PC-trained ones. However, as mentioned in Sec. 4.1.1 and Sec. 4.1.2, the *Lolo* uncertainty approach cannot comprehensively address all sources of uncertainty, as evidenced by the histogram's outgrowth in Figure C.5l. This is primarily due to missing diffusion coefficient data for certain temperature steps.

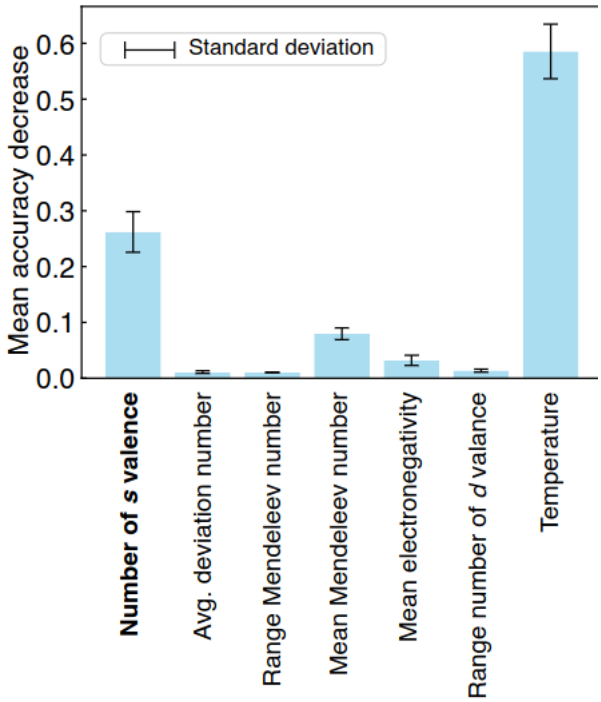


Figure 4.20: Feature importance – chemical diffusion in MCA media: Features of diffusing elements are highlighted in bold font and diffusion media are given in normal font.

When analyzing the feature importance derived from the *RF* used during training, we observed that 7 out of the 20 features used for training are significant based on their

Table 4.1: Performance overview of all models.

Diffusion Medium	Model	Number of features	R^2			MSE ($\times 10^{-19}$)		
			RF	DNN	SVR	RF	DNN	SVR
Impure metallic	Impurity	49	0.94	0.93	0.88	12.50	387.90	15.40
	Self	30	0.95	0.92	0.87	0.015	0.0480	0.047
Multi-component alloy	Impurity	54	*	0.98	0.97	*	1030.1	1363.4
	Self	54	*	0.96	0.90	*	0.0025	0.0021
	Chemical	20	0.94	0.96	0.93	0.0068	0.0092	0.0047

* Model is overfitting.

mean accuracy decrease score. These important features and their respective standard deviations are detailed in Figure 4.20. Notably, the *temperature* of the diffusion process emerges as the most crucial feature among them. However, only one feature related to diffusing elements, the *number of s valence* is identified as important. Similarly, within the subset of important features associated with diffusion media, both *mean Mendeleev number* and *mean electronegativity* were identified as significant.

4.2 Performance Analysis of Models

This section includes a comparative analysis of performance of models trained with RF, DNN and SVR algorithms. All models are trained with the methodology described in methodology section with corresponding feature space as described in sections 4.1.1 – 4.1.5. When evaluating the model's performance using R^2 and MSE scores, the results indicate that RF and DNN trained models outperform SVR models. Specifically, RF models demonstrate optimal performance in predicting impurity and self-diffusion in IM media and DNN models for impurity, self and chemical diffusion in MCA media, as given in Table 4.1. The same table also highlights the overfitting of RF models as the number of features increases in the case of impurity and self diffusion in MCA media. Since the highly correlated features of the DE and DM were removed during the feature engineering step, none of the features from the final feature space removed

to negotiate hyperparameter tuning time. This approach maximizes the model's predictive performance, as all features in the final feature space contribute, either directly or indirectly, to the model's efficiency.

The prediction bias and limitations of a ML model can be understood through the nature and diversity of the training data along with R^2, MAE score and uncertainty. Figure C.1 and Figure C.2 provide a comprehensive overview of the diffusion data used for training. The pie charts in Figure C.1 clearly illustrate that nearly 40% of DEs are from the d-block for both IM and MCA media, which explains the model's higher efficiency in predicting d-block elements as DE. Similarly, the average percentage contributions from the s, p, and f blocks are 15%, 32%, and 11%, respectively, for DE, leading to a corresponding bias in prediction accuracy. Furthermore, as shown in Figure C.2, the majority of DM is also composed of d-block elements, which results in the model being more inclined toward accurate predictions of diffusion coefficient for DM composed of d-block elements.

Chapter 5

GNN Assisted Modeling of Li-ion Transport in SEI

In this work is about a deep-learning-assisted framework to model Li-ion transport across the inorganic SEI by combining density functional theory (nudged elastic band) calculations with graph neural network learning. A systematic diffusion dataset was first generated for eight major inorganic SEI components, namely LiF, LiCl, LiBr, LiI, Li_2O, Li_2S, Li_3N, and Li_2CO_3, covering both grain diffusion and grain-boundary diffusion over representative low-energy surfaces and interfaces. This dataset includes homogeneous and heterogeneous grain boundaries, providing a unified design space for Li-ion migration in SEI environments. A path-aware graph variational autoencoder (GVAE) was then used to learn latent representations of NEB trajectories, and the learned embeddings were incorporated into a predictive GNN model for minimum-energy-path and migration-barrier estimation. The combined GVAE-GNN framework achieved strong predictive performance for both grain and grain-boundary diffusion, with test-set R^2 values of 0.93 and 0.94, respectively. Feature-importance and latent-space analyses further show that migration behavior is governed not only by composition, but also by local structural factors such as exposed surface, saddle-point character, and grain-boundary energetics. The results reveal clear transport trends across SEI chemistries, with halide-rich systems generally associated with narrower low-barrier

distributions, while Li_3N, Li_2CO_3, and structurally mismatched heterogeneous grain boundaries exhibit broader and higher-barrier landscapes. This study give a physics-informed machine-learning framework for mapping and predicting Li-ion migration in complex SEI structures and provides insight into how SEI chemistry and microstructure jointly control interfacial ion transport.

5.1 Motivation for Data-Driven Modeling

Earlier computational studies on dendrite formation and SEI behavior have largely focused on mapping Li-ion transport in a limited set of representative SEI components. Most of these investigations rely on density functional theory (DFT), particularly nudged elastic band (NEB) calculations, to determine Li-ion migration pathways and activation barriers. A notable study by Ramasubramanian et al. [81] examined LiF, Li_2O, and Li_2CO_3 and demonstrated Li-ion transport through the grain boundaries of these phases. Their results showed that grain boundaries create multiple open diffusion channels that facilitate faster Li-ion transport, with the highest diffusion rate observed for the heterogeneous LiF/Li_2O grain boundary compared with the corresponding homogeneous LiF/LiF and Li_2O/Li_2O boundaries. However this work include a few selected diffusion pathways and limited surface terminations for a given grain boundary. Similarly, Zheng et al. [82] investigated several ionic migration mechanisms in bulk LiF, Li_2CO_3, LiOH, and Li_2O. While this work attributed the relatively fast Li-ion transport in LiF compared to other components, the broader transport picture within the SEI remains unaddressed, as the SEI is inherently an amalgam of crystalline grains and grain boundaries. Soto et al. [83] reported, in their NEB study of Li-ion diffusion mechanisms in the grains of LiF and Li_2CO_3, that among the mechanisms considered—including knock-off, concerted exchange, vacancy diffusion,

and direct hopping—vacancy diffusion and knock-off are the most energetically favorable in these two components. Existing studies of Li-ion transport in SEI materials largely focus on one or a few components particularly about LiF, Li_2O and Li_2CO_3, with relatively limited attention to the halide-rich SEI chemistry observed in modern electrolytes.[84–87]. Also the studies incorporating grain boundary rich SEI model concentrate only on a limited number of migration pathways within selected grains or grain boundaries. This demands the need of an collective SEI modeling that include grain and grain boundary diffusion in SEI through all reported SEI components and their possible grain boundary configurations.

As a first phase of this study, we consider the major inorganic SEI components LiF, LiCl, LiBr, LiI, Li_2O, Li_2S, Li_3N, and Li_2CO_3. Li-ion diffusion pathways in these materials were mapped using NEB calculations. As grain formation in the SEI is strongly influenced by the exposed surface and its crystallographic orientation, grain-diffusion calculations were performed over a broad range of low to medium energy surfaces identified on the basis of surface energy. For grain-boundary diffusion, both homogeneous and heterogeneous grain boundaries were included using the listed SEI components. These grain-boundary pairs were constructed on the basis of grain-boundary energy and Coincidence Site Lattice (CSL) theory. For both grains and grain boundaries, all possible symmetry-unique Li-ion diffusion pathways were identified and considered for NEB calculations, with more details provided in the Methodology section. This procedure resulted in a large dataset describing Li-ion migration across the SEI, including diffusion coordinates, crystallographic orientations, migration energetics, surface energies, and grain-boundary energies. To the best of our knowledge, this is the first study to systematically map Li-ion migration across such a broad set of major inorganic SEI phases, their low-medium energy surface orientations, and representative grain-boundary configurations within a unified SEI design space.

In the second stage of this work, the Li-ion diffusion information generated from the DFT–NEB calculations is used to develop a graph neural network (GNN)-assisted predictive model for estimating Li-ion migration pathways in a given grain or grain-boundary environment of SEI components. This step is motivated by the high computational cost of DFT-NEB calculations, which makes exhaustive screening of the large number of possible SEI chemistries, surface orientations, and grain-boundary configurations impractical. For instance, in LiF, three stable surfaces are reported in literature with surface energy ranging from 20 – 50 meV/Å^2[81, 254]. This alone can results in three distinct grains of LiF with respective growth surfaces. Considering the symmetrically distinct diffusion sites in this grain which further demands respective number of times NEB calculations required to completely map the potential energy terrain of Li-ion intra-grain diffusion. As the slab thickness used in this work was intentionally kept small to enable high-throughput DFT-NEB calculations across a large number of SEI components and interfaces, the corresponding intra-grain diffusion should be interpreted mainly as surface or near-surface diffusion rather than fully bulk-like diffusion in large supercells. Therefore, a balance between computational cost and dataset diversity was adopted to generate diffusion data for multiple SEI chemistry, surfaces, and interface configurations. Although thicker slabs generally provide more bulk-like environments and quantitatively better-converged migration barriers, the thinner slabs used in this work were intentionally adopted to enable high-throughput generation of a diverse diffusion dataset spanning numerous SEI components, surfaces, and interface configurations.

Given the SEI components and their diverse local atomic distributions, crystallographic orientation, and interfacial environment involved in the diffusion dataset, crystal graph data is extensively used throughout the modeling in this work. A GNNs based modeling approach is therefore particularly well suited to this modeling, as they

can naturally encode atomic connectivity, local coordination, and geometric features that govern migration energetics, unlike traditional machine-learning models that rely primarily on fixed feature vectors and often struggle to capture such structural complexity. With recent advances in machine learning and its applications to materials science, state-of-the-art increasingly focused on the use of graph neural networks (GNNs) for the prediction of structural and material properties, the conditional generation of novel materials and molecules, and the design of new materials tailored to desired target properties[255–260].

When its comes to SEI and machine learning perspectives, a few works can be exemplified. One earlier work by Soleymanibrojeni et al. [261] used a kinetic Monte Carlo method to model SEI formation as a function of reaction barriers. It built an initial database using a design-of-experiments approach to train a Gaussian process classification model, which was later improved through active learning. However, a key limitation of this approach is that the migration barriers are not learned or predicted directly from atomistic structure; instead, they are treated as predefined coarse-grained input parameters whose ranges are approximated from first-principles calculations and literature data. In a similar work Li et al. [262] developed active-learning ML interatomic potentials trained on DFT data from amorphous SEI structures to predict Li transport and migration barriers in Li_2CO_3 and Li2EDC which covers only a limited subset of SEI chemistries, and remains computationally expensive for long-timescale simulations when using the more accurate neural-network potential. In general, there have been several attempts to use machine-learning-assisted simulations and predictions for battery interfaces, including SEI formation, lithium dendrite growth, interfacial ion transport, and atomistic modeling with machine-learned interatomic potentials[263]. However, these studies still rely largely on limited, chemistry-specific datasets—often focused on only one or two major SEI components—and their accuracy and transfer-

ability for migration-barrier prediction remain constrained by the limited availability of high-quality DFT- or simulation-derived training data. Based on these observations, we note that a GNN-based modeling approach has not yet been applied specifically to understanding Li-ion diffusion in the SEI, nor have DFT–NEB datasets spanning a wide range of SEI components been systematically integrated with machine learning to establish design rules for SEI architecture. In this scenario, the present study, which provides a large NEB dataset encompassing both grain and grain-boundary diffusion together with a GNN-based modeling approach, establishes a rational design space for SEI structures by the prediction of Li-ion migration behavior across a broad range of SEI components.

5.2 Dataset Description and Design Space

This study consists of two phases: (i) generation of Li-ion DFT-NEB migration-barrier data for selected SEI components namely, LiF, LiCl, LiBr, LiI, Li_2O, Li_2S, Li_3N, and Li_2CO_3 and (ii) development of GNN-based predictive models trained using DFT-NEB data. The methodology as a whole is illustrated as a flowchart as shown in Figure 5.1

The structures of the SEI components were obtained from the *Materials Project* repository using the MPRester API, with the lowest-energy-above-hull entries selected for each component [264]. These bulk structures were subsequently geometrically optimized through DFT calculations. DFT calculations were performed using the *Vienna Ab-initio Simulation Package* (VASP)[205]. The projector augmented-wave method was used to describe core–valence interactions, together with the Perdew–Burke–Ernzerhof (PBE) exchange–correlation functional within the generalized gradient approximation (GGA)[265–267]. A plane-wave kinetic-energy cutoff of 500 eV was applied throughout. Geometrical optimizations were continued until the forces on all

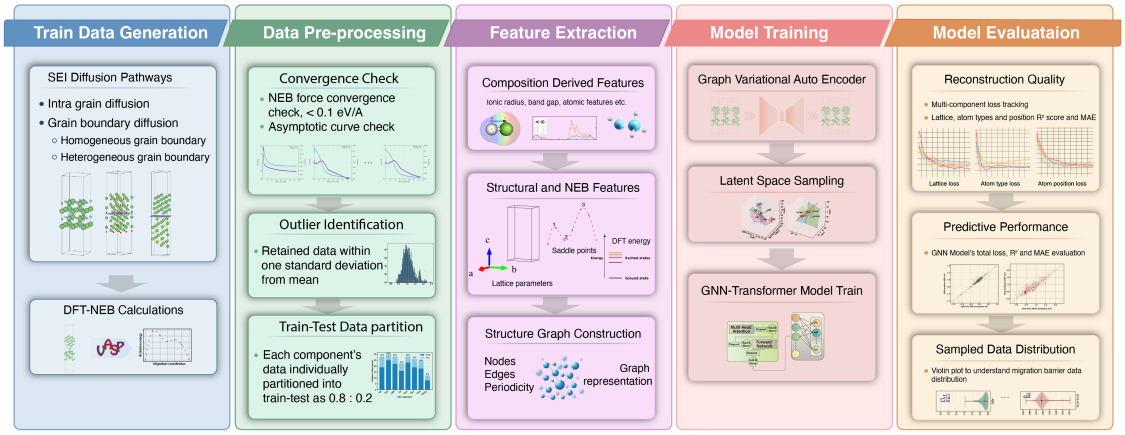


Figure 5.1: Workflow of modeling Li-ion transport in SEI. Diffusion minimum energy path and migration barrier estimated using nudged elastic band method implemented in DFT computational code. Graph variational autoencoder used to augment data and GNN transformer model for predictive modeling.

atoms were below 0.1 eV/Å. Brillouin-zone integrations employed Monkhorst–Pack k-point meshes of $7 \times 7 \times 7$ for bulk and $3 \times 3 \times 1$ for slab initial optimization calculations. The structural and energy information after the optimization step is given in Table C.4.

5.2.1 Diffusion Coefficient Data Generation

This study considered Li-ion vacancy diffusion to estimate migration barriers, following prior reports that vacancy-mediated diffusion is the most favorable mechanism in SEI components compared with concerted exchange and knock-off mechanisms [83, 85, 268]. The `MinimumDistanceNN()` class in Pymatgen was used to identify candidate diffusion sites and pathways in the grain structures while excluding symmetrically equivalent sites. Initial and final configurations for each diffusion event were then constructed and geometrically relaxed before NEB calculations. Intermediate images representing the Li-ion migration coordinates were then generated using the VTST scripts maintained by Henkelman Research Group[269]. For each diffusion process,

five intermediate images were introduced between the initial and final states to reduce the overall computational cost of the DFT calculations, with the images obtained through linear interpolation along the migration path. All images were then optimized simultaneously to determine the minimum energy path (MEP). Migration barriers were calculated using the NEB method as implemented in VASP, with the climbing-image NEB (CI-NEB) scheme employed to locate the saddle point accurately[179]. The migration barrier was defined as the maximum energy along the MEP relative to that of the initial state.

5.2.2 Grain Diffusion

The geometry-optimized bulk structures were used to construct slab models for migration-barrier calculations in grains. For each slab, a vacuum layer of 10 Å was introduced along the z-direction, while periodicity was preserved along the x and y directions. Slab thicknesses of 5–7.5 Å were chosen to balance physical accuracy with the computational cost associated with the multiple DFT calculations required for each NEB simulation. This vacuum-slab configuration was employed in the DFT-NEB calculations to reduce spurious interactions between adjacent images. Grain-diffusion slabs were subsequently generated using Pymatgen [237] by selecting exposed surfaces with surface energies below 250 meV/Å^2, as lower-energy surfaces are generally more stable and more likely to occur naturally in grain structures [81]. The surface energy, (γ_{surf}), was calculated using Equation 5.1

$$\gamma_{\text{surf}} = \frac{E_{\text{slab}} - NE_{\text{bulk}}}{S} \tag{5.1}$$

where E_{slab} is the total energy of the relaxed slab, E_{bulk} is the bulk energy per unit structure, N is the number of units, and S is the surface area of the slab.

Table 5.1: Statistical overview of grain surface energy for the SEI components considered in this study.

SEI component	Grain surface	Surface energy (meV/Å^2)		
		Maximum	Minimum	Average
LiF	(100), (110), (210), (211), (221)	107.1	74.4	85.9
LiCl	(100), (110), (210)	18.3	7.6	13.0
LiBr	(100), (110), (210)	10.8	10.5	10.6
LiI	(100), (110), (210)	22.1	7.2	12.2
Li_2O	(110), (111)	57.2	35.4	46.3
Li_2S	(110), (111)	32.7	22.8	27.7
Li_3N	(100), (110)	57.2	31.5	44.4
Li_2CO_3	(001), (100), (110)	105.5	39.7	35.0

The resulting structures of grain, together with their corresponding surface terminations and surface energies, are summarized in Table 5.1. Diffusion sites were then identified from these grain models using nearest-neighbor analysis to determine plausible Li migration pathways. When multiple diffusion sites were symmetrically equivalent, only one representative site was retained to avoid redundancy in the dataset. On average, 10–15 NEB calculations were performed for each grain structure, enabling systematic mapping of the diffusion-energy landscape.

5.2.2.1 Grain Boundary Diffusion

Homogeneous grain boundaries: Grain-boundary migration-barrier data were generated using homophase grain-boundary models constructed on the basis of Coincidence Site Lattice (CSL) theory. In this approach, the degree of lattice coincidence between two adjoining grains is quantified by the CSL parameter, defined as the ratio of the area of the coincidence site lattice to that of the fundamental lattice. To sample representative low-Σ boundaries, CSL values of 3, 5, 7, 9, 11, and 13 were considered. The corresponding rotation axes, rotation angles, grain-boundary planes, number of

grain-boundary planes, and interfacial spacings used in this work are summarized in Table 5.2.

Table 5.2: Coincident site lattice parameters used to construct low-Σ GB in SEI components.

Σ	Rotation axis	Rotation angle (°)	GB plane
3	[110]	70.52	$(\bar{1}11)$, $(1\bar{1}2)$, (110)
5	[001]	36.86	(012), $(0\bar{2}1)$, (100), (013), $(0\bar{3}1)$
7	[111]	38.21	$(1\bar{3}2)$, $(5\bar{1}\bar{4})$, (111)
9	[110]	38.94	$(\bar{1}1\bar{4})$, $(\bar{2}21)$, (110)
11	[110]	50.47	$(\bar{3}32)$, $(1\bar{1}3)$, (110)
13	[100]	22.61	$(0\bar{3}2)$, $(0\bar{2}\bar{3})$, (100), $(0\bar{5}1)$, $(0\bar{1}\bar{5})$

The grain-boundary structures were generated using the open-source Python package `aimsgb`, which enables construction of periodic grain-boundary models for both cubic and non-cubic crystals. For each SEI component, grain-boundary supercells were built from the parent crystal by joining grains A and B according to the prescribed CSL relationship. Default `aimsgb` settings were used for model generation, except 10 Å vacuum thickness, 1.75 Å interfacial separation beyond default construction, primitive-cell reduction enabled, and an atomic-plane tolerance factor of 0.25 Å. A few atomic layers were removed along the $\pm z$ directions to reduce the system size to approximately 100–150 atoms, thereby keeping the models computationally less demanding. The resulting grain-boundary slabs were constructed with thicknesses in the range of 5–10 Å. A few sample grain boundary structures constructed in such a way is illustrated in Figure 5.4.

To exclude energetically unfavorable grain boundaries, the grain-boundary energy of each model was evaluated using Equation 5.2:

$$\gamma_{\mathrm{GB}} = \frac{E_{\mathrm{AB}}^{\mathrm{GB}} - N_{\mathrm{A}} E_{\mathrm{A}} - N_{\mathrm{B}} E_{\mathrm{B}}}{2S} \tag{5.2}$$

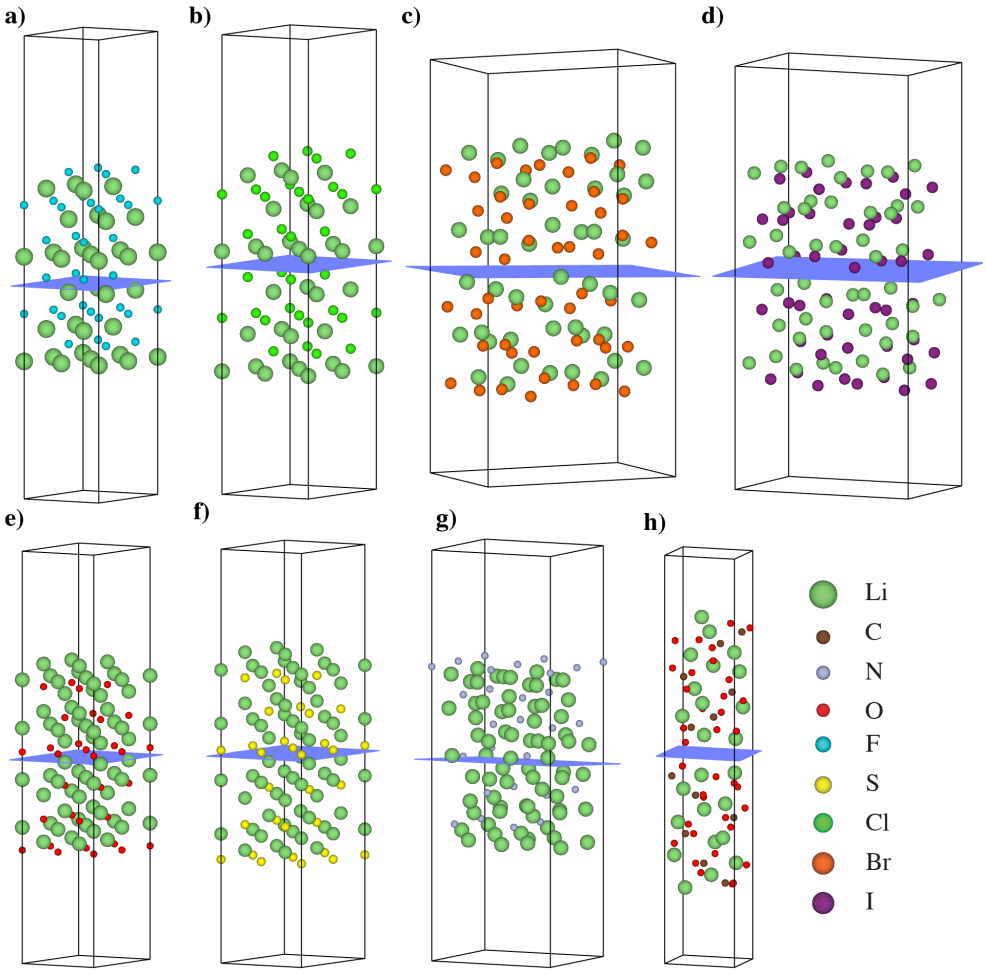


Figure 5.2: Representative homogeneous (Σ3) grain boundaries constructed by cleaving along the (-111) plane for (a) LiF, (b) LiCl, (c) LiBr (d) LiI, (e) Li_2O, (f) Li_2S, (g) Li_3N, and (h) Li_2CO_3. The grain-boundary interface is highlighted in blue.

where γ_{GB} is the grain-boundary energy, $E_{\mathrm{AB}}^{\mathrm{GB}}$ is the total energy of the relaxed grain-boundary structure, E_A and E_B are the bulk energies of structures A and B, N_A and N_B are the numbers of unit cells of A and B, respectively, and S is the interfacial area. Grain boundaries with energies greater than 1000 $\mathrm{mJ/m^2}$ were excluded from the dataset, since such high-energy interfaces are generally much less stable, less likely to form or persist under realistic conditions, and may therefore introduce physically less relevant diffusion pathways into the analysis.

To focus the diffusion calculations on the grain-boundary region, selective dynamics were employed to constrain atoms far from the interface, while atoms in and near the boundary region were allowed to relax. Candidate Li migration pathways were then identified by selecting diffusion sites across the grain boundary on the basis of local coordination analysis using Pymatgen[237]. In particular, the destination site for Li diffusion was chosen as a neighboring Li-vacancy site in the vicinity of the interface. Symmetrically equivalent initial and final diffusion sites were excluded to avoid redundant NEB calculations. The resulting grain-boundary diffusion pathways were subsequently used in climbing image-NEB calculations to determine the corresponding migration barriers.

Heterogeneous grain boundaries: In addition to homogeneous grain boundaries, heterogeneous grain-boundary models were also incorporated into the training dataset to account for interfacial diffusion across distinct SEI components. As classical CSL theory is not directly applicable to hetero-interfaces, these structures were constructed using a coherent lattice-matching approach based on the Zur–McGill algorithm[270], which identifies commensurate in-plane supercells between two dissimilar crystals under prescribed mismatch and angular tolerances. We used `CoherentInterfaceBuilder()` class from Pymatgen to build these systems. To maintain computational feasibility, only interface models with small supercell areas, average lattice mismatch below 5%,

and atom counts compatible with DFT calculations were retained. After lattice matching, the film was rotated and strained to match the substrate, and the interface was assembled with an appropriate interfacial gap ($\approx$ 1.5 Å) and vacuum spacing (10 Å). Only a limited number of such heterogeneous grain boundaries were included, as many candidate interfaces were found to be structurally less stable and associated with relatively high grain-boundary energies. A few representative heterogenous grain boundaries are given in Figure C.9 As in the homogeneous grain-boundary models, diffusion pathways were selected across the interface by excluding symmetrically equivalent sites and choosing nearby Li-vacancy destinations for NEB calculations.

5.2.3 Training Data

The training dataset was generated from two categories of diffusion data for SEI components: (i) grain diffusion and (ii) grain-boundary diffusion. For both categories, the target property is the Li-ion migration barrier, determined from the MEP of the diffusion process connecting the initial and final Li diffusion coordinates. The set of energies corresponding MEP of images in the NEB calculation, hereafter referred to as the profile energy along the MEP, was also included as a target, given that the migration barrier corresponds to the maximum energy value within this set.

The overview of grain diffusion training data is given in Figure 5.3, where the first subplot depicts the perpendicular nudged elastic force along the MEP, showing that the force distributions are generally centered near zero for most SEI components, which suggests reasonably well-converged NEB pathways. However, Li_3N and Li_2CO_3 exhibit noticeably broader spreads and larger extrema, indicating greater variability in local migration environments. The second subplot presents the profile energies along the diffusion path, which remain relatively narrow and close to zero for most components, whereas Li_3N shows a substantially wider distribution with pronounced negative excur-

sions, showing a more diverse set of intermediate-state energetics. The third subplot summarizes the migration barriers, one of the target data, revealing that LiCl, LiBr, and LiI are associated with comparatively lower and more compact barrier distributions, while Li_2O, Li_2S, and especially Li_3N display broader distributions and higher upper ranges, indicative of more high-energy diffusion pathways. LiF and Li_2CO_3 also show moderate-to-high barriers with appreciable spread. And, the last subplot shows the number of NEB runs used for model training and testing. Total number of NEB data generated for grain diffusion is 280 where LiF contributes the largest number of samples, while the remaining components maintain reasonably balanced train–test splits. Overall, the dataset captures both comparatively simple and highly variable grain-diffusion behaviors across the SEI components, providing a diverse basis for model training.

The grain-boundary diffusion dataset consists of 198 homogeneous and 104 heterogeneous grain boundary NEB calculations. Figure 5.4 (a) summarizes these data on a per-component basis. For homogeneous grain boundaries, each case is assigned to the corresponding SEI component since both grains belong to the same material. For heterogeneous grain boundaries, component-wise involvement counting was used. For example, if LiF forms grain boundaries with both Li_2S and Li_2O, its involvement is counted twice, once for the LiF/ Li_2S boundary and once for the LiF/ Li_2O boundary. Hence, the bars corresponding to the heterogeneous grain boundary in Figure 5.4 (a) represent the frequency with which a given SEI component participates in heterogeneous grain boundaries. For homogeneous grain-boundary cases, Figure 5.4(b) further resolves the data according to the CSL value of the interface, classified by the corresponding Σ values. This subplot therefore illustrates how the homogeneous grain-boundary dataset is being distributed across different boundary types for each SEI component.

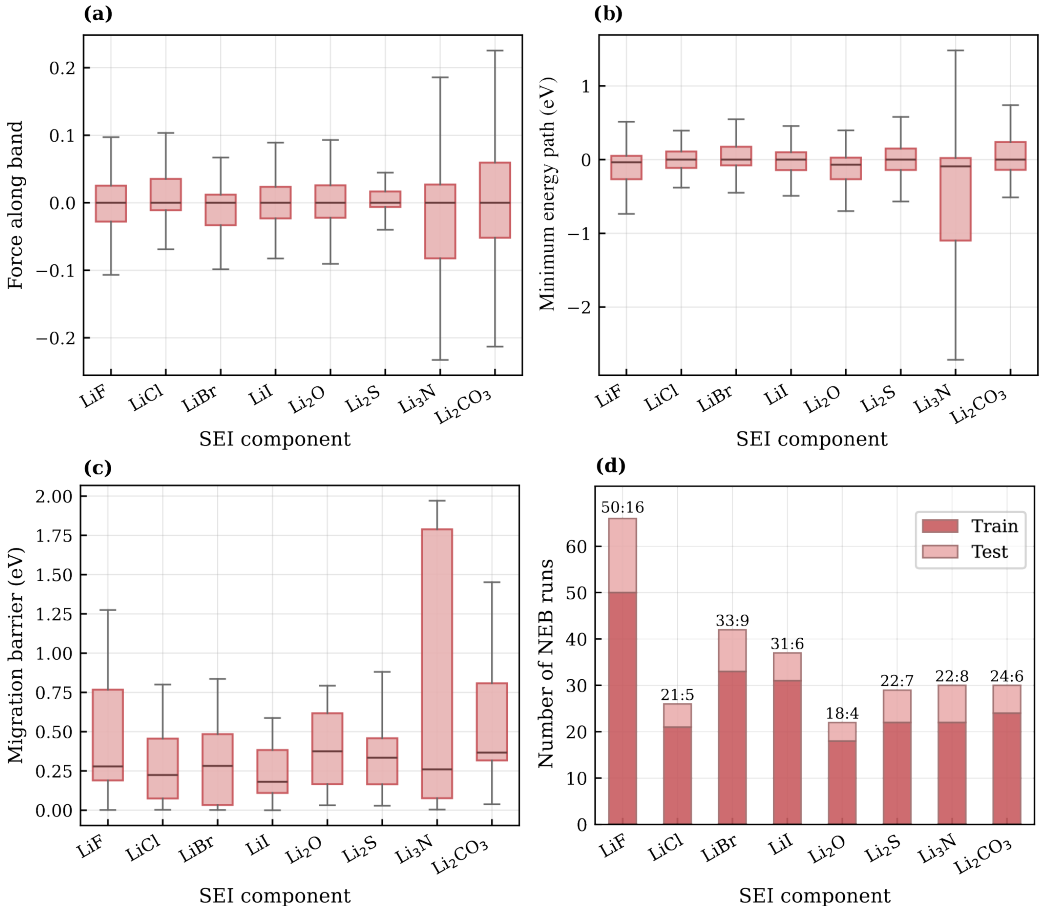


Figure 5.3: Overview of Li-ion grain diffusion through SEI components; a) box plot of average nudged elastic force b) energies of intermediate images in minimum energy path, c) migration barrier and number of NEB runs and their test–train partition in SEI components. Prima facie, lithium halides exhibit comparatively lower migration barriers for grain-boundary diffusion than other SEI components.

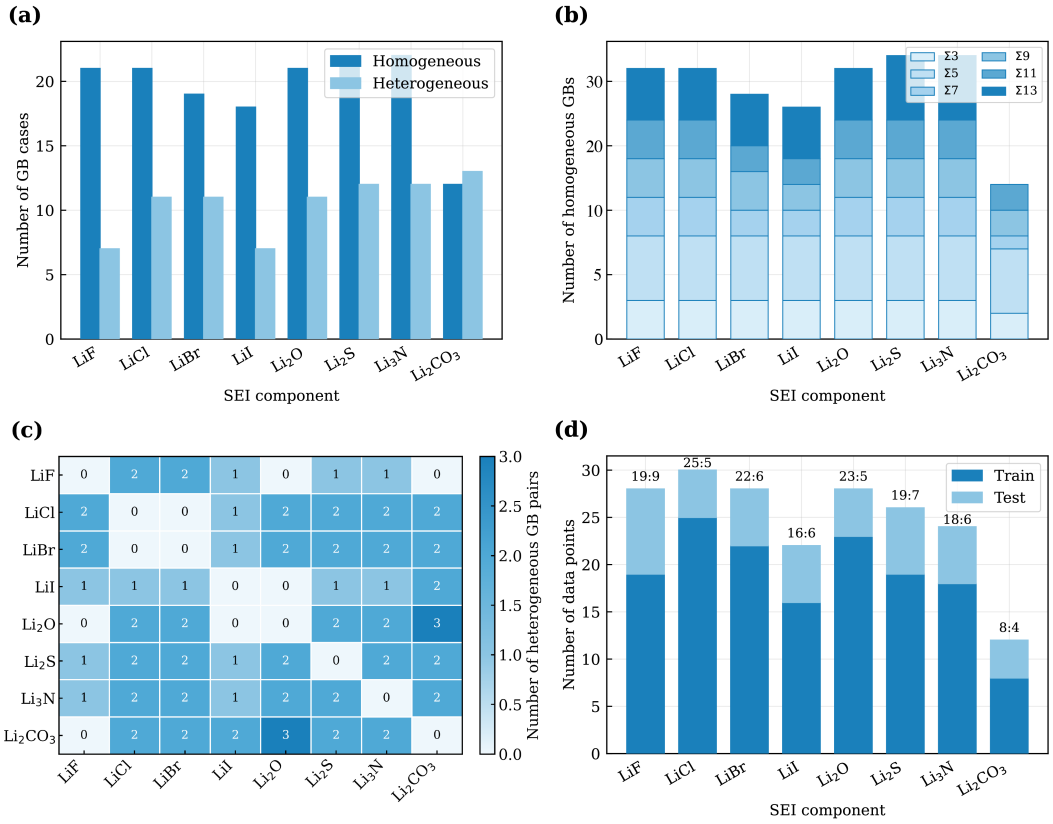


Figure 5.4: Summary of the diffusion dataset generated from grain boundaries formed between SEI components: (a) Numbers of homogeneous and heterogeneous grain boundary diffusion cases for each SEI component, (b) homogeneous grain-boundary structures according to the CSL parameter Σ, (c) heterogeneous grain-boundary pairs formed between different SEI components, and (d) train–test split of the total dataset for each SEI component, with the numbers above the bars indicating the corresponding counts of train and test samples used.

The heterogeneous grain-boundary dataset is summarized in Figure 5.4(c) as a pairwise component matrix, where each entry denotes the number of heterogeneous grain-boundary configurations formed between two SEI components. The planes involved such grain boundaries are given in Table C.5.

Together, the two types of grain boundaries contribute a total of 2114 data points as each NEB calculation consists of seven intermediate structures. Figure 5.4(d) shows the train–test split of this dataset for each SEI component. The labels above the bars indicate the corresponding numbers of training and test samples, which highlights the component-wise fraction of data used for training and testing. Figure 5.5 depicts the distribution of (a) NEB force along band, (b) profile energy, (c) migration barrier and (d) grain boundary energy in homogeneous grain boundaries.

Featurization: The final dataset contains both the scalar migration barrier and the profile energies along the diffusion pathway for each NEB calculation. To describe grain and grain-boundary diffusion environments, two categories of descriptors were considered: (i) composition-based chemical features and (ii) structure-based features.

For composition-based descriptors, we employed Magpie-preset featurization implemented in the *Matminer* library[243]. Specifically, the compositional feature set was generated using a `MultipleFeaturizer` combining `Stoichiometry()`, `ElementProperty()`, `ValenceOrbital()`, and `IonProperty()`. These descriptors capture complementary chemical information, including elemental fractions, statistical elemental-property attributes, average valence-orbital characteristics, and ionic-property-related features. The initial feature filtering was performed using Pearson's correlation coefficient; specifically, when two features exhibited a correlation greater than 90%, the feature with the larger mean absolute deviation was retained. For predictive modeling in materials science, the use of fundamental physicochemical properties of a system as input

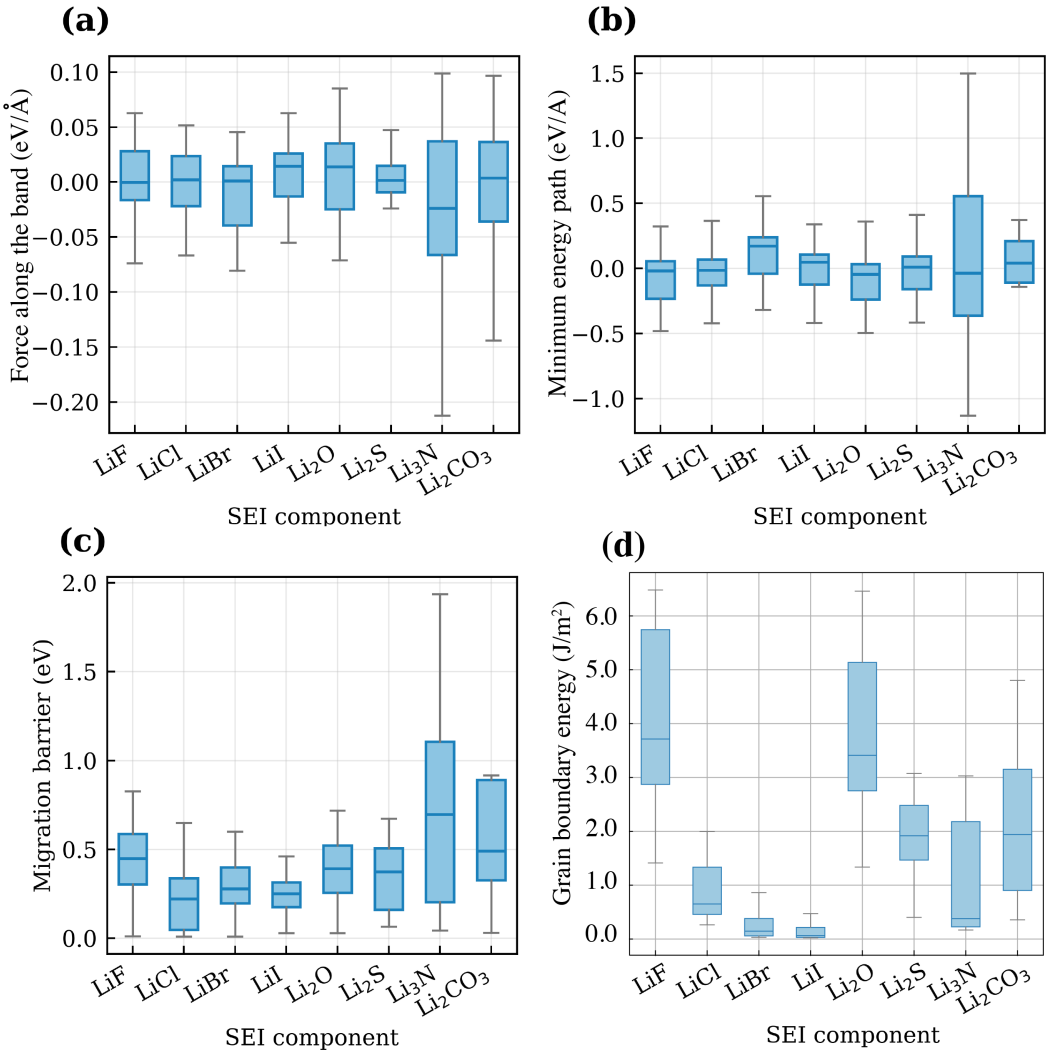


Figure 5.5: Statistical overview of NEB dataset for grain boundary diffusion: Boxplots of the (a) NEB force values along the diffusion pathway for converged NEB images, (b) energies of intermediate images in minimum energy path, (c) Li-ion migration barriers and (d) grain boundary energy. A lower migration barrier in grain boundaries composed lithium halides can be observable, wherein especially LiCl based grain boundary exhibit lower among all other lithium halides.

features has proven promising in previous studies[271–274]. The detailed information of the composition features used in this study are tabulated in Table C.6. The space-group information included in the feature space was determined from the local crystal structures associated with the NEB images and diffusion environments rather than from composition-based estimations. In addition to these composition-derived descriptors, several structural descriptors were incorporated in train data. These include the exposed surface of the grain slab model (or the grain-boundary surface for grain-boundary systems), surface energy (or grain boundary energy for grain-boundary slabs) and a binary indicator specifying whether a given NEB image corresponds to the saddle-point configuration. Importantly, slab models associated with the NEB pathway, including the initial, intermediate, and final images, were represented as graphs to preserve the local atomic connectivity and geometric environment during diffusion. More information about graph construction is given in subsection 5.2.4. Together, these composition and structure-based descriptors provide a unified representation of the chemical identity and atomistic diffusion environment of each SEI system.

It should be noted that some composition-derived descriptors, such as melting temperature and space-group number, are not interpreted here as direct causal variables governing Li-ion transport. Rather, these descriptors act as proxy representations of broader structural and bonding characteristics of the SEI components. In contrast, local structural descriptors such as exposed surface orientation, grain-boundary energetics, and saddle-point environment are more directly connected to the underlying diffusion physics because they influence Li-site connectivity, local coordination environment, bottleneck geometry, and interfacial structural disorder along the migration pathway.

Feature-dependence analysis was also performed to identify the most important features among the original descriptors that are directly correlated with the MEP.

For this, permutation importance was used. In this approach, the trained model kept fixed, and one feature is shuffled across the test samples while the prediction error for the MEP is recalculated. A large increase in error indicates that the shuffled feature is important for predicting the target property, MEP. This method is particularly suitable here because it measures the model's actual predictive reliance on each feature and remains valid even for nonlinear models.

5.2.4 Graph Neural Network

Crystal graph construction: The encoding process begins with the construction of a periodic crystal graph from a POSCAR and CONTCAR structures (VASP input/output files) corresponding to NEB images. Each structure is represented as a graph, $\mathcal{G} = (\mathcal{V}, \mathcal{E})$, where atoms correspond to nodes, $\mathcal{V} = \{v_i\}_{i=1}^{N}$, and edges, $\mathcal{E} \subset \mathcal{V} \times \mathcal{V}$, represent interatomic interactions within a cutoff radius. The featurizer extracts fractional atomic coordinates, $\mathbf{r}_i^{\text{fractional}} \in R^3$, atom types, Z_i, lattice parameters (lengths $\mathbf{a}$ and angles $\boldsymbol{\alpha}$), and periodic boundary information. The resulting `PyTorch Geometric` object contains node features, edge indices, and periodic image offsets, thereby enabling graph construction under periodic boundary conditions. This study uses 'Directional Message Passing Neural Network' (DimNet++) to generate graph embedding of grain and grain boundary structures[275, 276]. According to review articles published in recent years on GNN applications in materials science and drug design, DimeNet has been widely used in these domains[277–279]. Additional information about its architecture and message-passing scheme, including the fractional-to-Cartesian coordinate transformation, periodic distance computation, triplet construction for angular interactions, radial and spherical basis expansions, edge embedding, edge-to-node projection, angular interaction blocks, accumulated node representations, and graph-level readout, are briefly provided in the Supplementary Material.

Predictive model: A multi layered GNN model is used to predict diffusion energy profiles and migration barriers directly from initial NEB structures. Figure 5.6 (a) depicts the architecture of the model. Training data, the NEB trajectory consists of seven structures, including the two end point geometries, along the reaction coordinate, and each structures, as mentioned earlier, is represented as a periodic crystal graph. Individual structures are encoded using a GNN encoder using DimeNet++, producing embeddings $\mathbf{g}_i \in R^{256}$. Additionally, a pretrained graph variational autoencoder (GVAE) was used to incorporate SEI component distribution information into each NEB data point, thereby enabling each data point to retain awareness of its position within the SEI component space. A summery of GVAE used is provided in subsection 5.2.5.

The role of the GVAE pretraining in the present framework is primarily to learn embedded latent representations of the crystal graph structures and their configurational relationships (from the latent space) within the diverse SEI diffusion dataset. Although the GVAE is pretraining includes NEB trajectory information along with structure information, the resulting latent embeddings are intended to capture generalized structural characteristics of diffusion environments rather than directly encode explicit migration barriers or NEB energy profiles. During inference, the predictive GNN model operates on graph-based structural representations together with the pretrained latent embeddings, without directly requiring NEB energies, force profiles, or converged minimum-energy pathway information as input features.

To incorporate diffusion pathway information, each structural embedding is augmented with projected scalar physical descriptors ($\mathbf{f}_i$) namely exposed surface information, surface or grain boundary energy, saddle-point indicator, force along the band, DFT energy per atom and compositional features and a learnable positional embedding ($\mathbf{p}_i$) specifying the position of intermediate structure along the diffusion path. Thus

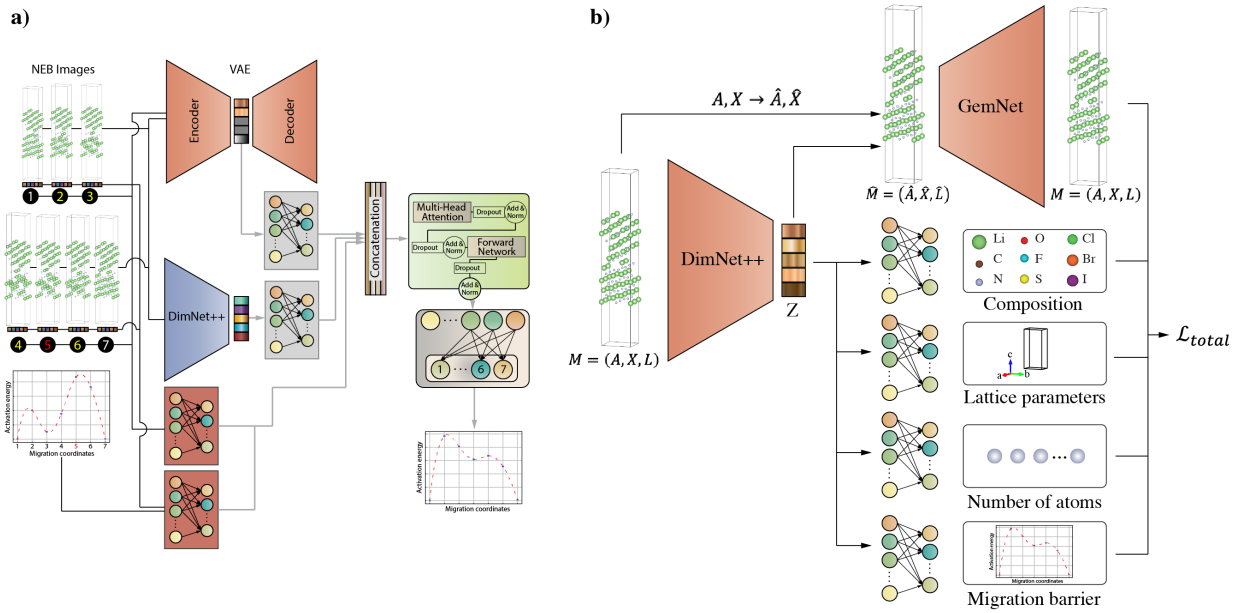


Figure 5.6: Schematic illustration of the (a) predictive GNN model architecture. A grain-boundary NEB data point for LiF is shown as an illustrative example. The NEB images marked in white indices represent the initial and final structures, those in yellow indicate intermediate structures, and marked in red corresponds to the saddle point. The representative boxes illustrated beneath each structure denote the compositional features. Black connecting lines represent pre-processing operations, while gray lines depict the on-the-fly training and testing pathway of the model. Panel (b) depicts architecture of of GVAE model where M is the ground truth structure and $\hat{M}$ is the noised counterpart. A, X, and L denotes atom types, atom positions and lattice parameters. Role of GVAE in this design is to provide embedded representation of a complete NEB calculation (include all images and their features) to the GNN.

the resulting per-image representation ($\mathbf{e}_i$) is given as;

$$\mathbf{e}_i = \mathbf{g}_i + \mathbf{f}_i + \mathbf{p}_i \tag{5.3}$$

which is then grouped into a sequence $\mathbf{E} = [\mathbf{e}_0, \ldots, \mathbf{e}_6]$ and processed using a multi-layer Transformer encoder. Self-attention across images enables the model to capture energy curvature, saddle localization, and collective structural evolution along the diffusion pathway.

From the contextualized embeddings, the model predicts per-image profile energies, $\hat{y}_i$, which are shifted to enforce the VTST[179] convention.

The migration barrier is then derived directly from the predicted profile. Depending on configuration, the barrier is computed as a differentiable softmax pooling,

$$\hat{E}_{\text{mig}} = \sum_i \left(\frac{\exp(\hat{y}_i/\tau)}{\sum_j \exp(\hat{y}_j/\tau)} \right) \hat{y}_i \tag{5.4}$$

where parameter τ controls smoothness. The model is trained using a multi-task objective combining profile energy regression, barrier regression, and a consistency regularizer enforcing agreement between the predicted barrier and the maximum predicted profile energy. This physics-informed formulation ensures that the learned representation captures both local structural manifold and global diffusion energetics within a unified pathway-level model.

5.2.5 Graph Variational Auto Encoder

A path-aware GVAE design logic is used in this study to learn structural latent representations of NEB data points. Unlike conventional crystal VAEs that treat configurations independently, VAE used here encodes all seven structures of an NEB trajectory

jointly as a single data point, allowing the model to learn collective geometric information along the reaction coordinate and positional awareness in SEI component space. This design enables the learning of diffusion processes in individual SEI components while preserving an intuitive understanding of the SEI as a whole.

The GVAE architecture illustrated in Figure 5.6 (b), is adapted from the Crystal Diffusion Variational Autoencoder developed by Xie et al. [280]. In contrast to a conventional reconstruction-based VAE, this framework employs a denoiser-based decoder, which is trained to recover the original input from slightly perturbed representations rather than simply reconstructing an unaltered ground-truth structure. For continuous attributes, such as atomic coordinates, a perturbation is introduced through Gaussian noise. For discrete attributes, such as atom types, direct addition of continuous noise is not meaningful; therefore, the training procedure instead perturbs the data by interpolating between the true and predicted probability distributions. Such a denoising objective improves the strength of the learned latent space and captures chemically and structurally relevant variations. Detailed information about training scheme using GVAE is given in supplementary material.

5.2.6 Training and Validation

Grain diffusion: The GVAE model developed in this work serves as a supportive module for the predictive GNN model. Its main function is to learn a latent representation for each NEB calculation in a higher-dimensional space. This latent representation encodes the relative position of each NEB calculation, and therefore each MEP, within the broader configurational space defined by all SEI components and their corresponding diffusion pathways.

The GVAE was tuned by varying the training batch size, latent-space dimension, and feature/target normalization strategy as shown in Figure C.10 (a–c). Based on

this analysis, the best overall performance was obtained with a batch size of 16, a latent dimension of 128, and a learning rate of 0.004. Since the GVAE used here follows a semi-latent-diffusion VAE scheme, the effect of latent diffusion strength was also examined by varying the perturbation applied to atomic coordinates and lattice parameters; these results are also summarized in Figure C.12.

The performance of the fine-tuned GVAE was further analyzed by varying the KL-divergence weight parameter, β, from 0.1 to 1.0, as shown in Figure 5.7(a). The parameter β controls the extent of latent-space regularization in the GVAE model[281]. In the present case, this regularization determines how the NEB data corresponding to different SEI components are distributed in the learned latent space. The corresponding KL-divergence convergence behavior is shown in Figure 5.7(b). Among the tested values, $\beta = 0.6$ provides the best balance between regularization and reconstruction quality. A visualization of this latent space in 3-D with t-Distributed Stochastic Neighbor Embedding (t-SNE) based dimensionality reduction technique is shown in Figure 5.10 (a). A clear clustering of SEI components are visible in this basis with LiF forms comparatively bigger hull among the components. Furthermore, as shown in Figure 5.7(c), this GVAE gives the most accurate reconstruction of lattice parameters, atomic coordinates, and atom types. Representative grain structures reconstructed by the GVAE are shown in Figure C.13, demonstrating that the model reproduces the lattice parameters, atomic coordinates, and atom types with good accuracy.

After training the GVAE with $\beta = 0.6$, the learned latent embeddings of the NEB structures were incorporated into the predictive GNN model. To evaluate the contribution of these embeddings to the predictive performance, the GNN was tested under three different input schemes: (1) using the original descriptors (graph representations of the NEB images and the composition-based chemical descriptors) together with the GVAE-derived latent embeddings, (2) using only the original descriptors, and (3)

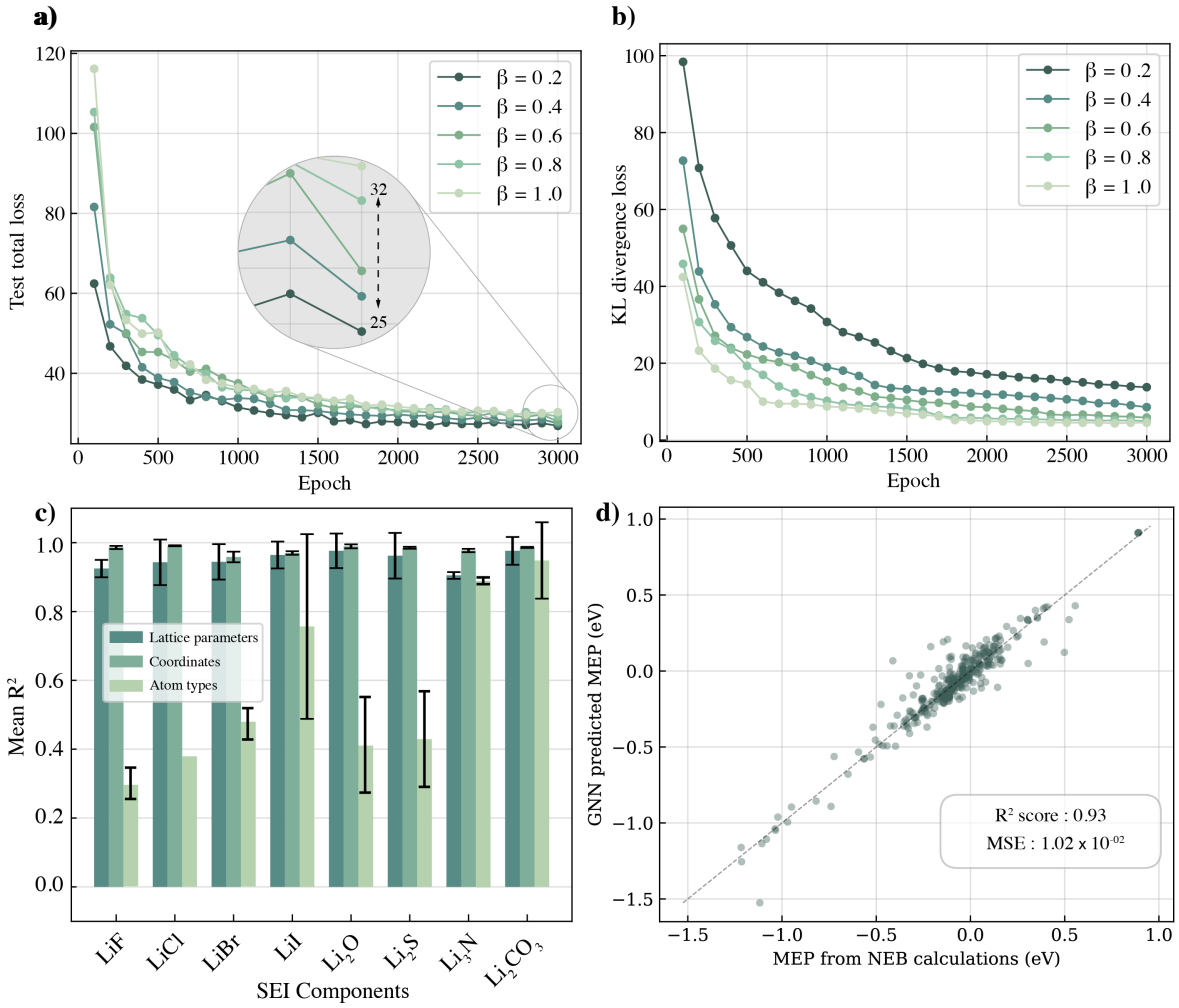


Figure 5.7: For grain diffusion, performance of the GVAE model in terms of convergence of the (a) total test loss and (b) KL divergence for different values of the weighting parameter β ranging from 0.2 to 1.0. The reconstruction performance of the GVAE for lattice parameters, atomic coordinates, and atom types is shown in (c), and the corresponding R^2 score for predicting MEP using GNN model is shown in (d).

using the GVAE-derived latent embeddings. In the first setting, original descriptors were concatenated with the latent embeddings learned by the GVAE. In the second setting, each NEB calculation was represented only by its original descriptors, without latent-space information. In the third setting, the GNN was trained using only the GVAE-derived latent representation. The performance of these three models was compared using the test R^2 score and mean absolute error (MAE) for MEP prediction, as shown in Figure C.11 (b – d).

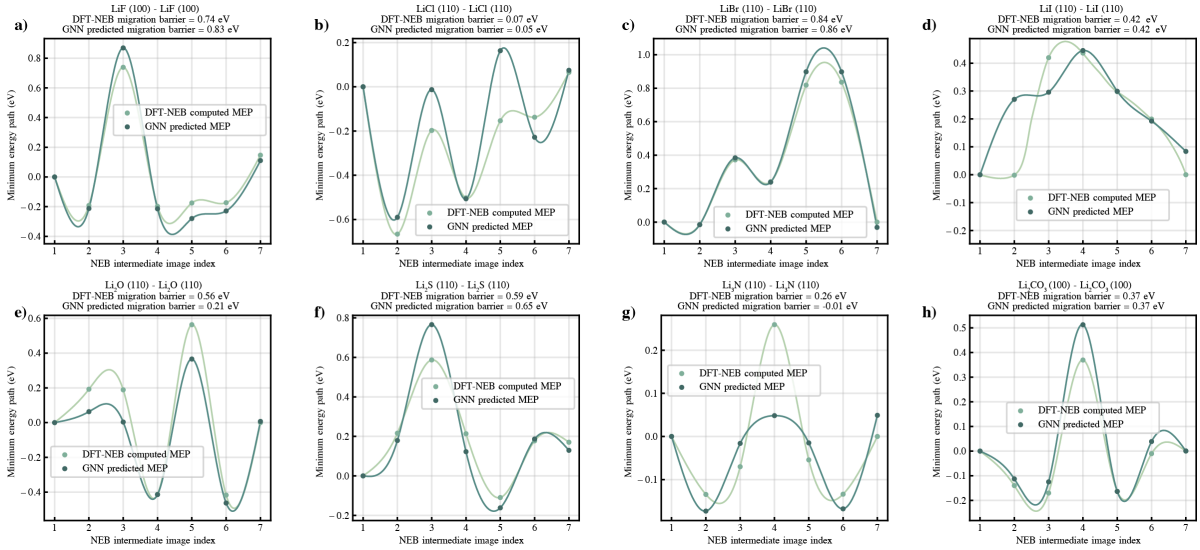


Figure 5.8: Comparison between the MEPs predicted by the GNN model and those obtained from NEB calculations for grain diffusion of (a) LiF (100), (b) LiCl (110), (c) LiBr (110), (d) LiI (110), (e) Li_2O (110), (f) Li_2S (110), (g) Li_3N (110), and (h) Li_2CO_3 (100). The exposed surface corresponding to each grain is indicated in the brackets. The model achieves a point-wise MEP MAE of approximately 0.05 – 0.08 eV and a migration barrier MAE of about 0.10 eV, which reduces to a range of 0.04 – 0.05 eV when clear outliers reported in the case of Li_2O and Li_3N are excluded.

Among the three training schemes, the GNN model that incorporated both the original descriptors and the GVAE-derived latent embeddings achieved the best predictive performance, with a test-set R^2 score of 0.93 and an MSE of 1.02×10^{-2}, as shown in Figure 5.7(d). This result indicates that the latent representation learned by the GVAE contains additional physically meaningful information from SEI component

space about the configurational relationships among diffusion pathways that is not fully captured by the original descriptors alone. Therefore, this model was selected for further benchmarking.

To assess its predictive reliability across the SEI components, representative test cases were selected from all components considered in this study with their low-index exposed surfaces. The corresponding minimum energy paths predicted by the GNN are compared with those obtained directly from NEB calculations in Figure 5.8 (a – h). Overall, the predicted MEPs reproduce the main features such as saddle points of the NEB calculated profiles with good agreement across the different grain systems, demonstrating that the combined GVAE-GNN framework is able to capture the Li-ion diffusion pathways in grain diffusion in selected SEI components.

To validate the model a separate sample set of grain models constructed for all SEI components described in this study. This set of data never been used in any part of training or testing. The validations results are provided in supplementary material (Figure C.17).

Feature-importance analysis was further carried out using the trained GNN model, and the corresponding importance scores are presented in Figure 5.9. Among the composition-derived descriptors shown in Figure 5.9 (a), melting temperature, space-group number, and ground-state volume emerge as statistically important features. However, these quantities should primarily be interpreted as proxy descriptors reflecting broader structural and bonding characteristics of the SEI components rather than direct causal variables governing Li-ion transport. For example, higher melting temperatures generally correlate with stronger ionic bonding and reduced lattice flexibility, which can suppress local structural relaxation during Li migration and thereby increase activation barriers. Similarly, the space-group symmetry influences the connectivity and anisotropy of Li-ion hopping pathways through its control over neighboring Li-site

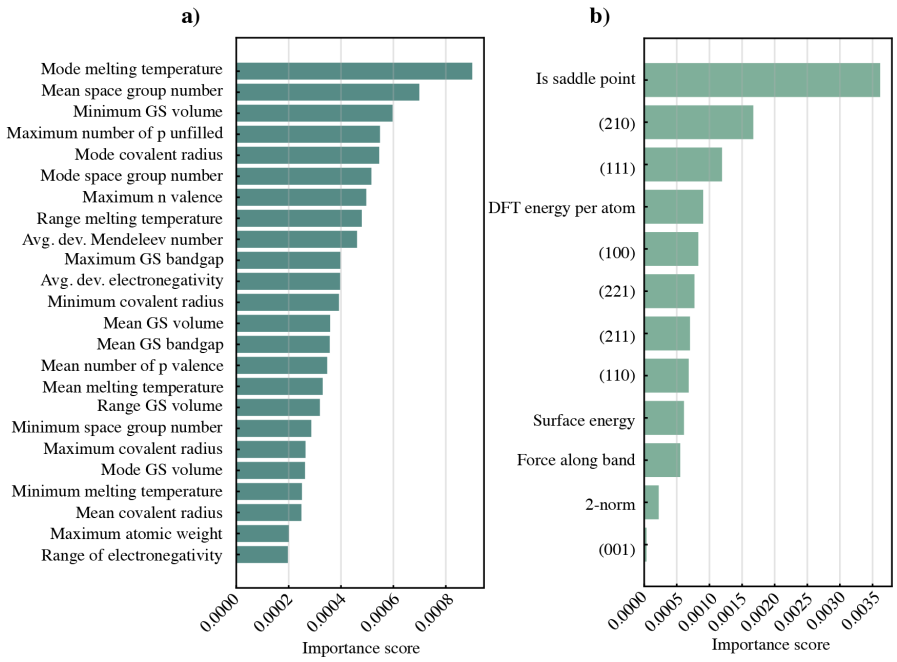


Figure 5.9: Feature importance analysis of grain diffusion: important features identified from the subset of a) composition-derived and b) structural features are listed based on mean accuracy decrease score. The statistical measures mentioned in the beginning of each composition-derived descriptors is attributed to the number and type of elements present in SEI component. A dominance of structure related features (grain exposed surfaces, DFT and surface energies) can be observable with the highest feature importance score compared to composition-derived features.

arrangement and diffusion-channel topology.

More physically direct insight is obtained from the structural descriptors shown in Figure 5.9 (b). The exposed surface orientation strongly affects the local Li coordination environment, surface relaxation behavior, and migration bottleneck geometry, all of which influence the smoothness of the migration-energy landscape. In particular, the relatively higher importance of the (210) and (111) surfaces suggests that local crystallographic topology plays a significant role in determining accessible low-energy diffusion channels. Likewise, the strong contribution of saddle-point and surface-energy descriptors indicates that Li-ion migration in SEI grains is governed not only by composition, but also by the local energetic roughness and structural continuity of the diffusion pathway. These trends are further consistent with the relatively smooth and narrow migration-barrier distributions observed for lithium halides compared with Li_3N and Li_2CO_3.

Latent-space analysis further indicates that the GVAE learns chemically distinct regions within the generative manifold. As shown by the PCA and t-SNE based projections in Figure C.14 (a and b), the latent representations exhibit clear component-dependent clustering for the major SEI phases, demonstrating that the model captures meaningful differences in their underlying structural and Li-ion diffusion characteristics. To visualize cluster separation, the original 256-dimensional latent vectors were projected onto a three-dimensional Cartesian basis using t-SNE, as shown in Figure 5.10 (a). This reduced representation clearly highlights both the separation and the partial overlap among the various SEI components, reflecting similarities and differences in their learned latent descriptors. Sampling points for migration barrier generated from each component-specific hull through the barrier head produced characteristic distributions for each SEI component. These data distributions are given as violin plots in Figure 5.10 (b and c) which further show that halides such as LiCl and LiI are

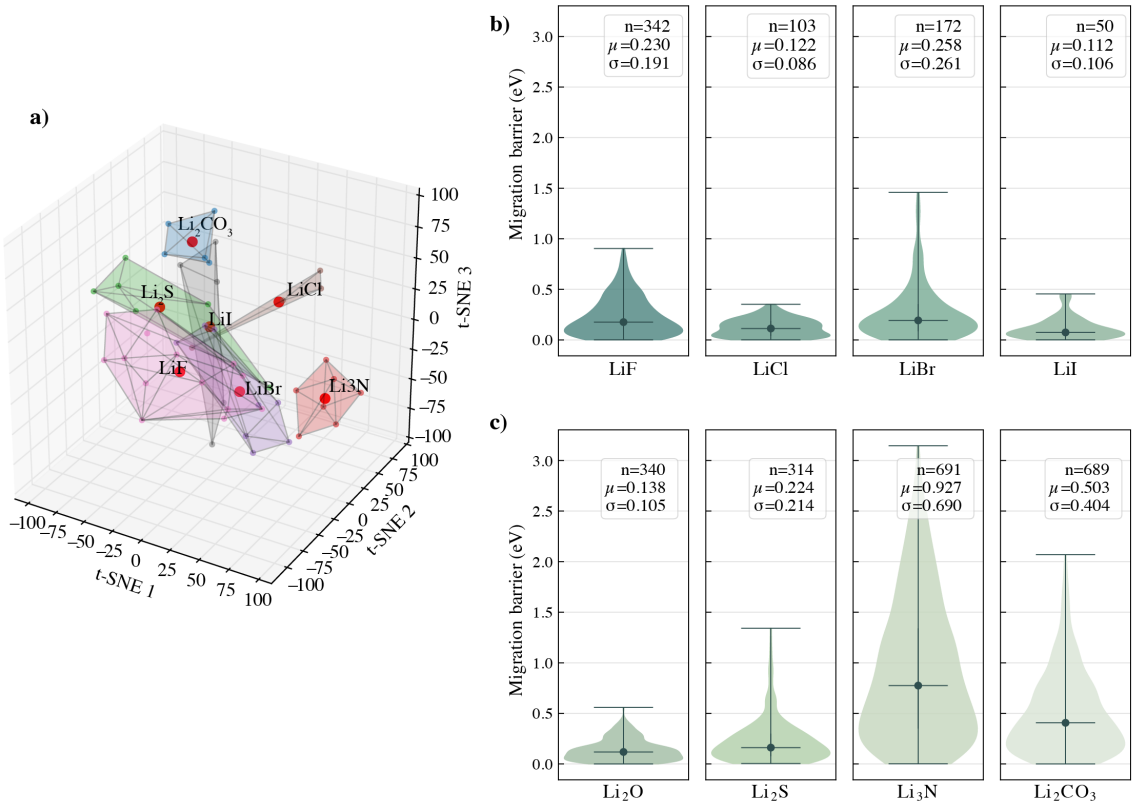


Figure 5.10: Data sampling scheme in latent space: (a) distribution of grain-diffusion data for different SEI components in the GVAE latent space, visualized in a 3-D Cartesian basis after t-SNE dimensionality reduction; (b and c) violin plots of the data generated from the hulls of the respective SEI components. The red dot in each hull indicates the hull center. Panel (b) shows that halide SEI components exhibit generally low migration barriers with narrow distributions, with LiCl and LiI being more favorable to Li-ion conduction and LiBr displaying comparatively broader variability.

associated with relatively narrow, low-barrier distributions, whereas Li_3N and Li_2CO_3 exhibit substantially broader and higher-barrier distributions, with Li_2O and Li_2S lying in between. Overall, these results suggest that the GVAE latent space is not only structured by composition, but also encodes physically relevant variations in ionic migration behavior across different SEI components.

Grain boundary diffusion: Following the procedure adopted for grain diffusion, the GVAE model for grain boundary diffusion was optimized through hyperparameter tuning for latent space dimension, batch quantity, learning rate, and weight decay, as shown in Figure C.15 (a – d). Among the tested configurations, a batch size of 8, a latent dimension of 128, and a learning rate of 0.001 yielded the best overall performance of GVAE model. Evolution of total test loss of the tuned model for KL-weight, $\beta = 0.2, 0.4, 0.6, 0.8$ and 1.0, shown in Figure 5.11 (a), indicates stable convergence. The corresponding KL-divergence also shown in Figure 5.11 (b) show that $\beta = 0.4$ provides the best balance between latent-space regularization and reconstruction fidelity. Then the reconstruction quality of GVAE model was assessed using the R^2 scores of reconstructed lattice parameters, atomic positions, and atomic types, as presented in Figure 5.11 (c). Overall, the model reconstructs the grain boundary slabs with high fidelity, achieving an average R^2 score of approximately 0.85. A representative set of samples from distinct grain boundaries are given in Figure C.13 (e – h) for a visual comparison of reconstruction efficiency.

Using the optimized GVAE latent representation, the predictive GNN model was subsequently trained for grain boundary diffusion. As in the grain diffusion case, three training schemes with distinct feature sets were considered. In addition to the NEB descriptors used in the case of grain diffusion, the feature space for grain boundary diffusion was expanded to include grain boundary type (homogeneous or heterogeneous),

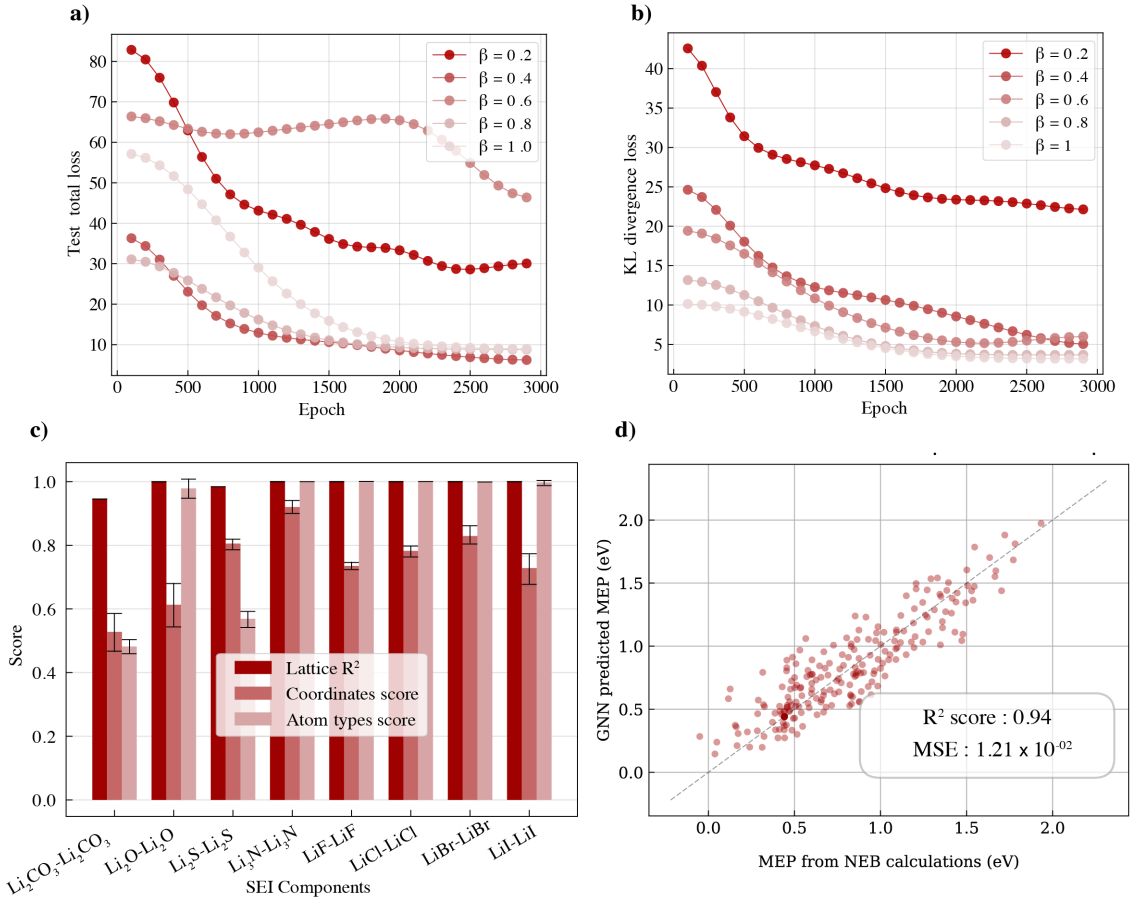


Figure 5.11: For grain boundary diffusion, performance of the GVAE model in terms of convergence of the (a) total test loss and (b) KL divergence for different values of the weighting parameter β ranging from 0.2 to 1.0. The reconstruction performance of the GVAE for lattice parameters, atomic coordinates, and atom types is shown in (c), and the corresponding R^2 score for migration-barrier prediction using GNN model is shown in (d).

grain boundary energy, and the exposed surface of the grain boundary. These additional descriptors were introduced to better capture the grain boundary configurations in such systems.

The GNN model for grain-boundary diffusion showed the best performance when the composition-derived features were combined with the latent embeddings learned by the GVAE model. A comparison of the three training settings is presented in Figure C.16 (a – c). The best-performing model Figure 5.11 (d) achieved an R^2 score of 0.94 with an MAE of 1.21×10^{-2}. This improvement indicates that the GVAE-derived latent embeddings transfer useful information about the distribution of different grain-boundary environments in the latent space, enabling the GNN model to predict the MEP more accurately compared to other two training approaches.

Using the best-performing GNN model, feature-importance analysis was further carried out, and the results are shown in Figure 5.12. Among the composition-derived descriptors given in Figure 5.12 (a), average melting temperature and space group number were identified as the most important similar to that identified in grain diffusion. Most important structural features, shown in Figure 5.12 (b) are saddle-point indicator, grain-boundary energy, DFT energy per atom, CSL Σ, and surface indices. The prominence of these geometric and structural features indicates that the MEP for Li-ion diffusion is strongly governed by the local structural environment, particularly the orientation of the surfaces forming the grain boundary. Among the important grain-boundary surfaces identified in this work, (-111), (110), (1$\bar{1}$2), (032), and (001) have also been reported in experimentally observed stable SEI configurations in earlier studies[282, 283].

More physically meaningful trends emerge from the structural descriptors shown in Figure 5.12 (b). The dominant importance of saddle-point environment, grain-boundary energy, CSL Σ, and exposed grain-boundary surfaces indicates that Li-ion

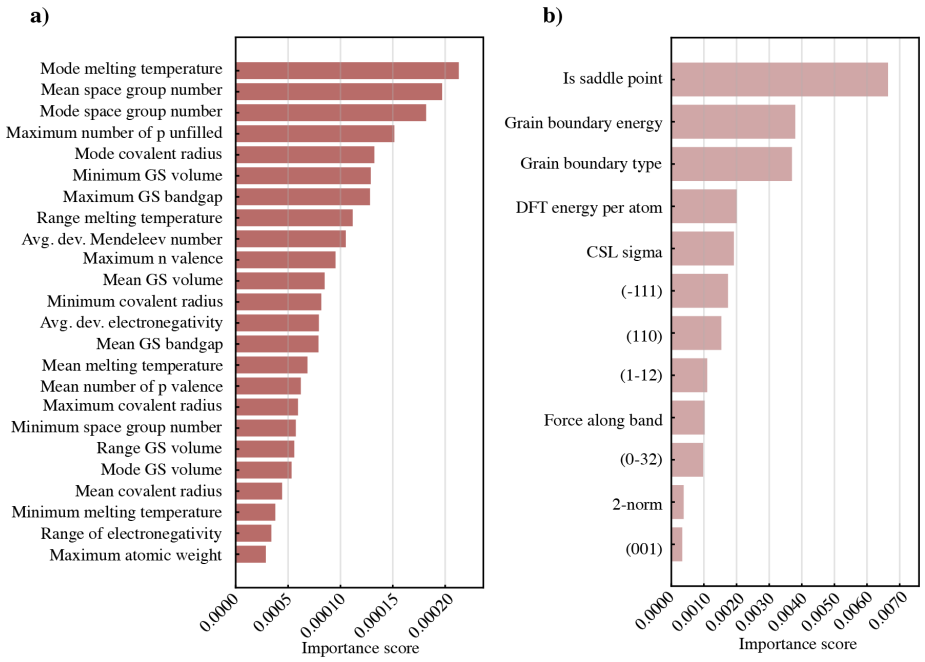


Figure 5.12: Feature importance analysis of grain boundary diffusion: important features identified from the subset of a) composition-based and b) structural features are listed based on mean accuracy decrease score. The statistical measures mentioned in the beginning of each composition-derived descriptors is attributed to the elements present in SEI component. A close examination on feature importance can tell that grain boundary diffusion is strongly governed by localized structural descriptors (saddle point and grain boundary energetics) showing a sharper and strong feature importance distribution compared to grain diffusion, where structural effects are more distributed across surface-related features.

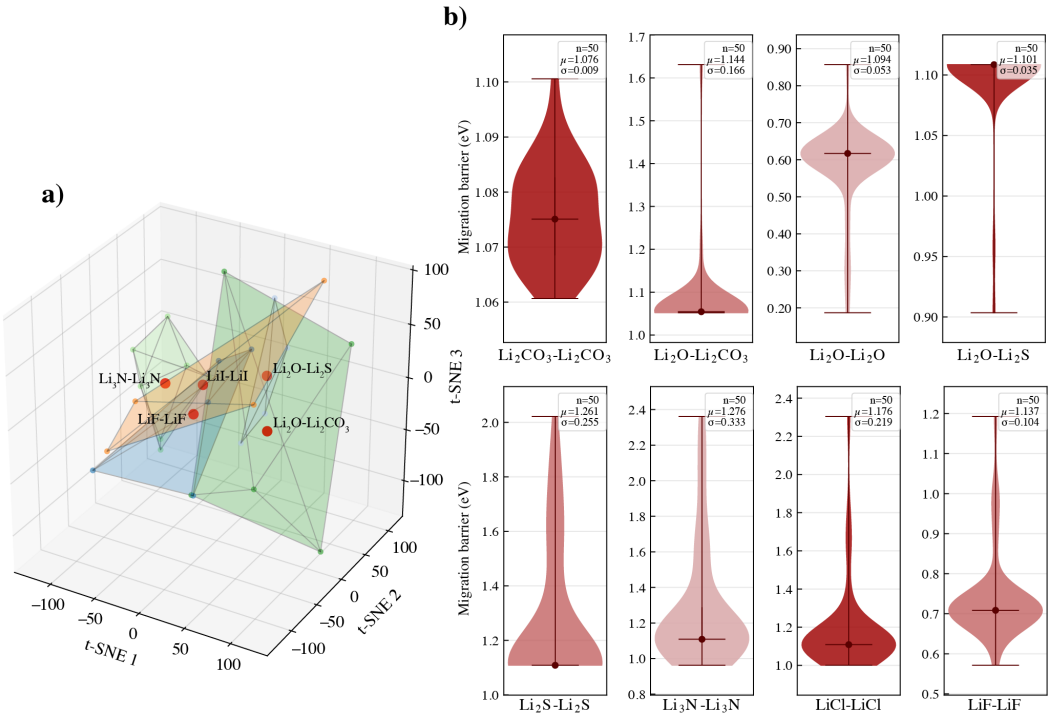


Figure 5.13: Data sampling scheme in latent space: (a) distribution of grain boundary diffusion data for different SEI components in the GVAE latent space, visualized in a 3-D Cartesian basis after t-SNE dimensionality reduction; (b) violin plots of the data generated from the hulls of the respective SEI components. The red dot in each hull indicates the hull center. A few clusters have been illustrated here for a better visualization. Panel (b) shows that grain boundary diffusion generally exhibits higher and more broadly distributed migration barriers compared to bulk, with more variability depending on the specific interface chemistry, particularly for mixed-component boundaries. Due to numerous grain boundary structures involved in the analysis, only important one selected based on migration energy barrier is included in the illustration.

transport across interfaces is governed primarily by local interfacial structure and energetic disorder. Grain-boundary energy is particularly important because it reflects the degree of lattice mismatch and structural distortion at the interface. Higher-energy interfaces generally exhibit more disrupted Li-site connectivity and a more heterogeneous local energy landscape, which increases migration barriers.

Similarly, the influence of CSL Σ suggests that crystallographic coherence between neighboring grains plays a key role in maintaining continuous low-energy diffusion pathways. Lower-Σ grain boundaries tend to preserve better atomic registry across the interface, whereas higher-Σ boundaries introduce more disordered migration environments. The importance of exposed surface orientation further indicates that the local coordination geometry at the interface strongly influences Li-ion mobility. These observations collectively suggest that interfacial transport in SEI is controlled not only by chemistry, but also by the structural compatibility and energetic stability of neighboring grains forming the interface.

Using the optimized GVAE model, the latent-space distribution was projected into three dimensions using t-SNE, as shown in Figure 5.13 (a). The visualization reveals tightly packed clusters corresponding to various grain boundaries, with only negligible overlap, indicating that the model effectively captures the diversity of grain-boundary environments. To further analyze migration-barrier trends, each cluster was enclosed within a hull and sampled within the latent space. The resulting migration-barrier distributions generated through the GVAE decoder are shown in Figure 5.13(b). These distributions indicate that heterogeneous grain boundaries generally exhibit higher migration barriers than homogeneous grain boundaries. Among the homogeneous grain boundaries considered, LiF–LiF and Li_2O-Li_2O show the lowest barrier ranges, approximately 0.58–1.20 eV and 0.20–0.86 eV, respectively. In contrast, among the heterogeneous grain boundaries, Li_2O-Li_2CO_3 gives a comparatively higher barrier range of

about 1.05–1.65 eV. Furthermore, grain boundaries involving lithium halides tend to produce migration barriers in the range of 0.5–1.5 eV. These results suggest that the chemical mismatch at heterogeneous interfaces creates a more resistive energy landscape for Li-ion transport than that found in homogeneous grain-boundary systems.

5.3 Model Performance and Analysis

In this work, we developed a unified DFT-NEB and GNN-based framework to describe Li-ion transport across both grains and grain boundaries formed in SEI. Widely reported components in SEI, namely LiF, LiCl, LiBr, LiI, Li_2O, Li_2S, Li_3N, and Li_2CO_3 are cosidered in this study. The generated diffusion dataset spans 280 grain-diffusion NEB calculations and grain-boundary dataset comprising 198 homogeneous and 104 heterogeneous grain boundaries, corresponding to a total of 261 diffusion data points. Each NEB diffusion data point consists of seven intermediate structures. The predictive framework achieved high accuracy for both transport regimes, with test $R^2 = 0.93$ for grain diffusion and $R^2 = 0.94$ for grain-boundary diffusion, showing that the combination of graph-based structural encoding and GVAE latent representations can reliably capture the minimum-energy-path landscape across a chemically and structurally diverse SEI design space.

Beyond predictive accuracy, the present results provide quantitative design insights into how SEI chemistry and microstructure jointly govern Li-ion migration. For grain diffusion, the latent-space sampling results show that lithium halides generally define the lowest-barrier and most spatially uniform transport landscape. In particular, LiCl and LiI exhibit mean migration barriers of only ≈ 0.12 and ≈ 0.11 eV, respectively, with narrow standard deviations of 0.08 and 0.10 eV. Li_2O also remains comparatively favorable, with $\mu \approx 0.14$ eV and $\sigma \approx 0.10$ eV. Further, Li_3N and Li_2CO_3 show much

broader and higher barrier distributions, with Li_3N reaching $\mu \approx 0.93$ eV and $\sigma \approx 0.69$ eV, and Li_2CO_3 yielding $\mu \approx 0.50$ eV and $\sigma \approx 0.40$ eV. These differences indicate that grain diffusion in the SEI is not controlled solely by composition, but also by the roughness of the underlying migration-energy landscape: halides and Li_2O provide both lower average barriers and better transport uniformity, whereas Li_3N and Li_2CO_3 introduce stronger local variability in Li-ion mobility. This is consistent with the observed feature-importance trends, where the dominant composition-based descriptors are melting point temperature, space-group number, and ground-state volume, while the saddle-point indicator and exposed surface orientation are the most influential structural factors. In the grain diffusion model, the saddle-point flag alone carries an importance score of about 0.03, far exceeding other structural descriptors, and among the exposed surfaces the (210) and (111) planes are more influential than (001), which contributes almost negligibly.

The grain-boundary results further show that interfacial transport is systematically more restrictive than intra-grain transport, and that the transport penalty depends strongly on interface type and boundary energetics. Even the most favorable sampled homogeneous grain boundaries, such as Li_2O-Li_2O and LiF-LiF, have mean migration barriers of 0.62 and 0.71 eV, which are already higher than the best grain-diffusion barriers. More resistive interfaces, including Li_2CO_3-Li_2CO_3, Li_2O-Li_2CO_3, Li_2O-Li_2S, Li_2S-Li_2S, Li_3N-Li_3N, and LiCl-LiCl, cluster around 1.08 to 1.28 eV, with the largest spreads observed for Li_3N-Li_3N ($\sigma \approx 0.33$ eV) and Li_2S-Li_2S ($\sigma \approx 0.25$ eV). These results indicate that grain boundaries can act as major bottlenecks for ionic transport even when the parent phases themselves are not intrinsically poor conductors. The feature-importance analysis reinforces this interpretation: in the grain-boundary model, the saddle-point indicator has the largest structural importance score, followed by grain-boundary energy, grain-boundary type, DFT energy per atom, and CSL Σ.

Thus, unlike grain diffusion, grain-boundary transport depends explicitly on interfacial stability and crystallographic matching, not merely on bulk material identity.

Another important outcome of this study is that lower-energy and lower-complexity interfaces tend to support more favorable Li-ion transport. The results indicate that lower CSL Σ boundaries are generally associated with lower migration barriers, whereas higher Σ interfaces tend to produce a more rugged barrier landscape. Similarly, lower-index grain-boundary planes tend to be more favorable, especially in the lithium halides. Among the important grain-boundary surfaces identified, $(\bar{1}11)$, (110), $(1\bar{1}2)$, $(0\bar{3}2)$, and (001) are also consistent with surfaces reported in experimentally observed stable SEI configurations in earlier studies. In addition, the present results show that heterogeneous interfaces are generally more resistive than homogeneous ones. This trend is especially significant for halide-carbonate combinations, for which the barrier distributions can exceed 1.50 eV, indicating that chemical mismatch across the interface can severely disrupt low-energy Li-ion pathways.

Despite the SEI design scope of the present framework, a few limitations of this model should be noted. First, the diffusion analysis is restricted to vacancy-mediated Li-ion transport, while other mechanisms such as interstitial and knock-off diffusion were not considered. Second, the study focuses only on crystalline inorganic SEI components and therefore does not capture the role of organic species, mixed inorganic-organic interfaces that are often present in SEI structures particularly found close to electrolyte. In addition, the calculations and model predictions are based on static DFT-NEB energetics and do not explicitly include temperature-dependent effects, dynamic structural disorder, or long-time interfacial evolution during electrochemical cycling. These factors should be incorporated in future work to extend the present structure-transport framework toward a more complete description of realistic SEI behavior.

Taken together, these results suggest a clear physical picture for SEI transport design. Fast and spatially uniform Li-ion conduction is most likely to arise in SEI morphologies enriched in halide and oxide grains with relatively low-barrier surfaces, while high fractions of Li_3N, Li_2CO_3, and energetically unfavorable heterogeneous interfaces are expected to increase transport heterogeneity. Since localized low-energy pathways can concentrate ionic flux and thereby promote nonuniform lithium deposition, the microstructural distribution of grains and grain boundaries is expected to be just as important as the SEI chemistry itself for suppressing dendrite nucleation and growth. In this sense, the present framework does not merely provide a predictive model for migration barriers; it establishes a quantitative structure-transport map for the inorganic SEI, showing that SEI performance should be engineered through control of phase selection, exposed surface orientation, grain-boundary character, and interface stability.

Chapter 6

MXene Integration in SEI: A Case Study

6.1 Motivation for MXene-Assisted SEI Engineering

Conventional SEI layers formed through spontaneous electrolyte decomposition are often structurally heterogeneous and mechanically fragile[34, 284]. Although inorganic-rich SEI components such as LiF, Li_2O, and Li_2CO_3 possess desirable properties including high mechanical strength and chemical stability, their ionic transport behavior strongly depends on the interfacial microstructure, grain boundaries, and defect distributions[12, 285, 286]. Further, many inorganic SEI phases exhibit nonuniform ionic diffusion pathways, leading to localized current hotspots that promote uneven lithium deposition on electrode surface[78, 287]. Such Lithium depositions eventually gives needle-like Lithium metallic structures, often referred as dendrites which then triggers internal short-circuit in battery pack[288]. Therefore, designing SEI architectures capable of simultaneously improving ionic conductivity, mechanical stability, and interfacial homogeneity has become a critical research objective in next-generation high-energy density battery systems particularly with Lithium metal electrodes.

In recent years, artificial SEI engineering has emerged as an effective strategy to sta-

bilize lithium-metal interfaces by introducing externally designed interfacial layers with controlled physicochemical properties[289, 290]. However, many existing artificial SEI materials suffer from limitations such as poor ionic conductivity, insufficient flexibility, weak interfacial adhesion, or inadequate accommodation of volumetric fluctuations during cycling[291]. Consequently, there remains a strong need for multifunctional interfacial materials that can provide stable ion transport properties while mechanically reinforcing the electrode surface.

MXenes have emerged as a promising candidates for such interfacial engineering applications due to their unique combination of metallic conductivity, tunable surface chemistry, layered morphology, and mechanical robustness. The two-dimensional (2-D) structure of MXenes provides large interfacial contact area and continuous ion diffusion pathways, while their surface functional groups such as $-O$, $-OH$, and $-F$ can strongly influence lithium adsorption and SEI chemistry[292, 293]. In particular, earlier studies suggests that fluorine-terminated MXenes may facilitate the formation of LiF-rich interphases, which are known to possess high interfacial stability and strong dendrite suppression capability[285, 294]. Additionally, the high mechanical flexibility of MXene nanosheets enables them to accommodate repeated interfacial deformation during lithium plating and stripping, thereby reducing crack formation and SEI failure.

Another major motivation for integrating MXenes into SEI architectures arises from their ability to regulate lithium nucleation behavior. Uneven lithium nucleation is often initiated by localized current density fluctuations and energetically favorable Lithium deposition sites. Due to their conductive and lithiophilic surfaces, MXenes can homogenize local electric fields and distribute Li-ion flux more uniformly across the electrode surface[295, 296]. Such behavior can potentially reduce the formation of isolated lithium protrusions that evolve into dendrites during long-term cycling. Also, the interlayer galleries within MXenes may serve as low-energy Li-ion transport

channels, improving interfacial ionic diffusion kinetics which directly results higher Lithium intercalation[297, 298].

From a computational perspective, MXenes also provide an ideal material category for systematic high-throughput screening and atomistic modeling. Their compositional diversity, tunable surface terminations, and structural versatility enable extensive exploration of structure-property relationships relevant to electrochemical interfaces. Parameters such as adsorption energy, work function, electronic conductivity, interfacial binding strength, and Li-ion migration barriers can be systematically evaluated using DFT calculations[299, 300]. Such computational approaches provide valuable mechanistic insights into how MXene chemistry and surface morphology influence SEI stability and ionic transport behavior at the atomic scale.

Therefore, the motivation of the present work is to investigate MXene-assisted SEI engineering as a pathway toward achieving mechanically stable, ionic conductive, and dendrite-resistant interfacial architectures for lithium-metal batteries. Although several isolated studies have explored the incorporation of specific MXene systems into artificial SEI architectures, a collective high-throughput investigation encompassing a broad spectrum of MXene compositions, surface terminations, and structural configurations for identifying optimal MXene integration within the SEI has not yet been systematically conducted[301]. In view of this, by combining high-throughput computational screening with detailed atomistic diffusion analysis, this study aims to identify optimal MXene structures capable of enhancing interfacial stability of Lithium electrode and facilitating uniform Li-ion transport through inorganic sublayer of SEI associated with Lithium electrode. The choice of selecting Lithium electrode for this study is due to its importance as a promising high-energy density electrode while suffering with the dendrite formation on cycling.

The proposed case study models the electrode–electrolyte interphase as a two-

dimensional MXene layer deposited onto a lithium-metal electrode surface, where subsequent electrochemical cycling results in the formation of an SEI layer. This MXene-assisted interfacial architecture is designed to serve as a mechanically robust and electrochemically favorable intermediate layer between the lithium metal electrode and the dynamically evolving SEI, thereby promoting interfacial stability and more uniform Li-ion transport.

6.2 Literature Review: MXenes as an Auxiliary Layer for SEI

The development of lithium-metal batteries has increasingly focused on engineering stable electrode–electrolyte interfaces capable of suppressing dendrite growth while maintaining efficient Li-ion transport. Among the emerging interfacial materials, MXenes have attracted considerable attention due to their metallic conductivity, tunable surface chemistry, mechanical flexibility, and layered two-dimensional structure. MXenes are generally represented by the formula $M_{n+1}X_nT_x$, where M corresponds to an early transition metal, X represents carbon and/or nitrogen, and T_x denotes surface terminations such as $-$O, $-$OH, and $-$F[292, 293]. These surface functionalities, combined with high electronic conductivity and structural tunability, make MXenes highly suitable for interfacial engineering in advanced battery systems. Experimental and theoretical studies have shown that MXenes can act not only as conductive substrates, but also as artificial SEI layers, lithiophilic hosts, and mechanically robust interlayers that regulate lithium deposition behavior[295, 296].

Recent experimental investigations have demonstrated that MXene-based coatings can significantly improve the stability of lithium deposition by homogenizing ion flux and suppressing dendritic growth[302]. In particular, Ti-based MXenes such

as $Ti_3C_2T_x$ have shown strong lithiophilic behavior owing to their surface functional groups and metallic nature[297]. The layered morphology of MXenes enables uniform distribution of local current density across the electrode surface, thereby minimizing localized lithium accumulation that typically initiates dendrite nucleation[287, 290]. Furthermore, the high mechanical strength and flexibility of MXene nanosheets allow them to accommodate repeated volume fluctuations during lithium plating and stripping, reducing interfacial fracture and SEI instability.

Several studies have further shown that MXenes contribute directly to the formation of stable inorganic-rich SEI layers[294, 296]. For example, surface terminations containing fluorine and oxygen facilitate the generation of LiF-rich interphases, which are widely recognized for their high mechanical modulus and chemical stability. LiF-rich SEI structures are particularly effective in suppressing dendrite penetration because they combine electronic insulation with sufficient Li-ion conductivity[285]. Experimental reports on MXene-modified lithium electrodes have revealed reduced nucleation overpotentials, smoother lithium morphology, and improved cycling stability even under high current density conditions[295, 296]. Additionally, hybrid artificial SEI structures composed of MXenes and secondary materials such as boron nitride, graphene derivatives, or polymeric coatings have demonstrated synergistic effects in simultaneously improving mechanical robustness and ionic transport pathways.

The unique layered structure of MXenes also plays a significant role in facilitating ion transport across interfaces. Unlike dense insulating coatings, MXenes possess open interlayer galleries that can provide low-energy Li-ion migration channels[297, 298]. Previous electrochemical studies have shown that expanded MXene interlayer spacing improves ion accessibility and enhances ionic diffusion kinetics. Moreover, the metallic conductivity of MXenes enables rapid electron transport while maintaining intimate interfacial contact with the lithium substrate[297, 303]. This combination of ionic

and electronic transport properties makes MXenes promising candidates for designing multifunctional artificial interphases that simultaneously regulate charge transfer, ionic conduction, and mechanical stability.

Beyond lithium-metal systems, MXenes have also been extensively investigated in sodium-ion and potassium-ion batteries, where severe volume expansion and unstable interfacial behavior present similar challenges[304]. In these systems, MXene frameworks have been shown to stabilize electrode architectures by constructing interconnected conductive networks capable of accommodating large structural deformation. For example, $Ti_3C_2T_x$-bonded hard carbon electrodes demonstrated significantly improved cycling stability and rate capability because the MXene network effectively buffered volume expansion and maintained structural integrity during repeated ion insertion and extraction[305]. The studies further revealed that MXene layers prevent particle pulverization, enhance charge transfer, and create continuous ion diffusion pathways through their open porous morphology.

The multifunctional role of MXenes observed in alkali-ion battery systems provides a strong scientific basis for their integration into SEI engineering strategies for lithium-metal batteries. In particular, the ability of MXenes to simultaneously act as conductive scaffolds, mechanical stabilizers, ion-transport mediators, and chemically active interfacial layers suggests that they can serve as ideal substrates for controlled SEI formation. Furthermore, the large compositional diversity of MXenes, including variations in transition metal species, carbon/nitrogen chemistry, surface terminations, and stacking configurations, offers a broad design space for tailoring interfacial properties. Recent high-throughput computational databases containing thousands of MXene structures have further accelerated this field by enabling systematic screening of electronic, structural, and surface characteristics relevant to electrochemical applications[306, 307].

Motivated by these developments, the present study investigates MXene-integrated SEI architectures through a combined high-throughput computational and atomistic modeling framework. The study focuses on identifying MXene candidates that exhibit strong interfacial stability with lithium metal, suitable electronic and mechanical compatibility with inorganic SEI components, and favorable Li-ion migration pathways across the MXene–SEI interface. By combining adsorption energy calculations, electronic structure analysis, and nudged elastic band calculations for interfacial Li-ion transport, this work aims to establish fundamental design logics for MXene-assisted SEI engineering in lithium-metal batteries.

6.3 MXene Database and Candidate Selection

The MXene structures investigated in this study were selected from the MXgap database, a machine-learning-oriented repository developed for predicting the electronic properties of MXene materials. The database originates from the work titled *MXgap: A MXene Learning Tool for Bandgap Prediction* developed by Diego Ontiveros, Sergi Vela, Francesc Vines, and Carme Sousa[308]. The dataset was constructed based on large-scale DFT screening studies reported in *Energy & Environmental Materials* (2024) and *Journal of Materials Chemistry A* (2023), where more than 4,000 MXene structures were systematically evaluated for their structural and electronic properties[309].

The MXgap dataset contains extensive information related to elemental composition, structural descriptors, density of states (DOS) features, and hybrid-functional bandgap values for a broad range of MXene systems. The MXene structures follow the general chemical formula $M_{n+1}X_nT_x$, where the transition metal component M includes Sc, Y, Ti, Zr, Hf, V, Nb, Ta, Cr, Mo, and W, while X represents either carbon or nitrogen[292, 309]. The surface termination groups T_x include various functional

species such as F, Cl, Br, I, O, S, Se, Te, H, OH, and NH, with layer thicknesses corresponding to $n = 1, 2, 3$. Additionally, multiple structural configurations and stacking arrangements were considered for each MXene system, allowing systematic evaluation of their electronic behavior. An overview of such MXene phases considered for high-throughput screening is illustrated in FIG.

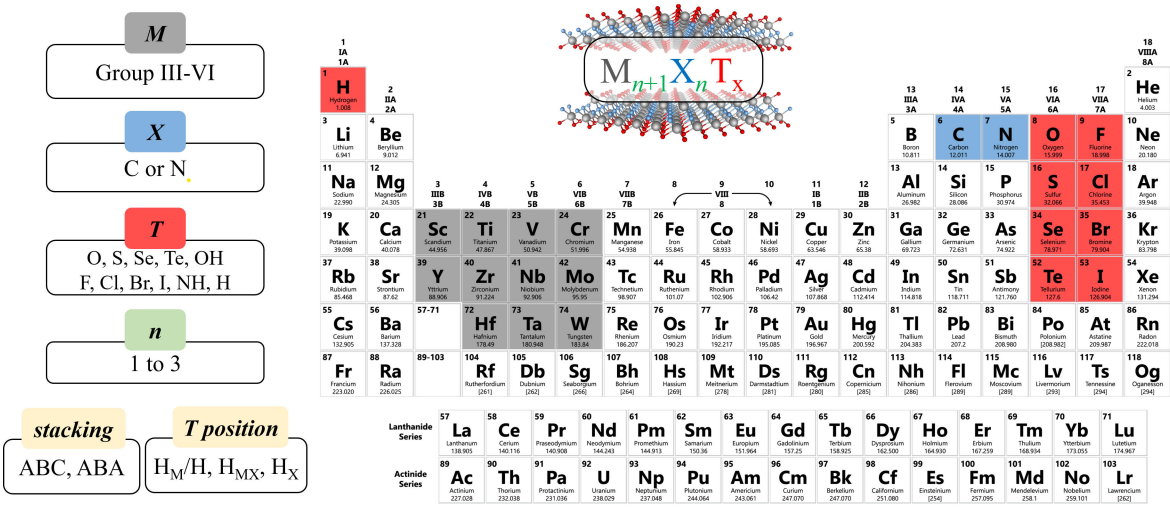


Figure 6.1: MXene phases considered for high-throughput screening for for integrating into SEI. Total of 4356 different MXene structures. In the figure M stands for transition metals, X for carbides/nitrides, T for surface terminations, and n is number of the layers in MXene phase. This structure database refereed from MXgap dataset developed by Ontiveros et al. [308]

The original database was generated through comprehensive first-principles calculations performed using DFT within the VASP package. The calculations employed projector augmented wave (PAW) pseudopotentials and plane-wave basis sets, while both generalized gradient approximation (PBE) and hybrid-functional (PBE0) approaches were used to accurately determine the electronic structures and bandgaps of the MXenes. Structural optimization, stacking stability, surface termination effects, and electronic density of states were systematically analyzed across the large compositional space of MXenes[310, 311].

In the present work, the MXgap database served as the primary source for identifying candidate MXene structures relevant for SEI engineering and interfacial stabilization studies. Since the objective of this study focuses on improving Li-ion transport and interfacial stability within inorganic SEI systems, candidate MXenes were selected based on several important criteria including structural stability, surface chemistry, electronic conductivity, and suitability for Li-ion interaction. Particular emphasis was given to terminated MXenes possessing chemically active surface groups, as these terminations strongly influence lithium adsorption behavior, interfacial charge transfer, and the formation of stable SEI phases.

Among the available MXene families, fluorine- and oxygen-terminated systems were considered especially relevant because of their potential role in promoting LiF-rich and inorganic-rich interphases, which are known to enhance SEI mechanical strength and suppress dendrite growth[299, 309]. Furthermore, transition-metal carbides and nitrides with stable layered structures and favorable electronic properties were prioritized for subsequent atomistic simulations and diffusion analysis. The large compositional diversity available within the MXgap dataset enabled efficient screening of multiple MXene chemistry and surface terminations prior to detailed first-principles investigations. In addition to the primary MXene dataset, the database also contains a separate collection of lanthanide-based MXenes that were excluded from the original machine-learning training process and instead used as unseen systems for validating predictive model performance.

6.4 High-Throughput Screening

6.4.1 MXene–Lithium Electrode: Adsorption Energy

To evaluate the interfacial stability between the selected MXene structures and the lithium-metal substrate, adsorption energy calculations were performed using slab-based DFT simulations. In this approach, optimized MXene monolayers were placed on top of low-index lithium metal surfaces to construct MXene–Li heterointerfaces, followed by full structural relaxation of the combined system. The adsorption energy was then calculated to quantify the thermodynamic affinity between the MXene coating and the lithium electrode. A strong negative adsorption energy indicates favorable interfacial interaction and suggests the formation of a mechanically stable 2-d layer on the lithium surface. On subsequent cycles, the SEI eventually then formed on this 2-D MXene layer.

The adsorption behavior plays a critical role in determining the effectiveness of MXenes as artificial SEI substrates. Weakly interacting interfaces may suffer from delamination during repeated lithium plating and stripping cycles, whereas excessively strong interactions may distort the MXene structure or adversely influence Li-ion transport across the interface. Therefore, an optimal MXene coating should exhibit sufficiently strong interfacial binding to maintain structural integrity while preserving favorable ionic transport characteristics.

The adsorption energy of the MXene–Li interface was calculated using:

$$E_{\text{ads}} = E_{\text{MXene/Li}} - E_{\text{Li}} - E_{\text{MXene}} \tag{6.1}$$

where $E_{MXene/Li}$ corresponds to the total energy of the fully relaxed MXene–Li heterostructure, E_{Li} represents the energy of the isolated lithium slab, and E_{MXene} is

the energy of the isolated MXene monolayer. Negative adsorption energies indicate energetically favorable adsorption and enhanced interfacial stability.

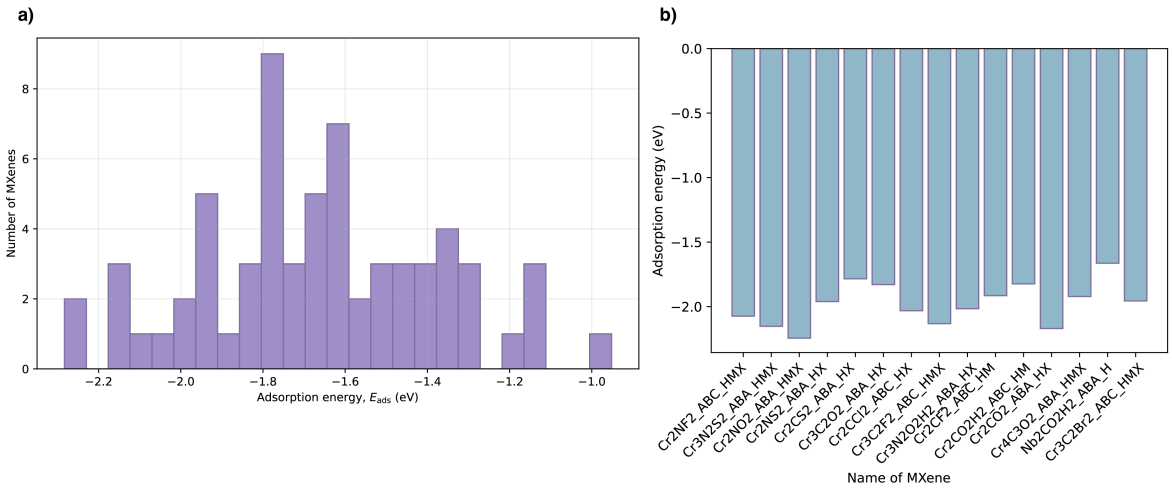


Figure 6.2: (a) Distribution of adsorption energies for Li–MXene heterostructures, showing adsorption energies ranging from −1.3 to −2.0 eV. (b) Selected top-performing MXenes exhibiting the strongest interfacial binding with Li metal. Stacking orientation mentioned in MX phase's name as ABA and ABC with termination configurations as H, HM, and HMX.

During the structural optimization process, particular attention was given to interfacial lattice matching, lateral stacking registry, surface termination orientation, and equilibrium interlayer separation between the MXene coating and the lithium substrate. To account for different possible adsorption environments at the Li–MXene interface, multiple lateral configurations corresponding to top-site, bridge-site, and hollow-site registries were systematically generated by translating the MXene sheet along the in-plane lattice directions (a a and b) prior to relaxation. In addition, several initial interfacial separations of 2.0, 2.5, and 3.0 Å were considered to identify the energetically most favorable equilibrium interface geometry. The resulting adsorption energies were subsequently used as an initial screening parameter for identifying MXene candidates capable of forming stable and mechanically robust interfaces with lithium metal. An overview of range of adsorption energy of such systems is shown in Figure 6.2

(a). Among the simulated systems, the MXene namely Cr_2NO_2 with ABA stacking observed to have strongest adsorption energy of -2.24 eV. The next highest MXene systems that shows stronger adsorption energies can be seen in Figure 6.2 (b).

6.4.2 Mechanical Property Screening

In addition to interfacial adsorption stability, the mechanical robustness of MXene coatings was evaluated through in-plane elastic stiffness and structural strain analysis. Since lithium dendrite propagation is strongly influenced by the local mechanical response of interfacial layers, mechanically stiff MXenes are expected to provide improved resistance against dendrite penetration and interfacial deformation during repeated plating and stripping cycles. Therefore, the elastic response of isolated MXene monolayers was considered as an important screening criterion for identifying mechanically stable interfacial coatings.

The in-plane elastic stiffness of MXenes was evaluated using the elastic tensor components C_{11} and C_{22}, which describe the resistance of the material against uniaxial deformation along the principal in-plane crystallographic directions. These elastic constants were obtained from strain–stress calculations using DFT by applying small lattice deformations to the optimized MXene structures. Higher values of C_{11} and C_{22} indicate greater mechanical rigidity and enhanced resistance toward structural deformation under electrochemical cycling conditions.

For two-dimensional MXene systems, the in-plane stiffness tensor can be expressed as:

$$C_{ij} = \frac{1}{A_0} \frac{\partial^2 E}{\partial \epsilon_i \partial \epsilon_j} \tag{6.2}$$

where A_0 represents the equilibrium surface area of the MXene monolayer, E is the

total energy of the strained structure, and ϵ_i corresponds to the applied in-plane strain component. In the present work, particular attention was given to the principal stiffness components C_{11} and C_{22} (due to the 2-D nature of MX-phases) for comparing the relative mechanical stability of different MXene candidates. The calculated in-plane elastic stiffness components, C_{11} and C_{22}, for the highest-reported MXene candidates are summarized in Figure 6.3. The calculated elastic stiffness heatmap indicates that several oxygen- and fluorine-terminated chromium-based MXenes exhibit exceptionally high in-plane stiffness, with C_{11} and C_{22} values approaching $\sim 290\ \mathrm{N\,m^{-1}}$. In particular, Cr_2CO_2 and Cr_2CF_2-based systems demonstrate the highest mechanical rigidity, suggesting their strong potential to mechanically reinforce the Li–MXene interface.

Along with elastic stiffness, the structural strain induced after adsorption on lithium metal was also evaluated. Excessive deformation of the MXene layer after interface formation may lead to structural instability, loss of mechanical integrity, and disruption of Li-ion migration pathways. Therefore, the lattice strain generated during MXene–Li interface formation was calculated as $\epsilon_l = \frac{l-l_0}{l_0} \times 100$, where l_0 is the equilibrium lattice parameter of the isolated MXene and l corresponds to the lattice parameters a or b after interface formation with lithium metal. This study uses the average structural strain, defined as $\epsilon_{\mathrm{avg}} = \frac{\epsilon_a+\epsilon_b}{2}$, along the in-plane a and b directions. Lower structural strain indicates improved interfacial compatibility and reduced distortion of the MXene coating.

Figure 6.4 reveals a clear positive correlation between lattice mismatch and average structural strain, showing that geometrically mismatched interfaces undergo larger structural deformation during interface formation. Most energetically stable Li–MXene heterostructures are distributed within a moderate mismatch range of approximately 2–3.5%, where the associated structural strain remains below $\sim$ 2%. In contrast, interfaces with larger mismatch values ($> 4\%$) generally exhibit substantially higher

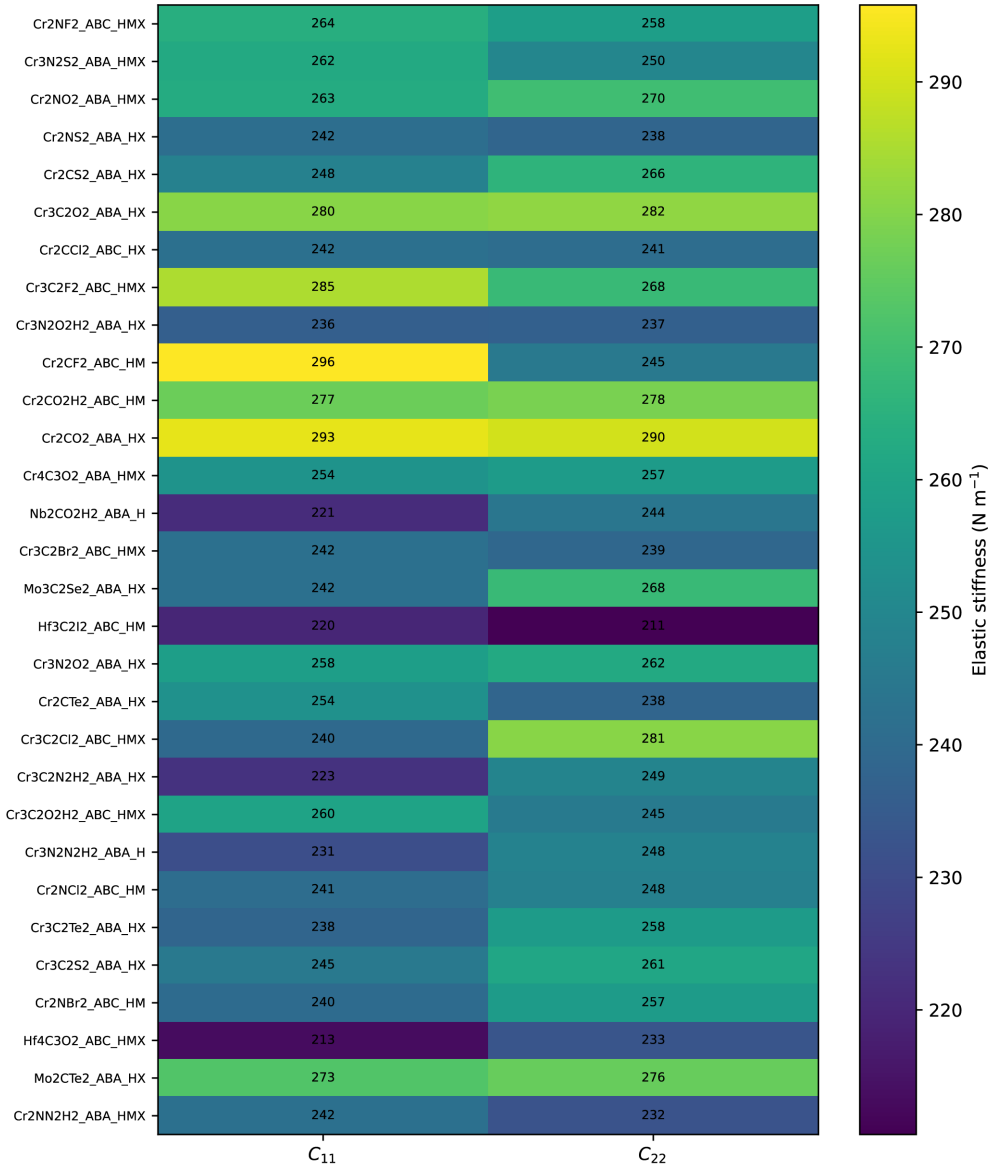


Figure 6.3: C_{11} and C_{22} of top 30 MXene phases along with their stacking orientation (ABA and ABC) and termination hollow-site configurations (H, HM, and HMX).

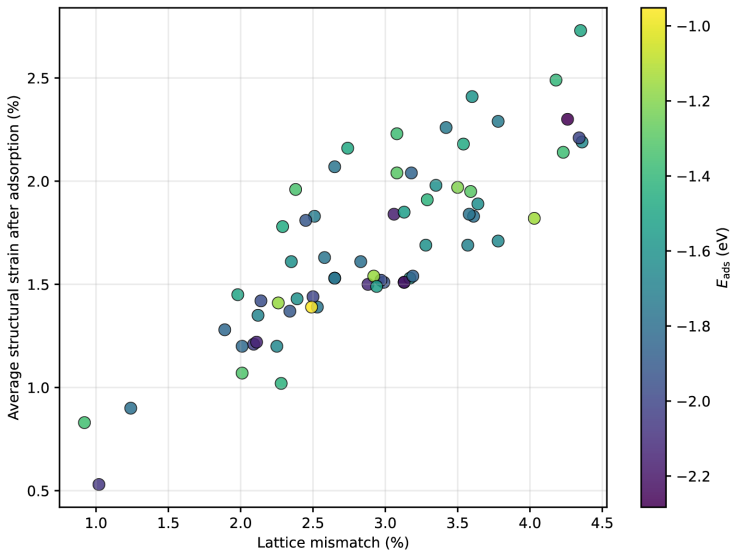


Figure 6.4: Scatter plot showing the relationship between lattice mismatch and average structural strain after MXene adsorption on Li metal. A positive correlation between the two descriptors is observed, indicating that larger lattice mismatch generally leads to increased interfacial distortion after adsorption. The color scale represents the adsorption energy of the corresponding Li–MXene heterostructures.

structural strain, indicating reduced interfacial compatibility and increased mechanical distortion. The adsorption-energy distribution further suggests that several strongly adsorbing MXenes maintain relatively low strain despite moderate lattice mismatch, indicating that favorable interfacial bonding can partially compensate for geometric incompatibility. Overall, the results indicate that achieving both low lattice mismatch and limited post-adsorption strain is essential for constructing mechanically stable and structurally coherent Li–MXene interfaces.

To further ensure stable interface formation, lattice mismatch between the MXene monolayer and lithium slab was systematically minimized during heterostructure construction. The lattice mismatch describes the geometric compatibility between the Li slab and MXene lattice. Since large mismatch values may introduce interfacial stress and structural instability, supercell combinations with the lowest mismatch were prioritized during the screening process. The lattice mismatch was evaluated using:

$$\delta = \frac{|a_{MXene} - a_{Li}|}{a_{Li}} \times 100 \tag{6.3}$$

where a_{MXene} and a_{Li} correspond to the in-plane lattice parameters of the MXene and lithium surface supercells, respectively. Interfaces exhibiting lower mismatch values were considered more favorable for stable heterointerface formation.

Together, the elastic stiffness, structural strain, and lattice mismatch descriptors provide insight into the mechanical suitability of MXenes as auxiliary layer for SEI. MXene coatings possessing high in-plane stiffness combined with low interfacial strain and small lattice mismatch are expected to maintain structural integrity during long-term electrochemical cycling and provide mechanically stable pathways for uniform lithium deposition.

6.4.3 Electronic Compatibility

The electronic compatibility of MXenes with lithium metal and inorganic SEI environments was evaluated using charge transfer analysis and intrinsic MXene bandgap characteristics. Since interfacial electronic structure strongly influences lithium nucleation behavior, charge redistribution, and electrochemical stability, these descriptors provide important insight into the suitability of MXenes as auxiliary layer for SEI engineering.

Charge transfer at the MXene–Li interface was investigated to quantify the redistribution of electronic density occurring after interface formation. The transfer of charge between lithium metal and the MXene surface directly affects interfacial bonding strength, lithiophilicity, and local electrostatic potential distribution[312].

The interfacial charge transfer was estimated using Bader charge analysis according to:

$$\Delta q = q_{\mathrm{MXene/Li}} - q_{\mathrm{MXene}} - q_{\mathrm{Li}} \tag{6.4}$$

where $q_{MXene/Li}$ corresponds to the total electronic charge of the combined heterointerface, while q_{MXene} and q_{Li} represent the charges associated with the isolated MXene and lithium slab, respectively. Positive and negative values of Δq indicate electron accumulation and depletion across the interface.

Figure 6.5 presents the distribution of interfacial charge transfer for MXenes with different surface terminations after adsorption on lithium metal. Among the investigated terminations, oxygen- and fluorine-functionalized MXenes exhibit the highest average charge transfer, indicating stronger electronic interaction and enhanced interfacial bonding with lithium metal. In contrast, hydrogen- and tellurium-terminated MXenes show comparatively lower charge redistribution, suggesting weaker electronic coupling at the interface. The relatively narrow distribution observed for oxygen-terminated MXenes further indicates consistent interfacial electronic behavior across different MXene compositions. The results suggests that surface termination chemistry strongly governs interfacial charge redistribution and plays a critical role in determining the electronic compatibility and stability of Li–MXene heterostructures.

In addition to interfacial charge redistribution, the intrinsic electronic properties of isolated MXenes were evaluated using bandgap data obtained from the MXgap database[313]. MXenes exhibiting moderate-to-low bandgaps were considered favorable for lithium-metal coating applications due to their limited electronic tunneling and improved interfacial charge redistribution characteristics[314–316]. Excessively conductive coatings may promote undesirable electron leakage toward the electrolyte and accelerate parasitic interfacial reactions.[20].

The bandgap values used in this study were obtained from hybrid-functional PBE0

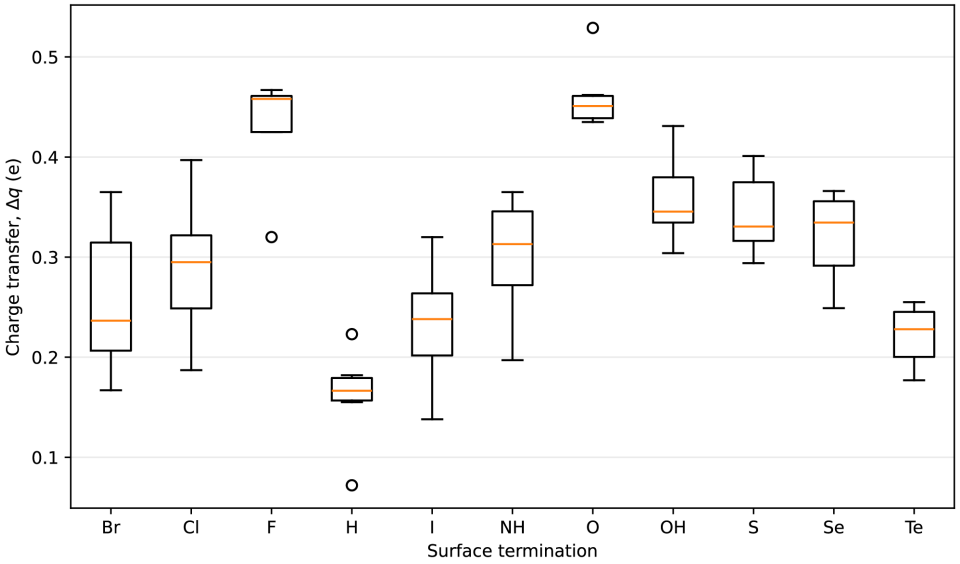


Figure 6.5: A comparative overview of charge transfer between MXene and Li-metal illustrated as box-plots. As expected, MXene with oxygen and fluorine surface terminations exhibits elevated charge transfer that point towards the comparatively better stability of adsorbed MXene.

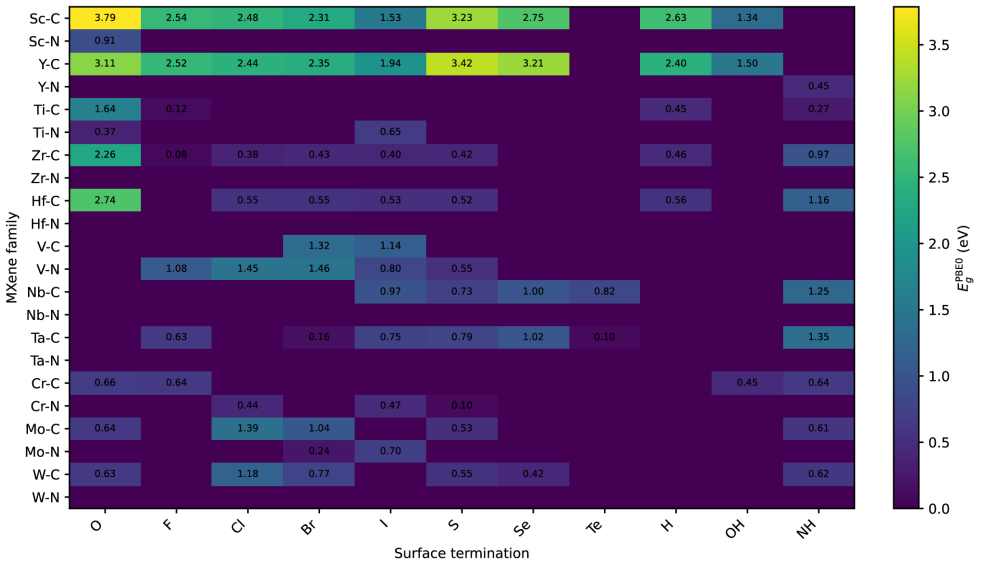


Figure 6.6: PBE0 bandgap distribution of the most stable MXene configurations with different transition metals, carbon/nitrogen compositions, and surface terminations. Numerical values correspond to the calculated PBE0 bandgap in eV, while cells marked as dark blue indicate metallic MXenes with negligible or zero bandgap. The results show that semiconducting behavior is more frequently observed in $n = 1$ MXenes, whereas increasing layer thickness generally promotes metallic character. Plots corresponding to $n = 2, 3$ are given in Figure C.18

calculations available within the MXgap dataset. Since the combined Li–MXene interface is expected to exhibit metallic behavior due to the presence of lithium metal, the intrinsic MXene bandgap was considered a more meaningful screening descriptor than the bandgap of the complete heterostructure.

Figure 6.6 presents the PBE0 bandgap distribution of stable MXene configurations with different transition-metal compositions and surface terminations. A strong dependence of electronic behavior on both transition-metal chemistry and surface functionalization can be observed. In particular, Sc- and Y-based MXenes exhibit comparatively large bandgaps, especially for oxygen-, sulfur-, and selenium-terminated surfaces, indicating pronounced semiconducting character. In contrast, several Ti-, Cr-, Mo-, and W-based MXenes remain metallic or possess very small bandgaps across most surface terminations. The results further show that oxygen-terminated carbides generally exhibit larger bandgaps relative to halide- or hydroxyl-functionalized systems, highlighting the significant role of surface chemistry in tuning the electronic structure. Overall, coexistence of metallic, semi-metallic, and semiconducting MXenes within the screened dataset provides substantial flexibility for tailoring interfacial electronic conductivity and charge redistribution behavior in artificial SEI applications.

6.4.4 Selection of MXene Candidates for MXene–SEI Interfaces

Following the high-throughput screening process, MXene candidates were ranked based on six primary descriptors: (i) adsorption energy, (ii) in-plane elastic stiffness (C_{11} and C_{22}), (iii) structural strain after adsorption, (iv) lattice mismatch with lithium metal, (v) interfacial charge transfer, and (vi) intrinsic MXene bandgap. The objective of this multi-parameter screening framework was to identify MXene coatings capable of

simultaneously providing strong interfacial adhesion, mechanical robustness, structural compatibility, and favorable electronic characteristics for lithium electrode.

MXenes exhibiting strongly negative adsorption energies, high in-plane stiffness, low interfacial strain, small lattice mismatch, and balanced charge redistribution were considered particularly suitable as a auxiliary layer between Li-metal electrode and SEI.

The top-performing MXene candidates identified through this screening procedure were subsequently employed for constructing MXene–SEI heterointerfaces involving major inorganic SEI components including LiX (X = F, Cl, Br, I), Li_2O, Li_2S, Li_2CO_3, and Li_3N. These interfaces were then used for atomistic Li-ion migration studies using CL-NEB calculations to investigate the role of MXene-assisted interfaces in regulating Li-ion transport across the SEI.

6.4.5 Screening Score

To systematically rank the large number of MXene candidates involved in the high-throughput screening workflow, a composite screening score was introduced by combining the key interfacial, mechanical, structural, and electronic descriptors into a single normalized metric. The screening score provides a convenient means of identifying MXene coating that simultaneously exhibit favorable adsorption stability, high mechanical stiffness, low interfacial strain, minimal lattice mismatch, balanced charge redistribution, and suitable electronic properties for lithium-metal interface stabilization. The score was calculated using a weighted combination of normalized descriptor functions according to:

$$S = w_1 f(E_{\text{ads}}) + w_2 f(C_{\text{avg}}) + w_3 f(\delta) + w_4 f(\epsilon_{\text{avg}}) + w_5 f(\Delta q) + w_6 f(E_g) \tag{6.5}$$

where E_{ads} is the adsorption energy, C_{avg} represents the average in-plane elastic stiffness, δ corresponds to the lattice mismatch, ϵ_{avg} denotes the average structural strain after adsorption, Δq is the interfacial charge transfer, and E_g is the intrinsic MXene bandgap. The functions $f(x)$ represent normalized forms of each descriptor, while w_i are weighting factors assigned according to the relative importance of the corresponding property toward interfacial stability and electrochemical performance. MXene candidates exhibiting higher screening scores were considered more suitable for subsequent MXene–SEI interface modeling and Li-ion migration barrier studies.

6.4.6 Score Analysis

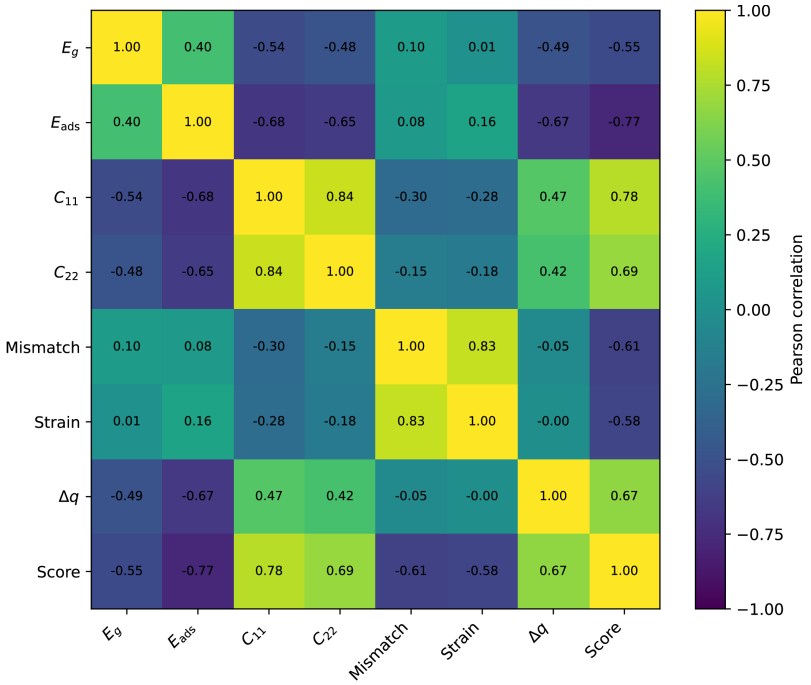


Figure 6.7: Pearson correlation coefficient between the normalized descriptors of Li-metal-MXene heterosystems.

The raw descriptors of Li-metal/MXene heterosystems are summarized in Table 6.1. Among the screened candidates, Cr-based MXenes dominate the top-ranked configurations, indicating their favorable balance between adsorption stability, mechanical

Table 6.1: Top Li–MXene candidates ranked using the composite screening score based on adsorption stability, mechanical stiffness, lattice compatibility, structural strain, and charge transfer characteristics.

MXene	$\mathbf{E_{ads}}$ (eV)	$\mathbf{C_{11}}$	$\mathbf{C_{22}}$	**Mismatch** (%)	**Strain** (%)	$\mathbf{\Delta q}$ (e^-)	**Score**
Cr2NF2(ABC) (HMX)	-2.074	264.0	258.2	1.02	0.53	0.425	0.887
Cr3N2S2(ABA) (HMX)	-2.153	262.2	249.8	2.11	1.22	0.388	0.817
Cr2NO2(ABA) (HMX)	-2.244	262.9	269.7	3.13	1.51	0.529	0.797
Cr2NS2(ABA) (HX)	-1.961	241.5	238.3	2.14	1.42	0.401	0.794
Cr2CS2(ABA) (HX)	-1.784	248.1	266.0	1.24	0.90	0.294	0.793
Cr3C2O2(ABA) (HX)	-1.829	280.5	281.6	1.89	1.28	0.437	0.793
Cr2CCl2(ABC) (HX)	-2.032	242.0	241.0	2.09	1.21	0.330	0.792
Cr3C2F2(ABC) (HMX)	-2.132	285.3	268.3	2.88	1.50	0.467	0.790
Cr3N2O2H2(ABA) (HX)	-2.016	236.3	236.7	2.50	1.44	0.431	0.790
Cr2CF2(ABC) (HM)	-1.915	295.8	245.2	2.34	1.37	0.461	0.786
Cr2CO2H2(ABC) (HM)	-1.824	276.8	278.5	2.01	1.20	0.346	0.772
Cr2CO2(ABA) (HX)	-2.170	292.8	290.0	3.06	1.84	0.458	0.765
Cr4C3O2(ABA) (HMX)	-1.922	254.2	257.3	2.45	1.81	0.435	0.762
Nb2CO2H2(ABA) (H)	-1.664	221.3	244.1	2.25	1.20	0.391	0.751
Cr3C2Br2(ABC) (HMX)	-1.956	241.9	239.1	2.97	1.52	0.365	0.743

robustness, and interfacial compatibility with lithium metal. In particular, fluorine- and oxygen-terminated Cr-based MXenes consistently exhibit strong adsorption energies in the range of approximately -1.9 to -2.2 eV, together with relatively high in-plane elastic constants exceeding 240 N/m in most cases. These results suggest that such interfaces can simultaneously provide strong Li affinity and sufficient mechanical rigidity to maintain structural stability during electrochemical cycling.

The highest-ranked candidate, Cr_2NF_2 with ABC stacking, achieved a composite screening score of 0.887, primarily due to its combination of strong adsorption energy, low lattice mismatch (1.02%), minimal structural strain (0.53%), and moderate charge redistribution. More generally, the top-performing MXenes tend to exhibit lattice mismatch values below $\approx 3\%$ and average structural strain below $\approx 1.8\%$, indicating good geometric compatibility with lithium metal. Oxygen-terminated MXenes, while often displaying comparatively larger charge transfer and stronger adsorption, also tend to induce slightly higher structural strain due to stronger interfacial interactions. In the meantime, sulfur- and chlorine-terminated systems generally maintain lower strain and mismatch values while still preserving favorable adsorption characteristics.

Another important observation from the table is that strong adsorption energy alone does not necessarily lead to the highest screening score. Instead, the composite ranking favors MXenes that achieve a balanced combination of adsorption stability, mechanical stiffness, low interfacial distortion, and moderate electronic interaction. This highlights the importance of considering multiple coupled descriptors simultaneously when designing MXene-assisted artificial SEI architectures for stable lithium-metal interfaces.

Figure 6.7 presents the Pearson correlation matrix between the major Li–MXene screening descriptors. A strong positive correlation is observed between C_{11} and C_{22} ($r = 0.84$), indicating that MXenes exhibiting high stiffness along one in-plane direction

generally maintain comparable mechanical rigidity along the other direction. Lattice mismatch and structural strain also show a strong positive correlation ($r = 0.83$), suggesting that larger lattice mismatch at the Li–MXene interface leads to increased structural distortion after adsorption. In contrast, adsorption energy exhibits a strong negative correlation with both C_{11} and C_{22}, implying that mechanically stiffer MXenes tend to form more stable and strongly bound interfaces with lithium metal. Charge transfer (Δq) shows moderate positive correlation with elastic stiffness and screening score, indicating that electronically active interfaces often coincide with mechanically strong MXene. The composite screening score is positively correlated with mechanical stiffness and charge transfer, while negatively correlated with lattice mismatch and structural strain, confirming that the most favorable Li–MXene interfaces are characterized by strong adsorption stability, low interfacial distortion, and enhanced mechanical strength.

Chapter 7

Conclusions and Future Directions

This thesis developed integrated computational and machine-learning frameworks for understanding and optimizing diffusion-controlled processes in energy-storage materials, with particular emphasis on Li-ion transport through the SEI. The work combines first-principles calculations, diffusion theory, data mining, feature engineering, and graph-based deep learning to address challenges associated with predicting atomic diffusion and engineering stable battery interfaces. The major contributions of the thesis can be summarized into three connected parts. First, a generalized machine-learning framework, named Machine Learned Diffusion Coefficient Estimator (ML-DiCE), was developed to predict diffusion coefficients in impure metallic and multi-component alloy systems. Second, a physics-informed graph neural network framework was established to model Li-ion migration in inorganic SEI components (considering its grains, and grain boundaries rich environment) using DFT-NEB data. Third, a design-oriented MXene case study was carried out to identify promising two-dimensional auxiliary layers for stabilizing Li-metal/SEI interfaces and regulating Li-ion flux. Together, these studies establish a computational foundation for accelerated diffusion modeling and provide design guidelines for engineering stable, fast ion-conducting, mechanically stable, and dendrite-resistant interfaces in lithium-based batteries.

7.1 Modeling Diffusion Coefficient

The first major contribution of this thesis is the development of the Machine Learned Diffusion Coefficient Estimator (ML-DiCE), a data-driven framework for predicting diffusion coefficients across different diffusion modes in impure metallic (IM) and multi-component alloy (MCA) systems. The framework was trained using experimentally reported diffusion data covering a broad range of diffusing elements, host media, compositions, temperatures, and diffusion environments. Five diffusion models were developed within this framework: impurity diffusion and self-diffusion in IM media, and self-diffusion, impurity diffusion, and chemical diffusion in MCA media. Separate featurization schemes were employed for the diffusing species and diffusion media using elemental descriptors, composition statistics, thermodynamic features, and temperature-dependent information. Random Forest (RF), Deep Neural Network (DNN), and Support Vector Regression (SVR) algorithms were systematically evaluated, with optimized models achieving prediction accuracies above 90% for several diffusion modes. These results demonstrate that ML-DiCE can serve as a generalized predictive framework for estimating diffusion coefficients in complex metallic systems, particularly conevnetional alloys.

A key outcome of the ML-DiCE study is that diffusion behavior can be learned directly from experimentally curated data without requiring explicit analytical formulations for every atomic transport process. The model captured nontrivial relationships between the diffusion coefficient, the intrinsic properties of the diffusing element, the chemical complexity of the diffusion medium, and the temperature of the diffusion process. In particular, the use of composition-aware descriptors significantly improved the prediction of diffusion in MCA systems, showing that the host environment plays a central role in determining diffusion kinetics. The model also revealed physically

meaningful feature dependencies. Descriptors such as atomic radius, atomic volume, electronegativity, number of unfilled orbitals, valence-orbital characteristics, ground-state volume, melting temperature, Mendeleev number, and temperature were found to influence diffusion predictions. These findings indicate that ML-DiCE is not only a predictive tool, but also a data-driven approach for identifying material descriptors that govern diffusion in alloy systems.

The broader significance of ML-DiCE lies in its ability to accelerate diffusion-informed materials design. Diffusion coefficients are critical parameters in heat treatment, phase transformation, microstructural evolution, oxidation, creep, coating design, and alloy development. However, experimental measurement of diffusion coefficients is often time-consuming, expensive, and difficult for multi-component systems. By enabling rapid estimation of diffusion coefficients from accessible physicochemical descriptors, ML-DiCE provides a useful screening tool for selecting diffusing species, optimizing alloy compositions, and guiding experiments or atomistic simulations. The framework developed in this part of the thesis also motivated the subsequent SEI-focused Li-ion diffusion modeling work, where diffusion prediction becomes even more challenging because of the complex chemistry, nanoscale morphology, and grain-boundary-rich nature of the inorganic SEI.

Despite its strong predictive capability, ML-DiCE has several limitations. The model performance is inherently dependent on the quality, diversity, and distribution of the available experimental data. Some diffusion modes and element groups remain underrepresented, which can introduce prediction bias toward more frequently occurring systems, particularly those dominated by transition-metal or d-block elements. In addition, the model is most reliable within the temperature, composition, and material domains represented in the training dataset, and its extrapolation to entirely unexplored systems should be treated with caution. Another important limitation is

that ML-DiCE primarily uses composition-level and elemental descriptors; therefore, it does not explicitly resolve atomistic migration pathways, defect energetics, local structural disorder, grain-boundary character, or diffusion-channel geometry. For this reason, ML-DiCE predictions should be interpreted alongside atomistic simulations, provided uncertainty estimates, and experimental validation when applied to new material systems.

7.2 SEI Design Insights

The second major contribution of this thesis is the development of a physics-informed graph neural network framework for modeling Li-ion transport in the inorganic SEI. A systematic diffusion dataset was generated using DFT-based climbing-image nudged elastic band (CI-NEB) calculations for eight major inorganic SEI components, namely LiF, LiCl, LiBr, LiI, Li_2O, Li_2S, Li_3N, and Li_2CO_3. Unlike earlier computational studies that focused mainly on a few representative SEI components such as LiF, Li_2O, and Li_2CO_3, this work considered a broader SEI chemistry and included both grain and grain-boundary diffusion environments. Representative low- and medium-energy exposed surfaces, homogeneous grain boundaries, and heterogeneous interfaces were incorporated to construct a unified design space for Li-ion migration in inorganic SEI systems.

To learn from this diffusion dataset, a path-aware graph variational autoencoder was employed to encode latent representations of NEB migration trajectories. These learned embeddings were then integrated into graph neural network models to predict minimum-energy pathways and migration barriers. The combined GVAE–GNN framework achieved strong predictive performance, with test-set R^2 values of 0.93 and 0.94 for grain and grain-boundary diffusion, respectively. This result demonstrates that

graph-based learning can effectively capture the structural and chemical complexity of SEI diffusion environments. More importantly, the use of graph representations allowed the model to incorporate atomic connectivity, local coordination, crystallographic orientation, and interfacial structure, which are difficult to represent using conventional fixed-vector descriptors alone.

The SEI-GNN study revealed several important structure–transport relationships. Halide-rich systems, particularly those containing LiCl, LiBr, and LiI, generally exhibited narrower and lower migration-barrier distributions, suggesting comparatively more uniform Li-ion transport characteristics. In contrast, Li_3N, Li_2CO_3, and structurally mismatched heterogeneous grain boundaries showed broader and higher-barrier transport landscapes. These trends indicate that SEI chemistry alone is not sufficient to determine ionic transport behavior. Instead, Li-ion migration is jointly governed by chemical composition, exposed surface orientation, grain-boundary structure, saddle-point environment, local coordination geometry, and grain-boundary energetics. The feature-importance analysis further showed that structural descriptors become especially important for grain-boundary diffusion, where localized interfacial disorder and saddle-point configurations strongly affect the migration barrier.

These findings provide direct insight into SEI design. A stable SEI should not merely contain ionically conductive phases; it should also promote spatially homogeneous Li-ion flux across grains and grain boundaries. If low-energy diffusion pathways are concentrated only in localized regions of the SEI, Li ions may preferentially migrate through these channels, creating nonuniform current distribution at the electrode surface. Such localized transport can promote uneven Li deposition, dendrite nucleation, and progressive interfacial instability. Therefore, engineering SEI microstructures with distributed low-barrier pathways, stable grain boundaries, and reduced interfacial mismatch is essential for achieving uniform lithium plating and long-term cycling stability.

The GVAE–GNN framework developed in this thesis provides a computational route to evaluate such structure–transport relationships before carrying out expensive large-scale atomistic simulations or experimental screening.

The third major contribution of this thesis is the MXene-assisted SEI case study, which explored two-dimensional MXene materials as potential auxiliary layers for stabilizing Li-metal/SEI interfaces. A high-throughput screening strategy was used to evaluate MXene candidates based on multiple descriptors, including Li–MXene adsorption energy, in-plane mechanical stiffness, lattice mismatch, structural strain, charge transfer, and electronic compatibility. This multi-criteria design approach was motivated by the fact that an effective interfacial modifier should simultaneously provide strong adhesion to Li metal, mechanical integrity, favorable interfacial compatibility, controlled electronic behavior, and the ability to promote uniform Li-ion transport. The screening results showed that several Cr-based MXenes, particularly F- and O-terminated configurations, exhibit favorable adsorption energetics and stable interfacial characteristics. Among the top candidates, Cr_2NF_2 with ABC stacking showed especially promising behavior, combining strong Li adsorption, low lattice mismatch, low structural strain, and favorable charge-transfer characteristics. These results suggest that properly selected MXene layers can act as functional interfacial modifiers to regulate Li-ion flux, reduce interfacial distortion, and improve SEI stability on Li-metal electrodes.

Although the SEI-GNN and MXene studies provide useful design guidelines, several limitations remain. The current SEI diffusion dataset primarily considers crystalline inorganic SEI phases under relatively idealized structural conditions, whereas realistic SEIs often contain amorphous regions, organic decomposition products, mixed inorganic–organic domains, impurities, defects, and dynamically evolving interfaces. The DFT-NEB calculations were also limited by computational cost, which restricted

the number of possible components, surfaces, interfaces, and diffusion mechanisms that could be explored. In addition, the present SEI-GNN framework focuses mainly on vacancy-mediated Li-ion diffusion and does not explicitly include coupled electro-chemo-mechanical effects, electronic transport, electrolyte decomposition, space-charge effects, or cycling-induced structural evolution. Similarly, the MXene case study provides a screening-level assessment, but further calculations are required to evaluate complete MXene–SEI–Li heterostructures, long-term stability, and Li-ion transport across realistic coated interfaces.

7.3 Future Research Directions

Several important research directions emerge from this thesis. For generalized diffusion-coefficient modeling, future work should focus on expanding the ML-DiCE dataset toward more diverse chemistries, diffusion modes, temperature regimes, and under-represented element groups. Incorporating additional data from experiments, first-principles calculations, molecular dynamics simulations, and CALPHAD-informed diffusion databases could improve the coverage and transferability of the model. Future versions of ML-DiCE should also include more rigorous uncertainty quantification, active learning, and out-of-distribution detection so that model predictions can be accompanied by reliability estimates. Another useful direction is to combine composition-level descriptors with structure-sensitive descriptors, such as defect formation energies, migration barriers, local coordination environments, and grain-boundary features. Such integration would bridge the gap between rapid data-driven diffusion prediction and atomistic diffusion physics.

For SEI-focused Li-ion transport modeling, future studies should extend the present crystalline inorganic SEI dataset toward more realistic SEI environments. This includes

amorphous inorganic structures, mixed organic–inorganic interfaces, electrolyte-derived decomposition products, doped SEI phases, and finite-temperature structural fluctuations. Reactive force-field simulations, ab-initio molecular dynamics, and machine-learning interatomic potentials could be used to generate larger and more diverse datasets beyond the scale accessible to DFT-NEB alone. Active-learning strategies can also be used to automatically identify the most informative diffusion pathways and reduce the number of expensive first-principles calculations. In addition, future models should include multiple diffusion mechanisms, such as interstitial diffusion, knock-off mechanisms, concerted exchange, and coupled vacancy–interstitial processes, rather than focusing only on vacancy-mediated migration.

A particularly important direction is the multiscale coupling of atomistic diffusion models with continuum-level electrochemical, mechanical, and thermal simulations. Migration barriers and local diffusion heterogeneity obtained from DFT and GNN models can be passed into phase-field models, kinetic Monte Carlo simulations, or continuum transport models to study Li deposition morphology, dendrite nucleation, stress evolution, and heat generation during cycling. Such a multiscale framework would directly connect atomistic SEI structure to macroscopic battery performance and safety. Experimental characterization methods such as cryogenic transmission electron microscopy, X-ray photoelectron spectroscopy, electrochemical impedance spectroscopy, and operando spectroscopy can further be used to validate the predicted SEI compositions, transport trends, and interfacial stability.

For MXene-assisted SEI engineering, future work should move beyond descriptor-level screening toward explicit modeling of complete Li-metal/MXene/SEI heterostructures. NEB calculations across MXene–SEI and Li–MXene–SEI interfaces would help determine whether the selected MXene candidates truly promote uniform Li-ion transport. The electronic properties of MXene coatings should also be optimized carefully,

since an ideal auxiliary layer must balance interfacial stability with electronic passivation to avoid continuous electrolyte reduction (from parasitic redox reactions). Additional studies should evaluate the chemical stability of MXenes against electrolyte decomposition products, the mechanical response of MXene-coated Li surfaces during repeated plating and stripping, and the role of different surface terminations in controlling Li affinity. Experimental validation of the top-ranked MXene candidates would be an important step toward confirming their practical relevance as artificial SEI or interfacial-modifier layers.

Deep learning-based generative modeling of material structures represents an important future direction for designing SEI components that can withstand dendrite formation in high-energy-density lithium-based electrodes. Such approaches may also be useful for addressing other interfacial degradation mechanisms, including electrode volume expansion commonly observed in silicon-based anode materials. In this research, an initial attempt was made to generate new lithium salt structures with uniform Li^+ migration energy barriers within its grain structure. However, due to the limited availability of migration barrier data across a wide range of lithium-based salts, this approach could not be extended to produce physically meaningful or conclusive results.

The proposed strategy was to train a graph variational autoencoder using controlled perturbations in lattice parameters, atomic coordinates, and atom types. The goal was to allow the model to learn the structural and energy landscape of lithium salts associated with specific Li^+ migration pathways and migration energy barriers. With a sufficiently large and diverse dataset, this approach could become a powerful framework for capturing the energy landscape of Li^+ diffusion in complex SEI materials. In the future, such generative models could be used to design new SEI-forming compounds with more uniform ion-transport pathways, improved interfacial stability, and enhanced resistance to dendrite growth.

Overall, this thesis demonstrates that combining first-principles calculations with machine learning can significantly accelerate the understanding and design of diffusion-controlled materials processes. ML-DiCE provides a generalized framework for predicting diffusion coefficients in metallic systems, while the GVAE–GNN model establishes a structure-physics-aware approach for predicting Li-ion migration in complex SEI environments. The MXene case study further illustrates how these computational insights can be translated into interfacial design strategies for lithium-metal batteries. The methodologies and findings developed in this work provide a foundation for future efforts aimed at engineering stable SEI architectures with controlled ion transport, improved mechanical integrity, and enhanced electrochemical stability for next-generation energy-storage systems.

Appendix A

Computational Resources

Table A.1: Summary of computational resources utilized for NEB calculations carried out using CHPC, PSC, and NREL computational facilities.

Category	**NEB calculations**	**Components per calculation**	**CPU hours**
Grain diffusion	282	8	1,128,000
Homogeneous grain boundaries	638	8	2,552,000
Heterogeneous grain boundaries	104	8	416,000
Total	**1024**	**8192 total components**	**4,096,000**

Each NEB workflow consisted of one initial relaxation, two geometry optimizations, and a five-image NEB calculation, corresponding to eight computational components per diffusion pathway.

The computational workload summarized in Table A.1 was distributed across multiple national high-performance computing facilities, including the Center for High Performance Computing (CHPC), the Pittsburgh Supercomputing Center (PSC), and the National Renewable Energy Laboratory (NREL) computational facilities. In total, approximately 4.1 million CPU hours were utilized for density functional theory and nudged elastic band (NEB) simulations performed throughout this study.

The GPU-based computational workload summarized in Table A.2 was carried out using multiple high-performance GPU computing facilities. These included L40S GPU resources from the University of Oklahoma Supercomputing Center for Education and Research (OSCER), GPU resources supported by the U.S. Department of Energy's Office of Critical Minerals and Energy Innovation and located at the National Laboratory of the Rockies, and NVIDIA RTX 3090 GPU resources available through the

Table A.2: Summary of GPU computational resources utilized for machine learning model development, hyperparameter optimization, and graph-based diffusion coefficient prediction.

Category	**Number of tasks**	**GPU hardware**	**GPU hours**
GVAE pretraining	3	NVIDIA L40S / RTX 3090	18
GNN model training and tuning	36	NVIDIA L40S / RTX 3090	288
Final model training and testing	3	NVIDIA L40S / RTX 3090	24
Additional validation runs	–	NVIDIA L40S / RTX 3090	–
Total	**42+**	**Multiple GPU facilities**	**330+**

GPU resources were primarily used for graph variational autoencoder (GVAE) pretraining, graph neural network (GNN) model training, hyperparameter optimization, and final model validation. The reported GPU hours are approximate and were estimated based on the number of training runs and the wall time required per run.

CHPC at the University of Utah. These resources were used primarily for training graph-based machine learning models, including graph variational autoencoders and graph neural networks, as well as for hyperparameter optimization and model validation. Overall, these GPU resources enabled the efficient training of deep learning models for predicting diffusion-related material properties and supported the machine learning component of this study.

Appendix B

Database and Codes

The machine learning and graph neural network frameworks developed in this work are publicly available through GitHub repositories at `https://github.com/skvarjun/ML-DiCE` and `https://github.com/skvarjun/gnn-dice`. These repositories include the source codes, training workflows, and implementation details used throughout this study. In addition, the datasets generated and utilized for the machine learning models are hosted on the Hugging Face platform at `https://huggingface.co/datasets/skvarjun/SEI-NEB` and `https://huggingface.co/datasets/skvarjun/Li-metal-MXene-SEI` to support transparency, reproducibility, and future development by the research community.

Appendix C

Supplementary Figures and Tables

C.1 Elemental Diffusion Coefficient Prediction in Conventional Alloys Using Machine Learning

C.1.1 Model Feasibility

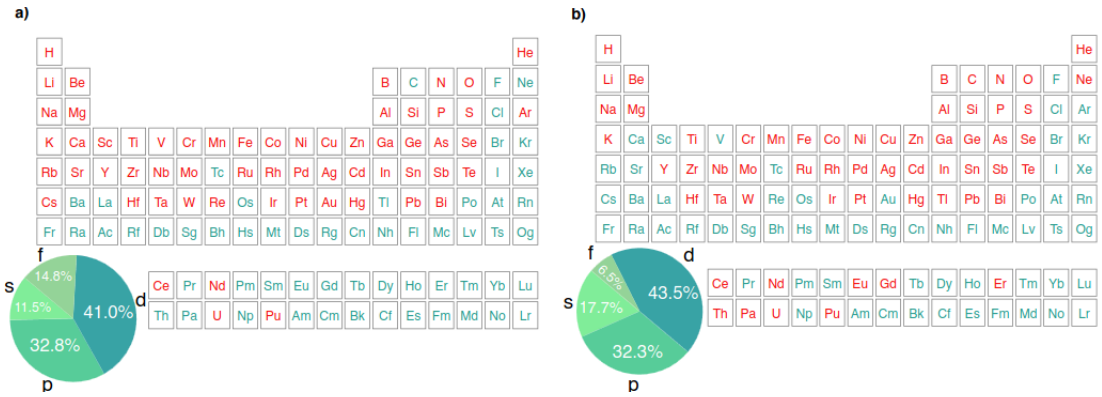


Figure C.1: Diffusing elements (highlighted in red color) and their cumulative percentage from each block (pie chart in the inset) of the periodic table for IM media a) and b) MCA media present in the data.

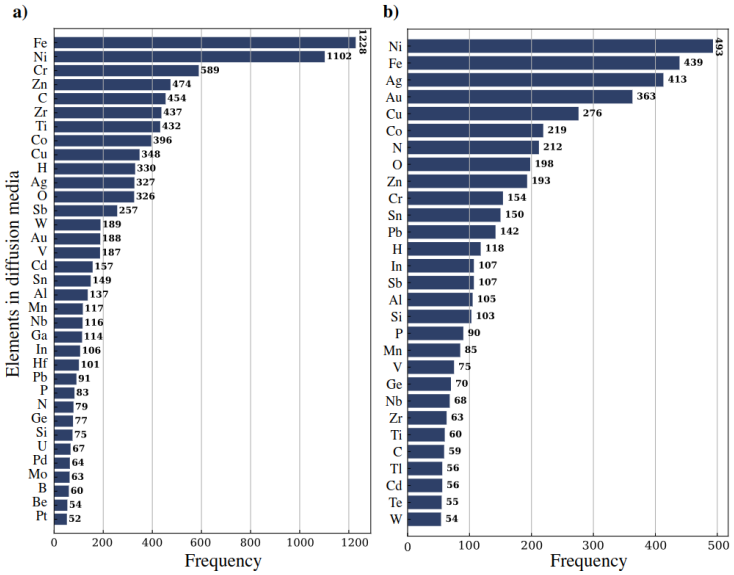


Figure C.2: Frequency of weighted percentage of elements present in the composition of a) IM media and b) MCA media present in the training data.

C.1.2 Data Preprocessing Steps

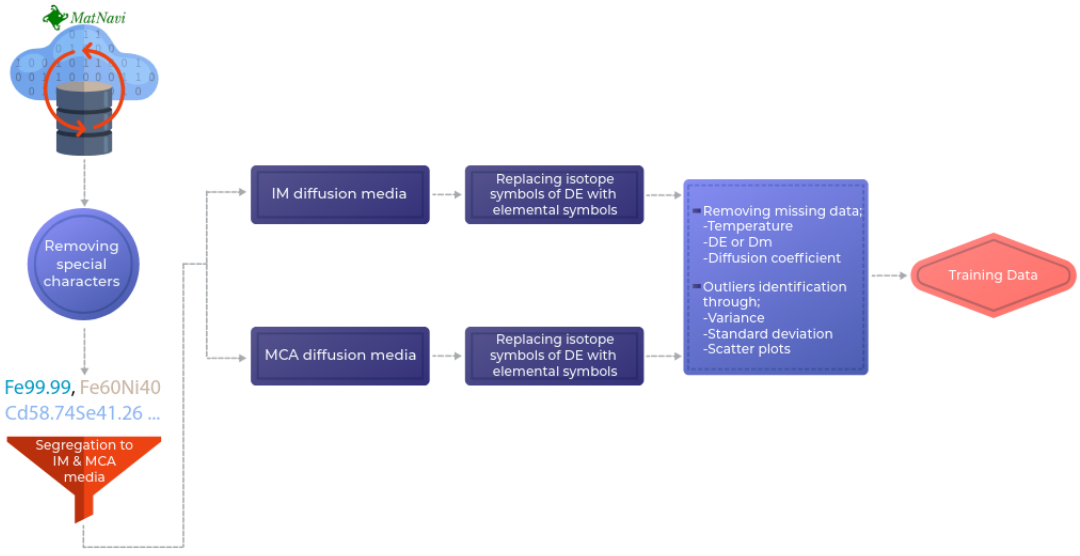


Figure C.3: Schematic diagram of material data proprocessing. The program used for preprocessing is available in GitHub repository, https://github.com/yanqingsu/ML-DiCE

C.1.3 Feature Information

Table C.1: Composition features along with the statistical operations considered for featurization of diffusing elements and diffusion media.

Feature	Statistical operations considered	Description
0-norm	0	Number of elements in composition
2-norm	2	Fractions of elements present
3-norm	3	Fractions of elements present
5-norm	5	Fractions of elements present
7-norm	7	Fractions of elements present
10-norm	10	Fractions of elements present
Number	Minimum, Maximum, Range, Mean, Average deviation, Mode	Atomic number
Mendeleev Number	Minimum, Maximum, Range, Mean, Average deviation, Mode	Ordering number listing the chemical elements column by column through the periodic system[317]
Atomic Weight	Minimum, Maximum, Range, Mean, Average deviation, Mode	Atomic weight in *amu*
Melting T	Minimum, Maximum, Range, Mean, Average deviation, Mode	Melting point in Kelvin
Column	Minimum, Maximum, Range, Mean, Average deviation, Mode	Column on periodic table
Row	Minimum, Maximum, Range, Mean, Average deviation, Mode	Row on periodic table
covalent Radius	Minimum, Maximum, Range, Mean, Average deviation, Mode	Single bond covalent radius
electronegativity	Minimum, Maximum, Range, Mean, Average deviation, Mode	Electronegativity scale proposed by Allen [318]
Ns Valence*	Minimum, Maximum, Range, Mean, Average deviation, Mode	Fraction of electrons from the s valence sub-shell between all present elements
Np Valence*	Minimum, Maximum, Range, Mean, Average deviation, Mode	Fraction of electrons from the p valence sub-shell between all present elements
Nd Valence*	Minimum, Maximum, Range, Mean, Average deviation, Mode	Fraction of electrons from the d valence sub-shell between all present elements
Nf Valence*	Minimum, Maximum, Range, Mean, Average deviation, Mode	Fraction of electrons from the f valence sub-shell between all present elements
N Valence	Minimum, Maximum, Range, Mean, Average deviation, Mode	Fraction of electrons from the valence shell between all present elements
Ns Unfilled*	Minimum, Maximum, Range, Mean, Average deviation, Mode	Fraction of unoccupied s sub-shell in all present elements
Np Unfilled*	Minimum, Maximum, Range, Mean, Average deviation, Mode	Fraction of unoccupied p sub-shell in all present elements
Nd Unfilled*	Minimum, Maximum, Range, Mean, Average deviation, Mode	Fraction of unoccupied d sub-shell in all present elements
GS volume	Minimum, Maximum, Range, Mean, Average deviation, Mode	Volume per atom in the ground state
GS bandgap	Minimum, Maximum, Range, Mean, Average deviation, Mode	Band gap of atom in the ground state
GS magnetic moment	Minimum, Maximum, Range, Mean, Average deviation, Mode	Magnetic moment per atom in the ground state

* Ref. Meredig et al. [319].

C.1.4 Standard Deviation of Target Variable and Temperature

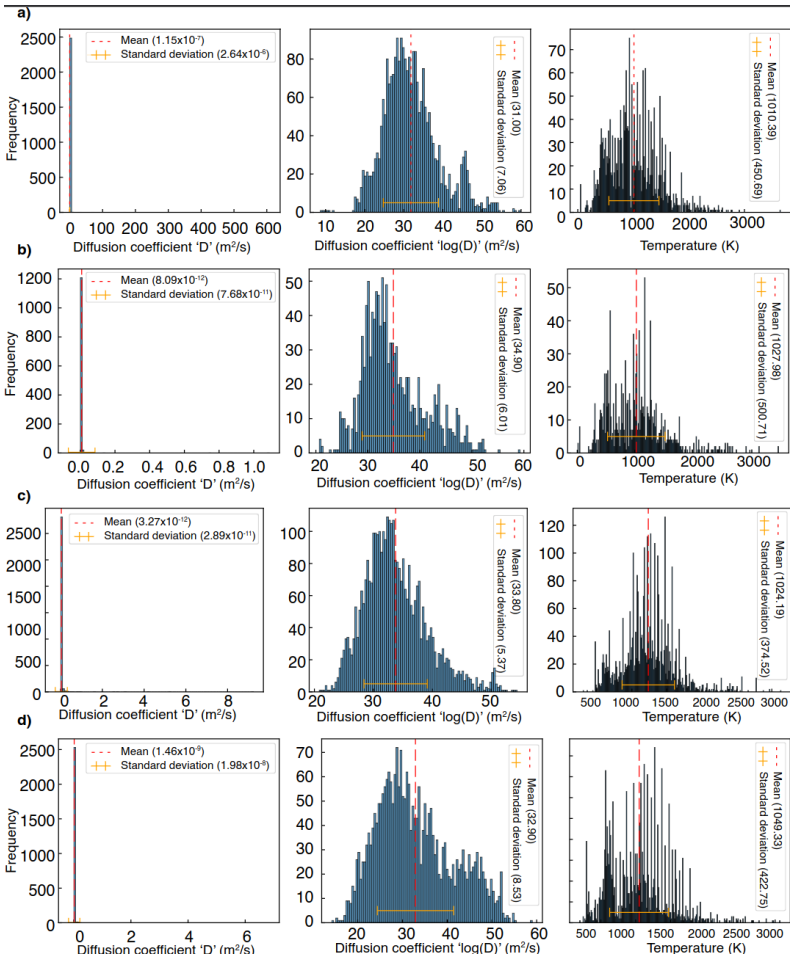


Figure C.4: In each graph set, the leftmost figure represents the standard deviation of the diffusion coefficient, the middle figure illustrates the standard deviation of the diffusion coefficient after taking the logarithm, and the rightmost figure displays the standard deviation of temperature. The data for a) impurity and b) self-diffusion modes in IM media, and impurity, self, and chemical diffusion in MCA media are represented by c), d), and e), respectively.

C.1.5 Uncertainty Analysis

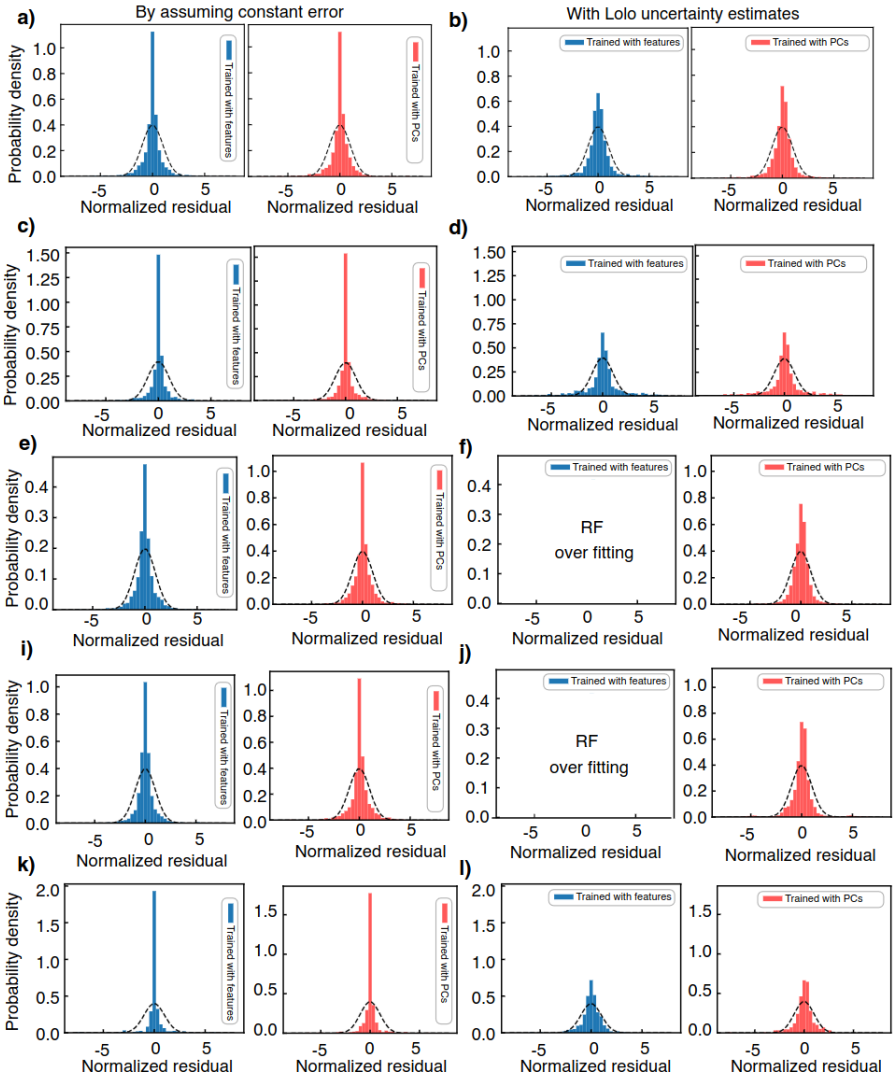


Figure C.5: Probability density distributions of normalized residuals, calculated through eight-fold cross-validation. Each graph set consists of two figures: on the left, it is assumed that all entries have constant error (out-of-bag errors), while on the right, the error distribution is depicted using *Lolo* uncertainty estimates calculated based on variability and correlation with inclusion of points in their randomly drawn training set. Graph sets a – d illustrate the uncertainty behavior of the impurity and self diffusion models in an IM media, while, graph sets c up to l present the uncertainty behavior of the self, impurity, and chemical diffusion in MCA media.

C.1.6 Correlation Analysis

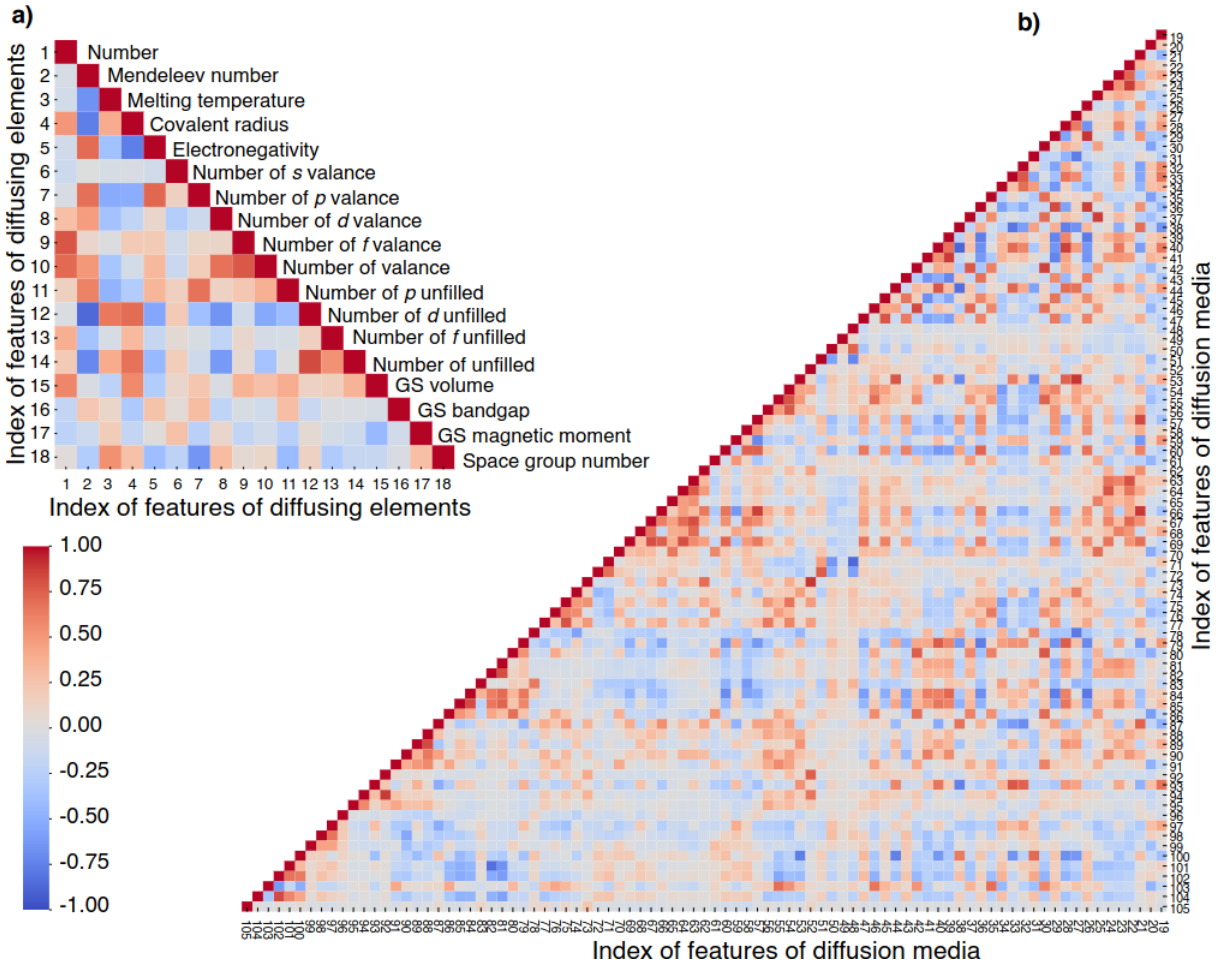


Figure C.6: Correlation values of features of a) diffusing elements and b) diffusion media for the model self diffusion in MCA media. Name of features of diffusion media with respective indices are given in Table C.2

Table C.2: Name of features of diffusion media along with their respective indices from the heatmap.

Index	Feature	Index	Feature	Index	Feature	Index	Feature
19	0-norm	41	Mean covalent radius	63	Max. number f valence	85	Range number unfilled
20	2-norm	42	Avg. dev. covalent radius	64	Mean number f valence	86	Avg. dev. number of Unfilled
21	Min. number	43	Min. electronegativity	65	Avg. dev. number f valence	87	Min. GS volume
22	Max. number	44	Max. electronegativity	66	Min. number Valence	88	Max. GS volume
23	Range number	45	Mean electronegativity	67	Max. number Valence	89	Range of GS volume
24	Mean number	46	Avg. dev. electronegativity	68	Range number Valence	90	Mean GS volume
25	Avg. dev. number	47	mode electronegativity	69	Mean number Valence	91	Avg. dev. GS volume
26	Min. Mendeleev number	48	Min. number s valence	70	Avg. dev. number Valence	92	Min. GS bandgap
27	Max. Mendeleev number	49	Max. number s valence	71	Max. number s unfilled	93	Max. GS bandgap
28	Range Mendeleev number	50	Mean number s valence	72	Avg. dev. number s unfilled	94	Mean GS bandgap
29	Mean Mendeleev number	51	Avg. dev. number s valence	73	Min. number p unfilled	95	Mode GS bandgap
30	Avg. dev. Mendeleev number	52	Min. number p valence	74	Max. number p unfilled	96	Min. GS magnetic moment
31	Min. melting temperature	53	Max. number p valence	75	Mean number p unfilled	97	Max. GS magnetic moment
32	Max. melting temperature	54	Mean number of p valence	76	Avg. dev. number p unfilled	98	Mean GS magnetic moment
33	Range melting temperature	55	Avg. dev. number p valence	77	Mode number p unfilled	99	Avg. dev. GS magnetic moment
34	Mean melting temperature	56	mode number p valence	78	Min. number d unfilled	100	Min. space group number
35	Avg. dev. melting temperature	57	Min. number d valence	79	Range number d unfilled	101	Max. space group number
36	Min. Column	58	Max. number d valence	80	Avg. dev. d unfilled	102	Mean space group number
37	Avg. dev. Row	59	Range number d valence	81	Max. number of f unfilled	103	Avg. dev. space group number
38	Min. covalent radius	60	Mean number d valence	82	Avg. dev. number of f unfilled	104	Mode space group number
39	Max. covalent radius	61	Avg. dev. number d valence	83	Min. number unfilled	105	Compound possible
40	Range covalent radius	62	Min. number f valence	84	Max. number unfilled		

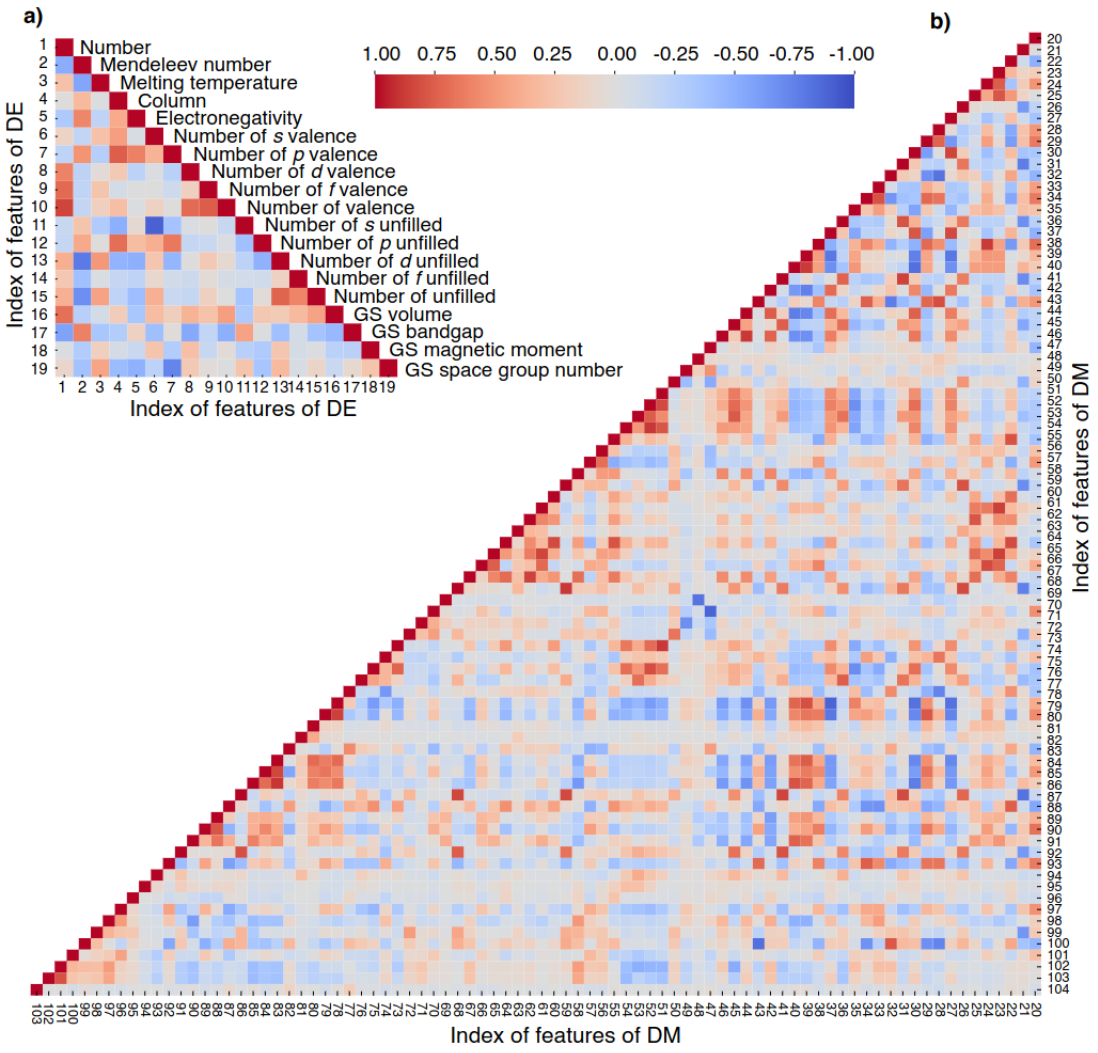


Figure C.7: Correlation values of features of a) diffusing elements and b) diffusion media for the model impurity diffusion in MCA media. Name of features with respective indices are given in Table C.3

Table C.3: Name of features of diffusion media along with their respective indices from the heatmap.

Index	Feature	Index	Feature	Index	Feature	Index	Feature
20	0-norm	40	Mean covalent radius	60	Min. number of f valence	80	Max. number of f unfilled
21	2-norm	41	Avg. dev. of covalent radius	61	Max. number of f valence	81	Avg. dev of number of f unfilled
22	Min. number	42	Min. electronegativity	62	Mean number of f valence	82	Min. number of unfilled
23	Max. number	43	Max. electronegativity	63	Avg. dev. of f valence	83	Max. number of unfilled
24	Range number	44	Mean electronegativity	64	Min. number of valence	84	Range number of unfilled
25	Mean number	45	Avg. dev of electronegativity	65	Max. number of valence	85	Mean number of unfilled
26	Avg. dev of number	46	Mode of electronegativity	66	Range number of valence	86	Avg. dev. of number of unfilled
27	Min. Mendeleev number	47	Min. number of s valence	67	Mean number of valence	87	Min. GS volume
28	Max. Mendeleev number	48	Max. number of s valence	68	Avg. dev. of number of valence	88	Max. GS volume
29	Range Mendeleev number	49	Mean number of s valence	69	Min. number of s unfilled	89	Range GS volume
30	Mean Mendeleev number	50	Avg. dev. of s valence	70	Max. number of s unfilled	90	Mean GS volume
31	Avg. dev. of Mendeleev number	51	Min. of p valence	71	Mean number of s unfilled	91	Avg. dev. GS volume
32	Min. Melting temperature	52	Mean number of p valence	72	Avg. dev. of number of s unfilled	92	Max. GS bandgap
33	Max. melting temperature	53	Avg. dev. of p valence	73	Min. number of p unfilled	93	Mean GS bandgap
34	Range of melting temperature	54	Mode number of p valence	74	Max. number of p unfilled	94	Mode GS bandgap
35	Mean of melting temperature	55	Min. number of d valence	75	Mean number of p unfilled	95	Min. GS magnetic moment
36	Avg. dev. of melting temperature	56	Max. number of d valence	76	Avg. dev. of number of p unfilled	96	Max. GS magnetic moment
37	Min. column	57	Range number of d valence	77	Min. number of d unfilled	97	Mean GS magnetic moment
38	Range of row	58	Mean number of d valence	78	Max. number of d unfilled	98	Avg. dev. GS magnetic moment
39	Max. covalent radius	59	Avg. dev. number of d valence	79	Range number of p unfilled	99	Min. space group number
						100	Max. of space group number
						101	Mean of space group number
						102	Mode of space group number
						103	Compound possible*

* Binary.

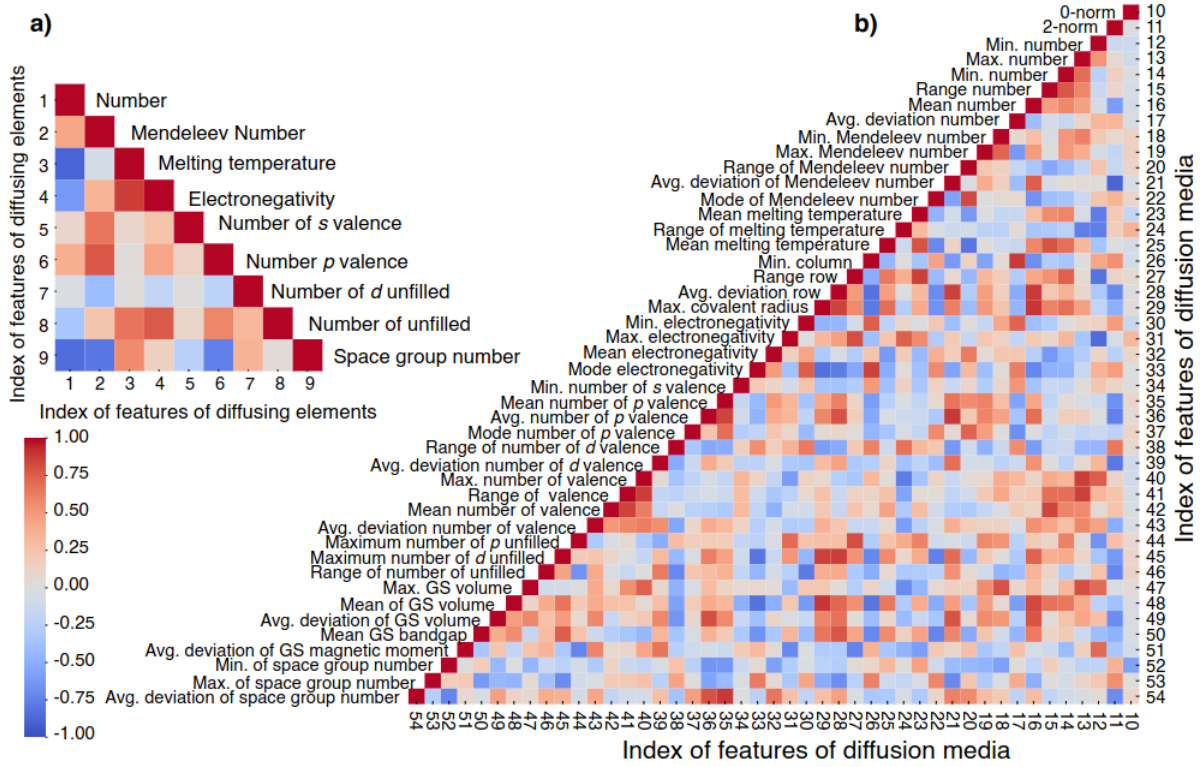


Figure C.8: Mutual correlation values of features of diffusing elements and diffusion media for the model impurity diffusion in MCA media.

C.2 Deep learning assisted modeling of Li-ion transport in SEI: A Graph neural network based study

C.2.1 SEI Components Considered for GNN Predictive Modeling

Table C.4: Optimized lattice parameters and DFT energy per atom of the SEI components considered in this study.

SEI component	Geometry	Lattice parameters ($\AA$)	Lattice angles (°)	DFT energy per atom (eV)
LiF		a=b=c=3.98	$\alpha = \beta = \gamma = 90$	-4.92
LiCl		a=b=c=5.15	$\alpha = \beta = \gamma = 90$	-3.68
LiBr		a=b=c=5.44	$\alpha = \beta = \gamma = 90$	-3.34
LiI		a=b=c=5.96	$\alpha = \beta = \gamma = 90$	-2.94
Li_2O		a=b=c=4.62	$\alpha = \beta = \gamma = 90$	-4.78
Li_2S		a=b=c=5.69	$\alpha = \beta = \gamma = 90$	-3.99
Li_3N		a=b=3.61,; c=3.85	$\alpha = \beta = 90, \gamma = 120$	-3.90
Li_2CO_3		a=8.38, b=5.01, c=6.29	$\alpha = \gamma = 90, \beta = 114.15$	-6.56

C.2.2 Construction of Heterogeneous Interfaces

Heterogeneous solid–solid interfaces were constructed using a coherent lattice-matching framework based on the Zur–McGill lattice-search (ZSL) algorithm, since classical Coincidence Site Lattice theory is applicable only to homophase grain boundaries. For a substrate (s) and film (f), coherent matching requires approximate commensurability between the in-plane lattice vectors, $m\mathbf{a}_f \approx n\mathbf{a}_s$, where $\mathbf{a}_f$ and $\mathbf{a}_s$ are the in-plane lattice vectors of the film and substrate, respectively, and m,n $\in \mathbf{Z}$. The lattice mismatch along a given in-plane direction is defined as $\epsilon = \frac{|\ell_f - \ell_s|}{\ell_s} \times 100\%$, where ℓ_f and ℓ_s are the magnitudes of the matched film and substrate vectors. Commensurate interface supercells were identified by finding integer transformation matrices $\mathbf{M}_f$ and $\mathbf{M}_s$ such that $\mathbf{A}_f\mathbf{M}_f \approx \mathbf{A}_s\mathbf{M}_s$, where $\mathbf{A}_f$ and $\mathbf{A}_s$ are the primitive in-plane lattice matrices of the film and substrate.

To ensure DFT-feasible interface models, the following constraints were imposed:

$$A = |\mathbf{a}_1 \times \mathbf{a}_2| < A_{\max}, \tag{C.1}$$

$$\text{with} \quad A_{\max} = 150\mathring{A}^2, \quad \epsilon_{\text{avg}} < 5\%, \quad \text{and} \quad |\theta_f - \theta_s| < 0.01 \text{ rad}. \tag{C.2}$$

These criteria were used to maintain manageable atom counts (< 200 atoms), moderate strain (typically 2–5%), and computational tractability.

After selecting the optimal lattice match, the film lattice was rotated and strained to match the substrate while preserving the out-of-plane direction, $\mathbf{A}'_f = \mathbf{RSA}_f$, where $\mathbf{R}$ is the rotation matrix and $\mathbf{S}$ is the strain tensor. The final interface was constructed as

$$\mathcal{I} = \mathcal{S}_{\text{sub}} \cup (\mathcal{S}_{\text{film}} + d\hat{z}), \tag{C.3}$$

where d is the interfacial gap. Vacuum spacing was added along the surface normal such that

$$L_z = t_{\text{sub}} + t_{\text{film}} + d + L_{\text{vac}}, \tag{C.4}$$

where t_{sub} and t_{film} are the slab thicknesses and L_{vac} is the vacuum spacing.

Among all valid ZSL matches, the final interface was selected by minimizing $\Phi = A$, subject to $\epsilon_{\text{avg}} < \epsilon_{\text{max}}$. This procedure yields the smallest-area coherent interface within acceptable strain limits.

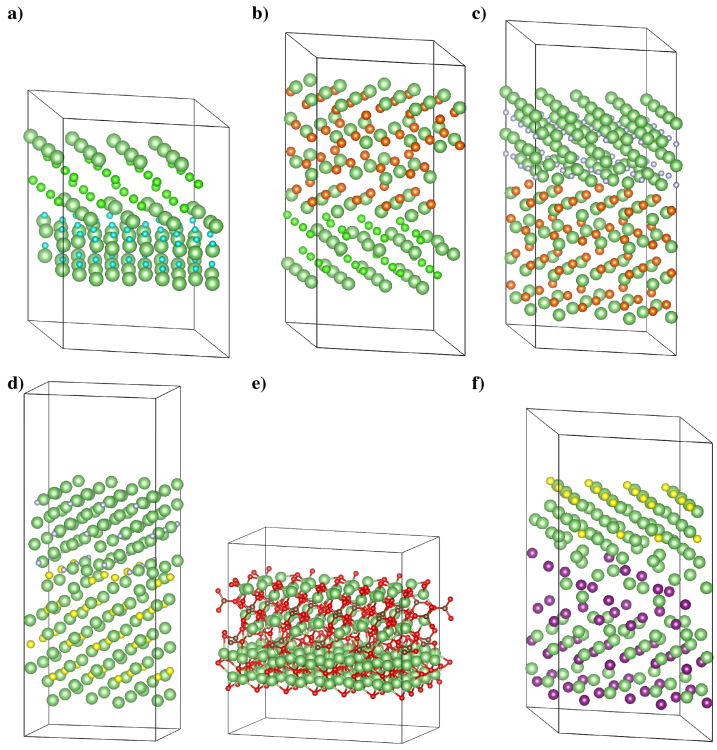


Figure C.9: Representative heterogeneous grain boundaries built using Zur–McGill algorithm for (a) LiF(111)-LiCl(111), (b) LiCl(111)-LiBr(001), (c) LiBr(110)-Li_3N(100) (d) Li_2S(001) -Li_3N(100), (e) Li_2O(001)-Li_2CO_3(100), and (f) LiI(001)-Li_2S(111).

Table C.5: Heterogeneous grain-boundary (GB) configurations included in the dataset. Each case is defined by the top grain and bottom grain together with their exposed surfaces used to construct the interface. The final column is reserved for representative GB images.

No.	Top grain	GB surface	Bottom grain	GB surface	Number of NEB calculations
1	Li_2O	(001)	Li_2CO_3	(100)	
2	Li_2O	(110)	Li_2S	(110)	
3	Li_2O	(111)	Li_3N	(001)	
4	Li_2S	(001)	Li_2CO_3	(001)	
5	Li_2S	(111)	Li_3N	(100)	
6	Li_3N	(001)	Li_2CO_3	(100)	
7	LiBr	(001)	Li_2CO_3	(001)	
8	LiBr	(001)	Li_2O	(111)	
9	LiBr	(001)	Li_2S	(111)	
10	LiBr	(001)	Li_3N	(001)	
11	LiBr	(110)	LiI	(100)	
12	LiCl	(001)	Li_2CO_3	(001)	
13	LiCl	(111)	Li_2O	(111)	
14	LiCl	(111)	Li_2S	(111)	
15	LiCl	(111)	Li_3N	(001)	
16	LiCl	(111)	LiBr	(001)	
17	LiCl	(111)	LiI	(001)	
18	LiF	(001)	Li_2S	(001)	
19	LiF	(110)	Li_3N	(100)	
20	LiF	(110)	LiI	(001)	
21	LiF	(111)	Li_2CO_3	(001)	
22	LiF	(111)	Li_2O	(111)	
23	LiF	(111)	LiBr	(001)	
24	LiF	(111)	LiCl	(111)	
25	LiI	(001)	Li_2O	(001)	
26	LiI	(001)	Li_2S	(111)	
27	LiI	(100)	Li_2CO_3	(010)	
28	LiI	(110)	Li_3N	(100)	

C.2.3 Feature Information

Table C.6: Retained composition features and the corresponding statistical operations used for featurization of diffusing elements and diffusion media.

Feature	Statistical operations considered	Description
Mendeleev Number	Average deviation	Ordering number listing the chemical elements column by column through the periodic system[317]
Atomic Weight	Maximum	Atomic weight in *amu*
Melting T	Minimum, Range, Mean, Mode	Melting point in Kelvin
Covalent Radius	Minimum, Maximum, Mean, Mode	Single-bond covalent radius
Electronegativity	Range, Average deviation	Electronegativity scale proposed by Allen [318]
Np Valence*	Mean	Fraction of electrons from the p valence sub-shell among all present elements
N Valence	Maximum	Fraction of electrons from the valence shell among all present elements
Np Unfilled*	Maximum	Fraction of unoccupied p sub-shell among all present elements
GS volume	Minimum, Range, Mean, Mode	Volume per atom in the ground state
GS bandgap	Maximum, Mean	Band gap of atom in the ground state
Space Group Number	Minimum, Mean, Mode	International space-group number associated with the crystal structure

* Ref. Meredig et al. [319].

C.2.4 Crystal Graph Construction

Fractional to Cartesian Coordinate Transformation: Atomic positions are initially stored in fractional coordinates. These are transformed into Cartesian coordinates using the lattice vectors ($\mathbf{L} \in R^{3\times3}$). For each atom i, $\mathbf{r}_i^{\text{cart}} = \mathbf{L}, \mathbf{r}_i^{\text{frac}}$. This transformation ensures that geometric quantities such as interatomic distances and angles are computed in physical space, preserving the crystallographic geometry.

Periodic Distance Computation: For each edge $(j \to i) \in \mathcal{E}$, the periodic displacement vector is computed as

$$\mathbf{d}_{ji} = \mathbf{r}_j^{\text{cart}} - \mathbf{r} * i^{\text{cart}} + \mathbf{o} * ji \tag{C.5}$$

where $\mathbf{o}_{ji}$ accounts for periodic image offsets. The interatomic distance is then $d_{ji} = |\mathbf{d}_{ji}|$. This ensures that the shortest periodic distance is used, preserving translational symmetry in crystalline systems.

Triplet Construction for Angular Information DimeNet++ explicitly models angular interactions by constructing triplets of atoms ($(k \to j \to i)$), representing two consecutive bonds. For each pair of edges sharing a common central atom j, a triplet is defined, enabling the computation of bond angles. This allows the model to incorporate three-body geometric interactions, which are essential for describing chemical bonding environments.

Radial Basis Expansion: Interatomic distances (d_{ji}) are expanded using a set of radial basis functions (RBFs), typically Bessel functions modulated by an envelope function:

$$\phi_n(d_{ji}) = e(d_{ji}) \cdot j_n! \left(\frac{\pi d_{ji}}{r_c} \right) \tag{C.6}$$

where (r_c) is the cutoff radius and (j_n) denotes the (n)-th Bessel function. This maps scalar distances into a high-dimensional continuous representation $\mathbf{r}_{ji} \in R^{N_r}$, enabling smooth and differentiable geometric encoding.

Spherical) Basis Expansion For each triplet $(k \to j \to i)$, the bond angle θ_{kji} is computed via

$$\cos\theta_{kji} = \frac{\mathbf{d} * ji \cdot \mathbf{d} * jk}{|\mathbf{d} * ji||\mathbf{d} * jk|} \tag{C.7}$$

Angular information is encoded using spherical harmonics combined with radial functions:

$$\psi_{l,m,n}(\theta_{kji}, d_{ji}) = Y_l^m(\theta_{kji}) \cdot \phi_n(d_{ji}), \tag{C.8}$$

producing a rich representation of directional geometry. This enables the model to capture rotationally equivariant three-body interactions.

Initial Edge Embedding: An embedding layer maps atomic types and radial features into edge-level embeddings: $\mathbf{x}*ji^{(0)} = \text{Embedding}(Z_i, Z_j, \mathbf{r}*ji)$, where $\mathbf{x}_{ji}^{(0)} \in R^H$ and H is the hidden dimensionality. These edge embeddings serve as the initial representation of pairwise atomic interactions. **Edge-to-Node Projection**: Edge embeddings are aggregated to produce node-level representations. For each atom i,

$$\mathbf{p} * i^{(0)} = \sum *j \in \mathcal{N}(i)\mathbf{W}\left(\mathbf{x} * ji^{(0)} \odot \mathbf{r} * ji\right) \tag{C.9}$$

where $\mathcal{N}(i)$ denotes neighbors of atom i, $\odot$ represents element-wise multiplication with radial basis features, and $\mathbf{W}$ is a learnable projection. This produces initial node embeddings $\mathbf{p}_i^{(0)}$.

Angular Interaction Blocks: Each interaction block updates edge embeddings using both radial and angular information. For block t, the update is

$$\mathbf{x} * ji^{(t)} = \mathbf{x} * ji^{(t-1)} + \sum_{k \in \mathcal{N}(j)} f_\theta! \left(\mathbf{x} * kj^{(t-1)}, \psi * kji \right) \tag{C.10}$$

where (f_θ) is a learnable function incorporating spherical basis features (ψ_{kji}). Residual connections and nonlinear transformations are applied to stabilize learning. This step allows information to propagate across multi-hop neighborhoods while explicitly modeling bond-angle geometry.

Accumulated Node Representations: After each interaction block, updated edge embeddings are again projected to nodes via output blocks, and contributions are accumulated:

$$\mathbf{P} * i = \sum * t = 0^T \mathbf{p}_i^{(t)}. \tag{C.11}$$

The final node representation $\mathbf{P}_i \in R^H$ encodes local atomic identity, bond distances, bond angles, and higher-order structural context.

Graph-Level Readout: To obtain a graph-level embedding for the entire crystal, node representations are aggregated using a permutation-invariant readout function. With mean pooling,

$$\mathbf{g} = \frac{1}{N} \sum_{i=1}^{N} \mathbf{P}_i \tag{C.12}$$

The resulting vector $\mathbf{g} \in R^H$ constitutes the structural embedding of the crystal. This embedding captures rotationally aware geometric information, periodic boundary effects, and multi-body atomic interactions, making it suitable for downstream tasks such as NEB profile and barrier prediction.

C.2.5 Graph Variational Autoencoder

In training using GVAE model, each NEB structure is represented as a periodic crystal graph and then processed using a DimeNet++ encoder to obtain a fixed-dimensional structural embedding $\mathbf{h}_i \in R^{256}$, where $i = 0, \ldots, 6$. These embeddings encode atomic connectivity, local geometric structure, and chemical identity. For each NEB path, embeddings are grouped as $\mathbf{H} = [\mathbf{h}_0, \ldots, \mathbf{h}_6] \in R^{7\times 256}$.

Diffusion-path information added to each structures by concatenating (i) positional encoding thus reflects structure's index along the reaction coordinate and (ii) a saddle-point indicator to $\mathbf{H}$. The resulting sequence is then processed through the VAE network.

From the contextualized embeddings ($\tilde{\mathbf{h}}_i$), we parameterize a variational posterior distribution for each image as

$$\boldsymbol{\mu}_i, \log \boldsymbol{\sigma} * i^2 = f * \theta(\tilde{\mathbf{h}}_i) \tag{C.13}$$

where μ is the mean, σ is the standard deviation of posterior distribution and θ is the learnable parameter. Then then sample latent variables (z) using the reparameterization operation with normal distribution as

$$\mathbf{z}_i = \boldsymbol{\mu}_i + \boldsymbol{\sigma}_i \odot \boldsymbol{\epsilon} \qquad \boldsymbol{\epsilon} \sim \mathcal{N}(0, \mathbf{I}) \tag{C.14}$$

The model is trained using a multi-task objective combining generative and supervised components whose loss calculated as,

$$\mathcal{L} = \mathcal{L}_{\text{KL}} + \mathcal{L}_{\text{coord}} + \mathcal{L}_{\text{lattice}} + \mathcal{L}_{\text{composition}} + \lambda_{\text{barrier}} \cdot \mathcal{L}_{\text{barrier}} \tag{C.15}$$

Here, $\mathcal{L}_{KL}$, the Kullback–Leibler (KL) divergence, regularizes the posterior toward

an isotropic Gaussian prior, enforces variational regularization. The structural reconstruction losses ($\mathcal{L}_{\text{coord.}}$, $\mathcal{L}_{\text{lattice}}$, $\mathcal{L}_{\text{composition}}$) ensure geometric fidelity, and $\mathcal{L}_{barrier}$ is the mean squared error between predicted and NEB calculated migration barriers/profile energies. This supervised barrier term encourages the latent manifold to align with physically meaningful diffusion descriptors.

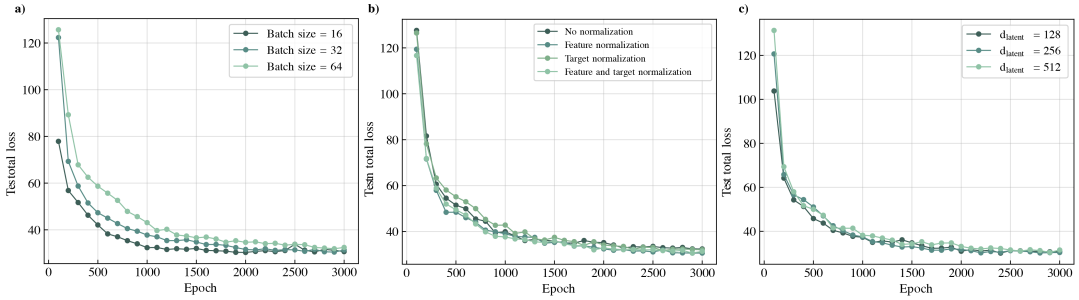


Figure C.10: Results of GVAE model tuning; a) total loss of test with varying batch sizes, b) normalization among feature/target, and latent dimension.

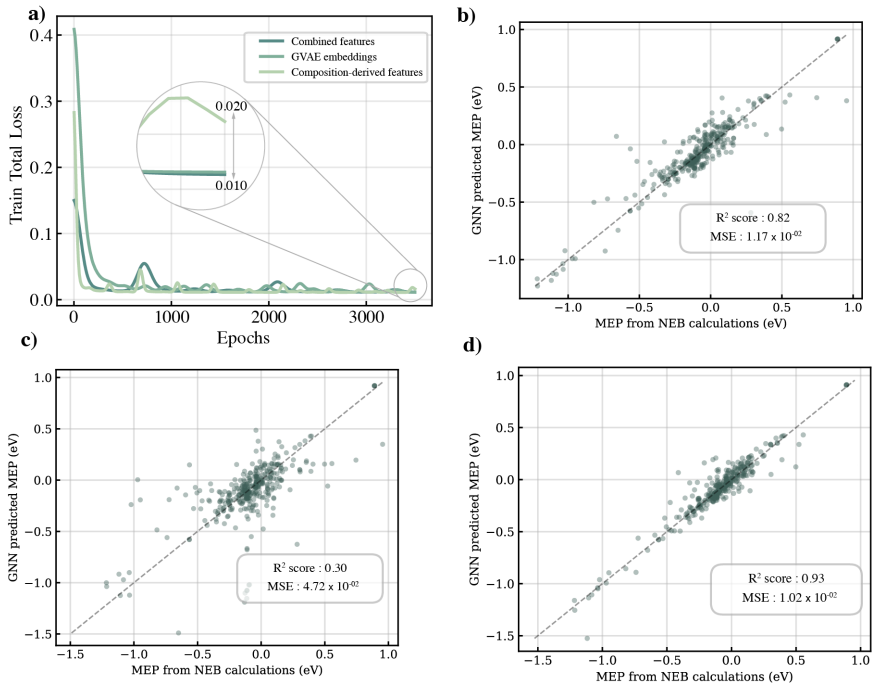


Figure C.11: Comparison of GNN model performance with three training schemes: a) total loss curves, R^2 scatter plots of training with a) composition derived features, b) GVAE latent embeddings, and c) combined features.

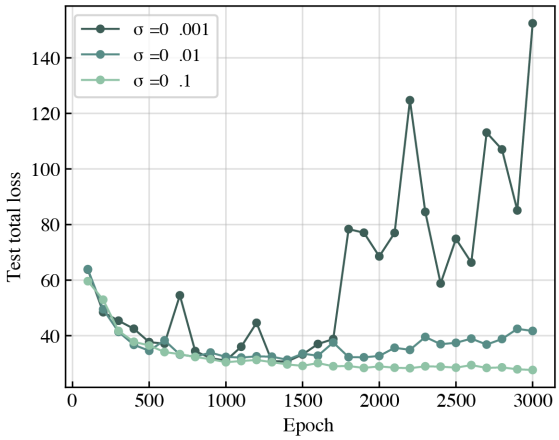


Figure C.12: Latent diffusion noise conditioning: Three trials with noise range 0.1 – 0.001 that used to perturb atomic positions.

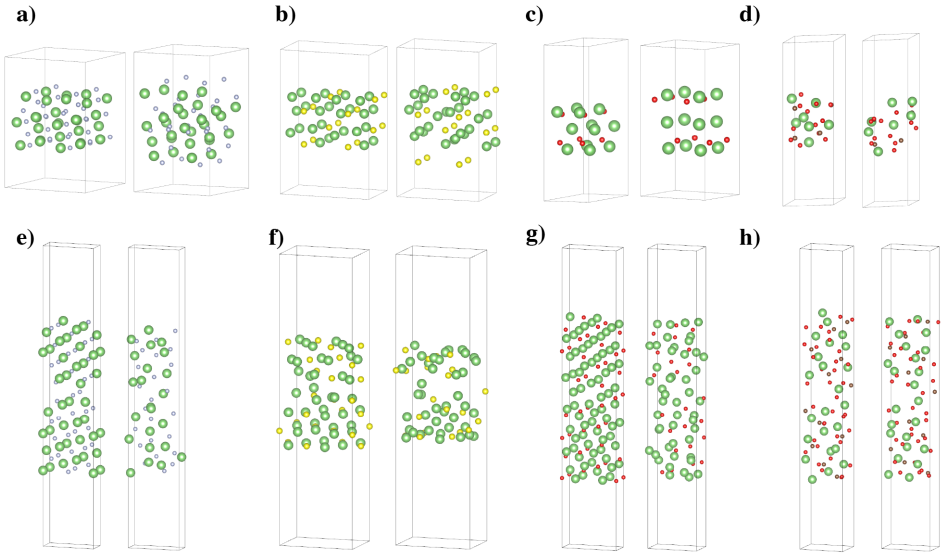


Figure C.13: Samples of ground truth and reconstructed grain structures of a) LiF, b) Li_2S, c) Li_2O, Li_2CO_3. Grain boundary structures of same components are given in (e – h) respectively. All structures are reconstructed with good accuracy for lattice and atomic positions. However it can also be seen that atom types of four oxygen atom are reconstructed as sulfur atoms.

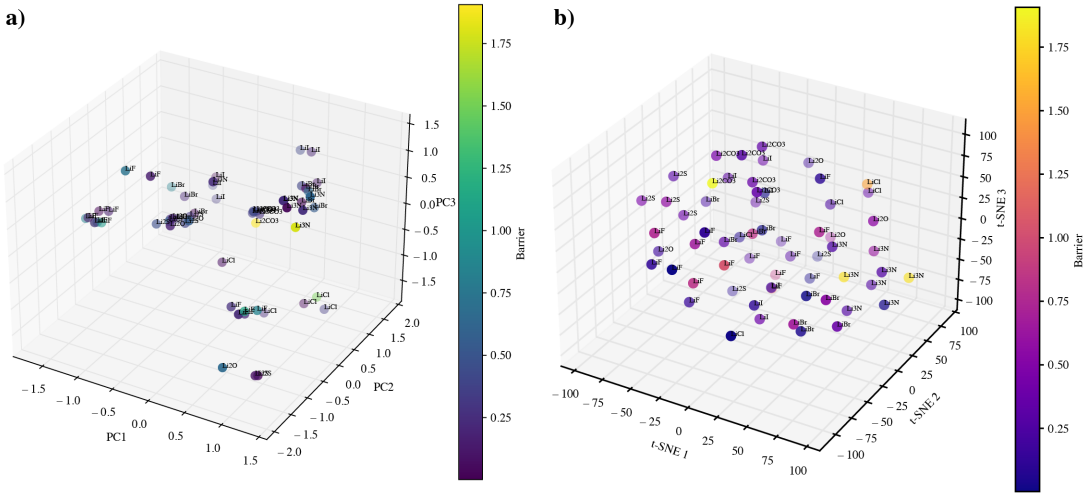


Figure C.14: Visualization of latent space clustering of SEI components using (a) PCA and (b) t-SNE based dimensionality reduction. A clear clustering can be observed in PC space three PCs compared to t-SNE based cluster classification.

C.2.6 Convergence test and benchmarking

Table C.7: Comparison of Li-ion migration barriers obtained in the present work with previously reported literature values for representative grain and grain-boundary diffusion pathways in SEI components.

System / Diffusion type	**Literature value (eV)**	**Present work (eV)**
LiF bulk grain diffusion	0.25[82]	0.249
Li_2CO_3 bulk grain diffusion	0.21[86]	0.233
Li_2O bulk grain diffusion	0.24–0.25[131]	0.287
LiF/LiF $\Sigma5$ grain boundary	0.68[83]	0.647
Li_2O/Li_2O $\Sigma15$ grain boundary	0.78[83]	0.792

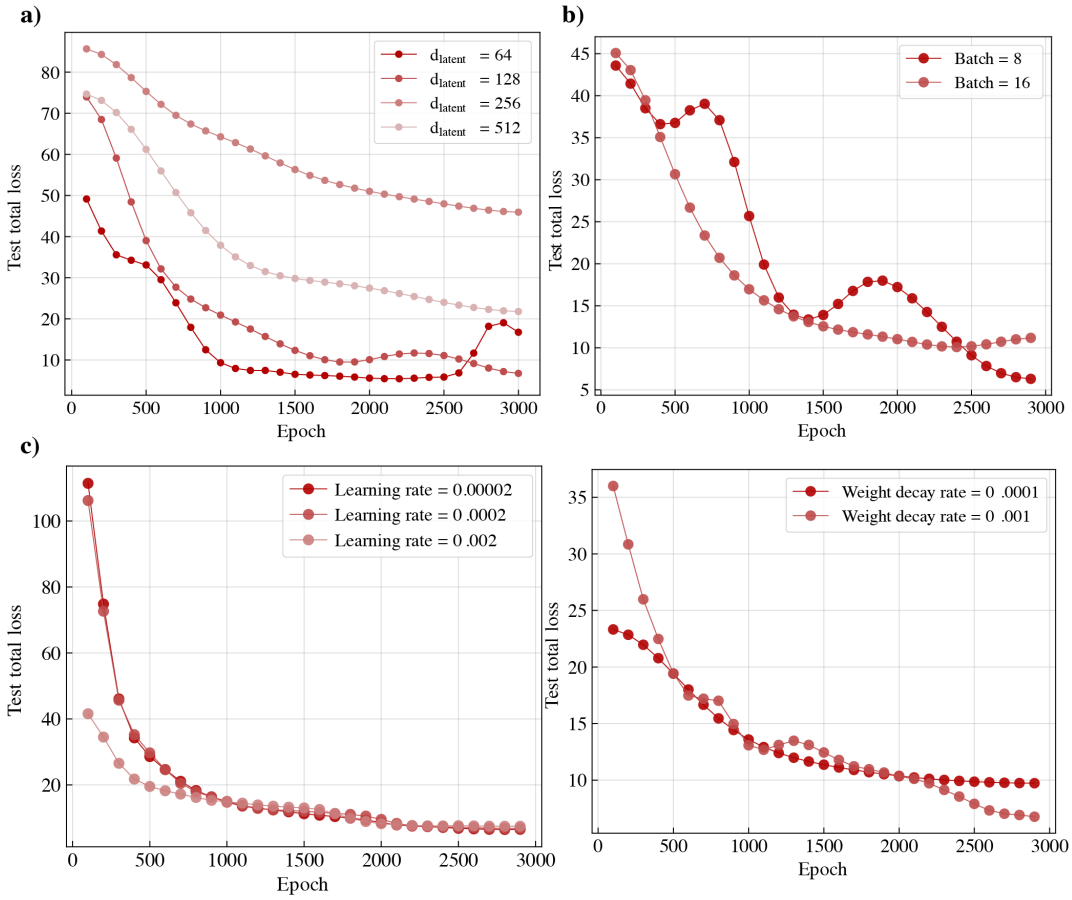


Figure C.15: Tuning of GVAE for grain boundary diffusion: a) latent dimension (d_{latent}), b) batch, c) learning rate and (d) weight decay rate in Adam optimizer.

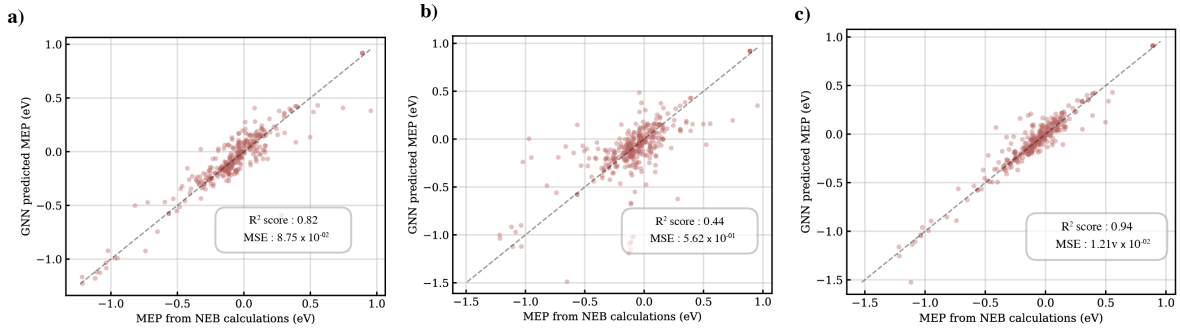


Figure C.16: Comparison of GNN model performance with three training schemes: R^2 scatter plots of training with a) composition derived features, b) GVAE latent embeddings, and c) combined features.

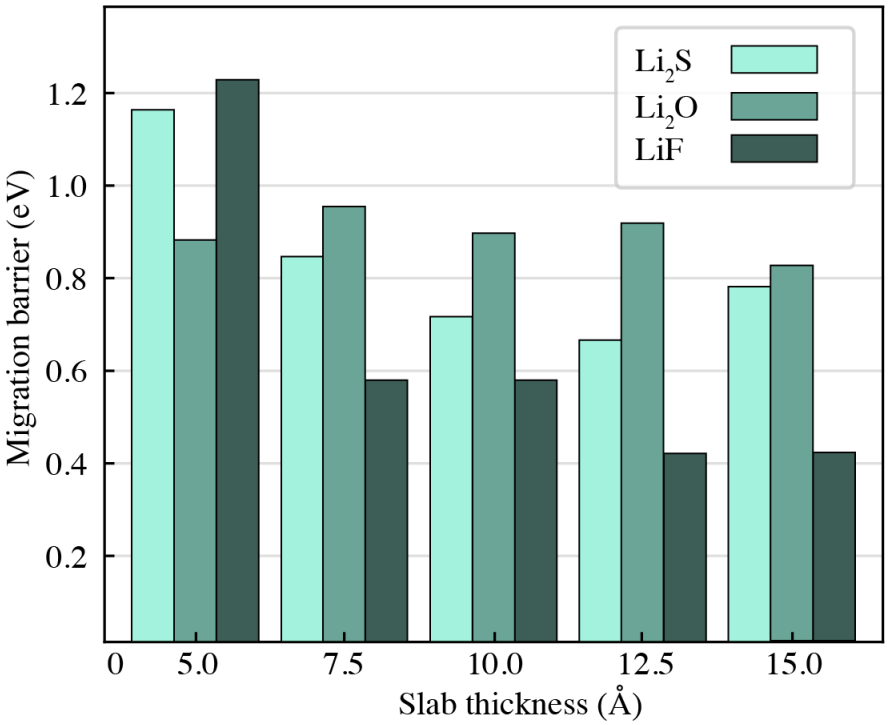


Figure C.17: Convergence test on slab thickness vs migration barrier in Li_2S, Li_2O and LiF.

C.3 MXene: Case Study

C.3.1 MXene band gap

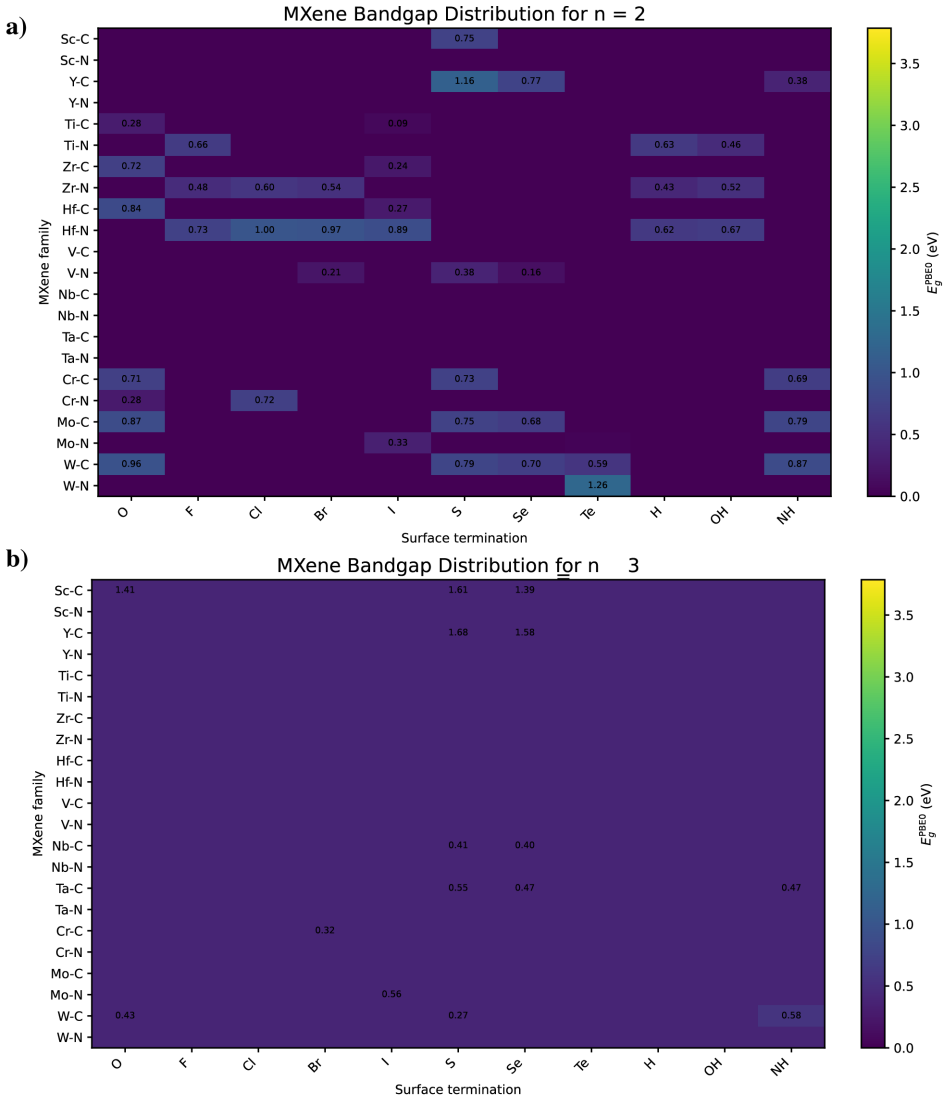


Figure C.18: PBE0 bandgap distribution of the MXene configurations with $n = 2, 3$.

Reference List

[1] Colin McKerracher, Ali Izadi-Najafabadi, Aleksandra O'Donovan, Nick Albanese, Nikolas Soulopolous, David Doherty, Milo Boers, Ryan Fisher, Corey Cantor, James Frith, Siyi Mi, and Andrew Grand. Electric vehicle outlook 2020. *Bloomberg New Energy Finance*, pages 2–3, 2020. URL `https://about.bnef.com/electric-vehicle-outlook-2020/`.

[2] Ghassan Zubi, Rodolfo Dufo-López, Monica Carvalho, and Guzay Pasaoglu. The lithium-ion battery: State of the art and future perspectives. *Renewable and Sustainable Energy Reviews*, 89:292–308, 2018. ISSN 1364-0321. doi: https://doi.org/10.1016/j.rser.2018.03.002. URL `https://www.sciencedirect.com/science/article/pii/S1364032118300728`.

[3] Matthew Li, Jun Lu, Zhongwei Chen, and Khalil Amine. 30 years of lithium-ion batteries. *Advanced Materials*, 30(33):1800561, 2018. doi: https://doi.org/10.1002/adma.201800561.

[4] Zachary P Cano, Dustin Banham, Siyu Ye, Andreas Hintennach, Jun Lu, Michael Fowler, and Zhongwei Chen. Batteries and fuel cells for emerging electric vehicle markets. *Nature Energy*, 3(4):279–289, 2018. doi: http://dx.doi.org/10.1038/s41560-018-0108-1.

[5] Nan Zhang, Tao Deng, Shuoqing Zhang, Changhong Wang, Lixin Chen, Chunsheng Wang, and Xiulin Fan. Critical review on low-temperature li-ion/metal batteries. *Advanced Materials*, 34(15):2107899, 2022. doi: https://doi.org/10.1002/adma.202107899.

[6] John B Goodenough and Kyu-Sung Park. The li-ion rechargeable battery: a perspective. *Journal of the American Chemical Society*, 135(4):1167–1176, 2013. doi: https://doi.org/10.1021/ja3091438.

[7] Arumugam Manthiram, Xingwen Yu, and Shaofei Wang. Lithium battery chemistries enabled by solid-state electrolytes. *Nature Reviews Materials*, 2(4):1–16, 2017. doi: https://doi.org/10.1038/natrevmats.2016.103.

[8] Mahdi Rouholamini, Caisheng Wang, Hashem Nehrir, Xiaosong Hu, Zechun Hu, and Hirohisa Aki. A Review of Modeling, Management, and Applications of Grid-Connected Li-Ion Battery Storage Systems. *IEEE Trans. Smart Grid*, 13(6):4505–4524, July 2022. doi: 10.1109/TSG.2022.3188598.

[9] Hossein Rostami, Johanna Valio, Pekka Tynjälä, Ulla Lassi, and Pekka Suominen. Life Cycle of LiFePO4 Batteries: Production, Recycling, and Market Trends. *ChemPhysChem*, 25(24):e202400459, November 2024. ISSN 1439-7641. doi: 10.1002/cphc.202400459.

[10] E. Peled. The Electrochemical Behavior of Alkali and Alkaline Earth Metals in Nonaqueous Battery Systems—The Solid Electrolyte Interphase Model. *J. Electrochem. Soc.*, 126(12):2047, December 1979. ISSN 1945-7111. doi: 10.1149/1.2128859.

[11] D. Aurbach, B. Markovsky, M. D. Levi, E. Levi, A. Schechter, M. Moshkovich, and Y. Cohen. New insights into the interactions between electrode materials and electrolyte solutions for advanced nonaqueous batteries. *J. Power Sources*, 81-82: 95–111, September 1999. ISSN 0378-7753. doi: 10.1016/S0378-7753(99)00187-1.

[12] Emanuel Peled. The electrochemical behavior of alkali and alkaline earth metals in nonaqueous battery systems—the solid electrolyte interphase model. *Journal of the Electrochemical Society*, 126(12):2047, 1979. doi: https://doi.org/10.1149/1.2128859.

[13] Doron Aurbach, Boris Markovsky, MD Levi, Elena Levi, Alex Schechter, Moty Moshkovich, and Yaron Cohen. New insights into the interactions between electrode materials and electrolyte solutions for advanced nonaqueous batteries. *Journal of Power Sources*, 81:95–111, 1999. doi: https://doi.org/10.1016/S0378-7753(99)00187-1.

[14] Pallavi Verma, Pascal Maire, and Petr Novák. A review of the features and analyses of the solid electrolyte interphase in li-ion batteries. *Electrochimica Acta*, 55(22):6332–6341, 2010. doi: https://doi.org/10.1016/j.electacta.2010.05.072.

[15] Yu-Xiao Lin, Zhe Liu, Kevin Leung, Long-Qing Chen, Peng Lu, and Yue Qi. Connecting the irreversible capacity loss in li-ion batteries with the electronic insulating properties of solid electrolyte interphase (sei) components. *Journal of Power Sources*, 309:221–230, 2016. doi: https://doi.org/10.1016/j.jpowsour.2016.01.078.

[16] Arun Patil, Vaishali Patil, Dong Wook Shin, Ji-Won Choi, Dong-Soo Paik, and Seok-Jin Yoon. Issue and challenges facing rechargeable thin film lithium batteries. *Materials Research Bulletin*, 43(8):1913–1942, 2008. ISSN 0025-5408. doi: https://doi.org/10.1016/j.materresbull.2007.08.031. URL `https://www.sciencedirect.com/science/article/pii/S0025540807003868`.

[17] Sungjemmenla, K. Vineeth S., Chhail Bihari Soni, Vipin Kumar, and Zhi Wei

Seh. Understanding the Cathode–Electrolyte Interphase in Lithium-Ion Batteries. *Energy Technology*, 10(9):2200421, July 2022. ISSN 2194-4296. doi: 10.1002/ente.202200421.

[18] Sebastian P. Kühn, Kristina Edström, Martin Winter, and Isidora Cekic-Laskovic. Face to Face at the Cathode Electrolyte Interphase: From Interface Features to Interphase Formation and Dynamics. *Adv. Mater. Interfaces*, 9(8): 2102078, January 2022. ISSN 2196-7350. doi: 10.1002/admi.202102078.

[19] Seong Jin An, Jianlin Li, Claus Daniel, Debasish Mohanty, Shrikant Nagpure, and David L Wood III. The state of understanding of the lithium-ion-battery graphite solid electrolyte interphase (sei) and its relationship to formation cycling. *Carbon*, 105:52–76, 2016. doi: https://doi.org/10.1016/j.carbon.2016.04.008.

[20] Aiping Wang, Sanket Kadam, Hong Li, Siqi Shi, and Yue Qi. Review on modeling of the anode solid electrolyte interphase (sei) for lithium-ion batteries. *npj Computational Materials*, 4(1):15, 2018. doi: https://doi.org/10.1038/s41524-018-0064-0.

[21] Siqi Shi, Peng Lu, Zhongyi Liu, Yue Qi, Louis G Hector Jr, Hong Li, and Stephen J Harris. Direct calculation of li-ion transport in the solid electrolyte interphase. *Journal of the American Chemical Society*, 134(37):15476–15487, 2012. doi: https://doi.org/10.1021/ja305366r.

[22] Peng Lu, Chen Li, Eric W Schneider, and Stephen J Harris. Chemistry, impedance, and morphology evolution in solid electrolyte interphase films during formation in lithium ion batteries. *The Journal of Physical Chemistry C*, 118(2): 896–903, 2014. doi: https://doi.org/10.1021/jp4111019.

[23] Peng Lu and Stephen J Harris. Lithium transport within the solid electrolyte interphase. *Electrochemistry Communications*, 13(10):1035–1037, 2011. doi: https://doi.org/10.1016/j.elecom.2011.06.026.

[24] Kristin Persson, Vijay A Sethuraman, Laurence J Hardwick, Yoyo Hinuma, Ying Shirley Meng, Anton Van Der Ven, Venkat Srinivasan, Robert Kostecki, and Gerbrand Ceder. Lithium diffusion in graphitic carbon. *The Journal of Physical Chemistry Letters*, 1(8):1176–1180, 2010. doi: https://doi.org/10.1021/jz100188d.

[25] Fernando A Soto, Asma Marzouk, Fedwa El-Mellouhi, and Perla B Balbuena. Understanding ionic diffusion through sei components for lithium-ion and sodium-ion batteries: insights from first-principles calculations. *Chemistry of Materials*, 30(10):3315–3322, 2018. doi: 10.1021/acs.chemmater.8b00635.

[26] Feng Zheng, Masashi Kotobuki, Shufeng Song, Man On Lai, and Li Lu. Review on solid electrolytes for all-solid-state lithium-ion batteries. *Journal of Power Sources*, 389:198–213, 2018. doi: https://doi.org/10.1016/j.jpowsour.2018.04.022.

[27] Jeffrey W Fergus. Ceramic and polymeric solid electrolytes for lithium-ion batteries. *Journal of Power Sources*, 195(15):4554–4569, 2010. doi: https://doi.org/10.1016/j.jpowsour.2010.01.076.

[28] Xiaotao Fu, Danni Yu, Junwen Zhou, Siwu Li, Xing Gao, Yuzhen Han, Pengfei Qi, Xiao Feng, and Bo Wang. Inorganic and organic hybrid solid electrolytes for lithium-ion batteries. *CrystEngComm*, 18(23):4236–4258, 2016. doi: https://doi.org/10.1039/C6CE00171H.

[29] Lu Han, Michelle L Lehmann, Jiadeng Zhu, Tianyi Liu, Zhengping Zhou, Xiaomin Tang, Chien-Te Heish, Alexei P Sokolov, Pengfei Cao, Xi Chelsea Chen, and Saito Tomonori. Recent developments and challenges in hybrid solid electrolytes for lithium-ion batteries. *Frontiers in Energy Research*, 8:202, 2020. doi: https://doi.org/10.3389/fenrg.2020.00202.

[30] Yu-Kun Liu, Chen-Zi Zhao, Juan Du, Xue-Qiang Zhang, Ai-Bing Chen, and Qiang Zhang. Research progresses of liquid electrolytes in lithium-ion batteries. *Small*, page 2205315, 2022. doi: https://doi.org/10.1002/smll.202205315.

[31] Kang Xu. Nonaqueous liquid electrolytes for lithium-based rechargeable batteries. *Chemical reviews*, 104(10):4303–4418, 2004. doi: https://doi.org/10.1021/cr030203g.

[32] Huicong Yang, Juan Li, Zhenhua Sun, Ruopian Fang, Da-Wei Wang, Kuang He, Hui-Ming Cheng, and Feng Li. Reliable liquid electrolytes for lithium metal batteries. *Energy Storage Materials*, 30:113–129, 2020. doi: https://doi.org/10.1016/j.ensm.2020.04.010.

[33] John Collins, Gerald Gourdin, Michelle Foster, and Deyang Qu. Carbon surface functionalities and sei formation during li intercalation. *Carbon*, 92:193–244, 2015. doi: https://doi.org/10.1016/j.carbon.2015.04.007.

[34] Jun-Fan Ding, Rui Xu, Chong Yan, Bo-Quan Li, Hong Yuan, and Jia-Qi Huang. A review on the failure and regulation of solid electrolyte interphase in lithium batteries. *Journal of Energy Chemistry*, 59:306–319, 2021. doi: https://doi.org/10.1016/j.jechem.2020.11.016.

[35] Xin-Bing Cheng, Rui Zhang, Chen-Zi Zhao, Fei Wei, Ji-Guang Zhang, and Qiang

Zhang. A review of solid electrolyte interphases on lithium metal anode. *Advanced Science*, 3(3):1500213, 2016. doi: https://doi.org/10.1002/advs.201500213.

[36] Hiroko Kuwata, Hidetoshi Sonoki, Masaki Matsui, Yasuaki Matsuda, and Nobuyuki Imanishi. Surface layer and morphology of lithium metal electrodes. *Electrochemistry*, 84(11):854–860, 2016. doi: http://dx.doi.org/10.5796/electrochemistry.84.854.

[37] Philip Niehoff, Stefano Passerini, and Martin Winter. Interface investigations of a commercial lithium ion battery graphite anode material by sputter depth profile x-ray photoelectron spectroscopy. *Langmuir*, 29(19):5806–5816, 2013. doi: https://doi.org/10.1021/la400764r.

[38] Natalia Schulz, Rene Hausbrand, Carolin Wittich, Lucangelo Dimesso, and Wolfram Jaegermann. Xps-surface analysis of sei layers on li-ion cathodes: Part ii. sei-composition and formation inside composite electrodes. *Journal of the Electrochemical Society*, 165(5):A833, 2018. doi: https://doi.org/10.1149/2.0881803jes.

[39] Doron Aurbach, Idit Weissman, Alexander Schechter, and Hagai Cohen. X-ray photoelectron spectroscopy studies of lithium surfaces prepared in several important electrolyte solutions. a comparison with previous studies by fourier transform infrared spectroscopy. *Langmuir*, 12(16):3991–4007, 1996. doi: https://doi.org/10.1021/la9600762.

[40] Alex Schechter, Doron Aurbach, and Hagay Cohen. X-ray photoelectron spectroscopy study of surface films formed on li electrodes freshly prepared in alkyl carbonate solutions. *Langmuir*, 15(9):3334–3342, 1999. doi: https://doi.org/10.1021/la981048h.

[41] Feng Hao, Ankit Verma, and Partha P Mukherjee. Mechanistic insight into dendrite–sei interactions for lithium metal electrodes. *Journal of Materials Chemistry A*, 6(40):19664–19671, 2018. doi: https://doi.org/10.1039/C8TA07997H.

[42] Guangyu Liu and Wei Lu. A model of concurrent lithium dendrite growth, sei growth, sei penetration and regrowth. *Journal of the Electrochemical Society*, 164(9):A1826, 2017. doi: http://dx.doi.org/10.1149/2.0381709jes.

[43] Danmiao Kang, Saydual Sardar, Rui Zhang, Hart Noam, Jingyun Chen, Linge Ma, Wenbin Liang, Chunsheng Shi, and John P Lemmon. In-situ organic sei layer for dendrite-free lithium metal anode. *Energy Storage Materials*, 27:69–77, 2020. doi: https://doi.org/10.1016/j.ensm.2020.01.020.

[44] Dacheng Kuai and Perla B. Balbuena. Inorganic Solid Electrolyte Interphase

Engineering Rationales Inspired by Hexafluorophosphate Decomposition Mechanisms. *J. Phys. Chem. C*, 127(4):1744–1751, February 2023. ISSN 1932-7447. doi: 10.1021/acs.jpcc.2c07838.

[45] Jeffrey Lopez. Understanding Organic Components of Solid Electrolyte Interphase on the Lithium Metal Anode. *Meet. Abstr.*, MA2024-01(2):480, August 2024. ISSN 2151-2043. doi: 10.1149/MA2024-012480mtgabs.

[46] Chuntian Cao, Travis P Pollard, Oleg Borodin, Julian E Mars, Yuchi Tsao, Maria R Lukatskaya, Robert M Kasse, Marshall A Schroeder, Kang Xu, Michael F Toney, and Steinrück Hans. Toward unraveling the origin of lithium fluoride in the solid electrolyte interphase. *Chemistry of Materials*, 33(18):7315–7336, 2021. doi: https://doi.org/10.1021/acs.chemmater.1c01744.

[47] L Benitez, D Cristancho, JM Seminario, JM Martinez De La Hoz, and PB Balbuena. Electron transfer through solid-electrolyte-interphase layers formed on si anodes of li-ion batteries. *Electrochimica Acta*, 140:250–257, 2014. doi: https://doi.org/10.1016/j.electacta.2014.05.018.

[48] Lydia Gehrlein, Christian Leibing, Kristina Pfeifer, Fabian Jeschull, Andrea Balducci, and Julia Maibach. Glyoxylic acetals as electrolytes for si/graphite anodes in lithium-ion batteries. *Electrochimica Acta*, page 140642, 2022. doi: https://doi.org/10.1016/j.electacta.2022.140642.

[49] Haoyu Zhu, Joshua A Russell, Zongtang Fang, Pete Barnes, Lan Li, Corey M. Efaw, Allison Muenzer, Jeremy May, Kailash Hamal, I Francis Cheng, Davis Paul H, Dufek EricJ, and Xiong Hui. A comparison of solid electrolyte interphase formation and evolution on highly oriented pyrolytic and disordered graphite negative electrodes in lithium-ion batteries. *Small*, 17(52):2105292, 2021. doi: https://doi.org/10.1002/smll.202105292.

[50] Seung Mi Oh, Jinju Song, Soyeon Lee, and Il-Chan Jang. Effect of current rate on the formation of the solid electrolyte interphase layer at the graphite anode in lithium-ion batteries. *Electrochimica Acta*, 397:139269, 2021. doi: https://doi.org/10.1016/j.electacta.2021.139269.

[51] Kyung Hoon Kim, Jong Hoon Cho, Jin Ung Hwang, Ji Sun Im, and Young-Seak Lee. A key strategy to form a lif-based sei layer for a lithium-ion battery anode with enhanced cycling stability by introducing a semi-ionic cf bond. *Journal of Industrial and Engineering Chemistry*, 99:48–54, 2021. doi: https://doi.org/10.1016/j.jiec.2021.04.002.

[52] Junli Shi, Niloofar Ehteshami, Jialing Ma, Hui Zhang, Haidong Liu, Xin Zhang,

Jie Li, and Elie Paillard. Improving the graphite/electrolyte interface in lithium-ion battery for fast charging and low temperature operation: Fluorosulfonyl isocyanate as electrolyte additive. *Journal of Power Sources*, 429:67–74, 2019. doi: https://doi.org/10.1016/j.jpowsour.2019.04.113.

[53] Niloofar Ehteshami, Lukas Ibing, Lukas Stolz, Martin Winter, and Elie Paillard. Ethylene carbonate-free electrolytes for li-ion battery: Study of the solid electrolyte interphases formed on graphite anodes. *Journal of Power Sources*, 451: 227804, 2020. doi: https://doi.org/10.1016/j.jpowsour.2020.227804.

[54] Guiomar Hernández, Andrew J Naylor, Yu-Chuan Chien, Daniel Brandell, Jonas Mindemark, and Kristina Edström. Elimination of fluorination: the influence of fluorine-free electrolytes on the performance of $lini_{1/3}mn_{1/3}co_{1/3}o_2$/silicon–graphite li-ion battery cells. *ACS Sustainable Chemistry & Engineering*, 8(27): 10041–10052, 2020. doi: https://doi.org/10.1021/acssuschemeng.0c01733.

[55] Ruijun Pan, Zehao Cui, Michael Yi, Qiang Xie, and Arumugam Manthiram. Ethylene carbonate-free electrolytes for stable, safer high-nickel lithium-ion batteries. *Advanced Energy Materials*, page 2103806, 2022. doi: https://doi.org/10.1002/aenm.202103806.

[56] E Peled, D Golodnitsky, C Menachem, and D Bar-Tow. An advanced tool for the selection of electrolyte components for rechargeable lithium batteries. *Journal of the Electrochemical Society*, 145(10):3482, 1998. doi: https://doi.org/10.1149/1.1838831.

[57] Bertrand Philippe, Rémi Dedryvère, Joachim Allouche, Fredrik Lindgren, Mihaela Gorgoi, Håkan Rensmo, Danielle Gonbeau, and Kristina Edström. Nanosilicon electrodes for lithium-ion batteries: interfacial mechanisms studied by hard and soft x-ray photoelectron spectroscopy. *Chemistry of Materials*, 24(6):1107–1115, 2012. doi: https://doi.org/10.1021/cm2034195.

[58] Catarina Pereira-Nabais, Jolanta Światowska, Alexandre Chagnes, Francois Ozanam, Aurelien Gohier, Pierre Tran-Van, Costel-Sorin Cojocaru, Michel Cassir, and Philippe Marcus. Interphase chemistry of si electrodes used as anodes in li-ion batteries. *Applied Surface Science*, 266:5–16, 2013. doi: https://doi.org/10.1016/j.apsusc.2012.10.165.

[59] Bertrand Philippe, Rémi Dedryvère, Mihaela Gorgoi, Håkan Rensmo, Danielle Gonbeau, and Kristina Edström. Role of the lipf6 salt for the long-term stability of silicon electrodes in li-ion batteries–a photoelectron spectroscopy study. *Chemistry of Materials*, 25(3):394–404, 2013. doi: https://doi.org/10.1021/cm303399v.

[60] Candace K Chan, Riccardo Ruffo, Seung Sae Hong, and Yi Cui. Surface chemistry and morphology of the solid electrolyte interphase on silicon nanowire lithium-ion battery anodes. *Journal of Power Sources*, 189(2):1132–1140, 2009. doi: https://doi.org/10.1016/j.jpowsour.2009.01.007.

[61] Jianhui Zheng, Zhijin Ju, Baolin Zhang, Jianwei Nai, Tiefeng Liu, Yujing Liu, Qifan Xie, Wenkui Zhang, Yao Wang, and Xinyong Tao. Lithium ion diffusion mechanism on the inorganic components of the solid–electrolyte interphase. *Journal of Materials Chemistry A*, 9(16):10251–10259, 2021. doi: https://doi.org/10.1039/D0TA11444H.

[62] Yitao He, Yaohui Zhang, Hirbod Maleki Kheimeh Sari, Zhihong Wang, Zhe Lü, Xiqiang Huang, Zhiguo Liu, Jiujun Zhang, and Xifei Li. New insight into li metal protection: Regulating the li-ion flux via dielectric polarization. *Nano Energy*, 89:106334, 2021. doi: https://doi.org/10.1016/j.nanoen.2021.106334.

[63] Orapa Tamwattana, Hyeokjun Park, Jihyeon Kim, Insang Hwang, Gabin Yoon, Tae-hyun Hwang, Yoon-Sok Kang, Jinhwan Park, Nonglak Meethong, and Kisuk Kang. High-dielectric polymer coating for uniform lithium deposition in anode-free lithium batteries. *ACS Energy Letters*, 6(12):4416–4425, 2021. doi: https://doi.org/10.1021/acsenergylett.1c02224.

[64] Xuning Feng, Mou Fang, Xiangming He, Minggao Ouyang, Languang Lu, Hao Wang, and Mingxuan Zhang. Thermal runaway features of large format prismatic lithium ion battery using extended volume accelerating rate calorimetry. *Journal of Power Sources*, 255:294–301, 2014. doi: https://doi.org/10.1016/j.jpowsour.2014.01.005.

[65] Qingsong Wang, Ping Ping, Xuejuan Zhao, Guanquan Chu, Jinhua Sun, and Chunhua Chen. Thermal runaway caused fire and explosion of lithium ion battery. *Journal of Power Sources*, 208:210–224, 2012. doi: https://doi.org/10.1016/j.jpowsour.2012.02.038.

[66] Xiangru Sun, Shaohua Yang, Ting Zhang, Yanbin Shi, Lei Dong, Guo Ai, Dejun Li, and Wenfeng Mao. Regulating li-ion flux with a high-dielectric hybrid artificial sei for stable li metal anodes. *Nanoscale*, 14(13):5033–5043, 2022. doi: https://doi.org/10.1039/D2NR01097F.

[67] Joongpyo Shim and Kathryn A Striebel. Cycling performance of low-cost lithium ion batteries with natural graphite and lifepo$_4$. *Journal of Power Sources*, 119:955–958, 2003. doi: https://doi.org/10.1016/S0378-7753(03)00297-0.

[68] Sufu Liu, Xinhui Xia, Shengjue Deng, Dong Xie, Zhujun Yao, Liyuan Zhang,

Shengzhao Zhang, Xiuli Wang, and Jiangping Tu. In situ solid electrolyte interphase from spray quenching on molten li: a new way to construct high-performance lithium-metal anodes. *Advanced Materials*, 31(3):1806470, 2019. doi: https://doi.org/10.1002/adma.201806470.

[69] Huwei Wang, Dengyun Zhai, and Feiyu Kang. Solid electrolyte interphase (sei) in potassium ion batteries. *Energy & Environmental Science*, 13(12):4583–4608, 2020. doi: https://doi.org/10.1039/D0EE01638A.

[70] Woo-Seong Kim, Kwang-il Chung, Jung-Hwan Cho, Dong-Won Park, Chan-Young Kim, and Yong-Kook Choi. Studies of a solid electrolyte interface coated with li_2co_3 on the carbon electrode in li-ion batteries. *Journal of Industrial and Engineering Chemistry*, 9(6):699–703, 2003.

[71] S Menkin, D Golodnitsky, and E Peled. Artificial solid-electrolyte interphase (sei) for improved cycleability and safety of lithium–ion cells for ev applications. *Electrochemistry Communications*, 11(9):1789–1791, 2009. doi: https://doi.org/10.1016/j.elecom.2009.07.019.

[72] Yang Luo, Tianyu Li, Hongzhang Zhang, Wei Liu, Xiaoben Zhang, Jingwang Yan, Huamin Zhang, and Xianfeng Li. Endogenous symbiotic li_3n/cellulose skin to extend the cycle life of lithium anode. *Angewandte Chemie International Edition*, 60(21):11718–11724, 2021. doi: https://doi.org/10.1002/anie.202017281.

[73] Chao Chen, Qianwen Liang, Gang Wang, Dongdong Liu, and Xunhui Xiong. Grain-boundary-rich artificial sei layer for high-rate lithium metal anodes. *Advanced Functional Materials*, 32(4):2107249, 2022. doi: https://doi.org/10.1002/adfm.202107249.

[74] Nimrod Harpak, Guy Davidi, and Fernando Patolsky. Breathing parylene-based nanothin artificial sei for highly-stable long life three-dimensional silicon lithium-ion batteries. *Chemical Engineering Journal*, 429:132077, 2022. doi: https://doi.org/10.1016/j.cej.2021.132077.

[75] Yuxuan Liu, Renzong Hu, Dechao Zhang, Jiangwen Liu, Fang Liu, Jie Cui, Zuopeng Lin, Jinsong Wu, and Min Zhu. Constructing li-rich artificial sei layer in alloy–polymer composite electrolyte to achieve high ionic conductivity for all-solid-state lithium metal batteries. *Advanced Materials*, 33(11):2004711, 2021. doi: https://doi.org/10.1002/adma.202004711.

[76] Yicheng Zhong, Yuanmao Chen, Yifeng Cheng, Qinglu Fan, Huajun Zhao, Huaiyu Shao, Yanqing Lai, Zhicong Shi, Xi Ke, and Zaiping Guo. Li alginate-based artificial sei layer for stable lithium metal anodes. *ACS Applied Materials*

& Interfaces, 11(41):37726–37731, 2019. doi: https://doi.org/10.1021/acsami.9b12634.

[77] Shilun Gao, Feiyuan Sun, Nian Liu, Huabin Yang, and Peng-Fei Cao. Ionic conductive polymers as artificial solid electrolyte interphase films in li metal batteries — a review. *Materials Today*, 40:140–159, 2020. ISSN 1369-7021. doi: https://doi.org/10.1016/j.mattod.2020.06.011. URL `https://www.sciencedirect.com/science/article/pii/S136970212030225X`.

[78] Jun-Fan Ding, Rui Xu, Chong Yan, Bo-Quan Li, Hong Yuan, and Jia-Qi Huang. A review on the failure and regulation of solid electrolyte interphase in lithium batteries. *Journal of Energy Chemistry*, 59:306–319, August 2021. ISSN 2095-4956. doi: 10.1016/j.jechem.2020.11.016.

[79] Xinhua Liu, Xingrui Wang, Lisheng Zhang, Kaiyi Yang, Feiran Li, Justice Delali Akoto, Nadeen S. B. M. Alotaibi, Rui Tan, Muyang Chen, and Mengzheng Ouyang. Lithium dendrite growth modeling under electrode surface morphology control. *Journal of Energy Chemistry*, 117:477–487, June 2026. ISSN 2095-4956. doi: 10.1016/j.jechem.2026.01.006.

[80] Minghua Sun, Hong-Gang Liao, Kaiyang Niu, and Haimei Zheng. Structural and Morphological Evolution of Lead Dendrites during Electrochemical Migration. *Sci. Rep.*, 3(3227):3227, November 2013. ISSN 2045-2322. doi: 10.1038/srep03227.

[81] Ajaykrishna Ramasubramanian, Vitaliy Yurkiv, Tara Foroozan, Marco Ragone, Reza Shahbazian-Yassar, and Farzad Mashayek. Lithium Diffusion Mechanism through Solid–Electrolyte Interphase in Rechargeable Lithium Batteries. *J. Phys. Chem. C*, 123(16):10237–10245, April 2019. ISSN 1932-7447. doi: 10.1021/acs.jpcc.9b00436.

[82] Jianhui Zheng, Zhijin Ju, Baolin Zhang, Jianwei Nai, Tiefeng Liu, Yujing Liu, Qifan Xie, Wenkui Zhang, Yao Wang, and Xinyong Tao. Lithium ion diffusion mechanism on the inorganic components of the solid–electrolyte interphase. *J. Mater. Chem. A*, 9(16):10251–10259, April 2021. ISSN 2050-7488. doi: 10.1039/D0TA11444H.

[83] Fernando Soto, Asma Marzouk, Fedwa El-Mellouhi, and Perla B. Balbuena. Understanding Ionic Diffusion through SEI Components for Lithium-Ion and Sodium-Ion Batteries: Insights from First-Principles Calculations. *Chem. Mater.*, 30(10):3315–3322, May 2018. ISSN 0897-4756. doi: 10.1021/acs.chemmater.8b00635.

[84] Arjun S. Kulathuvayal and Yanqing Su. Ionic Transport through the Solid Electrolyte Interphase in Lithium-Ion Batteries: A Review from First-Principles Perspectives. *ACS Appl. Energy Mater.*, 6(11):5628–5645, June 2023. doi: 10.1021/acsaem.3c00287.

[85] Siqi Shi, Peng Lu, Zhongyi Liu, Yue Qi, Louis G. Hector, Jr., Hong Li, and Stephen J. Harris. Direct Calculation of Li-Ion Transport in the Solid Electrolyte Interphase. *J. Am. Chem. Soc.*, 134(37):15476–15487, September 2012. ISSN 0002-7863. doi: 10.1021/ja305366r.

[86] H. Iddir and L. A. Curtiss. Li Ion Diffusion Mechanisms in Bulk Monoclinic Li2CO3 Crystals from Density Functional Studies. *J. Phys. Chem. C*, 114(48): 20903–20906, December 2010. ISSN 1932-7447. doi: 10.1021/jp1086569.

[87] Shihong Chen, Yaxin Wang, Lijuan Tong, Xiaochuan Chen, Junxiong Wu, Xiaoyan Li, and Yuming Chen. Interfacial Stability and Li+ Transport Trade-Off in Halide-Based SEI Components for LPSC: A First-Principles Study. *Carbon Neutralization*, 5(2):e70141, March 2026. ISSN 2769-3333. doi: 10.1002/cnl2.70141.

[88] Chuang Yu, Swapna Ganapathy, Niek JJ De Klerk, Irek Roslon, Ernst RH van Eck, Arno PM Kentgens, and Marnix Wagemaker. Unravelling li-ion transport from picoseconds to seconds: Bulk versus interfaces in an argyrodite li_6ps_5cl–li_2s all-solid-state li-ion battery. *Journal of the American Chemical Society*, 138(35): 11192–11201, 2016. doi: https://doi.org/10.1021/jacs.6b05066.

[89] Benjamin P. Williams, Haochuan Zhang, Yu Mu, James R. Wilkes, Haden Wikar, and Dunwei Wang. Li+ ion transport at the lithium metal anode: A fundamental picture and future perspectives. *The Journal of Physical Chemistry C*, 126(26): 10644–10652, 2022. doi: 10.1021/acs.jpcc.2c03215. URL `https://doi.org/10.1021/acs.jpcc.2c03215`.

[90] Rui Guo and Betar M Gallant. Li_2o solid electrolyte interphase: probing transport properties at the chemical potential of lithium. *Chemistry of Materials*, 32 (13):5525–5533, 2020. doi: https://doi.org/10.1021/acs.chemmater.0c00333.

[91] J Bourgoin and M Lannoo. *Defects in Solid*. Springer-Verlag, New York, 1984.

[92] K. C. Pandey. Diffusion without vacancies or interstitials: a new concerted exchange mechanism. *Physical Review Letters*, 57(18):2287, 1986. doi: https://doi.org/10.1103/PhysRevLett.57.2287.

[93] Oleg Borodin, Grant D Smith, and Peng Fan. Molecular dynamics simulations of lithium alkyl carbonates. *The Journal of Physical Chemistry B*, 110(45):22773–

22779, 2006. doi: https://doi.org/10.1021/jp0639142.

[94] P. Van Uffelen and M. Suzuki. 3.19 - oxide fuel performance modeling and simulations. In Rudy J.M. Konings, editor, *Comprehensive Nuclear Materials*, pages 535–577. Elsevier, Oxford, 2012. ISBN 978-0-08-056033-5. doi: https://doi.org/10.1016/B978-0-08-056033-5.00071-9. URL `https://www.sciencedirect.com/science/article/pii/B9780080560335000719`.

[95] Chao Wang, Shuan Wang, Yan-Bing He, Linkai Tang, Cuiping Han, Cheng Yang, Marnix Wagemaker, Baohua Li, Quan-Hong Yang, Jang-Kyo Kim, and Kang Feiyu. Combining fast li-ion battery cycling with large volumetric energy density: grain boundary induced high electronic and ionic conductivity in $li_4ti_5o_{12}$ spheres of densely packed nanocrystallites. *Chemistry of Materials*, 27(16):5647–5656, 2015. doi: https://doi.org/10.1021/acs.chemmater.5b02027.

[96] Zachary D Hood, Hui Wang, Amaresh Samuthira Pandian, Jong Kahk Keum, and Chengdu Liang. Li_2ohcl crystalline electrolyte for stable metallic lithium anodes. *Journal of the American Chemical Society*, 138(6):1768–1771, 2016. doi: https://doi.org/10.1021/jacs.5b11851.

[97] Joachim Maier. *Physical chemistry of ionic materials: ions and electrons in solids*. John Wiley & Sons, 2004.

[98] Robert Huggins. *Advanced batteries: materials science aspects*. Springer Science & Business Media, 2008.

[99] Jie Pan, Yang-Tse Cheng, and Yue Qi. General method to predict voltage-dependent ionic conduction in a solid electrolyte coating on electrodes. *Physical Review B*, 91(13):134116, 2015. doi: 10.1103/PhysRevB.91.134116.

[100] AV Chadwick, KW Flack, JH Strange, and J Harding. Defect structures and ionic transport in lithium oxide. *Solid State Ionics*, 28:185–188, 1988. doi: https://doi.org/10.1016/S0167-2738(88)80030-4.

[101] Simon Lorger, Robert Usiskin, and Joachim Maier. Transport and charge carrier chemistry in lithium oxide. *Journal of the Electrochemical Society*, 166(10): A2215, 2019. doi: https://doi.org/10.1149/2.1121910jes.

[102] Liang Tan, Xuexia Lan, Jinwei Chen, Hanyin Zhang, Renzong Hu, and Min Zhu. Lif-induced stable solid electrolyte interphase for a wide temperature sno_2-based anode extensible to -50°c. *Advanced Energy Materials*, 11(39):2101855, 2021. doi: https://doi.org/10.1002/aenm.202101855.

[103] Lan Zhang, Kaihang Zhang, Zhaohui Shi, and Suojiang Zhang. Lif as an artificial sei layer to enhance the high-temperature cycle performance of $li_4ti_5o_{12}$. *Langmuir*, 33(42):11164–11169, 2017. doi: https://doi.org/10.1021/acs.langmuir.7b02031.

[104] Tomoya Kawaguchi, Koki Shimada, Tetsu Ichitsubo, Shunsuke Yagi, and Eiichiro Matsubara. Surface-layer formation by reductive decomposition of $lipf_6$ at relatively high potentials on negative electrodes in lithium ion batteries and its suppression. *Journal of Power Sources*, 271:431–436, 2014. doi: https://doi.org/10.1016/j.jpowsour.2014.08.010.

[105] D Aurbach, M Daroux, P Faguy, and E Yeager. The electrochemistry of noble metal electrodes in aprotic organic solvents containing lithium salts. *Journal of Electroanalytical Chemistry and Interfacial Electrochemistry*, 297(1):225–244, 1991. doi: https://doi.org/10.1016/0022-0728(91)85370-5.

[106] Hidetoshi Sonoki, Masaki Matsui, and Nobuyuki Imanishi. Effect of anion species in early stage of sei formation process. *Journal of the Electrochemical Society*, 166(15):A3593, 2019. doi: http://dx.doi.org/10.1149/2.0191915jes.

[107] Bharathy S Parimalam and Brett L Lucht. Reduction reactions of electrolyte salts for lithium ion batteries: $Lipf_6$, $libf_4$, lidfob, libob, and litfsi. *Journal of the Electrochemical Society*, 165(2):A251, 2018. doi: https://doi.org/10.1149/2.0901802jes.

[108] Oleg Borodin, Xiaoming Ren, Jenel Vatamanu, Arthur von Wald Cresce, Jaroslaw Knap, and Kang Xu. Modeling insight into battery electrolyte electrochemical stability and interfacial structure. *Accounts of Chemical Research*, 50(12):2886–2894, 2017. doi: https://doi.org/10.1021/acs.accounts.7b00486.

[109] Paul G Kitz, Petr Novák, and Erik J Berg. Influence of water contamination on the sei formation in li-ion cells: an operando eqcm-d study. *ACS Applied Materials & Interfaces*, 12(13):15934–15942, 2020. doi: https://doi.org/10.1021/acsami.0c01642.

[110] Ivano E Castelli, Milena Zorko, Thomas M Østergaard, Pedro FBD Martins, Pietro P Lopes, Byron K Antonopoulos, Filippo Maglia, Nenad M Markovic, Dusan Strmcnik, and Jan Rossmeisl. The role of an interface in stabilizing reaction intermediates for hydrogen evolution in aprotic electrolytes. *Chemical Science*, 11(15):3914–3922, 2020. doi: https://doi.org/10.1039/C9SC05768D.

[111] YC Chen, CY Ouyang, LJ Song, and ZL Sun. Electrical and lithium ion dynamics in three main components of solid electrolyte interphase from density functional

theory study. *The Journal of Physical Chemistry C*, 115(14):7044–7049, 2011. doi: https://doi.org/10.1021/jp112202s.

[112] Kazuaki Toyoura, Yukinori Koyama, Akihide Kuwabara, Fumiyasu Oba, and Isao Tanaka. First-principles approach to chemical diffusion of lithium atoms in a graphite intercalation compound. *Physical Review B*, 78(21):214303, 2008. doi: https://doi.org/10.1103/PhysRevB.78.214303.

[113] Hakim Iddir and Larry A Curtiss. Li ion diffusion mechanisms in bulk monoclinic li_2co_3 crystals from density functional studies. *The Journal of Physical Chemistry C*, 114(48):20903–20906, 2010. doi: https://doi.org/10.1021/jp1086569.

[114] Hongjun Ye, Siwei Gui, Zaifa Wang, Jingzhao Chen, Qiunan Liu, Xuedong Zhang, Yushu Tang, Tingting Yang, Congcong Du, Li Hui, Dai Qiushi, Tang Yongfu, Zhang Liqiang, Yang Hui, and Huang Jianyu. In situ measurements of the mechanical properties of electrochemically deposited li_2co_3 and li_2o nanorods. *ACS Applied Materials & Interfaces*, 13(37):44479–44487, 2021. doi: https://doi.org/10.1021/acsami.1c13732.

[115] Junichiro Mizusaki, Hiroaki Tagawa, Ken Saito, Kenshi Uchida, and Meguru Tezuka. Lithium carbonate as a solid electrolyte. *Solid State Ionics*, 53:791–797, 1992. doi: https://doi.org/10.1016/0167-2738(92)90256-O.

[116] Yi Can Zhang, Hiroaki Tagawa, Shukuji Asakura, Junichiro Mizusaki, and Hidekazu Narita. Solid-state electrochemical co_2 sensor by coupling lithium ion conductor (li_2co_3-li_3po_4-asl_2o_3) with oxide ion-electron mixed conductor ($la_{0.9}sr_{0.1}mno_3$). *Solid State Ionics*, 100(3-4):275–281, 1997. doi: https://doi.org/10.1016/S0167-2738(97)00361-5.

[117] Guorong V Zhuang, Guoying Chen, Joongpyo Shim, Xiangyun Song, Philip N Ross, and Thomas J Richardson. Li_2co_3 in $lini_{0.8}co_{0.15}al_{0.05}o_2$ cathodes and its effects on capacity and power. *Journal of Power Sources*, 134(2):293–297, 2004. doi: https://doi.org/10.1016/j.jpowsour.2004.02.030.

[118] Siqi Shi, Yue Qi, Hong Li, and Louis G Hector Jr. Defect thermodynamics and diffusion mechanisms in li_2co_3 and implications for the solid electrolyte interphase in li-ion batteries. *The Journal of Physical Chemistry C*, 117(17):8579–8593, 2013. doi: https://doi.org/10.1021/jp310591u.

[119] Yixuan Guo, Jun Cheng, Zhen Zeng, Yuanyuan Li, Hongqiang Zhang, Deping Li, and Lijie Ci. Li_2co_3: Insights into its blocking effect on li-ion transfer in garnet composite electrolytes. *ACS Applied Energy Materials*, 5(3):2853–2861, 2022. doi: http://dx.doi.org/10.1021/acsaem.1c03529.

[120] Sanghamitra Moharana, Geoff West, Marc Walker, Xinjie S Yan, and Melanie Loveridge. Controlling li dendritic growth in graphite anodes by potassium electrolyte additives for li-ion batteries. *ACS Applied Materials & Interfaces*, 14(37): 42078–42092, 2022. doi: https://doi.org/10.1021/acsami.2c11175.

[121] Guorong V Zhuang and Philip N Ross. Analysis of the chemical composition of the passive film on li-ion battery anodes using attentuated total reflection infrared spectroscopy. *Electrochemical and Solid-State Letters*, 6(7):A136, 2003. doi: http://dx.doi.org/10.1149/1.1575594.

[122] Sang-Pil Kim, Adri CT Van Duin, and Vivek B Shenoy. Effect of electrolytes on the structure and evolution of the solid electrolyte interphase (sei) in li-ion batteries: A molecular dynamics study. *Journal of Power Sources*, 196(20):8590–8597, 2011. doi: https://doi.org/10.1016/j.jpowsour.2011.05.061.

[123] William D Richards, Lincoln J Miara, Yan Wang, Jae Chul Kim, and Gerbrand Ceder. Interface stability in solid-state batteries. *Chemistry of Materials*, 28(1): 266–273, 2016. doi: https://doi.org/10.1021/acs.chemmater.5b04082.

[124] JL Gavartin, CRA Catlow, AL Shluger, PWM Jacobs, and ZA Rycerz. Dynamics of lithium ions in lithium oxide. *Radiation Effects and Defects in Solids*, 134(1-4): 107–110, 1995. doi: https://doi.org/10.1080/10420159508227193.

[125] Hideo Ohno, Satoshi Konishi, Kenji Noda, Hidefumi Takeshita, Hiroshi Yoshida, Hitoshi Watanabe, and Toru Matsuo. Conductivities of a sintered pellet and a single crystal of li_2o. *Journal of Nuclear Materials*, 118(2-3):242–247, 1983. doi: https://doi.org/10.1016/0022-3115(83)90231-3.

[126] Tianbiao Zeng, Xingang Liu, Wenbin Kang, Hanna He, Jihai Zhang, Xiaolong Li, and Chuhong Zhang. In-situ templating growth of homeostatic gep nanobar corals with fast electron-ion transportation pathways for high performance li-ion batteries. *Angewandte Chemie*, 133(50):26422–26429, 2021. doi: https://doi.org/10.1002/anie.202111498.

[127] Masaaki Hirayama, Hedekazu Ido, KyungSu Kim, Woosuk Cho, Kazuhisa Tamura, Jun'ichiro Mizuki, and Ryoji Kanno. Dynamic structural changes at $limn_2o_4$/electrolyte interface during lithium battery reaction. *Journal of the American Chemical Society*, 132(43):15268–15276, 2010. doi: https://doi.org/10.1021/ja105389t.

[128] Joo-Seong Kim, KyungSu Kim, Woosuk Cho, Weon Ho Shin, Ryoji Kanno, and Jang Wook Choi. A truncated manganese spinel cathode for excellent power and lifetime in lithium-ion batteries. *Nano Letters*, 12(12):6358–6365, 2012. doi:

https://doi.org/10.1021/nl303619s.

[129] Ahmed M Hashem, Somia M Abbas, Xu Hou, Ali E Eid, and Ashraf E Abdel-Ghany. Facile one step synthesis method of spinel $limn_2o_4$ cathode material for lithium batteries. *Heliyon*, 5(7):e02027, 2019. doi: https://doi.org/10.1016/j.heliyon.2019.e02027.

[130] Caihua Jiang, Zilong Tang, Shitong Wang, and Zhongtai Zhang. A truncated octahedral spinel $limn_2o_4$ as high-performance cathode material for ultrafast and long-life lithium-ion batteries. *Journal of Power Sources*, 357:144–148, 2017. doi: https://doi.org/10.1016/j.jpowsour.2017.04.079.

[131] Mazharul M Islam and Thomas Bredow. Density functional theory study for the stability and ionic conductivity of li_2o surfaces. *The Journal of Physical Chemistry C*, 113(2):672–676, 2009. doi: https://doi.org/10.1021/jp807048p.

[132] S Panahian Jand and P Kaghazchi. The role of electrostatic effects in determining the structure of lif-graphene interfaces. *Journal of Physics: Condensed Matter*, 26(26):262001, 2014. doi: https://doi.org/10.1088/0953-8984/26/26/262001.

[133] Marco Bruno and Mauro Prencipe. Ab initio quantum-mechanical modeling of the (001),($\bar{1}$01) and (110) surfaces of zabuyelite (li_2co_3). *Surface Science*, 601 (14):3012–3019, 2007. doi: http://dx.doi.org/10.1016/j.susc.2007.05.004.

[134] Nicola Seriani. Ab initio thermodynamics of lithium oxides: from bulk phases to nanoparticles. *Nanotechnology*, 20(44):445703, 2009. doi: https://doi.org/10.1088/0957-4484/20/44/445703.

[135] Maxwell D Radin, Jill F Rodriguez, Feng Tian, and Donald J Siegel. Lithium peroxide surfaces are metallic, while lithium oxide surfaces are not. *Journal of the American Chemical Society*, 134(2):1093–1103, 2012. doi: https://doi.org/10.1021/ja208944x.

[136] Chen Ling, Ruigang Zhang, Kensuke Takechi, and Fuminori Mizuno. Intrinsic barrier to electrochemically decompose li_2co_3 and lioh. *The Journal of Physical Chemistry C*, 118(46):26591–26598, 2014. doi: https://doi.org/10.1021/jp5093306.

[137] Haesun Park, Hyun Seung Koh, and Donald J Siegel. First-principles study of redox end members in lithium–sulfur batteries. *The Journal of Physical Chemistry C*, 119(9):4675–4683, 2015. doi: https://doi.org/10.1021/jp513023v.

[138] Y Ren, Z Qi, X Ma, S Yang, C Zhang, X Tan, and X Liu. First-principles

study of the effect of mechanical strength on ion transport in la-doped lif-sei on the li (001) surface. *Materials Today Chemistry*, 20:100451, 2021. doi: https://doi.org/10.1016/j.mtchem.2021.100451.

[139] Xue-Qiang Zhang, Tao Li, Bo-Quan Li, Rui Zhang, Peng Shi, Chong Yan, Jia-Qi Huang, and Qiang Zhang. A sustainable solid electrolyte interphase for high-energy-density lithium metal batteries under practical conditions. *Angewandte Chemie*, 132(8):3278–3283, 2020. doi: https://doi.org/10.1002/anie.201911724.

[140] Ajaykrishna Ramasubramanian, Vitaliy Yurkiv, Tara Foroozan, Marco Ragone, Reza Shahbazian-Yassar, and Farzad Mashayek. Lithium diffusion mechanism through solid–electrolyte interphase in rechargeable lithium batteries. *The Journal of Physical Chemistry C*, 123(16):10237–10245, 2019. doi: https://doi.org/10.1021/acs.jpcc.9b00436.

[141] Min Feng, Jie Pan, and Yue Qi. Impact of electronic properties of grain boundaries on the solid electrolyte interphases (seis) in li-ion batteries. *The Journal of Physical Chemistry C*, 125(29):15821–15829, 2021. doi: https://doi.org/10.1021/acs.jpcc.1c03186.

[142] S Megahed and W Ebner. Lithium-ion battery for electronic applications. *Journal of Power Sources*, 54(1):155–162, 1995. doi: https://doi.org/10.1016/0378-7753(94)02059-C.

[143] L El Ouatani, R Dedryvère, J-B Ledeuil, C Siret, P Biensan, J Desbrières, and Danielle Gonbeau. Surface film formation on a carbonaceous electrode: Influence of the binder chemistry. *Journal of Power Sources*, 189(1):72–80, 2009. doi: https://doi.org/10.1016/j.jpowsour.2008.11.031.

[144] Van At Nguyen and Christian Kuss. Conducting polymer-based binders for lithium-ion batteries and beyond. *Journal of the Electrochemical Society*, 167 (6):065501, 2020. doi: https://doi.org/10.1149/1945-7111/ab856b.

[145] Lili Chai, Qunting Qu, Longfei Zhang, Ming Shen, Li Zhang, and Honghe Zheng. Chitosan, a new and environmental benign electrode binder for use with graphite anode in lithium-ion batteries. *Electrochimica Acta*, 105:378–383, 2013. ISSN 0013-4686. doi: https://doi.org/10.1016/j.electacta.2013.05.009. URL `https://www.sciencedirect.com/science/article/pii/S0013468613008955`.

[146] EMC Jones, ÖÖ Çapraz, SR White, and NR Sottos. Reversible and irreversible deformation mechanisms of composite graphite electrodes in lithium-ion batteries. *Journal of The Electrochemical Society*, 163(9):A1965, 2016. doi: https://doi.org/10.1149/2.0751609jes.

[147] Hongzhi Wang, Ning Qin, Yingzhi Li, Zhiqiang Li, Fangchang Zhang, Wen Luo, Chun Zeng, Zhouguang Lu, and Hua Cheng. Nafion as a facile binder additive stabilizes solid electrolyte interphase on graphite anode. *Carbon*, 205:435–443, 2023. doi: https://doi.org/10.1016/j.carbon.2023.01.058.

[148] Peng Zhao, Juping Yang, Yuming Shang, Li Wang, Mou Fang, Jianlong Wang, and Xiangming He. Surface modification of polyolefin separators for lithium ion batteries to reduce thermal shrinkage without thickness increase. *Journal of Energy Chemistry*, 24(2):138–144, 2015. doi: https://doi.org/10.1016/S2095-4956(15)60294-7.

[149] Chi-Kyun Park, Zhiwei Zhang, Zhiqiang Xu, Archana Kakirde, Kenny Kang, Chul Chai, George Au, and Laura Cristo. Variables study for the fast charging lithium ion batteries. *Journal of Power Sources*, 165(2):892–896, 2007. doi: https://doi.org/10.1016/j.jpowsour.2006.12.057.

[150] Christopher J Orendorff. The role of separators in lithium-ion cell safety. *The Electrochemical society interface*, 21(2):61, 2012. doi: https://doi.org/10.1149/2.F07122if.

[151] Lupeng Zhang, Xinle Li, Mingrui Yang, and Weihua Chen. High-safety separators for lithium-ion batteries and sodium-ion batteries: advances and perspective. *Energy Storage Materials*, 41:522–545, 2021. doi: https://doi.org/10.1016/j.ensm.2021.06.033.

[152] Wuxia Xu, Zhuyi Wang, Liyi Shi, Ying Ma, Shuai Yuan, Lining Sun, Yin Zhao, Meihong Zhang, and Jiefang Zhu. Layer-by-layer deposition of organic–inorganic hybrid multilayer on microporous polyethylene separator to enhance the electrochemical performance of lithium-ion battery. *ACS Applied Materials & Interfaces*, 7(37):20678–20686, 2015. doi: https://doi.org/10.1021/acsami.5b05457.

[153] XL Zhou, TS Zhao, Liang An, YK Zeng, and Lei Wei. Modeling of ion transport through a porous separator in vanadium redox flow batteries. *Journal of Power Sources*, 327:67–76, 2016. doi: https://doi.org/10.1016/j.jpowsour.2016.07.046.

[154] Bin Li, Qingtao Luo, Xiaoliang Wei, Zimin Nie, Edwin Thomsen, Baowei Chen, Vincent Sprenkle, and Wei Wang. Capacity decay mechanism of microporous separator-based all-vanadium redox flow batteries and its recovery. *ChemSusChem*, 7(2):577–584, 2014. doi: https://doi.org/10.1002/cssc.201300706.

[155] Yuria Saito, Wataru Morimura, Rika Kuratani, and Satoshi Nishikawa. Ion transport in separator membranes of lithium secondary batteries. *The Journal of Physical Chemistry C*, 119(9):4702–4708, 2015. doi: https://doi.org/10.1021/

acs.jpcc.5b00085.

[156] Ilya A Shkrob, James F Wishart, and Daniel P Abraham. What makes fluoroethylene carbonate different? *The Journal of Physical Chemistry C*, 119(27): 14954–14964, 2015. doi: https://doi.org/10.1021/acs.jpcc.5b03591.

[157] Nam-Soon Choi, Kyoung Han Yew, Kyu Youl Lee, Minseok Sung, Ho Kim, and Sung-Soo Kim. Effect of fluoroethylene carbonate additive on interfacial properties of silicon thin-film electrode. *Journal of Power Sources*, 161(2):1254–1259, 2006. doi: https://doi.org/10.1016/j.jpowsour.2006.05.049.

[158] Xue-Qiang Zhang, Xin-Bing Cheng, Xiang Chen, Chong Yan, and Qiang Zhang. Fluoroethylene carbonate additives to render uniform li deposits in lithium metal batteries. *Advanced Functional Materials*, 27(10):1605989, 2017. doi: https://doi.org/10.1002/adfm.201605989.

[159] Jorge L Olmedo-Martínez, Leire Meabe, Raphaël Riva, Gregorio Guzmán-González, Luca Porcarelli, Maria Forsyth, Agurtzane Mugica, Itxaso Calafel, Alejando J Müller, Philippe Lecomte, Jérôme Christine, and Mecerreyes David. Flame retardant polyphosphoester copolymers as solid polymer electrolyte for lithium batteries. *Polymer Chemistry*, 12(23):3441–3450, 2021. doi: https://doi.org/10.1039/D1PY00344E.

[160] Guangmin Zhou, Kai Liu, Yanchen Fan, Mengqi Yuan, Bofei Liu, Wei Liu, Feifei Shi, Yayuan Liu, Wei Chen, Jeffrey Lopez, Zhuo Denys, Zhao Jie, Tsao Yuchi, Huang Xuanyi, and Zhang Qianfan. An aqueous inorganic polymer binder for high performance lithium-sulfur batteries with flame-retardant properties. *ACS Central Science*, 4(2):260–267, 2018. doi: https://doi.org/10.1021/acscentsci.7b00569.

[161] Monisha Monisha, Preetham Permude, Arnab Ghosh, Ajit Kumar, Saad Zafar, Sagar Mitra, and Bimlesh Lochab. Halogen-free flame-retardant sulfur copolymers with stable li–s battery performance. *Energy Storage Materials*, 29:350–360, 2020. doi: https://doi.org/10.1016/j.ensm.2020.04.041.

[162] Piotr Jankowski, Władysław Wieczorek, and Patrik Johansson. Sei-forming electrolyte additives for lithium-ion batteries: development and benchmarking of computational approaches. *Journal of Molecular Modeling*, 23(1):1–9, 2017. doi: https://doi.org/10.1007/s00894-016-3180-0.

[163] Hyeon-Woo Yang, Woo Seung Kang, and Sun-Jae Kim. A significant enhancement of cycling stability at fast charging rate through incorporation of li_3n into lif-based sei in sio_x anode for li-ion batteries. *Electrochimica Acta*, 412:140107,

2022. doi: https://doi.org/10.1016/j.electacta.2022.140107.

[164] Jong Won Park, Doh Hee Park, Soohyun Go, Dae-Hyun Nam, Jihun Oh, Young-Kyu Han, and Hochun Lee. Malonatophosphate as an sei-and cei-forming additive that outperforms malonatoborate for thermally robust lithium-ion batteries. *Energy Storage Materials*, 50:75–85, 2022. doi: https://doi.org/10.1016/j.ensm.2022.05.009.

[165] Weina Xu, Xiaobin Liao, Wangwang Xu, Congli Sun, Kangning Zhao, Yan Zhao, and Chenguo Hu. Gradient sei layer induced by liquid alloy electrolyte additive for high rate lithium metal battery. *Nano Energy*, 88:106237, 2021. doi: https://doi.org/10.1016/j.nanoen.2021.106237.

[166] BA Boukamp, GC Lesh, and RA Huggins. All-solid lithium electrodes with mixed-conductor matrix. *Journal of the Electrochemical Society*, 128(4):725, 1981. doi: https://doi.org/10.1149/1.2127495.

[167] Yafei Huang, Haotian Yang, Yan Gao, Guorong Chen, Yan Li, Liyi Shi, and Dengsong Zhang. Mechanism and solutions of lithium dendrite growth in lithium metal batteries. *Mater. Chem. Front.*, 8(5):1282–1299, February 2024. ISSN 2052-1537. doi: 10.1039/D3QM01151H.

[168] Borong Li, Yu Chao, Mengchao Li, Yuanbin Xiao, Rui Li, Kang Yang, Xiancai Cui, Gui Xu, Lingyun Li, Chengkai Yang, Yan Yu, David P. Wilkinson, and Jiujun Zhang. A Review of Solid Electrolyte Interphase (SEI) and Dendrite Formation in Lithium Batteries. *Electrochem. Energy Rev.*, 6(1):7, December 2023. ISSN 2520-8136. doi: 10.1007/s41918-022-00147-5.

[169] Alex Cipolla, Céline Barchasz, Benoit Mathieu, Benoit Chavillon, and Sébastien Martinet. Effect of electrochemical and mechanical properties of SEI on dendritic growth during lithium deposition on lithium metal electrode. *J. Power Sources*, 545:231898, October 2022. ISSN 0378-7753. doi: 10.1016/j.jpowsour.2022.231898.

[170] Wei Zhong and Ji-Cheng Zhao. First experimental measurement of calcium diffusion in magnesium using novel liquid-solid diffusion couples and forward-simulation analysis. *Scr. Mater.*, 127:92–96, January 2017. ISSN 1359-6462. doi: 10.1016/j.scriptamat.2016.09.008.

[171] Nagraj S. Kulkarni, Robert J. Bruce Warmack, Bala Radhakrishnan, Jerry L. Hunter, Yongho Sohn, Kevin R. Coffey, Graeme E. Murch, and Irina V. Belova. Overview of SIMS-Based Experimental Studies of Tracer Diffusion in Solids and Application to Mg Self-Diffusion. *J. Phase Equilib. Diffus.*, 35(6):762–778, De-

cember 2014. ISSN 1863-7345. doi: 10.1007/s11669-014-0344-4.

[172] Marion H O'Leary. Measurement of the isotope fractionation associated with diffusion of carbon dioxide in aqueous solution. *The Journal of Physical Chemistry*, 88(4):823–825, 1984.

[173] C. Matano. On the Relation between the Diffusion-Coefficients and Concentrations of Solid Metals. *Japan. J. Phys*, 8:109, 1933. URL `https://cir.nii.ac.jp/crid/1570291224988438016`.

[174] J. S. Kirkaldy. DIFFUSION IN MULTICOMPONENT METALLIC SYSTEMS. *Can. J. Phys.*, February 2011. doi: 10.1139/p57-047.

[175] Lars Onsager. Reciprocal Relations in Irreversible Processes. I. *Phys. Rev.*, 37 (4):405–426, February 1931. ISSN 1536-6065. doi: 10.1103/PhysRev.37.405.

[176] Lars Onsager. Reciprocal Relations in Irreversible Processes. II. *Phys. Rev.*, 38 (12):2265–2279, December 1931. ISSN 1536-6065. doi: 10.1103/PhysRev.38.2265.

[177] G. M. Muralikrishna, B. Tas, N. Esakkiraja, V. A. Esin, K. C. Hari Kumar, I. S. Golovin, I. V. Belova, G. E. Murch, A. Paul, and S. V. Divinski. Composition dependence of tracer diffusion coefficients in Fe–Ga alloys: A case study by a tracer-diffusion couple method. *Acta Mater.*, 203:116446, January 2021. ISSN 1359-6454. doi: 10.1016/j.actamat.2020.10.065.

[178] Classical And Quantum Dynamics In Condensed Phase Simulations: Proceedings ... - Google Books, April 2024. URL `https://www.google.com/books/edition/Classical_And_Quantum_Dynamics_In_Conden/UoTVCgAAQBAJ?hl=en&gbpv=1&pg=PR5&printsec=frontcover`. [Online; accessed 9. Apr. 2024].

[179] Graeme Henkelman, Blas P. Uberuaga, and Hannes Jónsson. A climbing image nudged elastic band method for finding saddle points and minimum energy paths. *J. Chem. Phys.*, 113(22):9901–9904, December 2000. ISSN 0021-9606. doi: 10.1063/1.1329672.

[180] George H. Vineyard. Frequency factors and isotope effects in solid state rate processes. *J. Phys. Chem. Solids*, 3(1):121–127, January 1957. ISSN 0022-3697. doi: 10.1016/0022-3697(57)90059-8.

[181] Arthur F. Voter and Jimmie D. Doll. Transition state theory description of surface self-diffusion: Comparison with classical trajectory results. *J. Chem. Phys.*, 80(11):5832–5838, June 1984. ISSN 0021-9606. doi: 10.1063/1.446610.

[182] Andri Arnaldsson. Calculation of quantum mechanical rate constants directly from ab initio atomic forces. *University of Washington*, 2007. URL `https://hdl.handle.net/20.500.11815/717`.

[183] Arjun S. Kulathuvayal and Yanqing Su. Ionic transport through the solid electrolyte interphase in lithium-ion batteries: A review from first-principles perspectives. *ACS Applied Energy Materials*, 6(11):5628–5645, 2023. doi: 10.1021/acsaem.3c00287. URL `https://doi.org/10.1021/acsaem.3c00287`.

[184] Y. Z. Lü, Q. D. Wang, X. Q. Zeng, Y. P. Zhu, and W. J. Ding. Behavior of Mg–6Al–xSi alloys during solution heat treatment at 420°C. *Mater. Sci. Eng., A*, 301(2):255–258, March 2001. ISSN 0921-5093. doi: 10.1016/S0921-5093(00)01780-9.

[185] Sensen Huang, Jinhu Zhang, Yingjie Ma, Shilin Zhang, Sabry S. Youssef, Min Qi, Hao Wang, Jianke Qiu, Dongsheng Xu, Jiafeng Lei, and Rui Yang. Influence of thermal treatment on element partitioning in α+β titanium alloy. *J. Alloys Compd.*, 791:575–585, June 2019. ISSN 0925-8388. doi: 10.1016/j.jallcom.2019.03.332.

[186] Yuxin Li, Wenhui Yang, Rongzhi Dong, and Jianjun Hu. Mlatticeabc: Generic Lattice Constant Prediction of Crystal Materials Using Machine Learning. *ACS Omega*, 6(17):11585–11594, May 2021. doi: 10.1021/acsomega.1c00781.

[187] Chenxi Peng, Phuong Tran, H. Nguyen-Xuan, and A. J. M. Ferreira. Mechanical performance and fatigue life prediction of lattice structures: Parametric computational approach. *Compos. Struct.*, 235:111821, March 2020. ISSN 0263-8223. doi: 10.1016/j.compstruct.2019.111821.

[188] Sangryun Lee, Zhizhou Zhang, and Grace X. Gu. Generative machine learning algorithm for lattice structures with superior mechanical properties. *Mater. Horiz.*, 9(3):952–960, March 2022. ISSN 2051-6347. doi: 10.1039/D1MH01792F.

[189] Tian Wang, Cheng Zhang, Hichem Snoussi, and Gang Zhang. Machine Learning Approaches for Thermoelectric Materials Research. *Adv. Funct. Mater.*, 30(5):1906041, January 2020. ISSN 1616-301X. doi: 10.1002/adfm.201906041.

[190] Han Wei, Hua Bao, and Xiulin Ruan. Perspective: Predicting and optimizing thermal transport properties with machine learning methods. *Energy and AI*, 8:100153, May 2022. ISSN 2666-5468. doi: 10.1016/j.egyai.2022.100153.

[191] Manh-Kien Tran, Satyam Panchal, Vedang Chauhan, Niku Brahmbhatt, Anosh Mevawalla, Roydon Fraser, and Michael Fowler. Python-based scikit-learn ma-

chine learning models for thermal and electrical performance prediction of high-capacity lithium-ion battery. *Int. J. Energy Res.*, 46(2):786–794, February 2022. ISSN 0363-907X. doi: 10.1002/er.7202.

[192] Yao Ren, Kena Zhang, Yue Zhou, and Ye Cao. Phase-Field Simulation and Machine Learning Study of the Effects of Elastic and Plastic Properties of Electrodes and Solid Polymer Electrolytes on the Suppression of Li Dendrite Growth. *ACS Appl. Mater. Interfaces*, 14(27):30658–30671, July 2022. ISSN 1944-8244. doi: 10.1021/acsami.2c03000.

[193] Chade Lv, Xin Zhou, Lixiang Zhong, Chunshuang Yan, Madhavi Srinivasan, Zhi Wei Seh, Chuntai Liu, Hongge Pan, Shuzhou Li, Yonggang Wen, and Qingyu Yan. Machine Learning: An Advanced Platform for Materials Development and State Prediction in Lithium-Ion Batteries. *Adv. Mater.*, 34(25):2101474, June 2022. ISSN 0935-9648. doi: 10.1002/adma.202101474.

[194] Xiao Zhao, Tengfei Luo, and Hui Jin. Predicting Diffusion Coefficients of Binary and Ternary Supercritical Water Mixtures via Machine and Transfer Learning with Deep Neural Network. *Ind. Eng. Chem. Res.*, 61(24):8542–8550, June 2022. ISSN 0888-5885. doi: 10.1021/acs.iecr.2c00017.

[195] Joshua P. Allers, Chad W. Priest, Jeffery A. Greathouse, and Todd M. Alam. Using Computationally-Determined Properties for Machine Learning Prediction of Self-Diffusion Coefficients in Pure Liquids. *J. Phys. Chem. B*, 125(47):12990–13002, December 2021. ISSN 1520-6106. doi: 10.1021/acs.jpcb.1c07092.

[196] Calen J. Leverant, Jacob A. Harvey, Todd M. Alam, and Jeffery A. Greathouse. Machine Learning Self-Diffusion Prediction for Lennard-Jones Fluids in Pores. *J. Phys. Chem. C*, 125(46):25898–25906, November 2021. ISSN 1932-7447. doi: 10.1021/acs.jpcc.1c08297.

[197] Shuya Guo, Xiaoshan Huang, Yizhen Situ, Qiuhong Huang, Kexin Guan, Jiaxin Huang, Wei Wang, Xiangning Bai, Zili Liu, Yufang Wu, and Zhiwei Qiao. Interpretable Machine-Learning and Big Data Mining to Predict Gas Diffusivity in Metal-Organic Frameworks. *Adv. Sci.*, 10(21):2301461, July 2023. ISSN 2198-3844. doi: 10.1002/advs.202301461.

[198] Fabian Jirasek and Hans Hasse. Combining Machine Learning with Physical Knowledge in Thermodynamic Modeling of Fluid Mixtures. *Annual Review of Chemical and Biomolecular Engineering*, (Volume 14, 2023):31–51, June 2023. doi: 10.1146/annurev-chembioeng-092220-025342.

[199] Ismail Adewale Olumegbon, Ibrahim Olanrewaju Alade, Mojeed Opeyemi

Oyedeji, Talal F. Qahtan, and Aliyu Bagudu. Development of machine learning models for the prediction of binary diffusion coefficients of gases. *Eng. Appl. Artif. Intell.*, 123:106279, August 2023. ISSN 0952-1976. doi: 10.1016/j.engappai.2023.106279.

[200] Gaoyang Li, Yonghong Zhu, Yuting Guo, Takuya Mabuchi, Dong Li, Shengfeng Huang, Sirui Wang, Haiyi Sun, and Takashi Tokumasu. Deep Learning to Reveal the Distribution and Diffusion of Water Molecules in Fuel Cell Catalyst Layers. *ACS Appl. Mater. Interfaces*, 15(4):5099–5108, February 2023. ISSN 1944-8244. doi: 10.1021/acsami.2c17198.

[201] OBELiX: A Curated Dataset of Crystal Structures and Experimentally Measured Ionic Conductivities for Lithium Solid-State Electrolytes, February 2025. URL `https://arxiv.org/html/2502.14234v1`. [Online; accessed 30. Apr. 2026].

[202] Jing Zou, Jing Wu, Yizhou Wang, Fengxia Deng, Jizhou Jiang, Yizhou Zhang, Song Liu, Neng Li, Han Zhang, Jiaguo Yu, Tianyou Zhai, and Husam N. Alshareef. Additive-mediated intercalation and surface modification of MXenes. *Chem. Soc. Rev.*, 51(8):2972–2990, April 2022. ISSN 0306-0012. doi: 10.1039/D0CS01487G.

[203] Yangen Zhou, Xiao Zhang, Yu Ding, Jiwoong Bae, Xuelin Guo, Yu Zhao, and Guihua Yu. Redistributing Li-Ion Flux by Parallelly Aligned Holey Nanosheets for Dendrite-Free Li Metal Anodes. *Adv. Mater.*, 32(38):2003920, August 2020. ISSN 1521-4095. doi: 10.1002/adma.202003920.

[204] Yanyue Liu, Jiaxin Yu, Dongfang Guo, Zijiong Li, and Yanjie Su. Ti3C2Tx MXene/graphene nanocomposites: Synthesis and application in electrochemical energy storage. *J. Alloys Compd.*, 815:152403, January 2020. ISSN 0925-8388. doi: 10.1016/j.jallcom.2019.152403.

[205] G. Kresse and J. Furthmüller. Efficient iterative schemes for ab initio total-energy calculations using a plane-wave basis set. *Phys. Rev. B*, 54(16):11169–11186, October 1996. doi: 10.1103/PhysRevB.54.11169.

[206] G. Kresse and D. Joubert. From ultrasoft pseudopotentials to the projector augmented-wave method. *Phys. Rev. B*, 59(3):1758–1775, January 1999. doi: 10.1103/PhysRevB.59.1758.

[207] G. Kresse and J. Furthmüller. Efficiency of ab-initio total energy calculations for metals and semiconductors using a plane-wave basis set. *Comput. Mater. Sci.*, 6 (1):15–50, July 1996. ISSN 0927-0256. doi: 10.1016/0927-0256(96)00008-0.

[208] Philip Pechukas. Transition state theory. *Annual Review of Physical Chemistry*, 32(1):159–177, 1981. doi: https://doi.org/10.1146/annurev.pc.32.100181.001111.

[209] Eugene Wigner. The transition state method. *Transactions of the Faraday Society*, 34:29–41, 1938. doi: https://doi.org/10.1039/TF9383400029.

[210] TJ Delph, P Cao, HS Park, and JA Zimmerman. A harmonic transition state theory model for defect initiation in crystals. *Modelling and Simulation in Materials Science and Engineering*, 21(2):025010, 2013. doi: https://doi.org/10.1088/0965-0393/21/2/025010.

[211] Aleksandr O Lykhin, Danil S Kaliakin, Gwen E dePolo, Alexander A Kuzubov, and Sergey A Varganov. Nonadiabatic transition state theory: Application to intersystem crossings in the active sites of metal-sulfur proteins. *International Journal of Quantum Chemistry*, 116(10):750–761, 2016. doi: https://doi.org/10.1002/qua.25124.

[212] George H Vineyard. Frequency factors and isotope effects in solid state rate processes. *Journal of Physics and Chemistry of Solids*, 3(1-2):121–127, 1957. doi: https://doi.org/10.1016/0022-3697(57)90059-8.

[213] Arthur F Voter and Jimmie D Doll. Transition state theory description of surface self-diffusion: Comparison with classical trajectory results. *The Journal of Chemical Physics*, 80(11):5832–5838, 1984. doi: https://doi.org/10.1063/1.446610.

[214] Pavel F Bessarab, Valery M Uzdin, and Hannes Jónsson. Harmonic transition-state theory of thermal spin transitions. *Physical Review B*, 85(18):184409, 2012. doi: https://doi.org/10.1103/PhysRevB.85.184409.

[215] Vilhjálmur Ásgeirsson, Benedikt Orri Birgisson, Ragnar Bjornsson, Ute Becker, Frank Neese, Christoph Riplinger, and Hannes Jónsson. Nudged elastic band method for molecular reactions using energy-weighted springs combined with eigenvector following. *Journal of Chemical Theory and Computation*, 17(8):4929–4945, 2021. doi: https://doi.org/10.1021/acs.jctc.1c00462.

[216] Andri Arnaldsson. Calculation of quantum mechanical rate constants directly from ab initio atomic forces. pages 5–19, 2007. URL `https://hdl.handle.net/20.500.11815/717`.

[217] Gregory Mills, Hannes Jónsson, and Gregory K Schenter. Reversible work transition state theory: application to dissociative adsorption of hydrogen. *Surface Science*, 324(2-3):305–337, 1995. doi: https://doi.org/10.1016/0039-6028(94)00731-4.

[218] Donald G Truhlar. Accuracy of trajectory calculations and transition state theory for thermal rate constants of atom transfer reactions. *Journal of Physical Chemistry*, 83(1):188–199, 1979. doi: https://doi.org/10.1021/j100464a025.

[219] Hannes Jónsson, Greg Mills, and Karsten W Jacobsen. Nudged elastic band method for finding minimum energy paths of transitions. In *Classical and quantum dynamics in condensed phase simulations*, pages 385–404. World Scientific, 1998. doi: https://doi.org/10.1142/9789812839664_0016.

[220] Shin Sato. On a new method of drawing the potential energy surface. *The Journal of Chemical Physics*, 23(3):592–593, 1955. doi: https://doi.org/10.1063/1.1742043.

[221] Graeme Henkelman, Blas P Uberuaga, and Hannes Jónsson. A climbing image nudged elastic band method for finding saddle points and minimum energy paths. *The Journal of chemical physics*, 113(22):9901–9904, 2000. doi: https://doi.org/10.1063/1.1329672.

[222] Graeme Henkelman and Hannes Jónsson. Improved tangent estimate in the nudged elastic band method for finding minimum energy paths and saddle points. *The Journal of Chemical Physics*, 113(22):9978–9985, 2000. doi: https://doi.org/10.1063/1.1323224.

[223] Graeme Henkelman, Gísli Jóhannesson, and Hannes Jónsson. Methods for finding saddle points and minimum energy paths. In *Theoretical methods in condensed phase chemistry*, pages 269–302. Springer, 2002. doi: https://doi.org/10.1063/1.1329672.

[224] Ting Zhu, Ju Li, Amit Samanta, Hyoung Gyu Kim, and Subra Suresh. Interfacial plasticity governs strain rate sensitivity and ductility in nanostructured metals. *Proceedings of the National Academy of Sciences*, 104(9):3031–3036, 2007. doi: https://doi.org/10.1073/pnas.0611097104.

[225] Dengke Chen, Luke L Costello, Clint B Geller, Ting Zhu, and David L McDowell. Atomistic modeling of dislocation cross-slip in nickel using free-end nudged elastic band method. *Acta Materialia*, 168:436–447, 2019. doi: https://doi.org/10.1016/j.actamat.2019.02.035.

[226] Wu Li, Jesús Carrete, Nebil A. Katcho, and Natalio Mingo. ShengBTE: A solver of the Boltzmann transport equation for phonons. *Comput. Phys. Commun.*, 185 (6):1747–1758, June 2014. ISSN 0010-4655. doi: 10.1016/j.cpc.2014.02.015.

[227] Ting Liang, Wen-Qi Chen, Cui-E. Hu, Xiang-Rong Chen, and Qi-Feng Chen.

Lattice dynamics and thermal conductivity of lithium fluoride via first-principles calculations. *Solid State Commun.*, 272:28–32, April 2018. ISSN 0038-1098. doi: 10.1016/j.ssc.2018.01.004.

[228] Atsushi Togo, Laurent Chaput, Terumasa Tadano, and Isao Tanaka. Implementation strategies in phonopy and phono3py. *J. Phys. Condens. Matter*, 35(35): 353001, 2023. doi: 10.1088/1361-648X/acd831.

[229] Atsushi Togo. First-principles phonon calculations with phonopy and phono3py. *J. Phys. Soc. Jpn.*, 92(1):012001, 2023. doi: 10.7566/JPSJ.92.012001.

[230] Laurent Chaput. Direct Solution to the Linearized Phonon Boltzmann Equation. *Phys. Rev. Lett.*, 110(26):265506, June 2013. doi: 10.1103/PhysRevLett.110.265506.

[231] Gyaneshwar P. Srivastava. *The Physics of Phonons*. Taylor & Francis, Andover, England, UK, September 2022. ISBN 978-1-00314127-3. doi: 10.1201/9781003141273.

[232] J.M. Ziman. *Electrons and Phonons: The Theory of Transport Phenomena in Solids*. International series of monographs on physics. OUP Oxford, 2001. ISBN 9780198507796. URL `https://books.google.com/books?id=UtEy63pjngsC`.

[233] Zhen Tong, Shouhang Li, Xiulin Ruan, and Hua Bao. Comprehensive first-principles analysis of phonon thermal conductivity and electron-phonon coupling in different metals. *Phys. Rev. B*, 100(14):144306, October 2019. ISSN 2469-9969. doi: 10.1103/PhysRevB.100.144306.

[234] Atsushi Togo. First-principles Phonon Calculations with Phonopy and Phono3py. *J. Phys. Soc. Jpn.*, 92(1):012001, December 2022. ISSN 0031-9015. doi: 10.7566/JPSJ.92.012001.

[235] T.M. Tritt. *Thermal Conductivity: Theory, Properties, and Applications*. Physics of Solids and Liquids. Springer US, 2005. ISBN 9780306483271. URL `https://books.google.com/books?id=whJNfKmziiIC`.

[236] Ask Hjorth Larsen, Jens Jørgen Mortensen, Jakob Blomqvist, Ivano E. Castelli, Rune Christensen, Marcin Dułak, Jesper Friis, Michael N. Groves, Bjørk Hammer, Cory Hargus, Eric D. Hermes, Paul C. Jennings, Peter Bjerre Jensen, James Kermode, John R. Kitchin, Esben Leonhard Kolsbjerg, Joseph Kubal, Kristen Kaasbjerg, Steen Lysgaard, Jón Bergmann Maronsson, Tristan Maxson, Thomas Olsen, Lars Pastewka, Andrew Peterson, Carsten Rostgaard, Jakob Schiøtz, Ole Schütt, Mikkel Strange, Kristian S. Thygesen, Tejs Vegge, Lasse Vilhelmsen,

Michael Walter, Zhenhua Zeng, and Karsten W. Jacobsen. The atomic simulation environment—a Python library for working with atoms. *J. Phys.: Condens. Matter*, 29(27):273002, June 2017. ISSN 0953-8984. doi: 10.1088/1361-648X/aa680e.

[237] Shyue Ping Ong, William Davidson Richards, Anubhav Jain, Geoffroy Hautier, Michael Kocher, Shreyas Cholia, Dan Gunter, Vincent L. Chevrier, Kristin A. Persson, and Gerbrand Ceder. Python Materials Genomics (pymatgen): A robust, open-source python library for materials analysis. *Comput. Mater. Sci.*, 68: 314–319, February 2013. ISSN 0927-0256. doi: 10.1016/j.commatsci.2012.10.028.

[238] K. Momma and F. Izumi. VESTA: a three-dimensional visualization system for electronic and structural analysis. *J. Appl. Crystallogr.*, 41(3):653–658, June 2008. ISSN 0021-8898. doi: 10.1107/S0021889808012016.

[239] Alexander Stukowski. Visualization and analysis of atomistic simulation data with OVITO–the Open Visualization Tool. *Model. Simul. Mater. Sci. Eng.*, 18(1): 015012, December 2009. ISSN 0965-0393. doi: 10.1088/0965-0393/18/1/015012.

[240] Munetsugu Matsuo and Masayoshi Yamazaki. Diffusion database kakusan, July 2023. URL `https://samurai.nims.go.jp/misc_reports/21abef80-9b37-4d6e-8220-e025841f83e5?locale=en`. [Online; accessed 20. Jul. 2023].

[241] M Yamazaki, Y Xu, M Murata, H Tanaka, K Kamihira, and K Kimura. Nims structural materials databases and cross search engine œ matnavi. *BALTICA VII*, page 193, Jun 2007.

[242] Toshio Ogata and Masayoshi Yamazaki. New stage of matnavi, materials database at nims. 2012.

[243] Logan Ward, Alexander Dunn, Alireza Faghaninia, Nils E. R. Zimmermann, Saurabh Bajaj, Qi Wang, Joseph Montoya, Jiming Chen, Kyle Bystrom, Maxwell Dylla, Kyle Chard, Mark Asta, Kristin A. Persson, G. Jeffrey Snyder, Ian Foster, and Anubhav Jain. Matminer: An open source toolkit for materials data mining. *Comput. Mater. Sci.*, 152:60–69, September 2018. ISSN 0927-0256. doi: 10.1016/j.commatsci.2018.05.018.

[244] Logan Ward, Ankit Agrawal, Alok Choudhary, and Christopher Wolverton. A general-purpose machine learning framework for predicting properties of inorganic materials. *npj Comput. Mater.*, 2(16028):1–7, August 2016. ISSN 2057-3960. doi: 10.1038/npjcompumats.2016.28.

[245] Jacob Benesty, Jingdong Chen, Yiteng Huang, and Israel Cohen. Pearson

Correlation Coefficient. In *Noise Reduction in Speech Processing*, pages 1–4. Springer, Berlin, Germany, March 2009. ISBN 978-3-642-00296-0. doi: 10.1007/978-3-642-00296-0_5.

[246] The pandas development team. pandas-dev/pandas: Pandas, February 2020. URL `https://doi.org/10.5281/zenodo.3509134`.

[247] Henry F. Kaiser. The Application of Electronic Computers to Factor Analysis. *Educational and Psychological Measurement*, 20(1):141–151, April 1960. ISSN 0013-1644. doi: 10.1177/001316446002000116.

[248] Leandre R Fabrigar, Duane T Wegener, Robert C MacCallum, and Erin J Strahan. Evaluating the use of exploratory factor analysis in psychological research. *Psychological methods*, 4(3):272, 1999. doi: https://doi.org/10.1037/1082-989X.4.3.272.

[249] F. Pedregosa, G. Varoquaux, A. Gramfort, V. Michel, B. Thirion, O. Grisel, M. Blondel, P. Prettenhofer, R. Weiss, V. Dubourg, J. Vanderplas, A. Passos, D. Cournapeau, M. Brucher, M. Perrot, and E. Duchesnay. Scikit-learn: Machine learning in Python. *Journal of Machine Learning Research*, 12:2825–2830, 2011.

[250] Diederik P Kingma and Max Welling. Auto-encoding variational bayes. *arXiv preprint arXiv:1312.6114*, 2013.

[251] CitrineInformatics. lolo, April 2024. URL `https://github.com/CitrineInformatics/lolo`. [Online; accessed 23. Apr. 2024].

[252] Julia Ling, Maxwell Hutchinson, Erin Antono, Sean Paradiso, and Bryce Meredig. High-Dimensional Materials and Process Optimization Using Data-Driven Experimental Design with Well-Calibrated Uncertainty Estimates. *Integr. Mater. Manuf. Innov.*, 6(3):207–217, September 2017. ISSN 2193-9772. doi: 10.1007/s40192-017-0098-z.

[253] Ian T. Jolliffe and Jorge Cadima. Principal component analysis: a review and recent developments. *Philos. Trans. Royal Soc. A*, 374(2065), April 2016. ISSN 1471-2962. doi: 10.1098/rsta.2015.0202.

[254] S. Panahian Jand and P. Kaghazchi. The role of electrostatic effects in determining the structure of LiF-graphene interfaces. *J. Phys.: Condens. Matter*, 26 (26):262001, May 2014. ISSN 0953-8984. doi: 10.1088/0953-8984/26/26/262001.

[255] Josh Abramson, Jonas Adler, Jack Dunger, Richard Evans, Tim Green, Alexander Pritzel, Olaf Ronneberger, Lindsay Willmore, Andrew J. Ballard,

Joshua Bambrick, Sebastian W. Bodenstein, David A. Evans, Chia-Chun Hung, Michael O'Neill, David Reiman, Kathryn Tunyasuvunakool, Zachary Wu, Akvilė Žemgulytė, Eirini Arvaniti, Charles Beattie, Ottavia Bertolli, Alex Bridgland, Alexey Cherepanov, Miles Congreve, Alexander I. Cowen-Rivers, Andrew Cowie, Michael Figurnov, Fabian B. Fuchs, Hannah Gladman, Rishub Jain, Yousuf A. Khan, Caroline M. R. Low, Kuba Perlin, Anna Potapenko, Pascal Savy, Sukhdeep Singh, Adrian Stecula, Ashok Thillaisundaram, Catherine Tong, Sergei Yakneen, Ellen D. Zhong, Michal Zielinski, Augustin Žídek, Victor Bapst, Pushmeet Kohli, Max Jaderberg, Demis Hassabis, and John M. Jumper. Accurate structure prediction of biomolecular interactions with AlphaFold 3. *Nature*, 630:493–500, June 2024. ISSN 1476-4687. doi: 10.1038/s41586-024-07487-w.

[256] Rui Jiao, Wenbing Huang, Peijia Lin, Jiaqi Han, Pin Chen, Yutong Lu, and Yang Liu. Crystal Structure Prediction by Joint Equivariant Diffusion. *Advances in Neural Information Processing Systems*, 36:17464–17497, December 2023. URL `https://proceedings.neurips.cc/paper_files/paper/2023/hash/38b787fc530d0b31825827e2cc306656-Abstract-Conference.html`.

[257] Joseph L. Watson, David Juergens, Nathaniel R. Bennett, Brian L. Trippe, Jason Yim, Helen E. Eisenach, Woody Ahern, Andrew J. Borst, Robert J. Ragotte, Lukas F. Milles, Basile I. M. Wicky, Nikita Hanikel, Samuel J. Pellock, Alexis Courbet, William Sheffler, Jue Wang, Preetham Venkatesh, Isaac Sappington, Susana Vázquez Torres, Anna Lauko, Valentin De Bortoli, Emile Mathieu, Sergey Ovchinnikov, Regina Barzilay, Tommi S. Jaakkola, Frank DiMaio, Minkyung Baek, and David Baker. De novo design of protein structure and function with RFdiffusion. *Nature*, 620:1089–1100, August 2023. ISSN 1476-4687. doi: 10.1038/s41586-023-06415-8.

[258] Arne Schneuing, Charles Harris, Yuanqi Du, Kieran Didi, Arian Jamasb, Ilia Igashov, Weitao Du, Carla Gomes, Tom L. Blundell, Pietro Lio, Max Welling, Michael Bronstein, and Bruno Correia. Structure-based drug design with equivariant diffusion models. *Nat. Comput. Sci.*, 4:899–909, December 2024. ISSN 2662-8457. doi: 10.1038/s43588-024-00737-x.

[259] Suvo Banik, Debdas Dhabal, Henry Chan, Sukriti Manna, Mathew Cherukara, Valeria Molinero, and Subramanian KRS Sankaranarayanan. Cegann: Crystal edge graph attention neural network for multiscale classification of materials environment. *npj Computational Materials*, 9(1):23, 2023.

[260] Vijay Prakash Dwivedi, Chaitanya K. Joshi, Anh Tuan Luu, Thomas Laurent, Yoshua Bengio, and Xavier Bresson. Benchmarking graph neural networks. *Journal of Machine Learning Research*, 24(43):1–48, 2023. URL `http://jmlr.org/papers/v24/22-0567.html`.

[261] Mohammad Soleymanibrojeni, Celso Ricardo Caldeira Rego, Meysam Esmaeilpour, and Wolfgang Wenzel. An active learning approach to model solid-electrolyte interphase formation in Li-ion batteries. *J. Mater. Chem. A*, 12(4): 2249–2266, 2024. doi: 10.1039/D3TA06054C.

[262] Wen-Qing Li, Gang Wu, Juan Manuel Arce-Ramos, Yang Hao Lau, and Man-Fai Ng. Enabling accurate modelling of materials for a solid electrolyte interphase in lithium-ion batteries using effective machine learning interatomic potentials. *Mater. Horiz.*, 12(24):10770–10781, 2025. doi: 10.1039/D5MH01343G.

[263] Zhaojun Sun, Xin Li, Yiming Wu, Qilin Gu, and Shiyou Zheng. Machine Learning-Assisted Simulations and Predictions for Battery Interfaces. *Advanced Intelligent Systems*, 7(6):2400626, February 2025. ISSN 2640-4567. doi: 10.1002/aisy.202400626.

[264] Anubhav Jain, Shyue Ping Ong, Geoffroy Hautier, Wei Chen, William Davidson Richards, Stephen Dacek, Shreyas Cholia, Dan Gunter, David Skinner, Gerbrand Ceder, and Kristin a. Persson. The Materials Project: A materials genome approach to accelerating materials innovation. *APL Materials*, 1(1):011002, 2013. ISSN 2166532X. doi: 10.1063/1.4812323. URL `http://link.aip.org/link/AMPADS/v1/i1/p011002/s1&Agg=doi`.

[265] P. E. Blöchl. Projector augmented-wave method. *Phys. Rev. B*, 50(24):17953–17979, December 1994. doi: 10.1103/PhysRevB.50.17953.

[266] John P. Perdew, Adrienn Ruzsinszky, Gábor I. Csonka, Oleg A. Vydrov, Gustavo E. Scuseria, Lucian A. Constantin, Xiaolan Zhou, and Kieron Burke. Restoring the Density-Gradient Expansion for Exchange in Solids and Surfaces. *Phys. Rev. Lett.*, 100(13):136406, April 2008. doi: 10.1103/PhysRevLett.100.136406.

[267] John P. Perdew, Kieron Burke, and Matthias Ernzerhof. Generalized Gradient Approximation Made Simple. *Phys. Rev. Lett.*, 77(18):3865–3868, October 1996. doi: 10.1103/PhysRevLett.77.3865.

[268] Handan Yildirim, Alper Kinaci, Maria K. Y. Chan, and Jeffrey P. Greeley. First-Principles Analysis of Defect Thermodynamics and Ion Transport in Inorganic SEI Compounds: LiF and NaF. *ACS Appl. Mater. Interfaces*, 7(34):18985–18996, September 2015. ISSN 1944-8244. doi: 10.1021/acsami.5b02904.

[269] SCRIPTS — Transition State Tools for VASP, October 2025. URL `https://theory.cm.utexas.edu/vtsttools/scripts.html`. [Online; accessed 17. Mar. 2026].

[270] A. Zur and T. C. McGill. Lattice match: An application to heteroepitaxy. *J. Appl. Phys.*, 55(2):378–386, January 1984. ISSN 0021-8979. doi: 10.1063/1.333084.

[271] Mohammad Alghadeer, Nufida D. Aisyah, Mahmoud Hezam, Saad M. Alqahtani, Ahmer A. B. Baloch, and Fahhad H. Alharbi. Machine learning prediction of materials properties from chemical composition: Status and prospects. *Chem. Phys. Rev.*, 5(4):041313, December 2024. doi: 10.1063/5.0235541.

[272] Arjun S. Kulathuvayal, Yi Rao, and Yanqing Su. Elemental diffusion coefficient prediction in conventional alloys using machine learning. *Chem. Phys. Rev.*, 5 (4):041402, October 2024. doi: 10.1063/5.0222001.

[273] Cheuk Hei Chan, Mingzi Sun, and Bolong Huang. Application of machine learning for advanced material prediction and design. *EcoMat*, 4(4):e12194, July 2022. ISSN 2567-3173. doi: 10.1002/eom2.12194.

[274] Son Gyo Jung, Guwon Jung, and Jacqueline M. Cole. Automatic Prediction of Band Gaps of Inorganic Materials Using a Gradient Boosted and Statistical Feature Selection Workflow. *J. Chem. Inf. Model.*, 64(4):1187–1200, February 2024. ISSN 1549-9596. doi: 10.1021/acs.jcim.3c01897.

[275] Johannes Gasteiger, Janek Groß, and Stephan Günnemann. Directional message passing for molecular graphs. In *International Conference on Learning Representations (ICLR)*, 2020.

[276] Johannes Gasteiger, Shankari Giri, Johannes T. Margraf, and Stephan Günnemann. Fast and uncertainty-aware directional message passing for non-equilibrium molecules. In *Machine Learning for Molecules Workshop, NeurIPS*, 2020.

[277] Abdalaziz Al-Maeeni, Mikhail Lazarev, Nikita Kazeev, Kostya S. Novoselov, and Andrey Ustyuzhanin. Review on automated 2D material design. *2D Mater.*, 11 (3):032002, June 2024. ISSN 2053-1583. doi: 10.1088/2053-1583/ad4661.

[278] Patrick Reiser, Marlen Neubert, André Eberhard, Luca Torresi, Chen Zhou, Chen Shao, Houssam Metni, Clint van Hoesel, Henrik Schopmans, Timo Sommer, and Pascal Friederich. Graph neural networks for materials science and chemistry. *Commun. Mater.*, 3(93):93, November 2022. ISSN 2662-4443. doi: 10.1038/s43246-022-00315-6.

[279] Odin Zhang, Haitao Lin, Xujun Zhang, Xiaorui Wang, Zhenxing Wu, Qing Ye, Weibo Zhao, Jike Wang, Kejun Ying, Yu Kang, Chang-Yu Hsieh, and Tingjun

Hou. Graph Neural Networks in Modern AI-Aided Drug Discovery. *Chem. Rev.*, 125(20):10001–10103, October 2025. ISSN 0009-2665. doi: 10.1021/acs.chemrev.5c00461.

[280] Tian Xie, Xiang Fu, Octavian-Eugen Ganea, Regina Barzilay, and Tommi Jaakkola. Crystal Diffusion Variational Autoencoder for Periodic Material Generation. *arXiv*, October 2021. doi: 10.48550/arXiv.2110.06197.

[281] Christopher P. Burgess, Irina Higgins, Arka Pal, Loic Matthey, Nick Watters, Guillaume Desjardins, and Alexander Lerchner. Understanding disentangling in β-VAE. *arXiv*, April 2018. doi: 10.48550/arXiv.1804.03599.

[282] Min Feng, Jie Pan, and Yue Qi. Impact of Electronic Properties of Grain Boundaries on the Solid Electrolyte Interphases (SEIs) in Li-ion Batteries. *J. Phys. Chem. C*, 125(29):15821–15829, July 2021. ISSN 1932-7447. doi: 10.1021/acs.jpcc.1c03186.

[283] Ajaykrishna Ramasubramanian, Vitaliy Yurkiv, Tara Foroozan, Marco Ragone, Reza Shahbazian-Yassar, and Farzad Mashayek. Stability of Solid-Electrolyte Interphase (SEI) on the Lithium Metal Surface in Lithium Metal Batteries (LMBs). *ACS Appl. Energy Mater.*, 3(11):10560–10567, November 2020. doi: 10.1021/acsaem.0c01605.

[284] Wei Liu, Pengcheng Liu, and David Mitlin. Review of emerging concepts in sei analysis and artificial sei membranes for lithium, sodium, and potassium metal battery anodes. *Advanced Energy Materials*, 10(43):2002297, 2020. doi: https://doi.org/10.1002/aenm.202070177.

[285] Kang Xu. Electrolytes and interphases in li-ion batteries and beyond. *Chemical Reviews*, 114(23):11503–11618, 2014. doi: 10.1021/cr500003w.

[286] A. S. Hewage et al. Ionic transport mechanisms through the solid electrolyte interphase in lithium-ion batteries. *Journal of Materials Chemistry A*, 2023. doi: 10.1039/D3TA02048G.

[287] Charles Monroe and John Newman. The impact of elastic deformation on deposition kinetics at lithium/polymer interfaces. *Journal of The Electrochemical Society*, 152(2):A396–A404, 2005. doi: 10.1149/1.1850854.

[288] Xinyue Zhang, Aoxuan Wang, Xingjiang Liu, and Jiayan Luo. Dendrites in Lithium Metal Anodes: Suppression, Regulation, and Elimination. *Acc. Chem. Res.*, 52(11):3223–3232, November 2019. ISSN 0001-4842. doi: 10.1021/acs.accounts.9b00437.

[289] Cheng Yan et al. Lithium metal protection through artificial solid electrolyte interphase materials. *Advanced Energy Materials*, 9(7):1801907, 2019. doi: 10.1002/aenm.201801907.

[290] Xin-Bing Cheng, Rui Zhang, Cheng-Zhang Zhao, and Qiang Zhang. Toward safe lithium metal anode in rechargeable batteries: A review. *Chemical Reviews*, 117 (15):10403–10473, 2017. doi: 10.1021/acs.chemrev.7b00115.

[291] Wei Liu, Pengcheng Liu, and David Mitlin. Review of Emerging Concepts in SEI Analysis and Artificial SEI Membranes for Lithium, Sodium, and Potassium Metal Battery Anodes. *Adv. Energy Mater.*, 10(43):2002297, November 2020. ISSN 1614-6832. doi: 10.1002/aenm.202002297.

[292] M. Naguib, M. Kurtoglu, V. Presser, J. Lu, J. Niu, M. Heon, L. Hultman, Y. Gogotsi, and M. W. Barsoum. Two-dimensional nanocrystals produced by exfoliation of Ti3AlC2. *Advanced Materials*, 23(37):4248–4253, 2011. doi: 10.1002/adma.201102306.

[293] Babak Anasori, Maria R. Lukatskaya, and Yury Gogotsi. 2D metal carbides and nitrides (MXenes) for energy storage. *Nature Reviews Materials*, 2(2):16098, 2017. doi: 10.1038/natrevmats.2016.98.

[294] Xiao-Qing Zhang et al. Advanced solid electrolyte interphases for lithium metal anodes. *Advanced Materials*, 32(7):1908445, 2020. doi: 10.1002/adma.201908445.

[295] Wei Zhou et al. Mxene-based artificial interface toward highly stable lithium metal anodes. *Energy Storage Materials*, 24:435–442, 2020. doi: 10.1016/j.ensm.2019.05.028.

[296] D. Lin et al. Mxene-based materials for lithium metal anodes. *Advanced Functional Materials*, 31(9):2008081, 2021. doi: 10.1002/adfm.202008081.

[297] Qiang Tang and Zhou Zhou. Graphene-analogous low-dimensional materials. *Progress in Materials Science*, 58(8):1244–1315, 2018. doi: 10.1016/j.pmatsci.2013.04.003.

[298] Yue Xie et al. Role of surface structure on li-ion energy storage capacity of two-dimensional transition-metal carbides. *Journal of the American Chemical Society*, 136(17):6385–6394, 2014. doi: 10.1021/ja501520b.

[299] M. Khazaei, M. Arai, T. Sasaki, C. Y. Chung, N. S. Venkataramanan, M. Estili, Y. Sakka, and Y. Kawazoe. Novel electronic and magnetic properties of two-dimensional transition metal carbides and nitrides. *Advanced Functional*

Materials, 23(17):2185–2192, 2013. doi: 10.1002/adfm.201202502.

[300] Alexandre Champagne et al. Computational design of mxenes for energy storage and conversion. *Physical Chemistry Chemical Physics*, 22(18):10489–10527, 2020. doi: 10.1039/D0CP00903E.

[301] Chuanliang Wei, Yuan Tao, Yongling An, Yuan Tian, Yuchan Zhang, Jinkui Feng, and Yitai Qian. Recent Advances of Emerging 2D MXene for Stable and Dendrite-Free Metal Anodes. *Adv. Funct. Mater.*, 30(45):2004613, November 2020. ISSN 1616-301X. doi: 10.1002/adfm.202004613.

[302] Chao Zhang et al. Lithiophilic mxene enables dendrite-free lithium metal anodes. *Nano Energy*, 53:98–107, 2018. doi: 10.1016/j.nanoen.2018.08.037.

[303] Maria R. Lukatskaya, Oleg Mashtalir, Chang E. Ren, Yury Dall'Agnese, Patrice Rozier, Pierre-Louis Taberna, Michael Naguib, Patrice Simon, Michel W. Barsoum, and Yury Gogotsi. Cation intercalation and high volumetric capacitance of two-dimensional titanium carbide. *Science*, 341(6153):1502–1505, 2013. doi: 10.1126/science.1241488.

[304] Michael Naguib, Joseph Halim, Jun Lu, Kevin M. Cook, Lars Hultman, Yury Gogotsi, and Michel W. Barsoum. New two-dimensional niobium and vanadium carbides as promising materials for li-ion batteries. *Journal of the American Chemical Society*, 135(43):15966–15969, 2013. doi: 10.1021/ja405735d.

[305] Ming Li, Jing Lu, Kai Luo, Yuzhang Li, Kun Chang, Kai Chen, Jie Zhou, Johanna Rosen, Lars Hultman, Per Eklund, Per O. Å. Persson, Shaojun Du, Zhifeng Chai, Qing Huang, et al. Element replacement approach by reaction with lewis acidic molten salts to synthesize nanolaminated max phases and mxenes. *Journal of the American Chemical Society*, 141(11):4730–4737, 2019. doi: 10.1021/jacs.8b10339.

[306] Diego Ontiveros. MXenes Database, April 2026. URL `https://diegonti.github.io/mxene-db`. [Online; accessed 17. May 2026].

[307] IISc. Mxene Database | Project aNANt, May 2026. URL `https://anant.mrc.iisc.ac.in/apps/mxene`. [Online; accessed 17. May 2026].

[308] Diego Ontiveros, Sergi Vela, Francesc Viñes, and Carmen Sousa. MXgap: A MXene Learning Tool for Bandgap Prediction. *ACS Catal.*, 15(16):14403–14413, August 2025. doi: 10.1021/acscatal.5c04191.

[309] Diego Ontiveros, Sergi Vela, Francesc Viñes, and Carme Sousa. Bandgap engi-

neering of mxene compounds for water splitting applications. *Journal of Materials Chemistry A*, 11(25):13754–13764, 2023. doi: 10.1039/D3TA01933K.

[310] John P. Perdew, Kieron Burke, and Matthias Ernzerhof. Generalized gradient approximation made simple. *Physical Review Letters*, 77(18):3865–3868, 1996. doi: 10.1103/PhysRevLett.77.3865.

[311] Carlo Adamo and Vincenzo Barone. Toward reliable density functional methods without adjustable parameters: The PBE0 model. *The Journal of Chemical Physics*, 110(13):6158–6170, 1999. doi: 10.1063/1.478522.

[312] Xiaobin Hui, Xiaoli Ge, Ruizheng Zhao, Zhaoqiang Li, and Longwei Yin. Interface Chemistry on MXene-Based Materials for Enhanced Energy Storage and Conversion Performance. *Adv. Funct. Mater.*, 30(50):2005190, December 2020. ISSN 1616-301X. doi: 10.1002/adfm.202005190.

[313] Diego Ontiveros, Sergi Vela, Francesc Viñes, and Carme Sousa. Tuning mxenes towards their use in photocatalytic water splitting. *Energy & Environmental Materials*, 7(4):e12774, 2024. doi: 10.1002/eem2.12774.

[314] Xiao Tang, Xin Guo, Wenjian Wu, and Guoxiu Wang. 2d metal carbides and nitrides (mxenes) as high-performance electrode materials for lithium-based batteries. *Advanced energy materials*, 8(33):1801897, 2018.

[315] Haodong Shi, Chuanfang John Zhang, Pengfei Lu, Yanfeng Dong, Pengchao Wen, and Zhong-Shuai Wu. Conducting and Lithiophilic MXene/Graphene Framework for High-Capacity, Dendrite-Free Lithium–Metal Anodes. *ACS Nano*, 13(12): 14308–14318, December 2019. ISSN 1936-0851. doi: 10.1021/acsnano.9b07710.

[316] Yiran Li, Na Li, Shijun Zhao, Jun Fan, and Ji-Jung Kai. Strain-tunable electronic properties and lithium storage of 2D transition metal carbide (MXene) Ti 2 CO 2 as a flexible electrode. *J. Mater. Chem. A*, 8(2):760–769, 2020. doi: 10.1039/C9TA09185H.

[317] P. Villars, K. Cenzual, J. Daams, Y. Chen, and S. Iwata. Data-driven atomic environment prediction for binaries using the Mendeleev number: Part 1. Composition AB. *J. Alloys Compd.*, 367(1):167–175, March 2004. ISSN 0925-8388. doi: 10.1016/j.jallcom.2003.08.060.

[318] Leland C. Allen. Electronegativity is the average one-electron energy of the valence-shell electrons in ground-state free atoms. *J. Am. Chem. Soc.*, 111(25): 9003–9014, December 1989. ISSN 0002-7863. doi: 10.1021/ja00207a003.

[319] B. Meredig, A. Agrawal, S. Kirklin, J. E. Saal, J. W. Doak, A. Thompson, K. Zhang, A. Choudhary, and C. Wolverton. Combinatorial screening for new materials in unconstrained composition space with machine learning. *Phys. Rev. B*, 89(9):094104, March 2014. ISSN 2469-9969. doi: 10.1103/PhysRevB.89.094104.